EXPERIMENTAL STUDY OF THE EFFECT OF PARTICLE SIZE DISTRIBUTION ON HEAT TRANSFER WITHIN THE BED OF A ROTARY KILN

By

Sanjiv K. Dhanjal

B. Sc. (Chemical Engineering) University of Surrey, UK

A THESIS SUBMITTED IN PARTIAL FULFILLMENT OF

THE REQUIREMENTS FOR THE DEGREE OF

MASTER OF APPLIED SCIENCE

in

THE FACULTY OF GRADUATE STUDIES

DEPARTMENT OF CHEMICAL AND BIOLOGICAL ENGINEERING

We accept this thesis as conforming

to the required standard

THE UNIVERSITY OF BRITISH COLUMBIA

November 2000

In presenting this thesis in partial fulfilment of the requirements for an advanced degree at the University of British Columbia, I agree that the Library shall make it freely available for reference and study. I further agree that permission for extensive copying of this thesis for scholarly purposes may be granted by the head of my department or by his or her representatives. It is understood that copying or publication of this thesis for financial gain shall not be allowed without my written permission.

Department of Chemical Engineering

The University of British Columbia
Vancouver, Canada

Date Dec. 1, 2000

Abstract

Rotary kilns are some of the largest pieces of equipment found in industry. Their resilience and versatility makes them suitable for a wide variety of applications, such as the calcination of lime and alumina, reduction of iron ore, cement clinkering and solid waste incineration. Common to all of their uses is the need to thermally process a material, typically particulate, by directly firing a fossil fuel. A kiln consists of a refractory lined cylindrical furnace with its axis at a slight angle to the horizontal. Raw material is fed at the upper end and, by virtue of the kiln's rotation, it travels along its length. The burner is located at the lower end. As such, the kiln is a counter current heat exchanger, with hot combustion gases flowing upwards over a bed of particulate material traveling down.

To ensure efficient and quality processing, all of the material in a kiln needs to be heated up to temperature, without any of it overheating. This requires efficient heat transfer from the combustion gases to the bed and efficient heat transfer within the bed, to ensure all of the material is evenly heated. However, this is not always achieved. For example, it has been found in industry that fine material often remains unreacted. The reason has been attributed to the phenomenon of segregation, whereby the fines collect towards the center of the bed and so are shielded from the hot combustion gases.

Experiments on laboratory kilns have confirmed that segregation in the cross section of a kiln occurs rapidly. Within a few revolutions, the fines collect in the middle of the bed forming a core, often referred to as a "kidney". Since a kiln typically rotates at 1-2 rpm and material residence time is 1-4 hours, a bed that contains fines will be segregated for almost all of its time in the kiln. The fines will not be exposed to the hot gases and so may not react. On the other hand, a bed that contains mono-sized particles has been found to intimately mix. In such a bed all of the particles have an equal chance of being exposed to the hot gases. Since heat transfer within the bed is dominated by material advection, the bed is likely to be isothermal. From this it has been presumed that segregation is the cause of temperature non-uniformity in the bed cross-section.

While there has been no experimental data published confirming this, modeling work

has concurred with the premise that segregation is the cause of temperature non-uniformity in the bed cross section. The aim of this study is to investigate this through experimentation and to determine what level of fines cause temperature non-uniformity in the cross section of the bed.

To meet the study objectives a batch rotary kiln was designed. The furnace was lined with a dense refractory that, when hot, was used as the heat source for the bed. This would allow the heat rate to be calculated using radiation heat transfer theory. The furnace was first heated using a gas flame. When it was hot, material was inserted and the furnace rotated. The temperatures of the walls and in the cross section of the bed were measured using thermocouples and a data logger.

Sand was selected as the bed material since it is inert. A number of sand mixes with various levels of fines were made by using a sieve shaker. To quantify the level of fines the particle size standard deviation was calculated. This allowed the results to be extrapolated for other applications such as in industry where wide ranges of particle size distributions are common.

The design of the furnace was carried out by the use of models written specifically for this project. A one-dimensional model of the heat transfer between combustion gases and the furnace walls was written and used to ensure that the furnace could be heated using a gas flame. It was then modified to ensure the walls could in turn heat up the bed material. A two-dimensional model of the bed cross section was also written and used output data from the one-dimensional model to determine whether the temperature profile in the bed cross section could be measured practically. The models were used to design the pertinent furnace specifications. These were furnace I.D. = 400mm, sand bed depth = 100mm, lining = 70mm thick castable and insulation = 20mm thick blanket. These specifications formed the basis of the furnace mechanical design and were not altered once the experiments were started. Therefore, the models fulfilled their purpose.

The furnace was heated until the refractory hot face was 1100°C before the flame was extinguished. Sand was then inserted into it and the furnace rotated. Each test lasted for about 20 minutes and the bed was heated up to about 800°C. A temperature profile was subsequently obtained at select locations in the bed cross section. The number of bed

thermocouples was limited to four, since they tended to agitate the bed, affecting heat transfer. Since the locations were the same for each test, their range of temperatures was used to quantify the temperature non-uniformity in the bed. Using these temperatures, together with temperatures of the walls, the heat rate to the bed and corresponding heat transfer coefficient were calculated for each run.

In all runs it was found that the spread of the temperatures in the bed was between 100-200°C initially. The range dropped to less than 10°C after 20 minutes. The temperature data was used to calculate heat transfer coefficients and these were in the range 85-175 W/m^2K. A further interesting finding was that the rate of heat transfer across the covered bed surface was 3-6 times the rate across the exposed bed surface. This highlights the importance of conduction between the covered wall and particles adjacent to it. These data represent a significant contribution to the literature since very few studies are available at realistic kiln temperatures and for kilns with diameters above 0.25m.

To determine the effect of size distribution, the average range of temperature, heat rate to the bed and heat transfer coefficient were calculated for one minute time periods during each test. The values were then plotted with the standard deviation of particle size. Much scatter was observed in these plots and it appeared that size distribution had little effect on temperature uniformity in the bed and no effect on heat rate and heat transfer coefficient.

The results were somewhat surprising, since segregation was evident during the some of the runs. Finer particles could be seen underneath the layer of larger particles, below the bed surface. Therefore, for the size ranges studied segregation did not hinder heat transfer across the bed. Perhaps heat transfer is a stronger function of overall material flow and effective thermal diffusivity, as opposed to segregation.

This study provides a substantial amount of data at realistic kiln temperatures, something that is rare in the general literature. The data can be used for validating models of the heat transfer in the cross section of the bed, and so further understanding in this area.

Table of Contents

List of Tables

List of Figures

Acknowledgment

I am sincerely grateful to my supervisors Dr. A. P. Watkinson and Dr. P. V. Barr. Their guidance and support not only helped to develop this thesis but also my technical and personal skills.

I thank my friends and colleagues, for they provided a forum for discussing and resolving minor and major issues encountered in the course of this study. In particular, I am indebted to (in alphabetical order) Abba, Alissa, Diana, Gordon, Lee, Murugan, Nanda, Neeraj, Pierre, Robin (from University of Birmingham, UK), and Shawn for helping me take data during the high temperature trials and to Petar and Michael for providing computer support.

Finally, I thank my dear wife, Susan, who always stood by me. Her unconditional love, affection and encouragement carried me through this episode in my life.

Financial support for this work was provided by Dr. Watkinson's and Dr. Barr's NSERC grants.

Nomenclature

Symbol	Description	units
A	area	m^2
A_x, B_x, C_x	Factors used to simplify presentation	
A_y, B_y, C_y	of discretized Equation 4.8	
$\mathcal{A}$	variable in velocity profile	
	in rectangular grid	
$\mathcal{B}$	depth of active layer	m
	in rectangular grid	
b	parameter in Rosin-Rammler	
	distribution	
c	variable in velocity profile	
C	correlation coefficient	
c_p	specific heat capacity	J/kg K
d	diameter	m
$\bar{d}$	average diameter	m
ds_p	Sauter mean diameter	m
d_i	diameter of sand in	m
	sample i	
$E_{a,b}$	notation used to write out	
	discretized equations	
F	flux	
$\mathcal{F}$	View Factor	
g	acceleration due to gravity	m/s^2
h	heat transfer coefficient	W/m^2 K
$[I]$	identity matrix	

k	effective thermal conductivity	W/m K
l	linear distance	m
M	mass of sand sample	kg
m	variable used for clarification	
m_i	mass of size fraction of sand in sample i	kg
N	total number of particles	
n	variable used for clarification	
n_i	number of particles in sand sample	
n_{RR}	parameter in Rosin-Rammler distribution indicating width of particle size range	
$\vec{n}$	unit vector	
Q	heat transfer rate	W, kW
q	heat flux	W/m^2
R	resistance to radiative heat transfer	
Res	residual through sieve	kg
r	radius	m
S	sum of squares of residuals in in linear interpolation	
S_t	sum of squares of differences between average and point values	
s	standard deviation	
T	temperature	K
$\bar{T}$	average temperature	K

$\vec{\mathcal{T}}$	intermediate variable in approximate factorization	
t	time	s, min
t^*	dimensionless time	
u	velocity in horizontal direction	m/s
v	velocity in vertical direction	m/s
x	horizontal distance	m
y	vertical distance	m

Greek

α	thermal diffusivity	m^2/s
α_g	absorptivity of gas	
β	bed angle, as described in Figure 4.9	
ϵ	emissivity	
θ	angle in cylindrical coordinates	radians
θ^*	dimensionless temperature	
μ	viscosity	Pa s
ρ	density	kg/m^3
σ_{SB}	Stefan Boltzmann coefficient, 5.67×10^{-8}	W/m^2K^4
σ_p	population standard deviation of particle size	m
σ_p^*	normalized population standard deviation of particle size ($\frac{\sigma_p}{d_p}$)	
σ_T	population standard deviation of temperatures B1 to B4	K
ϕ	time advance variable = 1.0 for fully implicit = 0.5 for trapezoidal	

Ψ	ratio of heat transferred between covered wall and covered bed and exposed wall and exposed bed $\frac{Q_{cw \to cb}}{Q_{ew \to eb}}$	
Ω	temperature range	°C
	Max$[T_{B1} \ldots T_{B4}]$ - Min$[T_{B1} \ldots T_{B4}]$	
ω	rotational speed	rad/s

subscripts

a	ambient
CV	two dimensional control volume
b	bed
bs	bed surface exposed to wall
eb	exposed bed
ew	exposed wall
g	gas
I	max. horizontal cell number
	e.g. for 20 point mesh, $I = 20$
i	horizontal cell number
in	initial
j	vertical cell number
o	overall
p	particle
rad	radiative
s	rectangular bed surface
w	wall
x	horizontal direction
y	vertical direction

superscripts

n	time step
$*$	normalized
$\bar{}$	average

Chapter 1

Introduction

Industrial experience with rotary kilns has indicated that fine particles can be difficult to process. Isothermal experiments with particulate materials in laboratory kilns have have identified that when there are differences in the size of particles, segregation of finer particles to the center of the bed occurs. This has lead to the premise that segregation shields finer particles from the kiln heat source, leading to a temperature non-uniformity within the bed. To date, however, no experimental data has been found that verifies this. This thesis attempts to provide some. In particular this thesis will investigate the role of particle size distribution on heat transfer within the bed of a rotary kiln furnace.

A rotary kiln is a refractory lined cylindrical furnace that is used to thermally process particulate material. It is typically 2-4m in diameter, up to 100m long and inclined a few degrees to the horizontal, see Figure 1.1. Raw material is fed into the upper end and it travels along the kiln length as the kiln rotates. At the lower end a fossil fuel is fired, using a suitably designed burner, to provide the energy for the process. An induced air fan draws ambient air through the kiln providing oxygen for the fuel. Therefore, within the kiln there are two distinct regions; a free-board region, where the fuel burns and combustion gases flow, and a bed region, where the particulate material flows.

An efficient kiln is one where much of the energy from the fuel is transferred to the material being processed. This requires optimum fuel combustion, optimum heat transfer between the free-board and bed surfaces and optimum heat transfer through the bed to ensure all of the bed material receives the energy required to process it. In designing for such a system a thorough understanding of all of the energy transfer processes is necessary. This study attempts to further the understanding of one of these processes, heat transfer within the bed.

Heat is transferred through the bed of a rotary kiln primarily through advection, or material flow. This material flow is complex and studies have identified a number of

different modes of bed flow behavior. The most desirable of them is the rolling mode, see Figure 1.2, because it provides good mixing with a steady angle of repose. The latter ensures continuous surface renewal, which in turn facilitates efficient particle agitation. Heat transfer is maximized, allowing reactions to proceed, without causing attrition and and excessive dust generation. Therefore, much of this study will focus on the rolling mode.

In the rolling mode there are two distinct regions, see Figure 1.2. Nearer to the surface, the material cascades downwards in a continuously shearing region (active region or layer), while close to the walls a plug flow region is established, where material moves in a rigid body motion, $\frac{\partial u}{\partial \theta} = 0$.

The rolling bed maximizes heat transfer to and throughout the bed, helping to uniformly process all of the material. However, as particles cascade down in the active layer, the particle ensemble dilates. Differences in the size of the particles then leads to segregation, as smaller particles pass through the voids created between the larger ones. Segregation, therefore, causes de-mixing and, it is believed, hinders heat transfer.

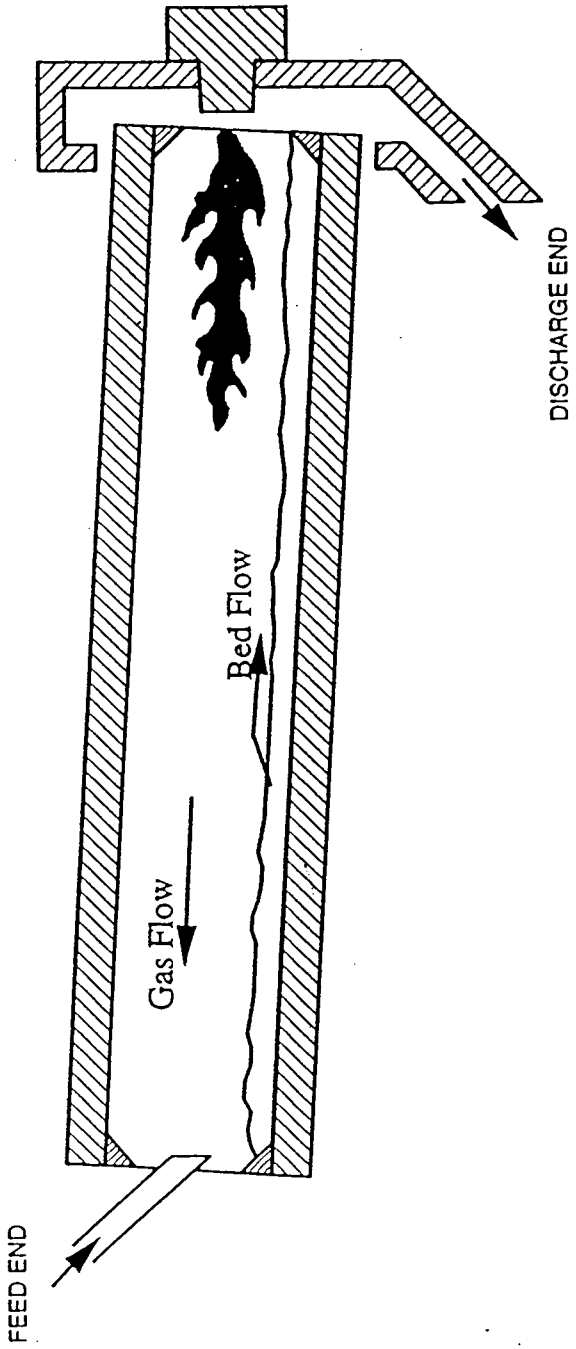

Figure 1.1: Schematic of Rotary Kiln

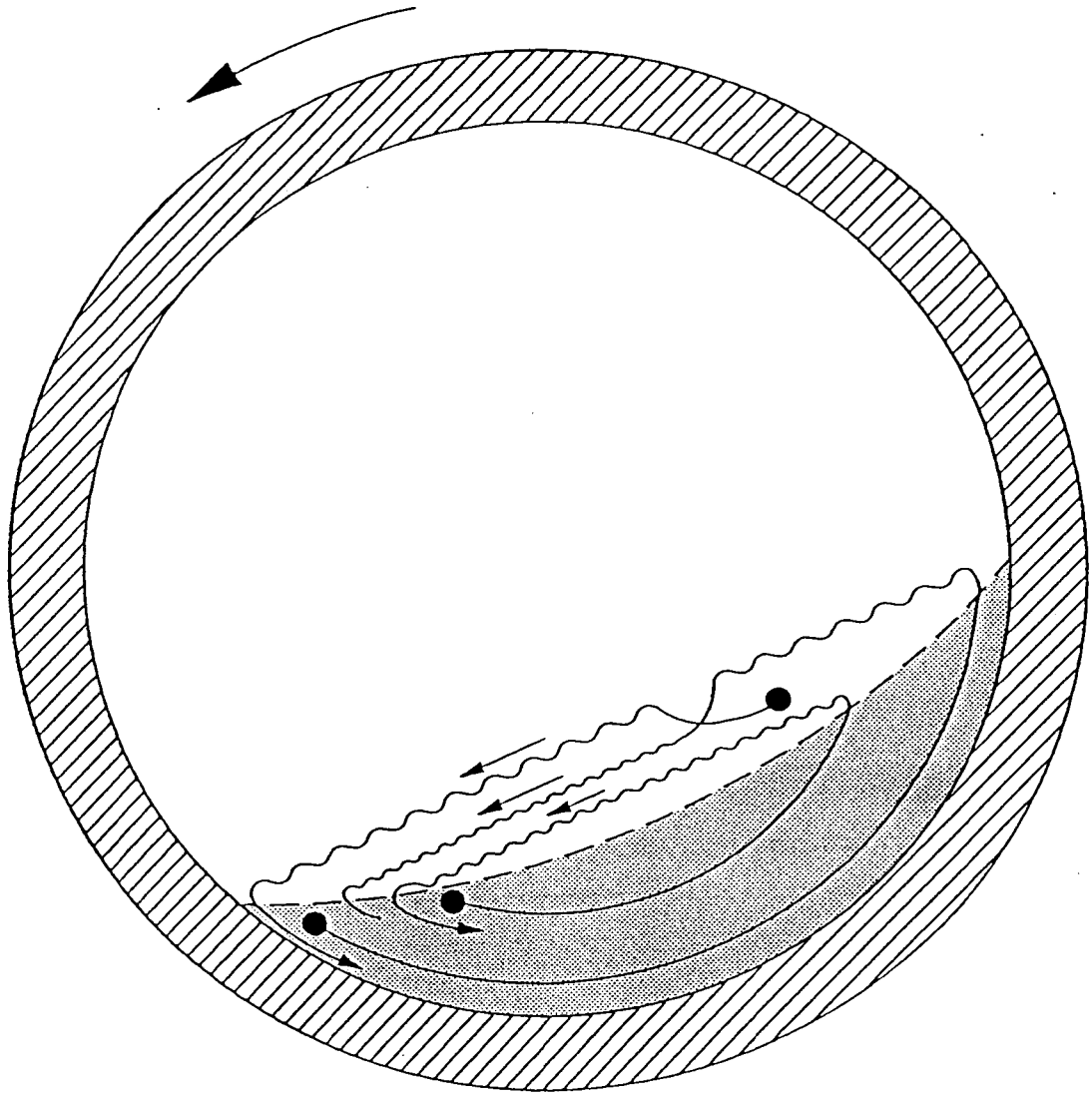

Figure 1.2: Rolling Bed Motion Depicting a Top Active Layer and Bottom Plug Flow Region

Chapter 2

Literature Review

Relative to the free-board, there is little literature pertaining to the bed of a rotary kiln and it tends to concentrate on material flow and mixing. Few workers have extended the studies to include heat transfer in the bed.

This section will first review work carried out in the area of material flow and mixing in the cross-section of a rotary kiln. Following this studies more specific to material segregation, which is a major cause of de-mixing, will be described. Finally heat transfer will be reviewed.

2.1 Material Flow

Material flow in a rotary kiln may be resolved in the axial and transverse direction. However, it is transverse flow that determines most of the transport processes. Transverse flow determines the degree of mixing (or segregation) as well as the axial motion because material only advances axially when it is turned over in the cross-section. Therefore, one can appreciate the importance of transverse motion in heat transfer.

Flow studies associated with the cross section of a kiln have indicated that bed motion changes with rotational speed (Henein 1980). As the rotational speed is increased, the bed motion changes from slipping to slumping followed by rolling, cascading, cataracting and finally centrifuging, see Figure 2.1.

When a kiln with a particulate bed is rotated slowly, the bed behaves as a bulk and rotates with the kiln. If the gravitational force is greater than the centrifugal force and frictional force between the bed particles and wall surface, then the bed will "slip". At higher rotational speeds and/or with rougher walls there comes a point when the gravitational force is overcome by the centrifugal and frictional forces, and so the bed will continue to rotate with the kiln. This occurs until the bed's radial inclination exceeds

the static angle of repose of the particles. As the kiln is further rotated, the weight of the particles associated with the region above the static angle of repose will eventually overcome the shear stresses within the particulate body, and these particles will avalanche down the surface of the bed. The angle at which the particles begin to avalanche is sometimes called the maximum angle of stability (McCarthy, Shinbrot, Metcalfe, Wolf, and Ottino 1996) and once the avalanche is complete, the bed inclination adopts the static angle of repose. As the kiln continues to rotate, so will the bed until the maximum angle of stability is once again reached. Then the whole cycle is repeated. This type of bed behavior is referred to as "slumping".

If the rotational speed of the kiln is high enough such that the bed rotates to its maximum angle of stability before the avalanching particles come to a halt, the bed is said to be "rolling". The avalanching particles produce a continuously shearing region, which is referred to as the "active region", "active layer" or "shear layer". This layer takes on a lens type shape. At the bottom of the avalanche the particles leave the active layer and enter a "plug flow" region where they rotate with the kiln in rigid body motion. In the rolling mode particles continuously enter and leave the active and plug flow regions.

A further increase in kiln rotation causes the top part of the bed, called the apex, to rise above the bed surface before gravitational forces bring the particles down to "cascade" over the bed surface. Even further increases in rotational speed lead to "cataracting" and finally "centrifuging". In the centrifuging mode, the particles centrifugal force overcomes gravity, and hence a rotational Froude number ($\frac{\omega^2 r}{g}$) of 1.0 indicates the onset of centrifuging.

Of the various types of bed behavior described above, rolling is preferred in industrial rotary kilns. Rolling provides good mixing at a steady angle of repose. Surface renewal is continuous which allows for efficient heat transfer. Cascading, in fact, appears to provide better particle mixing. Workers have operated test kilns in the cascading mode to ensure intimate mixing prior to segregation studies (Nityanand, Manley, and Henein 1986; Pollard and Henein 1989). This would imply that cascading provides better heat transfer also. However, cascading can lead to attrition and excessive generation of dust. Furthermore, kiln operation in a cascading mode would require extra mechanical power.

In the rolling mode, there are two distinct regions, see Figure 2.2. Nearer to the surface of the bed the material travels downward in a continuously shearing region (the active region) while closer to the wall a plug flow region is established where material moves in rigid body motion. The particles enter the shearing region from the plug flow region once they reach their static angle of repose and re-enter the plug flow region towards the lower part of the active layer.

In his extensive study of the transverse motion in the bed of a rotary cylinder, Henein (1980) was able to develop bed behavior diagrams that delineated the various types of bed behavior. He was able to relate bed behavior to rotational speed, bed depth, percentage fill and rotational Froude number. This allows one to predict the mode in which a bed behaves. Another important finding of Henein (1980) was that axial motion, to the extent that would occur in a rotary kiln, does not significantly alter transverse behavior. Therefore, he was able to utilize batch experiments to investigate bed behavior in a continuous kiln.

In the case of particles with similar size, shape and density, experiments indicate that intimate mixing of particles eventually occurs with a rolling bed (Woodle and Munro 1993). The reason is that particle mixing within the active region is intense and so particles entering the active region have an equal chance of re-entering the passive region at any radial location. The rate at which mixing occurs, however, is dependent on kiln loading and particle/wall and particle/particle friction (Woodle and Munro 1993; Nityanand, Manley, and Henein 1986).

2.2 Segregation

In industrial rotary kilns mixing is not always adequate and it has been observed that, for example, smaller particles of lime take longer to calcine than larger ones (Sunnergren 1979; Von Wedel 1973). This implies that smaller particles are not exposed to the hot gases for as long as the larger particles, for if they were, then the time required for them to calcine would be less. The reason for this is attributed to particle segregation, which in the examples cited is due to size. Numerous workers have shown that smaller particles

tend to congregate in the middle of the bed rather than travel to the region of the bed that is exposed to the free-board.

Segregation due to density differences has also been observed . One example is in the direct reduction of iron ore (Henein 1980), where denser iron ore particles segregate to the middle of the bed in the same way as the smaller limestone particles described above. The iron ore particles are surrounded by lighter coal particles which form an annulus around them.

A review of segregation by Williams (1976) indicates that segregation may occur due to differences in particle size, density, shape and resilience, although he stated that segregation due to particle size is by far the most common in industry. The three segregation mechanisms that he described are

Trajectory Segregation The distance that a particle is projected is equal to $\frac{u_{in}\rho_p d_p^2}{18\mu}$. Therefore, a particle with larger mass and/or diameter will be projected further, if all other parameters are kept the same.

Percolation In mixtures of different sized particles, the size of the voids between larger particles may become large enough for smaller particles to pass through them. This will result in smaller particles percolating through the voids of the larger ones leading to segregation. If the particles are in motion, then the voids will be larger, due to dilation of the particle ensemble. This allows percolation of particles of a size that would not pass through the voids formed when the particulate mass is stationary. Therefore, in a bed under motion, percolation can occur even when there is a only a small difference between the sizes of the larger and smaller particles.

Vibration In the case of a vibrating bed, large particles will rise to the surface while smaller particles will segregate to the bottom. Since there is little, if any, vibration in rotary kilns, this type of segregation will not be discussed further.

Dolgunin, Kudy, and Ukolov (1998) conducted segregation experiments on mixtures of particles avalanching down an inclined surface. They found that larger and denser particles tended to concentrate towards the center of the particulate mass. They attributed

this to particle collisions. When particles collide the exchange of momenta means that larger and denser particles end up with lower velocities than smaller and lighter particles. As particles travel down a chute, a high solids concentration occurs in the center which is favorable to particles with a smaller velocity fluctuation amplitude. Therefore, larger and denser particles migrate towards the center. This segregation mechanism would tend to negate the effects of trajectory segregation, described above, in granular flows.

2.2.1 Segregation Experiments

Segregation may occur axially or radially in a rotary kiln. Roseman and Donald (1962) investigated segregation in horizontal cylinders and concluded that radial segregation always occurs whereas axial segregation may or may not occur.

The rate of axial segregation is relatively slow. Literature reports that axial segregation may not fully develop for 500-10,000 revolutions (Roseman and Donald 1962; Carley-Macauly and Donald 1962) . This equates to between 4 and 80 hours for a kiln that is rotating at 2 rpm. Since overall residence times in industry are less, axial segregation is unlikely to fully develop. However, a degree of axial segregation affects the residence time of individual particles. Although this may not be significant with respect to heat transfer, the extent of chemical or physical reaction may be affected, possibly to an extent that impacts quality.

Radial segregation is a much more rapid process and takes 2-10 revolutions. Nityanand, Manley, and Henein (1986) and Pollard and Henein (1989) have conducted tests on the kinetics of radial segregation and concluded that the rate followed first zero kinetics, that is, the rate of segregation is a constant. These workers quoted, however, that other studies had reported the kinetics to be first order, that is rate is proportional to the degree of segregation.

Henein (1980) took quantitative measurements of the segregation phenomenon. He used binary mixtures of sand and limestone, and investigated mixes with about 5-25% fines concentration. The size ratios were 2.2:1 for the sand and 8:1 for the limestone. He made the following significant findings

- Bed behavior is not affected by fines. For example, in the case of a rolling bed, the dynamic angle of repose and active layer thickness do not change and, in a slumping bed, the static angle of repose, shear angle and slumping frequency do not change when the quantity of fines is varied.

- Since the flow characteristics of the bed are not significantly altered by the presence of fines, segregation by flow must be negligible. Therefore, the primary cause of segregation in a rotary kiln is percolation.

- The segregated core is composed of all of the fines packed together with a quantity of the coarser particles such that the packing density is maximum for that particular mixture. The segregated core is surrounded by an annulus of coarse particles.

- From the above, the size of the segregated core may be deduced. Its shape was found to be similar to the shape of the bed.

- A second segregated region close to the apex is also formed. This consists of very fine material that is able to percolate through the shear layer and through the plug flow region. The size of these fines are less than about 15% of the size of the larger particles (Boateng and Barr 1996a).

2.2.2 Segregation Modeling

Boateng (1993) developed a model of the transverse flow of particles in a rotary kiln . He employed the continuum assumption and developed a mean velocity profile by solving constitutive equations that are normally associated with granular flows. In such models analogy is made with kinetic theory. In granular flow individual particles have velocities that are different to the mean velocity associated with all of the particles within a finite volume, in a manner similar to molecules in a gas. The property that is analogous to thermal temperature of a gas is called granular temperature (units m^2s^{-2}) and this is a measure of the particle kinetic energy. A balance of granular temperature forms one of the constitutive equations and it needs to be solved together with the mass and momentum balance, see for example Lun, Savage, Jeffrey, and Chepurnity (1984).

Boateng (1993) applied granular flow theory to the active layer where it is appropriate for such analysis. In the plug flow region this is not required since plug flow exists. The resulting velocity profile was then used in a segregation model that was applied to the active region, implying that the fines are not small enough to percolate through the plug flow region.

The segregation model considered a binary mixture of particles and used published modeling techniques for the phenomenon. Boateng's model, which is also described in Boateng and Barr (1996a), used the terms jetsam, to describe sinking particles and flotsam to describe floating particles. Essentially, a net percolation velocity is assigned to the bed and used to solve for jetsam particles. Determining the net percolation is the challenge and it is a function of the voids. The net percolation velocity was determined using a model developed by Savage and Lun (1988). The model results compared well with the experimental results of Henein (1980).

Dolgunin, Kudy, and Ukolov (1998) developed a segregation model that is similar to the one used by Boateng. They added a migration term that is related to the mean distance between particles. With the addition of the new term, they found improved agreement with experimental results, especially for the case of segregation due to density differences.

In addition to the continuum approach, several workers have developed discrete particle models to investigate segregation. Meakin and Jullien (1992) describe two- and three-dimensional models of particles of different sizes being deposited onto a heap of particles. In these models the path of a single particle is tracked as it falls down the heap taking the steepest path. Once the particle arrives at a location where further movement down is prevented by other particles, the particle stops and its location is then fixed. Only one particle moves at any one time and its size is selected randomly from a specified range. Their results demonstrate segregation due to size.

Ristow (1994) has used "molecular dynamics" to model particles of the same size but different density and particles of the same density but different size in a rotating drum in two dimensions. In his article he states that he modeled 600 particles, twelve of which were tracer particles. He tracked the tracer particles to determine how long they took to

segregate.

Baumann, Jánosi, and Wolf (1994) investigated segregation of particles due to size in a rotating drum using a tracking model that seems to be similar, in principle, to that of Meakin and Jullien (1992) above. They referred to their technique as "bottom-to-top restructuring", or "BTR". They used a "molecular-dynamics simulation" type model and excluded inertial and elasticity effects. They started their simulation with the drum full of particles (which are in fact discs because the model is two-dimensional) that are well mixed. Then the drum is allowed to rotate by a small angle $\leqq 1°$. The lowest particle is allowed to fall along the path of steepest descent until it arrives at a local minimum. After this the next particle above falls in the same manner. By doing this segregation occurs because smaller particles get stuck in niches along an incline that larger particles would pass over. Once all of the particles have moved, the drum is rotated further by the same small angle.

Their model results show segregation, indicating that geometric affects alone can lead to it. They do recognize, however, that in the case of irregular shaped particles, friction, inertial effects and collective organization also play a role.

2.3 Heat Transfer

Studies of the free-board have identified the heat transfer paths in a rotary kiln as those shown in Figure 2.3 (Barr, Brimacombe, and Watkinson 1989a). They are

1. Free-board gas to exposed bed (radiation and convection)
2. Free-board gas to exposed wall (radiation and convection)
3. Exposed wall to exposed bed (radiation)
4. Exposed wall to exposed wall (radiation)
5. Covered wall to covered bed (radiation and conduction)
6. Loss to surroundings (conduction through refractory and convection to atmosphere)

In addition heat is also transferred within the bed in a manner similar to a packed bed, but with an added advective component. The heat transfer paths within a packed bed are shown in Figure 2.4. These paths are

1. Within particle conduction
2. Conduction across the particle-particle contact area
3. Particle to particle radiation
4. Interstitial gas convection

In this section the free-board studies will be reviewed first, followed by studies that concentrate on the bed.

2.3.1 Heat Transfer in the Free-Board

Due to the high temperatures that occur in a kiln, radiation is the dominant mode of heat transfer. Analysis of such heat transfer is complex because of the arduous radiation paths. For example, a portion of the energy from the free-board that radiates to the exposed wall is reflected and re-absorbed back into the free-board. Another portion is reflected onto another part of the exposed wall only to be partly absorbed and partly reflected back to the bed, etc.

Another complicating factor is that the walls play a regenerative role in the heat transfer process (Barr, Brimacombe, and Watkinson 1989a). When the wall is exposed to the free-board it gains a net amount of energy from the free-board. As the kiln rotates, the part of the wall that was previously exposed becomes covered by the bed and, since the bed is cooler (or warmer in some cases), energy transfer occurs. Studies by Barr, Brimacombe, and Watkinson (1989a) have shown that this regenerative effect produces a cyclical temperature in a region of the inner refractory wall, a region that they called the "active" refractory region.

Barr, Brimacombe, and Watkinson (1989a) investigated the various heat transfer paths in a kiln by way of a two-dimensional cross sectional model that was marched along the

length of the kiln. The cross sectional model accounted for all of the heat transfer paths described above, except for the heat transfer within the bed, implying that the bed was well mixed. The results of the model agreed well with experimental data and suitable values for heat transfer coefficients for the paths shown in Figure 2.3 were determined.

The fact that a cross sectional model that is marched along the length of the kiln can adequately describe the heat transfer process indicates, as Barr, Brimacombe, and Watkinson (1989a) mentioned, that heat transfer in a kiln is a local phenomenon, dominated by parameters at that particular axial location. This was further confirmed in a study by Jenkins (1998), who compared the results of a three-dimensional radiative model of a kiln with the same model but in only one dimension. It was discovered that the overall heat flux to the walls within the flame region only differed by a few percent, although the local heat fluxes differed more.

In order to predict the heat transfer characteristics of the free-board one must appreciate a number of phenomena. First, combustion gases that have an electric (e.g. dipole or quadrapole) moment, such as CO_2, CO, H_2O, NH_3 and hydrocarbons, absorb and emit radiation only within certain wavelengths. Their radiative characteristics need to be determined. Second, the velocity and concentration profiles of the gas need to be known. Since, these are a function of the combustion of the fuel and system aerodynamics, determining them can be a challenge. Only with knowledge of the radiative characteristics and the velocity and concentration profile of the free-board gas, can the heat transfer be calculated. One must also understand that all these phenomena are coupled.

The radiative characteristics of the gas may be determined using the weighted summation method (Smith, Shen, and Friedman 1982). Jenkins and Moles (1981) and Barr, Brimacombe, and Watkinson (1989b) have used this method in their models. The velocity profile requires a flow model or measurements, if possible. Jenkins and Moles (1981) developed a relatively simple but effective aerodynamic flow model by calculating how much combustion air would be entrained by the flame jet. The velocity profile is then used as input to a combustion model to calculate a concentration profile. Finally, the Hottel zone method can be used to calculate heat transfer (Hottel and Sarofim 1967).

Establishing the velocity profile inside a rotary kiln can be quite a daunting task, es-

pecially if the air entering a kiln is awkward and causes uneven aerodynamics. The aerodynamics have a dominating effect on combustion, and hence, heat transfer. Therefore, this is an area of extensive study and it is making use of computational fluid dynamics, (Alyaser, Barr, and Brimacombe 1997; Bui, Simard, Charette, Kocaefe, and Perron 1995; Mastorakos, Massias, Tsakiroglou, Goussis, Burganos, and Payatakes 1998).

2.3.2 Heat Transfer in the Bed

Many of the earlier studies of kilns paid little attention to heat transfer within the bed. The bed was typically considered isothermal (Barr 1986; Gorog, Brimacombe, and Adams 1981) or not considered at all (Jenkins and Moles 1981). In the latter citation the bed and wall were considered as a single heat sink. These studies, nevertheless, provided useful insights into the operation and performance of rotary kilns. One reason is that bed studies have indicated that when a bed is well mixed the thermal resistance within it is small (Imber and Paschkis 1962). However, in the case of a segregated bed, this may not be the case and so heat transfer within such beds needs to be investigated.

As mentioned above, the heat transfer paths within the bed of a rotary kiln are similar to those in a packed bed. However, the bed in a rotary kiln has an additional advective component due to material transport. The bed of a rotary kiln may, therefore, be analyzed in a manner similar to that of a packed bed as long as advection is accounted for.

One method used to investigate packed beds is to consider the particles and the interstitial fluid as a continuum. By doing so, a single temperature represents a packet of particles and gas and so one equation can be used to represent the heat transfer. The drawback with this method is that particle surface temperatures, which determine radiative properties, and local particle dynamics, that can be used to describe a particle reaction, are not considered. Nevertheless, a continuum model has been developed for the bed and this will be described next.

Following on from the flow and segregation model, described in Section 2.2.2, Boateng (1993) continued with the continuum assumption to develop a heat transfer model of the cross section of the bed. He solved the energy equation using an effective conductivity term (Schotte 1960) to describe the diffusive heat transfer component within the bed.

This effective conductivity term was enhanced in the active region by a factor relating to the mixing rate, as determined in the flow model. The boundary conditions for the cross-sectional model, essentially heat fluxes, were calculated independently using a one dimensional model of the kiln along the axial direction which was similar to the model developed by Barr, Brimacombe, and Watkinson (1989b).

The validation of the above model was carried out largely by converting the two-dimensional model results into one-dimensional average values at axial locations and comparing them with experimental data. Some two-dimensional validation was carried out but it appears that no measurements were taken in the bed, only in the free-board and walls. Even so, agreement with experimental data was good lending "some confidence" to the model (Boateng and Barr 1996a).

Boateng (1993) reported that non-uniformity in the cross-sectional temperature is only significant when there is radial segregation. When uniformly sized particles were used the bed was well mixed and the resulting temperature profile was isothermal. This latter point would explain why studies employing the well mixed bed assumption have been successful.

It is worth mentioning some other studies where heat transfer within the bed of a rotary kiln has been considered. Bui, Simard, Charette, Kocaefe, and Perron (1995) developed a three-dimensional model of a coke calcining kiln using a computational fluid dynamics package that is comprised of a number of sub models. The bed is simulated as a pseudo fluid with a higher viscosity in the plug flow region and a lower viscosity in the active region. A third value for viscosity is applied in the axial direction to ensure correct axial mass flow. The overall model results were validated using pilot and full size data and agreement was reasonable. However, the authors did recognize that analysis of the bed in such a manner limits the model's capabilities.

Yang and Farouk (1997) developed a two-dimensional cross-sectional model and a one-dimensional axial model of the kiln. The two models are used together similar to the model by Boateng and Barr (1996a). However, these authors used the equations developed for granular flow theories throughout the whole of the bed cross-section. This is not strictly applicable because granular flow theories compare the motion of particles to

the motion of molecules in a gas. This is appropriate for granular flow down an inclined chute or in the active layer because such particles are in a state of random motion whereas material in the plug flow region of the bed behaves as a rigid body. Their model results for bulk temperatures along the kiln axis, however, compared well with experimental data.

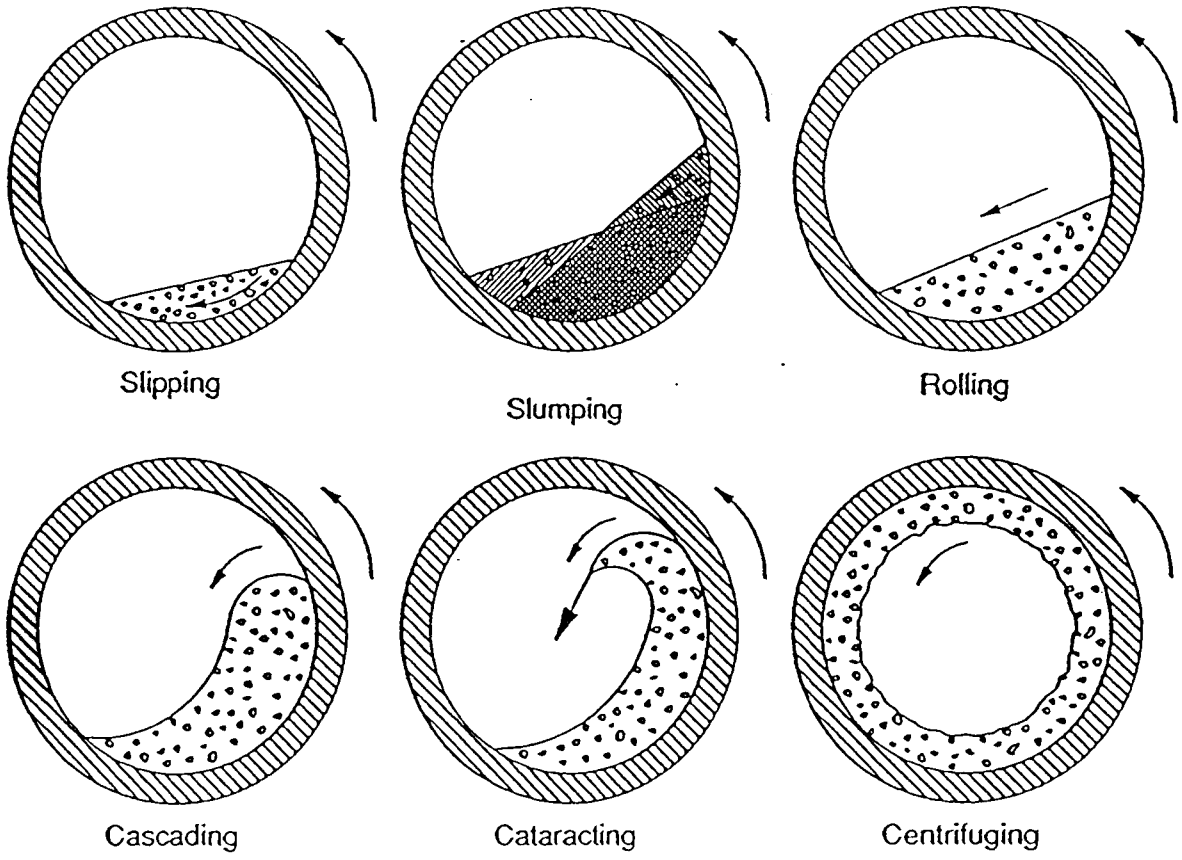

Figure 2.1: Modes of Bed Behavior in a Rotary Kiln

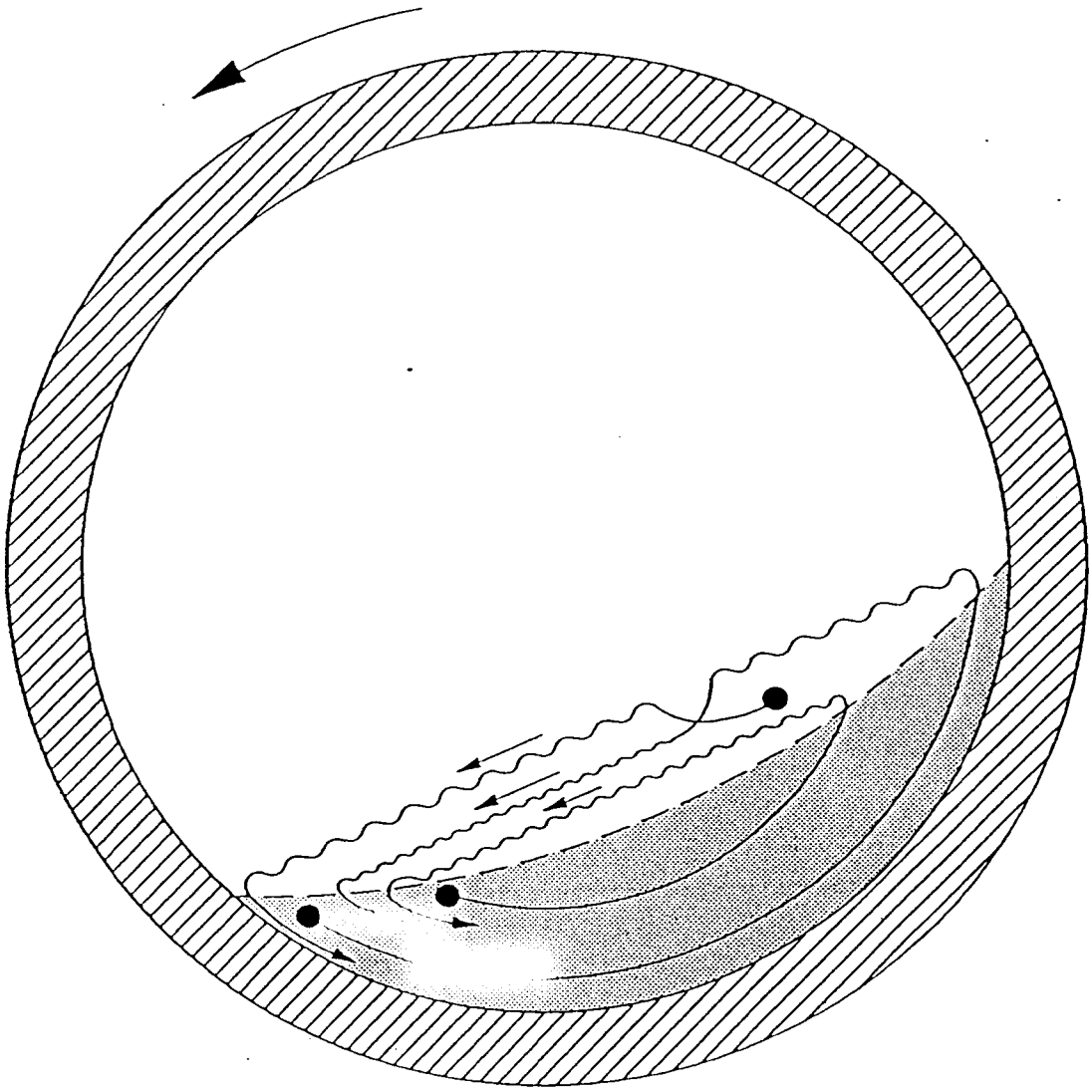

Figure 2.2: Rolling Bed Motion Depicting a Top Active Layer and Bottom Plug Flow Region

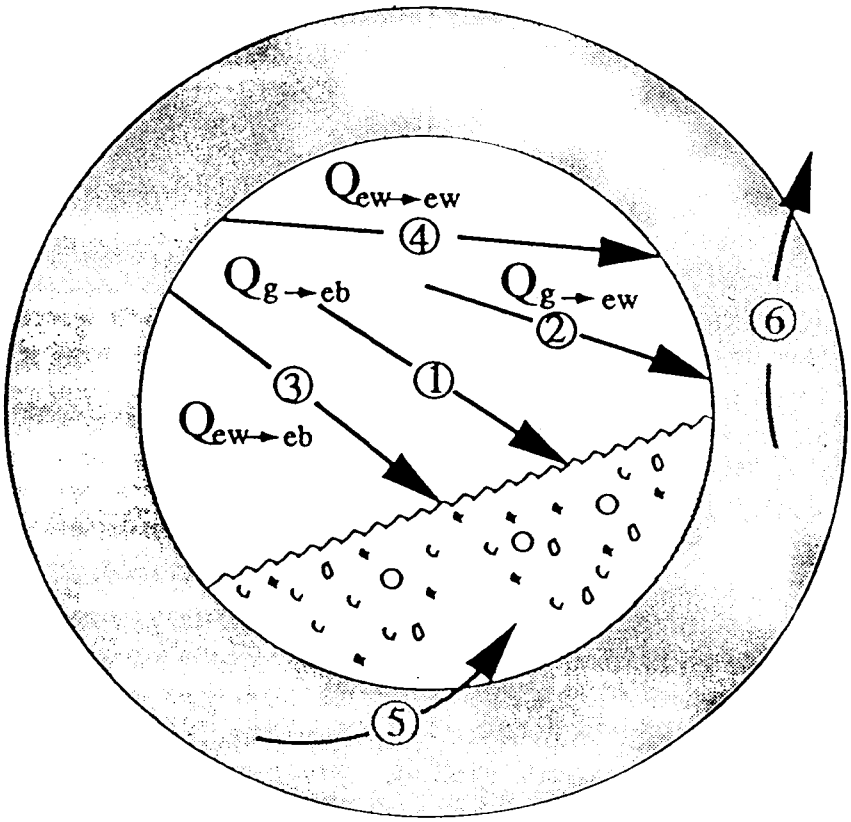

Figure 2.3: Heat Transfer Paths Inside a Rotary Kiln

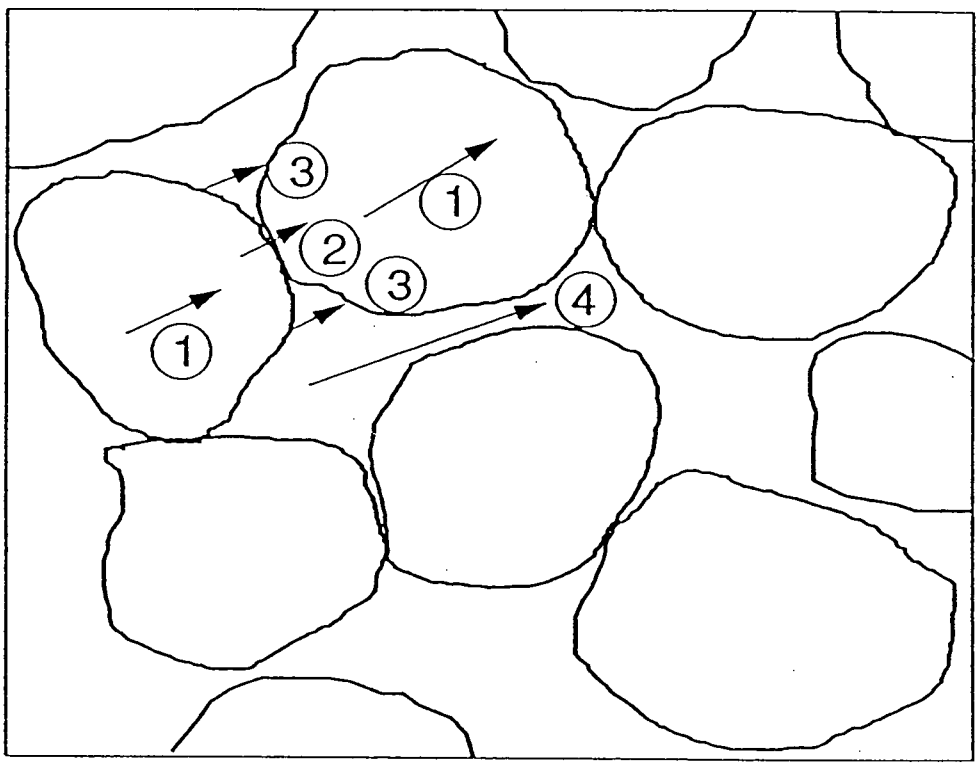

Figure 2.4: Heat Transfer Paths Within a Packed Bed

Chapter 3

Objectives and Scope of Study

Studies of the material flow in rotary kilns have provided the following useful information.

- Transverse flow plays the dominant role in the particle mixing rate and, therefore, heat transfer and reaction rate. Axial flow and, hence, overall residence time, is also determined by the transverse flow because the material only advances axially when it is turned over in the cross-section.

- The are a number of modes of transverse bed behavior depending on material and operational properties, see Section 2.1. Of the various modes, rolling is preferred because it allows for maximum particle mixing and heat transfer without excessive particle agitation and dust generation.

- When the size distribution of the particulate burden in the kiln is such that a quantity of fines below a certain size range exist, segregation occurs. Segregation may be axial or radial, see Section 2.2.2.

- Axial segregation affects particle residence time. While this may not affect heat transfer significantly, it may affect the degree of chemical reaction. Therefore, axial segregation may play an important role in determining product quality.

- When radial segregation occurs, the fines create a primary core at the center of the bed and, in cases of very small diameter fines, less than 15% of the diameter of larger particles, a secondary core at the kiln walls close to the apex. The overall effect of segregation is one of de-mixing and is, therefore, detrimental to the heat transfer process.

- The fines do not alter the overall transverse bed behavior.

- The mechanism by which segregation occurs is predominantly percolation.

- The primary core consists of all the fines (excluding those in the secondary core) plus a quantity of coarser materials, such that the bulk density of the core is maximum for that particular mixture. Therefore, one can estimate the size of the core, see Henein (1980). The shape of the core is similar to the shape of the bed.

- The rate of segregation is rapid, occurring between 2-10 revolutions of the kiln (Pollard and Henein 1989; Nityanand, Manley, and Henein 1986). Therefore, unless the bed is continuously agitated, the bed remains segregated throughout the length of the kiln.

Radial segregation is suspected to be the primary cause of temperature non-uniformity in the cross section of a bed (Boateng 1993). However, most investigations of the segregated core are focused on flow and, hence, experiments are conducted for the isothermal case. While these studies have provided interesting and informative insights, the mineral processing rotary kiln industry requires to know the effect on heat transfer within the bed, which ultimately determines product quality.

It is appreciated that axial segregation may also impact product quality, however, it will not be the focus of this study and will remain outside the scope.

Boateng (1993) provided advancement in this area by his study of the transverse flow and heat transfer in a rotary kiln, see Sections 2.2.2 and 2.3.2. In his study he developed a model of the flow and heat transfer in the transverse section of the kiln. Included was a segregation model for a binary mixture of particles, which was validated independently of the heat transfer, using the cold segregation experimental data of Henein (1980). His hot model results were validated using experimental results from Barr (1986) plus his own experiments. However, the hot runs were largely for a well mixed bed with a narrow size range of particles.

Giving that radial segregation is perhaps the dominant cause of temperature non-uniformity in the transverse section of a bed, which may lead to product inconsistencies, what appears to be lacking in the literature is a thorough study of heat transfer in a segregated bed. Therefore, the objective of this work is to initiate such a study. The first step is to provide hot data for a segregated bed that can be used to develop a

better understanding of segregation and its effect on heat transfer. With this information predictive models may be developed. A second objective is to establish what level of fines causes significant temperature non-uniformities. To quantify the level of fines, particle size distribution is to be used. This is a more practical method than using binary mixtures with fine and coarse particles. The results can be applied in industry to determine whether a particular kiln feed material is suitable or not for processing in a kiln. Finally, an inert bed material, sand, is to be used to avoid complexities associated with chemical reactions.

In view of the above the following constitutes a scope of study that will meet the study objectives:

1. Design and build apparatus suitable for the study of heat transfer in the cross section of the bed.

2. Make a range of sand mixes with varying size distributions. For each mix make qualitative measurements of the flow characteristics. Apply a heat source to each mix and measure the temperature in the transverse section.

3. Determine how uniform the temperature is and calculate heat transfer data that can be used for modeling purposes.

Chapter 4

Test Furnace Design

Having established the scope of the research program, the next stage was to develop a test furnace in which suitable experiments could be performed. Since axial temperature gradients are negligible with respect to heat transfer, and axial motion has a negligible effect on radial motion, a batch furnace would suffice for this exercise. The batch furnace was developed by adopting a stepwise procedure.

First a bed depth in which measurable temperature gradients occur was determined. The bed depth also needed to be small enough for laboratory convenience. Understanding that a practical rotary test furnace can be operated up to 20% full, this bed depth would also establish the furnace inside diameter. A two-dimensional model of the cross sectional heat and material transfer in a rotary furnace was developed as the tool to investigate bed depth.

The second step was to design a rotating test furnace that provided a controlled and measurable amount of energy to the bed. This posed a challenge because, while the heat energy required to raise the bed temperature was relatively small, the energy required to raise the temperature of an amount of insulating refractory was large. A gas flame would have been able to provide this energy but its heat transfer characteristics are not fully predictable and, hence, a degree of uncertainty would be introduced if one were to be used. A heated element provides a more predictable heat source but it would not provide sufficient energy. Therefore, it was decided, if feasible, to use the hot refractory walls as the heat source. The heat flux to the bed could then be calculated using standard radiation theory. The furnace would be first heated. Once hot, the furnace is charged with sand and rotated.

In designing such a furnace it was necessary to ensure that the refractory could be heated with a practical flame and then, once hot, it could provide sufficient heat for the bed material. A one-dimensional model of the heat transfer between the hot gas and walls

and walls and bed material was developed in order to carry out the design.

Once the furnace process design was complete, a mechanical and instrumentation design was carried out and finally the equipment was procured.

4.1 Bed Depth

The objective here was to determine a bed depth in which one could measure a non-uniform temperature and yet is small enough to be convenient in a laboratory. To meet the objective, a model of the energy transfer in the transverse section of a bed was developed. Since the purpose of the model was to obtain approximate information, some simplifying assumptions were made. They were:

- A rectangle was used to approximate the bed cross-section. This allowed for a simple grid structure.
- The continuum assumption was made to represent the particle bulk.
- An effective conductivity was utilized to represent diffusive heat transfer.
- A velocity profile for the particles was approximated using bulk particle velocity data from Boateng (1993).
- The particle mixing caused by shear in the active layer was modeled by enhancing the effective conductivity.

4.1.1 Two-dimensional Bed Cross-Section Code

The system has advective and diffusive transport of energy and so can be represented as

$$\frac{\partial T}{\partial t} - \frac{1}{\rho c_p}\frac{\partial}{\partial x}\left(k\frac{\partial T}{\partial x}\right) + \frac{\partial uT}{\partial x} - \frac{1}{\rho c_p}\frac{\partial}{\partial y}\left(k\frac{\partial T}{\partial y}\right) + \frac{\partial vT}{\partial y} = 0 \tag{4.1}$$

This equation was then solved in finite volume form as follows. First it was integrated over a two dimensional control volume[1], see Figure 4.1.

$$\begin{aligned}
\int_{CV} \frac{\partial T}{\partial t} dA + \int_{CV} \frac{\partial F_x}{\partial x} dA + \int_{CV} \frac{\partial F_y}{\partial y} dA &= 0 \\
\int_{CV} \frac{\partial T}{\partial t} dA + \int_{CV} \nabla . \begin{pmatrix} F_x \\ F_y \end{pmatrix} &= 0 \\
\int_{CV} \frac{\partial T}{\partial t} dA + \oint_{\partial(CV)} \vec{F} . \vec{n} dl &= 0
\end{aligned} \tag{4.2}$$

where

$$\begin{aligned}
F_x &= uT - \frac{k}{\rho c_p} \frac{\partial T}{\partial x} \\
F_y &= vT - \frac{k}{\rho c_p} \frac{\partial T}{\partial y}
\end{aligned} \tag{4.3}$$

The last transformation above uses Gauss's theorem.

In the finite volume method we are concerned with computing the average value in a control volume. In this case, it is the average temperature. Therefore, $\bar{T} \equiv \frac{1}{A} \int_{CV} T dA$. Since the mesh is fixed, the first term in equation 4.2 can be written as $A \frac{\partial \bar{T}}{\partial t}$ and discretized for the control volume i, j to $A_{i,j} \frac{\delta \bar{T}_{i,j}}{\Delta t}$.

The second term in equation 4.2 is the integral of the normal flux around the control volume. This is computed as follows

$$\oint_{\partial(CV)} \vec{F} . \vec{n} dl = (F_{x;i+\frac{1}{2},j} - F_{x;i-\frac{1}{2},j}) \Delta y + (F_{y;i,j+\frac{1}{2}} - F_{y;i,j-\frac{1}{2}}) \Delta x \tag{4.4}$$

The following second order approximations for the fluxes can then be made

$$uT|_{i-\frac{1}{2},j} = u_{i-\frac{1}{2},j} \left(\frac{\bar{T}_{i,j} + \bar{T}_{i-1,j}}{2} \right) \tag{4.5}$$

$$k \frac{\partial T}{\partial x}\bigg|_{i-\frac{1}{2},j} = k_{i-\frac{1}{2},j} \left(\frac{\bar{T}_{i,j} - \bar{T}_{i-1,j}}{\Delta x} \right) \tag{4.6}$$

Finally, by denoting $\delta T \equiv T^{n+1} - T^n$, where the superscript n represents the time step,

[1] In the two-dimensional case it is in fact a control area

and applying an implicit time advance, equation 4.2 becomes

$$
\begin{aligned}
A_x\ \delta\bar{T}_{i-1,j} + B_x\ \delta\bar{T}_{i,j} & \\
+\ C_x\ \delta\bar{T}_{i+1,j} \qquad & +\Delta t\left[u_{i-\frac{1}{2},j}\left(\frac{\bar{T}^n_{i,j}+\bar{T}^n_{i-1,j}}{2\Delta x}\right) - \alpha_{i-\frac{1}{2},j}\left(\frac{\bar{T}^n_{i,j}-\bar{T}^n_{i-1,j}}{\Delta x^2}\right)\right] \\
+A_y\ \delta\bar{T}_{i,j-1} + B_y\ \delta\bar{T}_{i,j} \qquad & -\Delta t\left[u_{i+\frac{1}{2},j}\left(\frac{\bar{T}^n_{i+1,j}+\bar{T}^n_{i,j}}{2\Delta x}\right) - \alpha_{i+\frac{1}{2},j}\left(\frac{\bar{T}^n_{i+1,j}-\bar{T}^n_{i,j}}{\Delta x^2}\right)\right] \\
= & \\
+\ C_y\ \delta\bar{T}_{i,j+1} \qquad & +\Delta t\left[v_{i,j-\frac{1}{2}}\left(\frac{\bar{T}^n_{i,j}+\bar{T}^n_{i,j-1}}{2\Delta y}\right) - \alpha_{i,j-\frac{1}{2}}\left(\frac{\bar{T}^n_{i,j}-\bar{T}^n_{i,j-1}}{\Delta y^2}\right)\right] \\
+\ \delta\bar{T}_{i,j} \qquad & -\Delta t\left[v_{i,j+\frac{1}{2}}\left(\frac{\bar{T}^n_{i,j+1}+\bar{T}^n_{i,j}}{2\Delta y}\right) - \alpha_{i,j+\frac{1}{2}}\left(\frac{\bar{T}^n_{i,j+1}-\bar{T}^n_{i,j}}{\Delta y^2}\right)\right]
\end{aligned}
\tag{4.7}
$$

where

$$
\begin{aligned}
A_x &= \phi\Delta t\left(-\frac{u_{i-\frac{1}{2},j}}{2\Delta x} - \frac{\alpha_{i-\frac{1}{2},j}}{\Delta x^2}\right) \\
B_x &= \phi\Delta t\left(-\frac{u_{i-\frac{1}{2},j}}{2\Delta x} + \frac{\alpha_{i-\frac{1}{2},j}}{\Delta x^2} + \frac{u_{i+\frac{1}{2},j}}{2\Delta x} + \frac{\alpha_{i+\frac{1}{2},j}}{\Delta x^2}\right) \\
C_x &= \phi\Delta t\left(\frac{u_{i+\frac{1}{2},j}}{2\Delta x} - \frac{\alpha_{i+\frac{1}{2},j}}{\Delta x^2}\right) \\
A_y &= \phi\Delta t\left(-\frac{v_{i,j-\frac{1}{2}}}{2\Delta y} - \frac{\alpha_{i,j-\frac{1}{2}}}{\Delta y^2}\right) \\
B_y &= \phi\Delta t\left(-\frac{v_{i,j-\frac{1}{2}}}{2\Delta y} + \frac{\alpha_{i,j-\frac{1}{2}}}{\Delta y^2} + \frac{v_{i,j+\frac{1}{2}}}{2\Delta y} + \frac{k_{i,j+\frac{1}{2}}}{\Delta y^2}\right) \\
C_y &= \phi\Delta t\left(\frac{v_{i,j+\frac{1}{2}}}{2\Delta y} - \frac{\alpha_{i,j+\frac{1}{2}}}{\Delta y^2}\right)
\end{aligned}
\tag{4.8}
$$

and $\phi = 0.5$ for a trapezoidal time advance and $\phi = 1.0$ for a fully implicit time advance.

Note, that $\alpha = \frac{k}{\rho c_p}$ is thermal diffusivity. At the interface of two cells the interfacial conductivity is best represented by the harmonic mean of the conductivity of the two adjacent cells (Patankar 1980)

$$
k_{i+\frac{1}{2},j} = \frac{2k_{i,j}k_{i+1,j}}{k_{i,j} + k_{i+1,j}} \tag{4.9}
$$

This allows for a better representation of the heat flux through the boundary when there is an abrupt change in the conductivity between cells, such as the one that occurs at the boundary between the active and plug flow regions. In such an event, the interfacial conductivity is dependent on the lower conductivity, and one can see that equation 4.9 allows for this. In saying this, however, in this case the plug flow region has a conductivity much lower than the active region, and so the effective conductivity at the boundary was taken to be that of the plug flow region.

By using the notation $E_{a,b}\delta\bar{T}_{i,j} \equiv \delta\bar{T}_{i+a,j+b}$ the left hand side of equation 4.7 can be written in a more convenient form as

$$\begin{aligned}(A_xE_{-1,0} + B_x + C_xE_{+1,0} & \\ +A_yE_{0,-1} + B_y + C_yE_{0,+1} + 1)\ \delta\bar{T}_{i,j} \ &\approx\ (A_xE_{-1,0} + B_x + C_xE_{+1,0} + 1) \\ & \quad (A_yE_{0,-1} + B_y + C_yE_{0,+1} + 1)\ \delta\bar{T}_{i,j} \end{aligned} \tag{4.10}$$

Equation 4.10 represents approximate factorization; an approximation that allows for ease of solution while maintaining second order accuracy. The system of equations may then be solved as follows. First, for every line of constant j, an intermediate variable, $\vec{T}$ is solved for.

$$([A_x + B_x + C_x] + [I])_j\ \vec{T} \ = \ [\text{right hand side of equation 4.7 }]$$

Then, for every line of constant j, the temperature update, $\vec{\delta T}$ is solved for.

$$([A_y + B_y + C_y] + [I])_i\ \vec{\delta T} \ = \ \vec{T}$$

The above requires the solution of two sets of linear algebraic equations whose coefficients form a banded matrix with a bandwidth of three. These can be solved simultaneously using a tridiagonal solver, such as the Thomas algorithm (Chapra and Canale 1988).

4.1.2 Boundary Conditions

Normal to the boundary there is a diffusive flux only since there is no material flow leaving or entering the system. The concept of a ghost cell is used to implement this boundary condition.

In the case of $i = I$, we can say

$$-k_{I+\frac{1}{2},j}\frac{(T_s - \bar{T}_{I,j})}{\frac{\Delta x}{2}} = h(T_s - T_a) \tag{4.11}$$

We can also introduce the ghost cell; a fictitious cell outside of the mesh domain, see figure 4.2, that has a mean temperature, $T_{I+1,j}$ such

$$-k_{I+\frac{1}{2},j}\frac{(\bar{T}_{I+1,j} - \bar{T}_{I,j})}{\Delta x} = h(T_s - T_a) \tag{4.12}$$

Combining the above equations gives a

$$T_{I+1.j} = \frac{-4k_{I+\frac{1}{2},j}\bar{T}_{I,j} - 2h\Delta x T_a}{-2k_{I+\frac{1}{2},j} - h\Delta x} - \bar{T}_{I,j} \tag{4.13}$$

The ghost cell temperature is first calculated and then used to solve the matrix of equations.

4.1.3 Velocity Profile

The velocity profile was developed by assuming an x-wise velocity and calculating the y-wise velocity through mass conservation.

Figure 4.3 depicts the velocity profile on the rectangular grid as used in this code. The upper region represents the active region. Along the vertical center line, parallel to the y-axis, the x-wise velocity increases from $-u_s$ at the center of the upper surface to zero at the interface between the active and plug flow regions, in the form $u = \mathcal{A}y^c$, where $\mathcal{A} = \frac{u_s}{\mathcal{B}^c}$, c is a variable coefficient and $\mathcal{B}$ is the depth of the active layer. If c is set to 2, then the velocity profile is parabolic.

Along the x direction, at constant y, absolute x-wise velocity decays from the value at the center line to zero at the vertical boundaries in a form identical to the velocity profile down the center of the active region. Note that x-wise velocity is zero along the active layer-plug flow region boundary.

The y-wise velocity is then determined at each point by ensuring mass conservation. Finally y-wise velocity is set to zero at the vertical boundaries.

4.1.4 Code Testing:

The diffusive terms were tested by solving the two-dimensional heat equation with the boundary conditions given in figure 4.4. With an initial condition of $T(x, y, 0) = \sin(\pi y)$ the exact solution is (Ollivier-Gooch 1998)

$$T(x,y,t) = \sin(\pi y)\left[\frac{\sinh(\pi x)}{\sinh x} + \left(\sum_{m=1}^{\infty} \exp(-(1+m^2)\pi^2 t)\left(\frac{2(-1)^{m+1}}{m\pi(1+m^2)}\right)\sin(m\pi x)\right)\right]$$

With a time step of 0.01 and a 40 $\times$ 40 mesh the L2 error norm was 6.4×10^{-4} at time = 1.0, implying that the diffusive terms were computed satisfactorily. Further checks were carried out to ensure that the code was second order accurate.

In order to check the convective boundary condition the code was tested with the boundary conditions shown in figure 4.5. The exact steady-state solution is (Ollivier-Gooch 1998)

$$T(x,y) = 1 + 2x$$

With a time step of 0.01 and a 40 $\times$ 40 mesh the L2 norm at time = 50 was 6×10^{-6}, implying that the convective boundary condition was implemented correctly.

The above checks implied that the diffusive terms and the convective boundary conditions were implemented satisfactorily. In order to check the advective terms associated with material transport a mass balance is conducted over each cell. Should the L2 error norm for mass conservation over all of the cells be greater than 10^{-15}, which is effectively machine zero, a warning is printed when running the code.

The last check was that of input parameters. This was carried out by using data from an experimental study of bed and free-board temperatures in a pilot kiln firing gas and fed with Ottawa sand (Barr, Brimacombe, and Watkinson 1989a). In test T4 of the study the sand feed was 62 kg/h and the authors indicate that the fill was 12%. Bulk density of the sand is given as 1460 kg/m^3 and since the kiln I.D. was 406 mm, the particle residence time equates to 140 minutes. Therefore, this test may be simulated using the current code and computing for 140 minutes.

Table 4.1 gives input data used to simulate the results of test T4 from Barr, Brimacombe, and Watkinson (1989a). In determining the data it was assumed that the active layer is 30% of the bed depth and that the transverse flow is three times the axial flow. This resulted in $u_s = -0.0022$ m/s.

In order to reproduce the temperature results the heat transfer coefficients were 50 W/m^2 K for the free-board to exposed bed and 10 W/m^2 K for the covered wall to covered bed. They were were within the ranges reported by Barr, Brimacombe, and Watkinson (1989b). Wall temperature was calculated as the mean of the free-board and bed.

The results are given in figure 4.6. Figure 4.7 compares the results with approximate data from the experiment. In general the agreement appears to be reasonable implying that the input data may be used to design the test rig. It is interesting to note that temperature gradients within the bed are small. After 40 minutes the difference between the hottest part of the bed and coldest part is about 50°C. This may justify the well mixed assumption made by Barr, Brimacombe, and Watkinson (1989a).

4.2 Furnace Refractory Design

In the test furnace a controlled and measurable heat source is required to ensure that the heat flux at the exposed and covered surface of the bed is known. Only then can conclusions regarding the heat transfer within the bed be drawn. One method is to use the hot refractory walls to radiate heat to the bed. Then, by measuring the refractory and bed temperatures, the energy exchange between them can be calculated using radiation heat transfer theory.

In order to design a suitable set-up, the heat transfer between a gas flame and the refractory and the bed and refractory, once it is hot, were modeled. The former model was used to determine whether the refractory could be practically heated and to determine the temperature profile of the refractory when the refractory was hot. This temperature profile was then used as the initial refractory temperature in the latter model where the heat up of the bed was simulated. Finally, the inside wall temperature history, obtained from the results of the latter model, was used as a boundary condition for the two-dimensional code described in Section 4.1.1 to ensure that a measurable temperature differences occurred in the bed cross section.

The following assumptions were made in order to simplify the models:

- In the refractory radial heat transfer dominates over a small axial length of the furnace and so axial conduction is ignored.
- Intimate radial mixing occurs in the freeboard gas and within the bed. Hence, they are isothermal over a small axial length.
- Axial heat transfer occurs only through convection. Hence, the hot freeboard gases transfer heat along the furnace length. When the bed is being heated up by the refractory walls there is no axial heat transfer within it since there is no axial flow.
- The above means that the model can be reduced to a one-dimensional model in cylindrical coordinates that is marched along the length of the kiln.
- For heat up of the furnace pure methane was assumed to be the fuel gas and the combustion process was assumed to be complete within the burner prior to entering

the furnace. This allowed the composition of the gases entering the furnace to be calculated by equating the combustion chemical reaction formulae.

- The radiative properties, emissivity and absorbtivity, for the flues gases within the furnace were obtained using a weighted sum of gray gases model obtained from Barr (1999).

In essence the model solves the one-dimensional transient heat equation in cylindrical coordinates. However, the challenge comes from determining the inside boundary condition, which is determined by the hot gas temperature in the case of refractory heat up, and bed temperature in the case of bed heat up.

Figure 4.8 shows the model calculation domain. During heat up, hot gases enter the first axial slice of the furnace and transfer heat to the refractory. The amount of heat transferred during a finite time step, Δt, to the walls is then used as the inside wall boundary condition. At the outside wall, heat transfer by ambient conduction occurs. The heat lost by the hot gases in the first slice is used to calculate the new temperature of the gases as they enter the second slice. This calculation procedure is repeated for each slice until the end of the furnace is reached. Following this, the calculation over the whole furnace is repeated for the next time step and so on and so forth until the furnace is hot.

Once hot, the temperature profile of the refractory is used as an initial condition in modeling the heat up of the bed material. The model is identical in all respects except that the hot gases are replaced by the bed material. The gases that will be inside the furnace when the bed is being heated are O_2 and N_2, i.e. air, which are radiatively transparent and so may be ignored in the calculation.

It should be noted that in this model, since there is no axial movement of the bed material and axial thermal diffusion has been ignored, the calculation over one slice does not affect another slice. The differences between slices are due to the different initial temperature of the refractory.

A more detailed explanation of the calculation procedure follows.

4.2.1 Hot Gas Mass Flow and Temperature

For stoichiometric conditions, the combustion of methane in air occurs as follows:

$$\begin{array}{ccccccc} n\mathrm{N_2} + \mathrm{O_2} + \mathrm{CH_4} & \longrightarrow & n\mathrm{N_2} + \mathrm{CO_2} + 2\mathrm{H_2O} \\ m\mathrm{g} \quad 64\mathrm{g} \quad 16\mathrm{g} & & m\mathrm{g} \quad 44\mathrm{g} \quad 36\mathrm{g} \end{array}$$

Since ambient air contains 21% (vol/vol) oxygen with the remainder nitrogen, $n = 79/21$ and $m = 210.7$. In the case of excess air, as is necessary to ensure complete combustion, additional N_2 and O_2 appears on both sides of the above equation. The heat of combustion is 50.04 MJ/kg CH_4. Therefore, by fixing a heat input and excess air level the mass flows can be established.

In order to calculate the temperature of the hot gases a mean value for specific heat capacity, $c_{p,g}$, was used. With 25% excess air and at 1400K, $c_{p,g} = 1.35$ kJ/kg K. The assumption of constant specific heat capacity is in accordance with all of the other simplifying assumptions made for this calculation.

4.2.2 Heat Up of Refractory by Gases

The average heat flux from an isothermal gas volume at T_g to its entire bounding gas surface at, for example, T_w is

$$q_{g \to w} = \epsilon_w \sigma_{SB} (\epsilon_g T_g^4 - \alpha_g T_w^4) \tag{4.14}$$

where

q = heat flux in $\mathrm{W/m^2}$

ϵ_w = emissivity of the refractory wall

ϵ_g = emissivity of the gas

α_g = absorbtivity of the gas

σ_{SB} = Stefan-Boltzman coefficient, $5.67 \times 10^{-8} \mathrm{W/m^2K^4}$

Over a short axial length T_g and T_w are constant and so ϵ_g and ϵ_w can be considered constant. Therefore, equation 4.14 was used to determine the radiative exchange between the hot gas and refractory wall in one slice of the model. ϵ_g and α_g were calculated using a weighted sum of gray gas model obtained from Barr (1999). A value of 0.87 was used for ϵ_w.

4.2.3 Heat Up of Bed by the Refractory Walls

Figure 4.9 depicts the cross section of the test furnace when it is loaded with charge. Since the exposed surface of the charge "sees" only the refractory wall, the rate of heat transfer can be described by the following expression:

$$Q_{ew \to eb} = \frac{\sigma_{SB}(T_{ew}^4 - T_{eb}^4)}{R} \tag{4.15}$$

where

$$\begin{aligned} R &= \frac{1-\epsilon_w}{\epsilon_w A_{ew}} + \frac{1}{A_{eb}\mathcal{F}_{eb \to ew}} + \frac{1-\epsilon_b}{\epsilon_b A_{eb}} \\ T_{ew} &= \text{exposed wall temperature in degrees K} \\ T_{eb} &= \text{exposed bed temperature in degrees K} \\ A_{ew} &= \text{exposed wall area per unit length in } \mathrm{m}^2/\mathrm{m} \\ A_{eb} &= \text{exposed bed area per unit length in } \mathrm{m}^2/\mathrm{m} \\ \mathcal{F} &= \text{view factor} \end{aligned}$$

In this calculation a uniform bed temperature is assumed, as would be in the case of perfect mixing. Also, the wall is assumed to be of uniform temperature in one axial slice. Hence, $T_{eb} = T_b$ and $T_{ew} = T_w$. From Figure 4.9 it can seen that A_{eb} = chord length XY and $A_{ew} = 2\pi r\left(\frac{2\pi-\beta}{2\pi}\right)$. Another assumption made here is that heat transfer between the walls and bed occurs dominantly through radiative exchange between the exposed wall and exposed bed.

4.2.4 Heat Transfer Within the Refractory Walls

Heat transfer within the refractory can be described by the transient one-dimensional heat equation expressed in cylindrical coordinates:

$$\rho c_p \frac{\partial T}{\partial t} - \frac{1}{r}\frac{\partial}{\partial r}\left(kr\frac{\partial T}{\partial r}\right) = 0 \tag{4.16}$$

Re-arranging, integrating over a control volume and applying Gauss's rule gives:

$$\int_{CV} r\rho c_p \frac{\partial T}{\partial t} dV - \oint_{\partial(CV)} \left[\left(kr\frac{\partial T}{\partial r}\right) \cdot \vec{n}\right] dA = 0 \tag{4.17}$$

In the one-dimensional case $dV = \Delta r$ and $dA = 1$. By carrying out the same analysis as for the two-dimensional bed cross section code, Equation 4.17 can be expressed in discretized form as

$$\begin{aligned} & \delta T_{i-1}\left(\frac{\Delta t}{r_i\rho_i c_{p,i}\Delta r^2}\right)(k_{i-\frac{1}{2}} r_{i-\frac{1}{2}}) \\ \delta T_i\left[\frac{-\Delta t}{r_i\rho_i c_{p,i}\Delta r^2}(k_{i-\frac{1}{2}} r_{i-\frac{1}{2}} + k_{i+\frac{1}{2}} r_{i+\frac{1}{2}}) - 1.0\right] &= \frac{-\Delta t}{r_i\rho_i c_{p,i}\Delta r^2}\left[k_{i+\frac{1}{2}} r_{i+\frac{1}{2}}(T^n_{i+1} - T^n_i)\right. \\ & \delta T_{i+1}\left(\frac{\Delta t}{r_i\rho_i c_{p,i}\Delta r^2}\right)(k_{i+\frac{1}{2}} r_{i+\frac{1}{2}}) \qquad \left. -k_{i-\frac{1}{2}} r_{i-\frac{1}{2}}(T^n_i - T^n_{i-1})\right] \end{aligned} \tag{4.18}$$

Equation 4.18 can now be solved using either a tri-diagonal matrix inversion solver or guass seidel.

The code allows for two different types of refractory insulation. Their interfacial conductivity is represented by the harmonic mean of the conductivity of the two insulations (Patankar 1980)

$$k_{i+\frac{1}{2}} = \frac{2k_i k_{i+1}}{k_i + k_{i+1}} \tag{4.19}$$

4.2.5 Heat Transfer to Atmosphere

Heat transfer to atmosphere was calculated using a constant external heat transfer coefficient. A value of 7.5 W/m^2 K was used.

4.2.6 Implementing Boundary Conditions

At the boundary the rate of heat exchange may be expressed in terms of a radiative heat transfer coefficient. For example, in the case of heat up of the bed, (refer to section 4.2.3)

$$Q_{ew \to eb} = h_{rad,ew \to eb} A_{eb} (T_{ew} - T_{eb}) \tag{4.20}$$

Equations 4.15 and 4.20 may be combined to give

$$h_{rad,ew \to eb} = \frac{\sigma_{SB}(T_w^2 + T_b^2)(T_w + T_b)}{R A_{eb}} \tag{4.21}$$

This radiative heat transfer coefficient can be applied at the boundary using the concept of the ghost cell, as in the case of the two-dimensional bed cross section code. For example at the $i = I$ boundary, the heat flux at the surface is,

$$\begin{aligned} \mathrm{F} = h(T_{I+\frac{1}{2}} - T_a) &= \frac{k}{\Delta r}(T_I - T_{I+1}) \\ &= \frac{k}{\frac{\Delta r}{2}}(T_I - T_{I+\frac{1}{2}}) \end{aligned} \tag{4.22}$$

where F is the heat flux normal to the surface and T_a is the ambient temperature, in this case either the temperature of the gas or the temperature of the bed material. On re-arranging,

$$T_{I+1} = \frac{-4k_{I+\frac{1}{2}} T_I - 2h\Delta r T_a}{2k_{I+\frac{1}{2}} - h\Delta r} - T_I \tag{4.23}$$

4.2.7 Code Testing

The problem of transient heat conduction has been solved for some simple geometries. Incopera and Dewitt (1981) presents the solution for the infinite slab, infinite cylinder and sphere in graphical form. Use has been made of the solution for the infinite slab in checking the current code. The one-dimensional grid was modified to represent a thin cylindrical shell of a large inside diameter. The system may then be approximated as a infinite slab for heat transfer analysis thereby allowing the solution to be checked.

Tables 4.2 and 4.3 give input data for the code and the graphical calculation described in Incopera and Dewitt (1981). Table 4.4 gives the solutions. It can be seen that the solutions are similar although not exactly the same. The difference is due to approximations in reading graphical data. However, this provides confidence that the code is correct.

4.3 Bed Depth and Furnace Sizing

The two-dimensional bed cross section code was first run with approximate data. It was found that with a bed depth of 100mm the difference between the surface temperature and temperature inside the bed was about 25°C, which is large enough to be reliably measured. Understanding that a rotary furnace that is up to 20% full may be used for the experimental study, this implied that a test furnace with an inside diameter of 400mm would serve our needs. To confirm this and size the refractory, the two codes described above were utilized.

The one-dimensional code was used to size the refractory, ensuring that it could be heated up with a flame and that it would be hot enough and hold sufficient energy to heat the bed. A number of different refractory designs were investigated. They all consisted of a high density, highly conductive inner layer and an insulating outer layer. The final design only is presented here.

The final design consisted of a 70mm inner refractory layer of Thor 60 castable (approx. 60% SiC, 23% Al_2O_3 and 14% SiO_2) surrounded by a 20mm layer of Durablanket, see Appendix A. The exact inner and outer diameters were chosen for practical reasons. Table 4.5 gives the design data and computer input data when heat up of the furnace was

investigated. The results for a central slice of the furnace are given in figure 4.10. The refractory temperature profile was then used as input to investigate how a cold bed, with an initial temperature of 30°C, heats up in the furnace. All other input data are for this run are given in Table 4.6. The results are presented in Figure 4.11 for a central slice in the furnace.

The above results indicate that a furnace of this design may be heated up with a practical flame and, after the walls are hot, there is sufficient energy stored to heat the bed. The temperature distribution within the bed was then investigated using the two-dimensional bed cross section code. This was done as follows. The initial temperature of the bed material was again 30°C. The inside wall temperature history as the bed is heated was taken from the one-dimensional code and used as the boundary condition in the two-dimensional code. The wall to bed heat transfer coefficients were calculated in the same way as in the one-dimensional code. Also, the rectangular bed perimeter and depth to width ratio were made identical to the real bed, in an attempt to maintain the same resistance to heat transfer between the refractory wall and bed surface. This meant that the cross sectional area and, hence, bed volume were different in the two cases. To ensure that the bed's thermal capacity remained constant the specific heat capacity was modified.

The results of the computer run are presented in Figure 4.12 and the temperature profile down the center of the bed is given in Figure 4.13.

If one compares Figures 4.11 and 4.12, it can be seen that the bed is heated sufficiently for this experimental program. The two-dimensional results, Figure 4.12, show a slightly slower heating rate. After 20 minutes the average bed temperature is approximately 800°C with the two-dimensional code but almost 900°C with the one-dimensional code. This is due to mixing within the bed not being intimate and so the bed surface is hotter than the center of the bed leading to a reduced temperature driving force for heat transfer to the bed. After 30 minutes the bed temperatures are similar, see Figures 4.11 and 4.12. This provides some confidence in the trends of the results. Figure 4.13 shows that after 20 minutes a temperature difference of about 30-40°C between the center of the bed and bed surface should develop, which is indeed measurable.

From the results obtained one can conclude that this design is suitable for the current experimental program. The furnace can be heated using a gas flame. Then, once hot, the refractory walls will heat up the bed. Finally, during heat up, significant temperature gradients will form in the cross-section. The resulting temperature non-uniformity would be large enough to be measured.

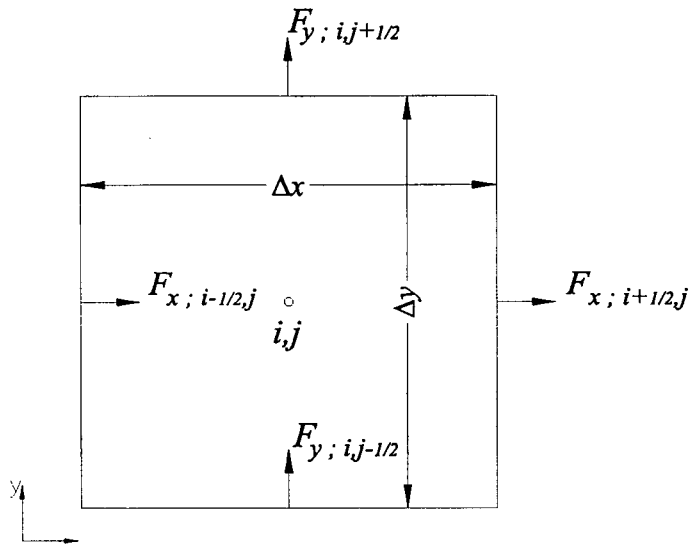

Figure 4.1: Flux Entering and Leaving Finite Control Volume (Area in 2D case)

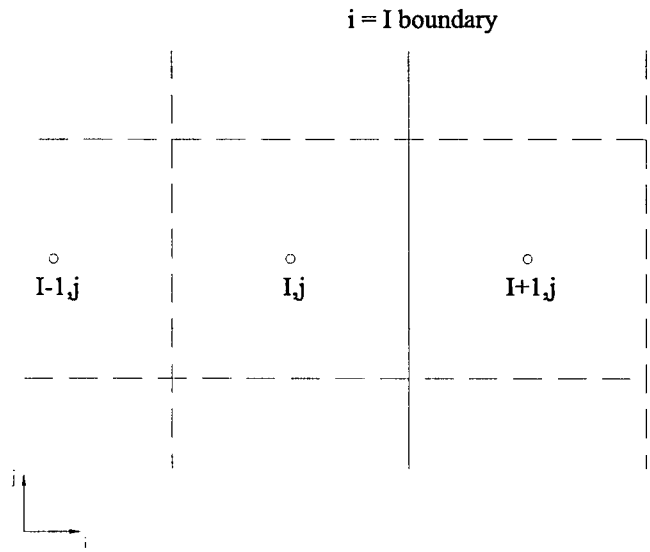

Figure 4.2: Depiction of Ghost Cell at $i = I$ boundary

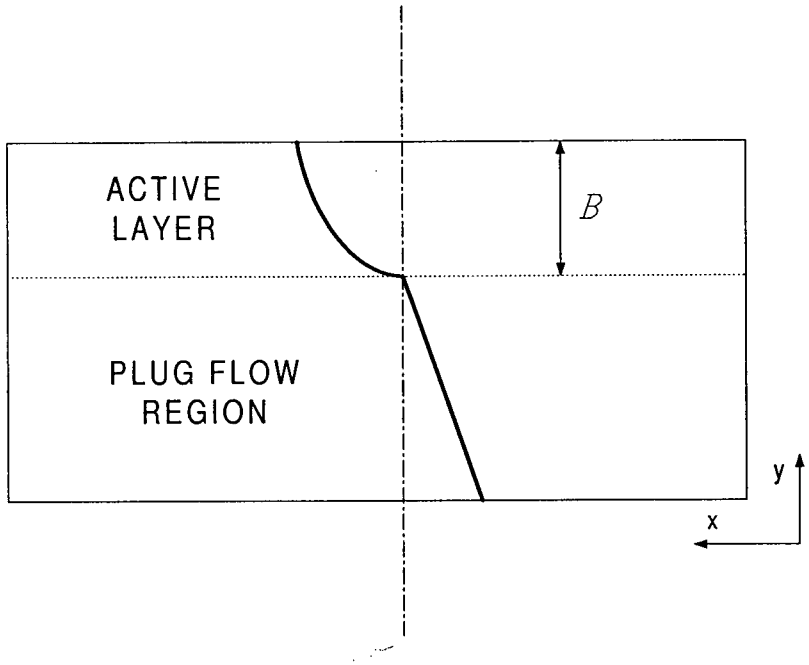

Figure 4.3: Velocity Profile in Two-Dimensional Grid

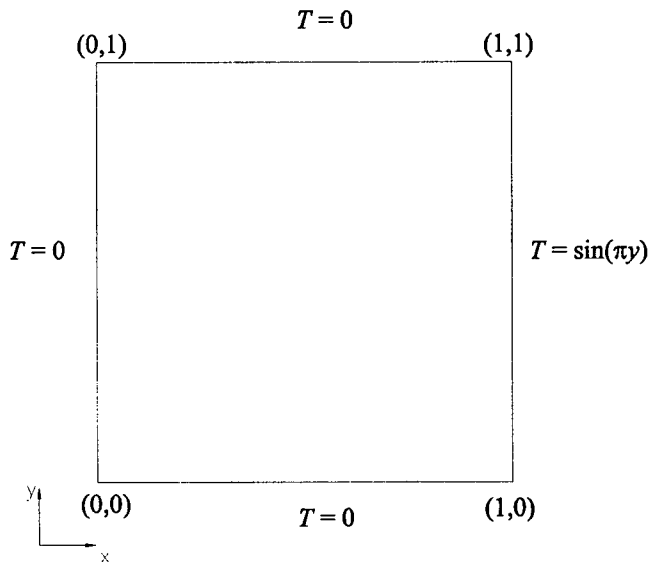

Figure 4.4: Boundary Conditions For Test of Transient Conditions: $T(x, y, 0) = x \sin(\pi y)$

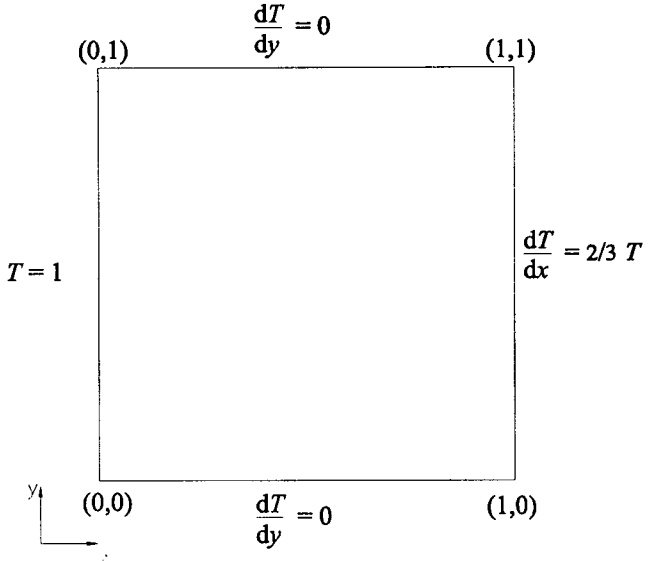

Figure 4.5: Boundary Conditions For Test of Convective Flux at Boundary

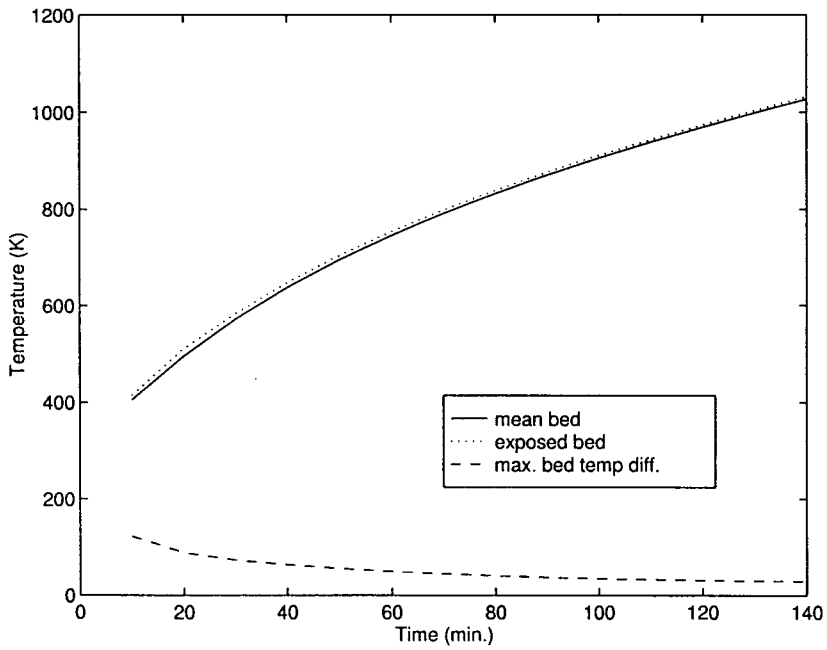

Figure 4.6: Simulation of Results

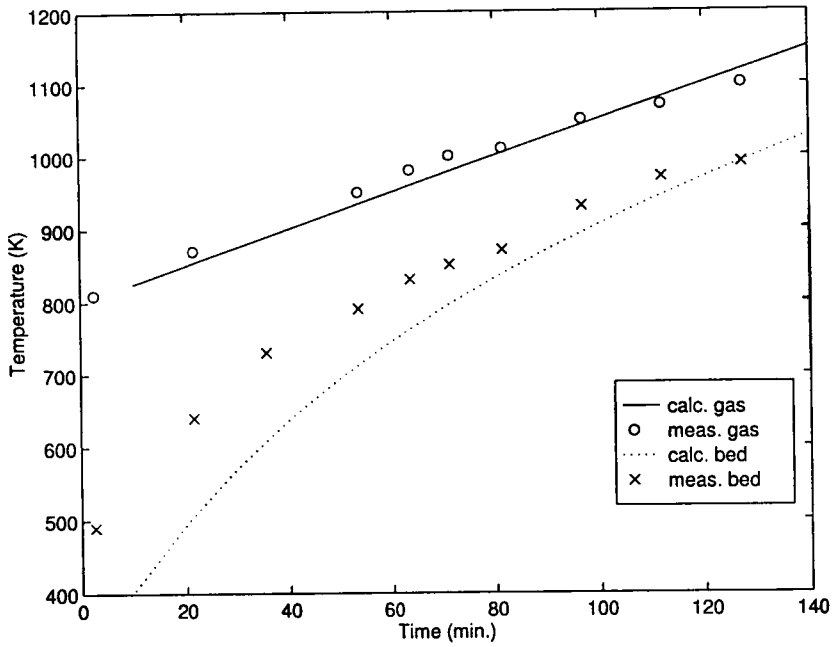

Figure 4.7: Comparison with Experiment

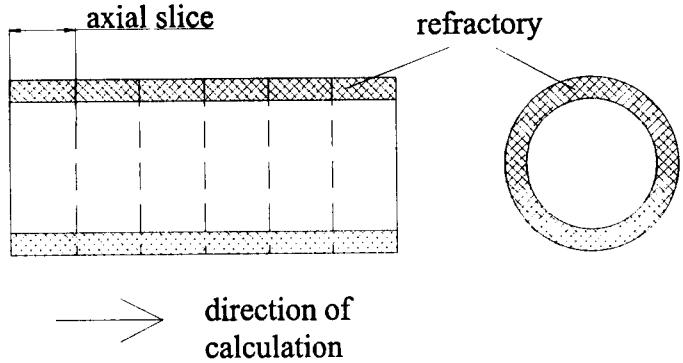

Figure 4.8: Refractory Model Structure

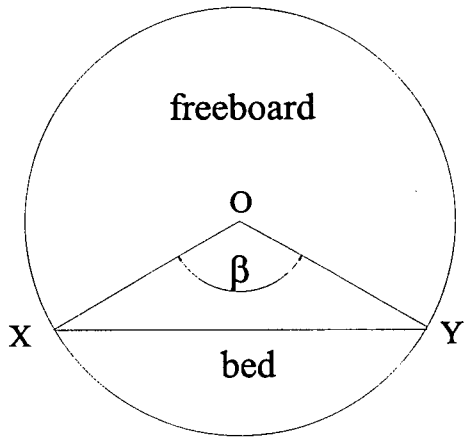

Figure 4.9: Cross Section of Test Furnace

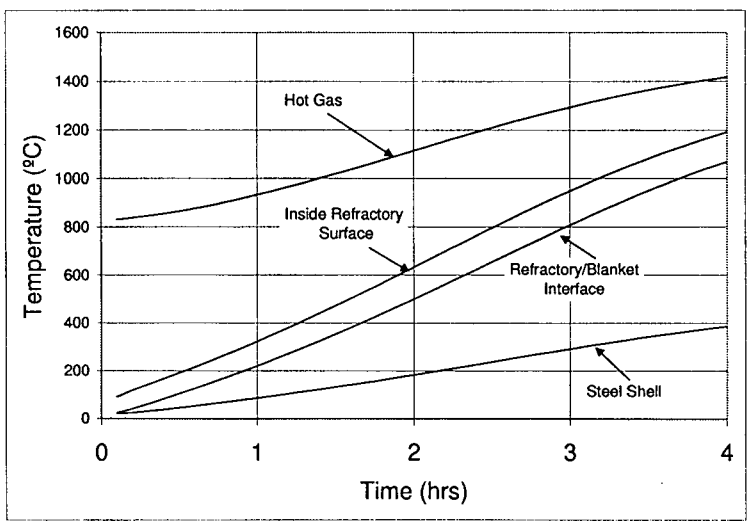

Figure 4.10: Heat Up of Furnace - Slice 6

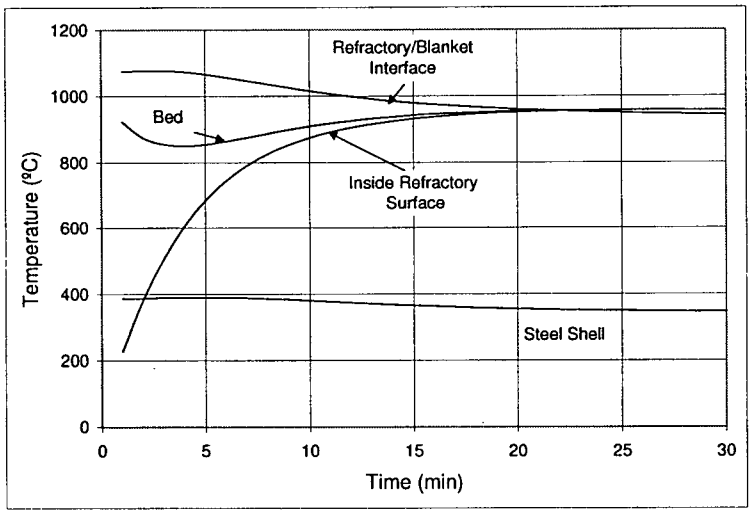

Figure 4.11: Heat Up of Bed - Slice 6

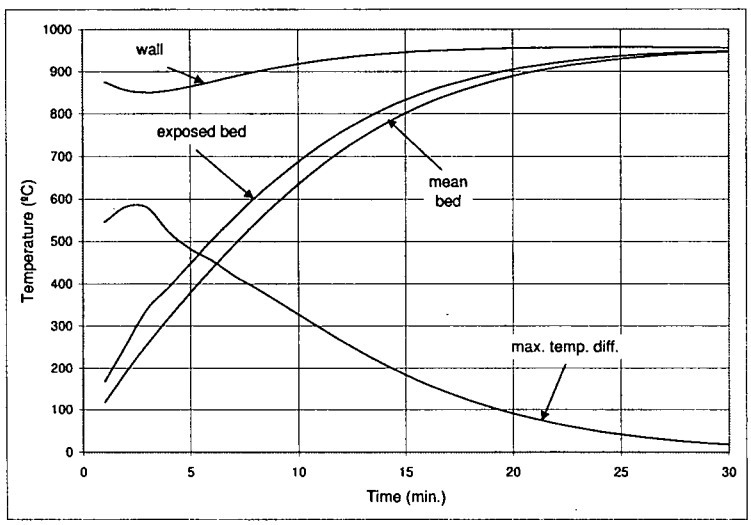

Figure 4.12: Heat Up of Bed Using 2D code

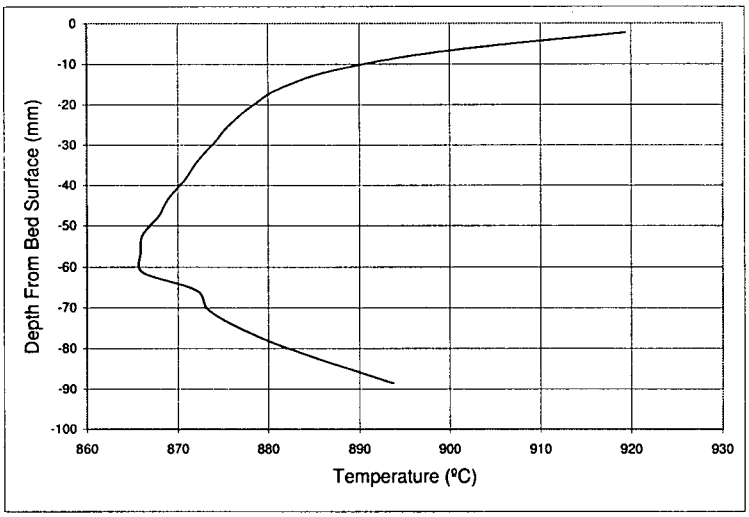

Figure 4.13: Temperature Profile in Center of Bed after 20 minutes

Table 4.1: 2D Code Input Data for Test Case

Bed Width (m)	0.32
Bed Depth (m)	0.08
Active Layer Size (%)	30
Mesh Size	20 × 20
Time increment (min.)	0.05
Free-board to Bed HTC (W/m2 K)	50
Wall to Bed HTC (W/m2 K)	10
Effective Conductivity (W/m K)	1.5
Specific Heat Capacity (kJ/kg K)	1100
Bulk Density (kg/m^3)	1460
Initial Free-board Temp (K)	800
Final Free-board Temp (K)	1150
v_T (m/s)	0.0022

Table 4.2: 1D Code Input Data for Test Case

Inner Radius (m)	5
Outer Radius (m)	5.2
Ambient Temperature (K)	1100
Initial Temperature (K)	100
Heat Transfer Coefficient (W/m^{2}K)	10
Refractory Conductivity (W/m K)	1
Specific Heat Capacity (kJ/kg K)	1000
Density (kg/m^3)	1000

Table 4.3: Graphical Method Input Data for Test Case

Slab Thickness (m)	0.1
Ambient Temperature (K)	1100
Initial Temperature (K)	100
Heat Transfer Coefficient (W/m^{2}K)	10
Refractory Conductivity (W/m K)	1
Specific Heat Capacity (kJ/kg K)	1000
Density (kg/m^3)	1000

Table 4.4: 1D Code. Test Case Results

Time (sec.)	t* ($\frac{\alpha t}{L^2}$)	θ^* ($\frac{T-T_a}{T_i-T_a}$)	Center Temp. 1D code (K)	Center Temp. calculated (K)
10^4	1.0	0.55	550	566
2×10^4	2	0.25	850	845
5×10^4	5	0.024	1076	1072

Table 4.5: Input Data - Heat Up of Furnace Using Flame Gases

Furnace ID (mm)	416
Furnace Length (m)	1.0
Thor 60 Castable (mm)	70
k (W/m °C)	5.9
ρ (kg/m^3)	2600
c_p (J/kg °C)	1100
Durablanket (mm)	20
k (W/m °C)	0.08
ρ (kg/m^3)	128
c_p (J/kg °C)	1130
Fuel (Gas) input (kW)	50
Fuel heat content (MJ/kg)	50.037
Fuel air/fuel ratio (wt/wt)	17.17
Excess air (% of stoich.)	25
Flue gas c_p (J/kg °C)	1350
Mean beam length (mm)	416
Part. press. CO_2 and H_2O (atm)	0.25
Inside refractory emissivity	0.87
Initial temp (°C)	20
Ambient temp (°C)	20
External wall to ambient H.T.C. (W/m^2 °C)	7.5
Radial cells in refractory	90
Axial cells	10

Table 4.6: Input Data - Heat Up of Bed Using Hot Refractory Walls

Fill (%)	20
Initial bed temp (°C)	20
Bed bulk ρ (kg/m^3)	1460
Bed c_p (J/kg °C)	1100
Covered wall/bed H.T.C. (W/m^2 °C)	$h_{ew \rightarrow eb}$
Bed surface emissivity	0.9
Exp bed to exp wall view factor	1.0

Chapter 5

Description of Experimental Set-Up

The dimensions and refractory selected in Chapter 4 formed the basis for the mechanical design of the test furnace that was manufactured for this work. A description of the mechanical design will be given in this chapter. A description of the instrumentation and the experimental procedure used in this study will also be presented here.

Prior to the description, the principle of the experimental procedure will be recapitulated. In essence the furnace walls are heated using a gas flame. Once the walls are hot, the flame is extinguished and the furnace is charged with an inert granular material, which, for this study, is sand. The furnace is then rotated and, as it rotates, the walls heat the bed. The temperature at select locations in the transverse section is recorded to determine the degree of temperature uniformity in that section. The refractory temperatures are also monitored so that the heat flux to the bed surface may be calculated.

5.1 Furnace

Figure 5.1 shows the pertinent details of the furnace. A photograph of the furnace is contained in Figure 5.2.

The body of the furnace consists of a 600mm (24") N.B., sch. 10, carbon steel pipe that is 1110mm long. The furnace is lined with an approximately 70mm thick layer of Thor 60 castable refractory which is backed with 25mm (1") of Fiberfax Durablanket. These products were obtained from VRD Canada, in Langley, BC. Their details can be found in Appendix A.

The Thor 60 was chosen for its high density (2600 kg/m^3) and high conductivity (5.9 W/mK at 800°C). Its high density allows it to hold sufficient thermal energy so that once hot it has sufficient energy to heat the bed as required. Its high conductivity ensures that

the hot face temperature remains high enough to provide a thermal driving force between it and the bed.

Furnace insulation is provided for by the Durablanket which has a low thermal conductivity (0.6 W/mK at 800°C).

The ends of the furnace have 200mm diameter openings that are concentric with the furnace diameter. They are lined with 100mm of Plicast LWI 24R which is a light castable. This material provides thermal insulation. It was also purchased from VRD Canada and is described in Appendix A.

The furnace rests on a support structure whose load bearing beams are manufactured from W4 × 13 "I" section, see Figure 5.2. The structure holds four rollers on which the furnace rests and is allowed to rotate. The furnace is coupled to a 5.5m long pilot rotary kiln in the high head room area of UBC's Advanced Materials and Process Engineering Laboratory (AMPEL) which is in The Brimacombe Building. This pilot kiln, which is described in Barr, Brimacombe, and Watkinson (1989a), drives the test furnace rotation.

Further details of the mechanical design of the furnace and the support structure can be found in the engineering drawings contained in Appendix B.

5.2 Instrumentation

Instrumentation for the furnace allows for temperature monitoring of the high density castable, which is used as the heat source for the bed, and also the temperatures within the bed.

5.2.1 Refractory Temperatures

Inserted into the refractory at three axial and two radial locations are nine type K thermocouple probes. The exact locations are shown in Figure 5.3. At each axial location two probes are designed to indicate the refractory hot face temperature and the other one is designed to measure the refractory cold face temperature. Note that the refractory cold face temperature is in fact the interface between the Thor 60 castable and the Durablanket.

The thermocouples were manufactured in-house using either 18 or 20 A.W.G. type K thermocouple wire and ceramic sheaths. The hot junction was formed by welding the wires and it was embedded into the refractory at the locations indicated on Figure 5.3.

All nine of the thermocouples are connected to a 2 pole 10 position rotary selector switch, model OSW3-10, and then to a single input digital thermometer, model HH21. Cold junction compensation is included for electronically within the thermometer. Both of these instruments were supplied by Omega and details can be found in Appendix C.

The instrumentation set-up is depicted in Figure 5.4.

As one can deduce from the above description, the refractory temperatures are to be manually recorded. Refractory temperatures are indicated on the digital thermometer after selecting the desired thermocouple using the rotary switch. These temperatures are then manually recorded by the experimentalist.

5.2.2 Bed Temperatures

Figure 5.5 shows the probe that was designed specifically to measure bed temperatures. Its dimensional details are given in Figure 5.6. The probe consists of four thermocouples, each one passing through a 3/16" by 0.035" wall stainless steel tube. The thermocouples are type K and were produced using duplex insulated thermocouple wire. This wire has an A.W.G. number of 20 and has nextel ceramic insulation. It was purchased from Omega and details can be found in Appendix C.

At the hot junction of each thermocouple the insulation has been removed and the wire has been passed through a 25mm long ceramic sheath and then welded together to form an exposed hot junction.

From Figures 5.5 and 5.6 one can see that the thermocouple ends are positioned at different radial locations. These locations were selected to obtain the temperature distribution in the cross-section of the bed. Figure 5.7 gives the location of each thermocouple in the bed cross section.

For data logging, each thermocouple in the probe was connected to a signal conditioning board to convert the thermocouple signal to a $\pm$ 5V signal. Cold junction

compensation was also carried out by this board. The signal conditioning board was connected to a data acquisition board in a 486 computer that ran at 66MHz with 24MB of RAM. Figure 5.5 shows a photograph of the set-up with the bed probe and Figure 5.4 depicts it diagrammatically.

The signal conditioning board is model CIO-EXP-16 and the data acquisition board is model CIO-DAS08. Both of these items were purchased from Computer Boards in Vancouver and further details of them can be found in Appendix C.

5.3 Calibration

The portable digital temperature indicator used to measure the thermocouples in the refractory was purchased calibrated to within 0.1% or 1°C accuracy. This instrument was used to check the calibration of the bed temperature data logging equipment.

In order to check the calibration of the data logging equipment a micro-volt signal generator was used. A signal was provided across the terminals that the thermocouples were connected to on the data logging equipment. The temperatures displayed on the computer were subsequently compared to those displayed by the digital thermometer to determine accuracy. Table 5.1 shows the results of this test and it can be seen that the data logging equipment is no more than 4°C inaccurate in approximately 680°C, which is quite acceptable for this study.

Stability of the data logging equipment was checked using the same signal generator and recording the temperature for one minute. Figure 5.8 shows the results. It can be seen that the signals were quite stable. The electrical technician responsible for the signal generator advised that the slight drift was most likely caused by drift in the signal generator.

5.4 Preparation of Bed Material

Sand was selected as the bed material for this study. It is inert, readily available and its properties are well known. Two types of sand were used and both were obtained from

Target Products Ltd. in Burnaby, BC. One was a coarse sand and referred to as "1/16 to 1/8 inch filter sand and gravel". It was composed of 66% silica with the remainder largely alumina with some iron oxide and calcium oxide. The other sand was finer and referred to as "10-20 filter sand". The numbers indicated approximate mesh size range. This sand was over 93% silica.

While it is appreciated that the two sands used were not of a consistent composition, the properties of interest in this study were relatively similar. These properties are specific heat capacity, thermal conductivity and density. Also the particle shapes were irregular and appeared to be similar and, as will be reported in the results, the dynamic angle of repose was constant. Although no measurements were carried out, it was expected that the coefficient of restitution for the sand particles was also similar.

Further details, including composition and MSDS sheets, of the sand are provided in appendix D. Photographs of the sand are contained in Figures 5.9 and 5.10.

The purpose of this study was to investigate the effect of particle size distribution on temperature gradients in the cross-section of the of the bed. Therefore, a number of sand mixes with varying size distributions were prepared using the two sands described above. A sieve shaker, model TS1 manufactured by Gilson Screen Company, with appropriately sized sieves was used to prepare the sand mixes.

Six mixes in total were prepared for this study. They ranged from a wide size distribution to a narrow one. Table 5.2 gives details of the sand mixes and the size distribution charts are given in Appendix E.

Each mix has been characterized by an average particle size and standard deviation. The average particle size is based on volume and calculated as follows

$$\bar{d}_p = \sqrt[3]{\frac{M}{\sum \frac{m_i}{d_i^3}}} \tag{5.1}$$

where m_i and d_i are the mass and characteristic linear dimension[1] respectively for each size fraction and M is the total mass of the sample. For comparative purposes the Sauter

[1]The mean size of the aperatures of the two sieves used to create a particular size fraction have been used. For example, for the size fraction greater than 1.0mm and smaller than 1.4mm, d_i is 1.2mm

mean diameter, which is the diameter of a particle with the same volume to surface area ratio as the bulk, was also calculated. The Sauter mean diameter, ds_p, is calculated as

$$ds_p = \frac{\sum n_i d_i^3}{\sum n_i d_i^2} \tag{5.2}$$

where n_i is the number of particles in size fraction i, of characteristic linear dimension d_i. The standard deviation is calculated by

$$s = \sqrt{\frac{\sum n_i (\bar{d}_p - d_i)^2}{N-1}} \tag{5.3}$$

where n_i is the number of particles in size fraction i and N is the total number of particles in the sample. The number of particles is simply calculated by using the density of the sand. Since the density of each particle is constant and the number of particles is large, and so the population standard deviation and sample standard deviation are effectively the same, the standard deviation may be calculated as

$$\sigma_p = \sqrt{\frac{\sum m_i (\bar{d}_p/d_i)^3 (\bar{d}_p - d_i)^2}{M}} \tag{5.4}$$

Here the notation for standard deviation has changed to σ_p to indicate population as opposed to sample.

Finally, the standard deviation has been normalized by dividing by the average particle size to allow comparison, $\sigma_p^* = \frac{\sigma_p}{d_p}$. The average size and normalized standard deviation for each sand mix is given in Table 5.2

Another method to quantify the size and size distribution of each mix is by determining the parameters of a Rosin-Rammler distribution plot. Rosin and Rammler (Rosin and Rammler 1933) demonstrated that the fineness of pulverized coal may be represented analytically in exponential form. The analytical expression can also be applied to other granular materials

The Rosin-Rammler distribution may be expressed by the following exponential law

$$Res = 100 \ \exp(-b d_p^{n_{RR}}) \tag{5.5}$$

where

Res = percent mass residue on sieve of size x mm

b, n_{RR} = parameters that indicate mean size and extent of size distribution, respectively

By rearranging and taking logs twice the above equation can be written as

$$\log\left(\log\frac{100}{Res}\right) = n_{RR}\log d_p + \log b + \log(\log e) \tag{5.6}$$

Therefore, a plot of $\log\left(\log\frac{100}{Res}\right)$ against $\log d_p$ will result in a straight line. The gradient of this line will determine n_{RR} and the intercept will allow b to be calculated. Such a plot has been made for each mix and included in Appendix E.

In order to quantify how well the data fits a straight line, the coefficient of determination (Chapra and Canale 1988) was calculated. This coefficient is calculated as

$$C = \frac{S_t - S}{S_t} \tag{5.7}$$

where

$$S = \sum_{i=1}^{n}(y_i - y_{funct})^2$$

$$S_t = \sum_{i=1}^{n}(y_i - \bar{y})^2$$

For n data points, y_i is the value at each point, $\bar{y}$ is the average value of all data points and y_{funct} is value calculated by the linear fit.

The coefficient of determination is 0.95 or higher for each mix, see table 5.2. Therefore, the Rosin-Rammler distribution may also be used to characterize the mixes. Table 5.2 also gives the n_{RR} values. It should be noted that a high value of n_{RR} indicates a narrow size range and vice-versa.

The Rosin-Rammler index, n_{RR}, and the normalized particle size standard deviation, σ_p^*, are well related, as shown on Figure 5.11. The straight line relationship means that

either can be used to quantify the spread of the particle size distribution for the sand mixes in the same manner. The only difference is that as the spread of the size distribution increases, the Rosin-Rammler index, n_{RR}, decreases while the normalized standard deviation, σ_p^*, increases. In this study, as is common in the study of particles, the standard deviation, σ_p^*, will be predominantly used.

It should be noted that the size distribution was tested twice for mixes 1, 2 and 5. Hence, there are two values for all parameters given in Table 5.2. Mixes 3, 4, and 6 were made specifically for this study and are composed of particles with a narrower size distribution. Therefore, it was deemed that one test of the size range would suffice.

5.5 Experimental Procedure

After conducting some preliminary runs, three issues were identified as being important to ensure that satisfactory results were obtained. They were addressed prior to conducting the final experiments.

First, the thermocouple tubes in the bed probe, Figure 5.5, disrupted the flow. Therefore, the number of thermocouples in the probe was kept to a maximum of four. This probe, described in Section 5.2.2 above, was used to investigate temperature gradients down the center of the bed.

Second, the location of the bed probe had to be known during each run otherwise analysis of the results would be near impossible. To determine this, the probe was inserted into the cold furnace when filled with sand and its position was adjusted so that the thermocouple ends were at the required location inside the sand bed. As this was carried out the furnace was manually rotated to ensure that the bed was inclined at the correct angle. Then, the probe was fastened to its frame and the frame position relative to the furnace was recorded. During the hot test, the same frame to furnace relative position was maintained. Finally, to ensure that the probe did not move due to the force imparted upon it by the sand, a 30kg weight was placed on the probe frame.

Third, since this study is concerned with heat transfer in a rotating furnace, the time at which the bed is inside the furnace while the furnace is stationary had to be

minimized. It was imperative to load the furnace as quickly as possible. This was achieved by using a specially designed filling tube for loading the sand. Three such filling tubes were manufactured, each from six inch diameter, 24 gauge, spiral pipe that was purchased from Ecco in Vancouver, BC. Each tube was closed at one end and had slots cut out for filling and discharging material, see Figure 5.12. By filling two tubes up to 0.64m, sufficient material for a 100mm deep bed was collected. The third tube was used as a spare. The tubes allowed the furnace to be charged within one to two minutes.

The above was incorporated into the experimental procedure. This procedure is summarized next.

1. The material is charged into a cold furnace. The bed probe is inserted into the bed. By slowly rotating the furnace to ensure the bed inclination is the same as during the run, the bed thermocouple is positioned. It is fastened onto it's frame and the relative position of the probe frame and furnace is identified.

2. The probe and sand are removed. The furnace is coupled to the pilot kiln and the burner is placed in position.

3. The furnace is gradually heated at a firing rate sufficient to increase the refractory at 150-200°C/hr until the hot face temperatures are above 1100°C. The cold face temperatures, on thermocouples R3, R6 and R9 should be above 800°C. This normally took about 6 hours.

4. The gas and air flows are shut off and the burner is pulled back away from furnace.

5. The furnace is allowed to cool for about 5 minutes until the hot face temperatures are approximately 1000°C. This allows the refractory temperature to stabilize and prevents too high a drop in the hot face temperature when sand is added.

6. The furnace is rotated so that R1, R2 and R3 are in the lowest position. This allows the covered wall temperature to be measured when the sand is charged. Also the furnace position is consistent for all runs.

7. All refractory temperatures, R1-R9, are recorded. The stop watch and data logging are started.

8. The sand is inserted followed by the bed probe. The position of the bed probe is set.

9. After 3 minutes furnace rotation is initiated. This ensured that furnace rotation would be started at the same time in all runs. The time was selected to ensure that all of the above tasks were satisfactorily completed.

10. Refractory temperatures are recorded approximately every 2-3 minutes. Bed temperatures are recorded automatically on the data logger.

11. When no temperature gradient is evident in the bed, data recording is ceased.

12. The bed probe is retracted out from the furnace. The motion of the bed is visually checked to ensure that it is rolling (or slumping, as required by the test). The dynamic angle of repose is measured using a manual angle meter.

13. The experiment is complete.

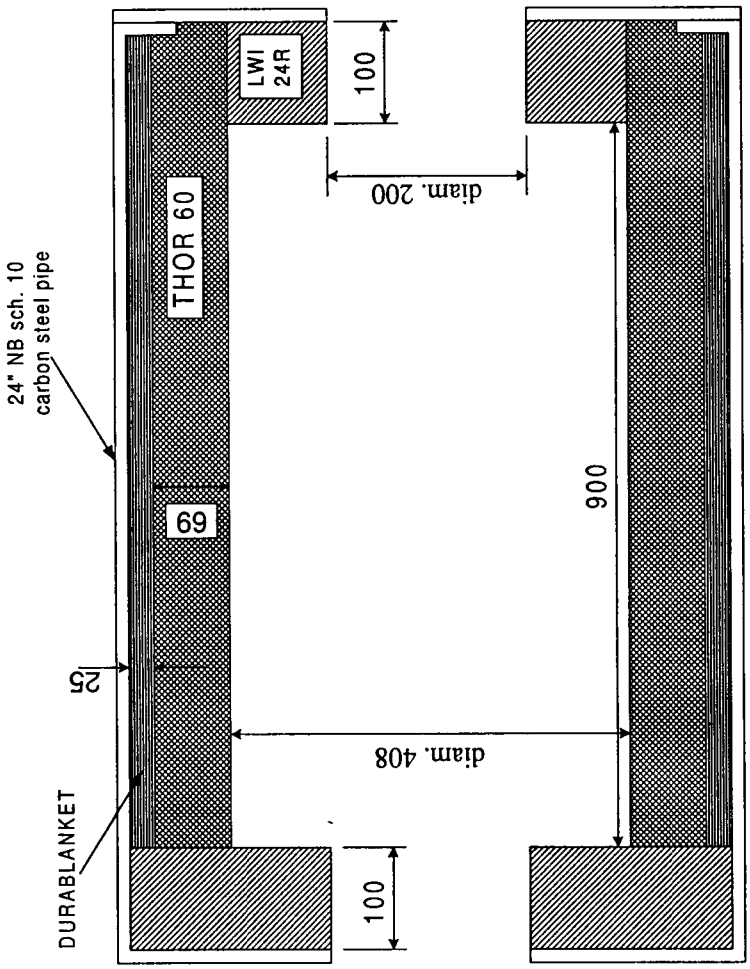

Figure 5.1: Test Furnace General Assembly

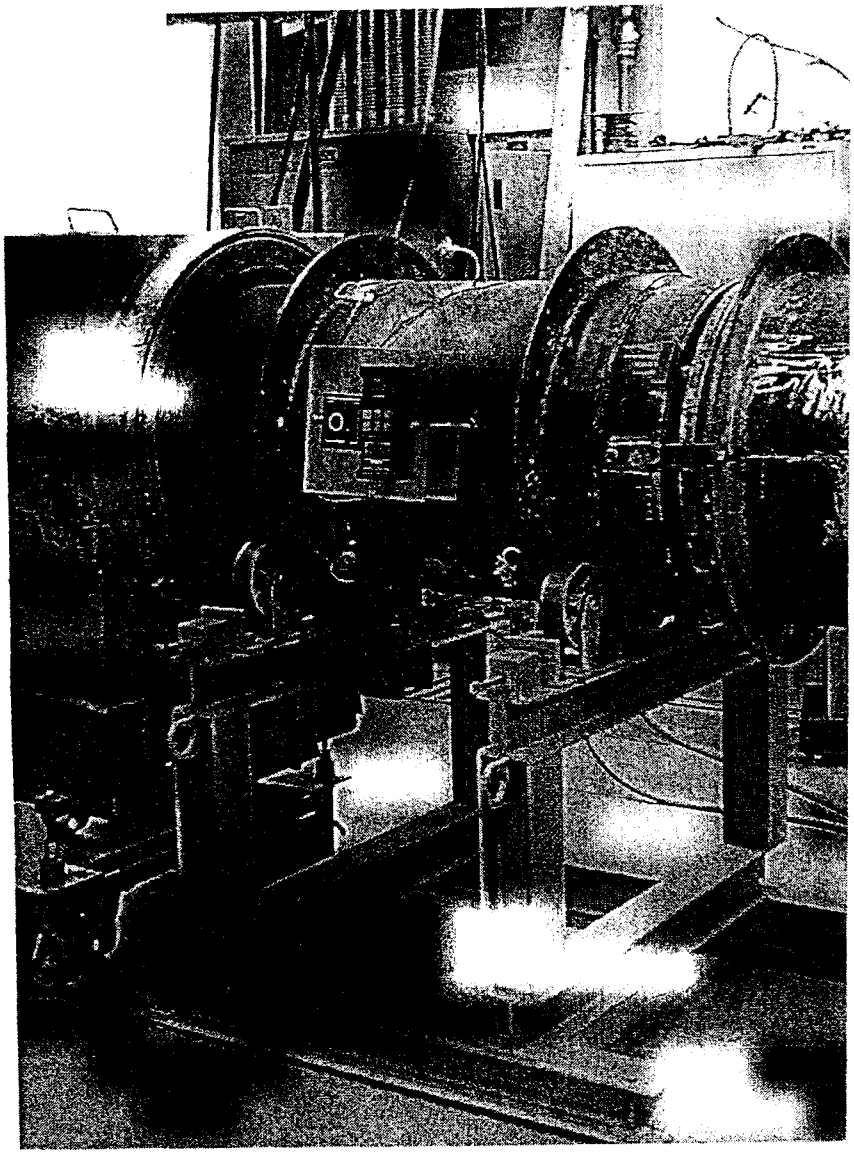

Figure 5.2: Experimental Furnace and Support

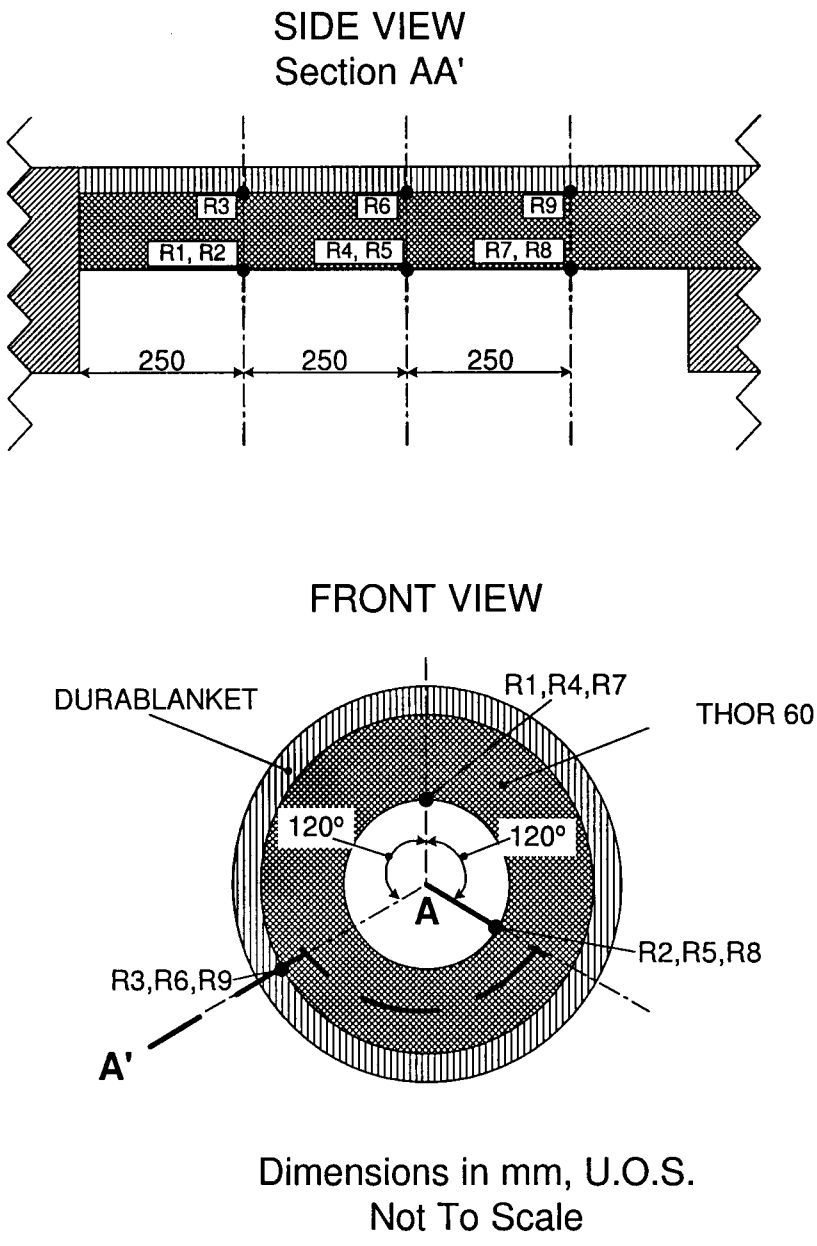

Figure 5.3: Location of Refractory Thermocouples

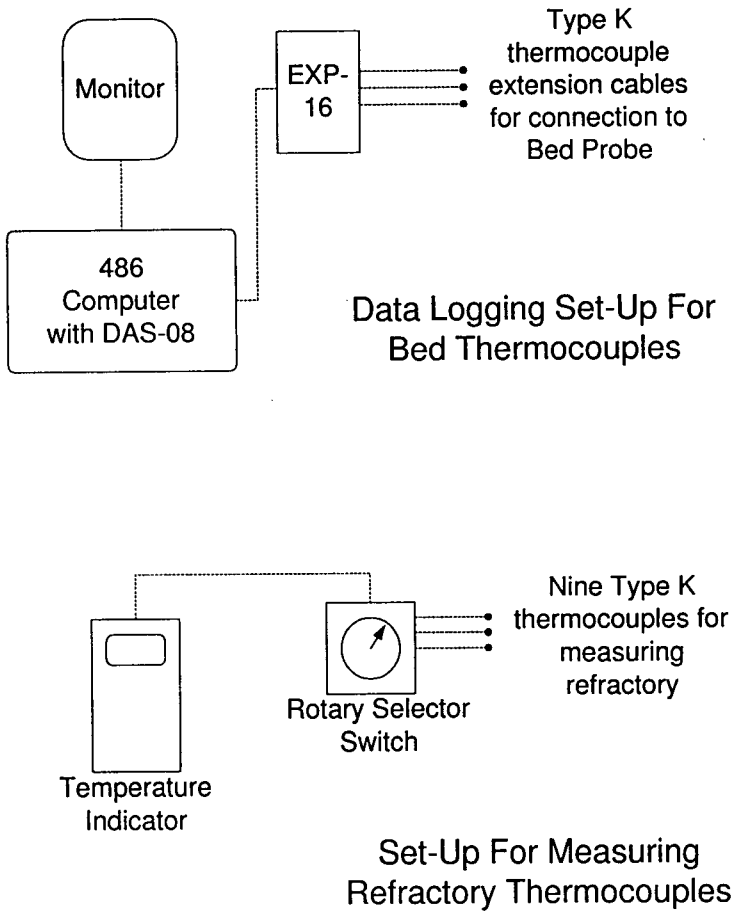

Figure 5.4: Instrumentation Set Up

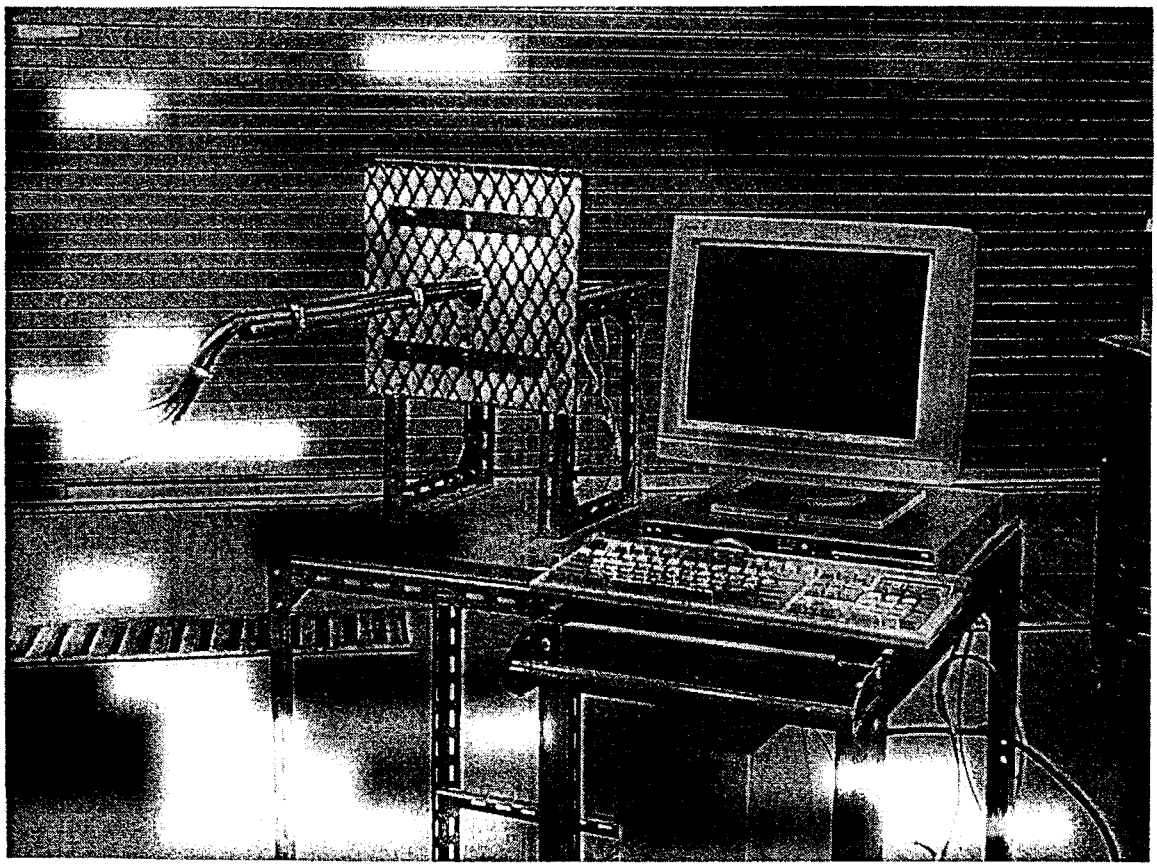

Figure 5.5: Bed Probe and Data Logging Equipment

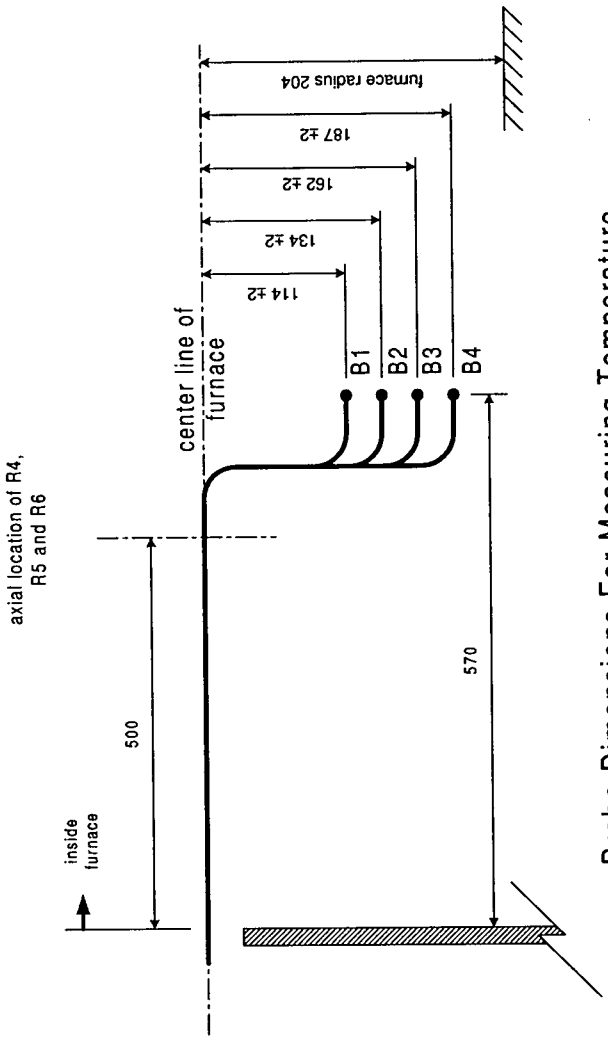

Figure 5.6: Dimensional Details of Bed Probe

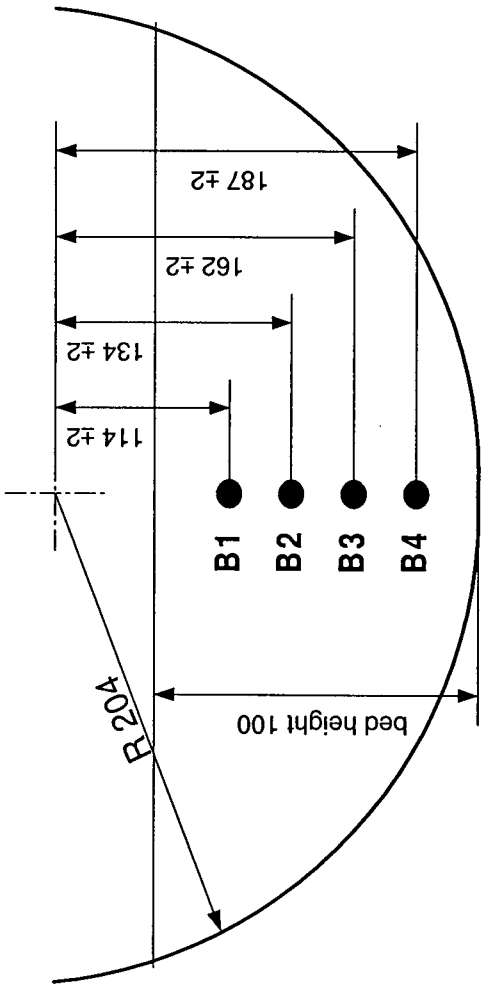

Figure 5.7: Location of Probe Thermocouples in Bed Cross-Section

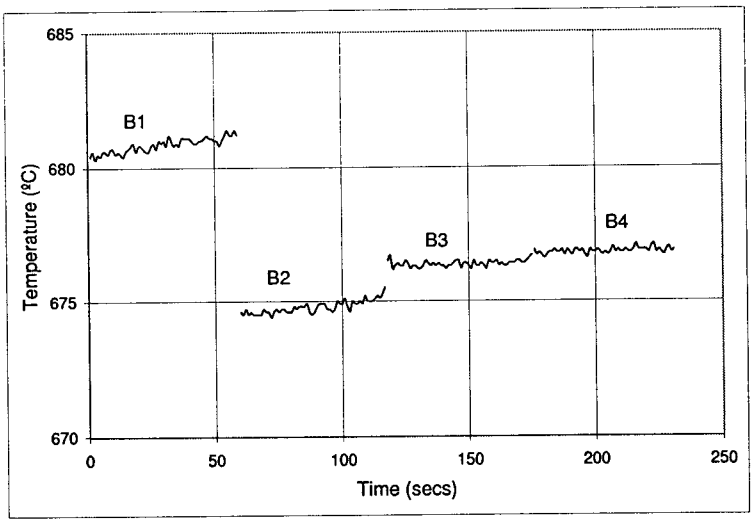

Figure 5.8: Temperature Indicated by Data Logger when Constant Millivolt Signal Applied

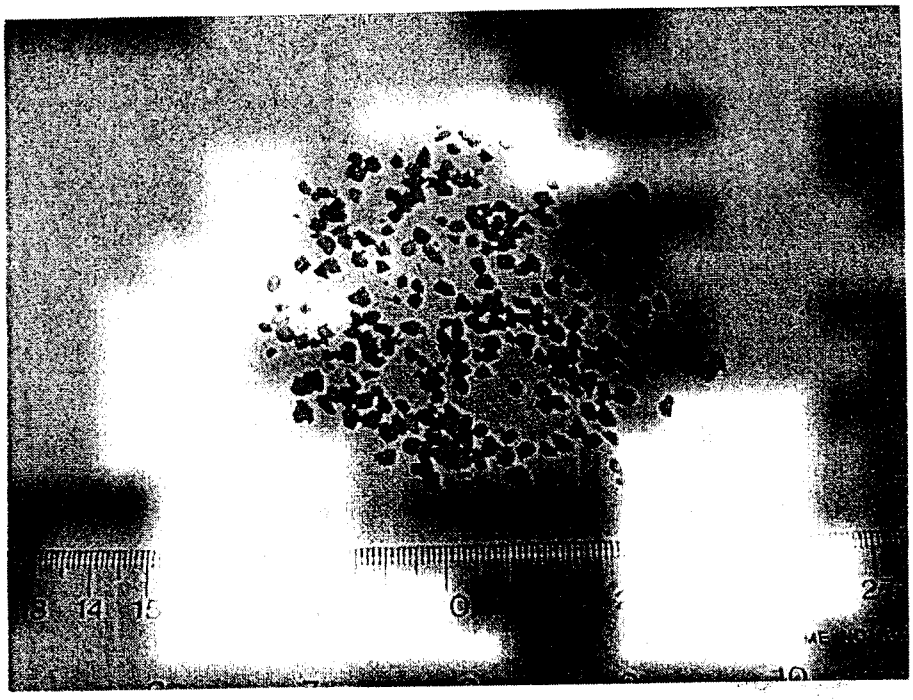

Figure 5.9: Coarse Sand Sample. 1/16-1/8 inch Filter Sand and Gravel

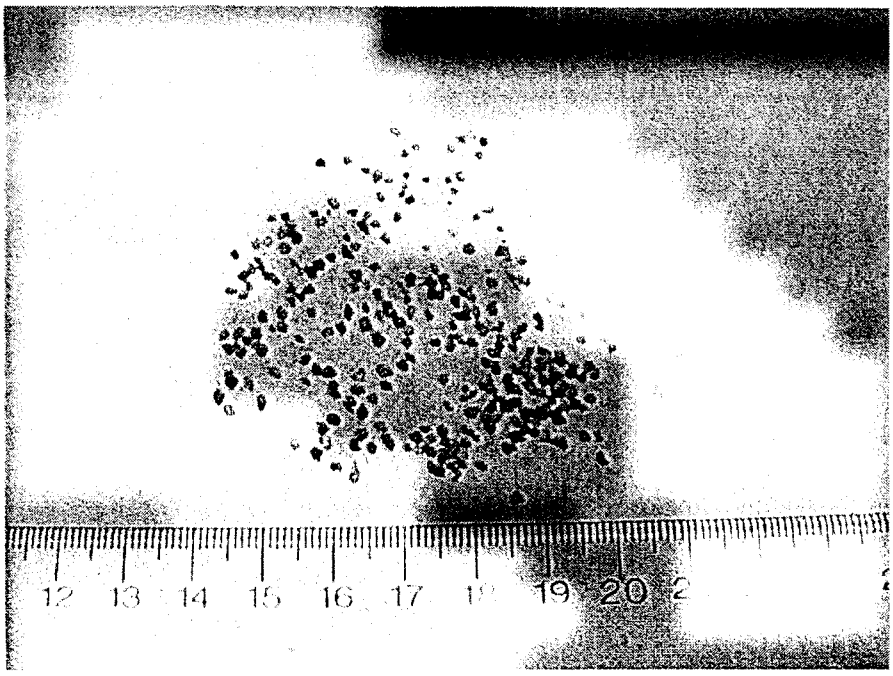

Figure 5.10: Fine Sand Sample. 10-20 Filter Sand

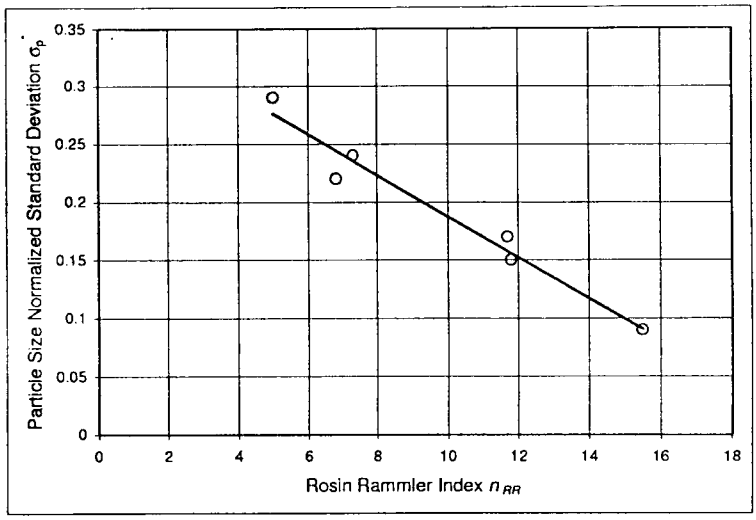

Figure 5.11: Relationship Between Rosin-Rammler Index, n_{RR}, and Normalized Standard Deviation of Particle Size, σ_p^*

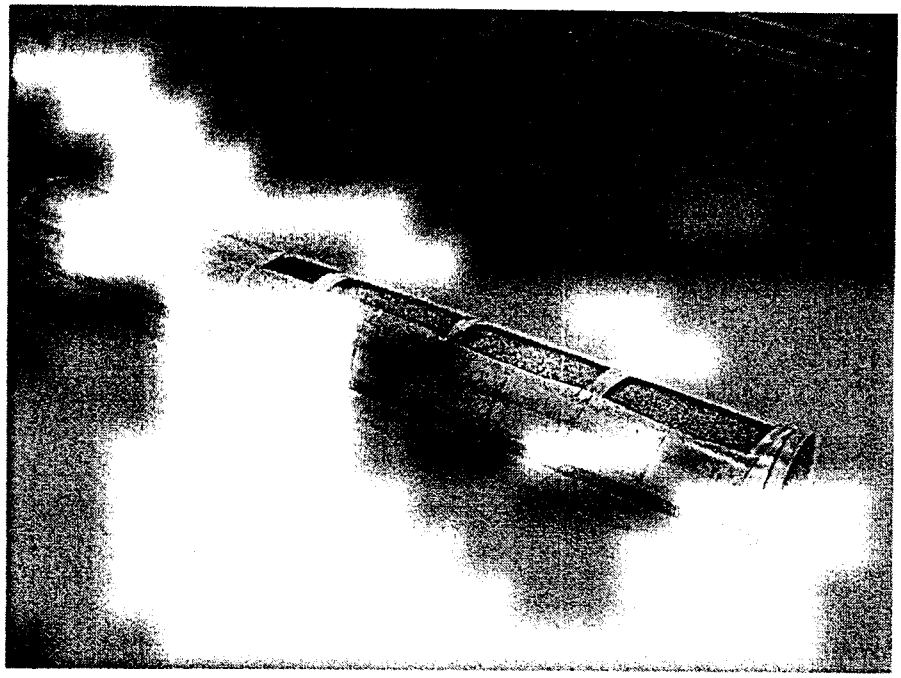

Figure 5.12: Furnace Filling Tube

Table 5.1: Calibration of Bed Data Logger

Signal Setting	1	2	3
Display on B1 (°C)	157	353	688
Display on B2 (°C)	156	353	685
Display on B3 (°C)	154	351	686
Display on B4 (°C)	154	350	685
Display on digital indicator (°C)	155	351	684

Table 5.2: Details of Prepared Sand Mixes

Mix	Description	Mean Vol. diam. (mm) ($\bar{d}_p$)	Sauter Mean (ds_p)	Relative Standard Deviation (σ_p^*)	Rosin-Rammler Index (n_{RR})	Coef. of Determination for Rosin-Rammler Plot (C)	Bulk Density kg/m^3	void fraction
1	50% coarse sand & 50% fine sand	1.4	1.5-1.6	.25-.33	4.1-5.8	0.95 & 0.89	1440	0.37
2	coarse sand as purchased	1.7-2.0	1.8-2.1	.22-.26	7.0-7.6	0.98 & 0.94	1446	0.39
3	coarse sand 2.3-3.3mm	2.4	2.4	.17	11.7	0.97	1422	0.39
4	coarse sand 2.8-3.3mm	3.0	3.0	.09	15.5	0.99	1433	0.39
5	fine sand as purchased	1.2	1.3-1.2	.22-.21	7.0-8.3	0.96 & 0.99	1428	0.37
6	fine sand 1.2-1.7mm	1.3	1.3	.15	11.8	0.99	1410	0.4

Chapter 6

Results and Discussion

The experimental test procedure, described in detail in the preceding chapter, consists of heating the furnace until the inside walls are 1100°C, charging it with sand and rotating it. When the furnace rotates, the temperature at select locations in the cross section of the bed is measured and recorded using the bed probe and data logger. The wall temperatures are measured and recorded manually using a portable temperature indicator.

This test procedure was followed for a number of runs and Table 6.1 describes them all. Runs 1 and 2 were carried out to determine whether the experimental apparatus was suitable for the study and to finalize the test procedure. Runs 3 to 19 provided the pertinent data, except for Runs 6 and 7, when equipment problems prevented the collection of data.

All runs were carried out with a bed height of 100mm, which is a fill of approximately 20% of the cross-sectional area of the test furnace. This was the maximum fill possible with the furnace and preliminary calculations, in Section 4, indicated that measurable temperature differences in the cross-section would exist in the bed. A furnace rotational speed of 1rpm was selected as the baseline because at this speed the bed motion was rolling, which is the bed mode of interest. After this other rotational speeds were investigated.

6.1 Recorded Data

A large amount of data was generated during the course of the experimental campaign. Therefore, in order to avoid unnecessarily confusing the reader with volumes of data, only certain results will be presented in the body of this chapter. These results are typical of the results obtained for all runs. Their presentation will serve to familiarize the reader with the type of data that was obtained for all of runs, as well as to highlight key observations. All results are, however, enclosed in Appendix F.

6.1.1 Bed Temperatures

For each run a temperature history down the center of the bed cross section was obtained by way of temperatures recorded by thermocouples B1, B2, B3 and B4. Figure 6.1 shows the location of the thermocouples in the bed cross-section. Axially, the thermocouples were at the center of the furnace, to ensure end effects were minimized. The temperature history was plotted for each run and the plots can be found in Appendix F.

To provide the reader with specific details in a somewhat compact form, temperatures for the four bed thermocouples, B1 to B4, at selected times for each run have been extracted and presented in Table F.1 which can be found in Appendix F . These times are 5, 7.5, 10, 12.5, 15 and 20 minutes.

The temperature histories recorded for all runs followed a typical pattern which is exemplified in Figure 6.2, which shows the temperature history plot for Run 5. From this figure one can note the following

- For the first 1-2 minutes only ambient temperatures are recorded on thermocouples B1-B4. During this time the furnace is being charged with sand and the probe is outside of the furnace.

- As the probe is moved into the furnace, the temperature rises rapidly due to radiation from the hot walls. Thermocouples B2-B4, the lower three of the four, enter the sand bed almost immediately and so their temperature rise is halted abruptly as they contact the sand inside the bed. Thermocouple B1, the upper thermocouple, remains outside of the sand bed while the probe is being located and so its temperature rises to a relatively high value before entering the bed.

- The trend for thermocouple B1 was common but not consistent, as can be seen in Figure 6.3, which shows data for Run 8. In this case thermocouple B1 entered the sand bed soon after the probe was put into the furnace.

- Once kiln rotation started, after 3 minutes, the thermocouples attained the bed temperature within approximately 1 minute. In some cases, as in Run 5, B1 took over a minute to attain the bed temperature. One can see on Figure 6.2 that it

continued to drop for a while after the 3 minute mark and then it rises as the bed temperature rises. This would negate the use of data prior to at least 5 minutes in any subsequent analysis.

- In most runs isothermal and maximum bed temperatures were reached after about 20 minutes. In Runs 15 and 16, see Figure 6.4 for example, the time is a little longer than 20 minutes because of the slower rotation of the kiln. These tests were at 0.43 rpm and the bed was slumping.

- Runs 15 and 16, Figure 6.4, also differ by the fact that their heat up curves are not as smooth as all of the other runs. Their heat up curves, especially B4, adopt a step wise trend which is attributed to the slumping nature of the bed motion. The only other run where this was observed was Run 9, Figure 6.5, which was at 3 rpm. One reason for this will be discussed in the paragraph after the next one. The output from these runs indicated that the response of the thermocouples was fast enough to detect changes in heat transfer due to bed behavior.

- After 5 minutes, at any particular time, B1, the thermocouple nearest the bed surface is always the coldest. B2 is the next warmest, then B3 and finally B4, nearest the wall, is the hottest. This would imply that the upper thermocouple, B1, is located closest to the cold core of the bed. B1 is most likely not in the active layer, for if it was, then it should record the highest temperature. In the active layer heat transfer is enhanced due to particle mixing and so the temperature would be close to the surface temperature which is the highest. This trend occurs for all runs except Run 9, Figure 6.5, which was at 3 rpm. In Run 9, B3 and B4 are similar but B3 is slightly warmer. This may be due to instrumentation errors since the differences between B3 and B4 are small.

- Also Run 9 should have a deeper active layer due to its higher rotational speed. Therefore, thermocouple B1 may be close in proximity to the boundary between the active layer and passive layer. B1 may be intermittently in contact with the active layer particles, causing its temperature to rise and then drop, creating the stepwise heat up curve.

- In many of the runs it was found that temperatures B1 and B2 were similar and B3 and B4 were similar, as in the case of Run 5, Figure 6.2. However, this was not always the case. In Run 8, Figure 6.3, while B3 and B4 are similar, B1 and B2 differ significantly. Also in Run 11, Figure 6.6, B1 is a little lower than B2, B3 and B4, which are all similar.

- Thermocouples B1 to B4 provide the temperature profile down the center of the bed. This has been plotted at certain times during the test for Runs 5 and 8, see Figures 6.7 and 6.8. As well as describing the results in a different perspective, these plots highlight the points raised in the last paragraph. For example, Figure 6.7 shows that temperatures B1 and B2 were similar and that B3 and B4 were similar during Run 5.

6.1.2 Wall Temperatures

The wall temperatures were measured manually at 2-3 minute intervals during the runs. Figure 6.9 gives the location of the thermocouples. Thermocouples R1, R2, R4, R5, R7 and R8 are embedded into the refractory about 1-2mm from the hot face. They are used to measure the hot face temperature of the refractory. R3, R6 and R9 are located between the refractory and the insulating blanket. From Figure 6.9 one can see that R4 and R5 are located towards the center of the furnace. They are at the same axial distance from the end but are 120° apart. R6 is also at the same axial location as R4 and R5, but because it measures the temperature of the interface between the refractory and blanket, its radial location is different. R6 is also 120° apart from R4 and R5. These thermocouples are located approximately at the same axial distance into the furnace as the bed thermocouples, B1-B4.

R1, R2 and R3 are located similarly to R4, R5 and R6, respectively, but at a different axial location, closer to the feed end. R7, R8 and R9 are also located similarly to R4, R5 and R6, respectively, but at a different axial location, closer to the drive end.

The data for Run 5 is given in Figures 6.10 and 6.11. Figure 6.10 shows the hot face temperatures (R1, R2, R4, R5, R7 and R8) and Figure 6.11 shows the temperatures at

the interface between the castable and blanket, R3, R6 and R9. As mentioned above, the area of interest is the center of the furnace. The data for the thermocouples at this location, R4, R5 and R6, is plotted on Figure 6.12. The data has been split in this way to avoid unnecessarily congesting the graphs with many curves.

Again these results are typical. R3, R6 and R9 measure the temperature at the interface between the high density refractory and the insulating blanket and so their initial temperatures are initially lower than the others, approximately 800°C as opposed to 1100°C, see Figure 6.11. Their temperatures tend to fall only slightly for the first ten or so minutes, and then the rate of temperature drop increases. The initial slow drop is most likely due to the the center of the refractory being much warmer than the interface during this initial time. Once this energy has escaped, the temperature falls rapidly.

The hot face temperatures, Figure 6.10, fall dramatically once the the sand is charged, from approximately 1100°C to 800°C. It can be noted that although the temperatures on R1, R4 and R7 fall once the sand is charged, they increase slightly when rotation starts. This is because these thermocouples are in the lower position, 6 o'clock position, when the sand is charged. Therefore, they cool more than R2, R5 and R8. Once furnace rotation commences they gain heat due to conduction from inside the refractory and radiation from the hotter parts of the wall and so their temperature rises slightly before cooling.

The reason for having thermocouples at three axial locations was to see whether large axial temperature gradients existed inside the furnace. From Figure 6.10 it can be seen that the hot face temperatures are indeed quite similar. This trend was seen for all runs and another example can be seen on Figure 6.13. However, it is evident that the interface temperatures are different, with R9 being the warmest, then R3 and R6 being the coolest. These differences are most likely due to slight differences in refractory thickness. The sensitivity of refractory thickness is investigated next.

In order to determine how sensitive the thermocouple readings are to differences in refractory and blanket thickness, the one dimensional model used to design the furnace and described in Section 4.2.2, was utilized. Measurements during the fabrication stage indicated that the blanket thickness ranged from 25-29mm. The refractory thickness ranged from 65-70mm. Table 6.2 gives the measurements that were taken at each re-

fractory thermocouple location. Based on this information, Table 6.3 gives the average refractory and blanket thickness and four variations of it that may exist in the furnace as built. These thicknesses were used in the one- dimensional code. Other input data for this code is given in Table 4.5.

The model was run for 120 minutes and this produced hot face and interface temperatures similar to those measured. In order to do so, however, the conductivities of the refractory and blanket were modified slightly. The results are also given in Table 6.3. It can be seen that the interface temperatures are more sensitive to changes in refractory thickness than blanket thickness. In this former case, differences in temperature at the interface are some 70°C, see the results for interface temperatures for tests 2 and 3 on Table 6.3. Although the differences between R3, R6 and R9 are larger, differences in refractory thickness are most likely the cause.

The furnace steel temperature was also measured using a surface thermometer which attached onto the steel magnetically. For all runs and all axial locations the steel temperature was 290-300°C for the duration of the experimental run. From Table 6.3 one can see that the calculated temperature is approximately 300°, which agrees with the measured value. The reason why the measured value was similar in all axial locations is likely due to thermal conduction across the steel shell, rather than a constant temperature of the blanket surface adjacent to the steel.

In order to carry out heat transfer analysis, see Section 6.3, a hot face temperature is required. As mentioned above, in all of the runs R5 was consistently higher than all of the other thermocouples, see Figures 6.10 and 6.13. In many case R5 was up to 100°C higher. The temperature values of the other hot face thermocouples were closer together. The only reason for this was instrument peculiarity, and so the data for R5 was excluded in calculating the temperature that represents the hot face. Therefore, the hot face temperature was taken as the average of all thermocouples on the hot face of the refractory except R5. Hot face temperature data, together with cold face temperature, is plotted for all runs and included in Appendix F. Figure 6.14, which shows the data for run 5, is an example. Note, the cold face temperature is that of R6, which is located at the center of the furnace. This value is dependent on the refractory thickness, which,

as previously discussed, is not constant throughout the furnace. The value is therefore specific to the location. It is plotted merely to complete presentation of data and is not used in the subsequent results analysis.

6.1.3 Other Observations

The dynamic angle of repose was measured using a hand held angle meter. In all runs the angle was approximately 31-35°. In the case of Runs 15 and 16, where the bed was slumping, the angle at the start of the slump was approximately 35° and approximately 32° at the end of the slump.

With sand mixes 1, 2 and 5 segregation was evident at the end of the runs. After runs with these mixes, when the sand was being removed from the furnace, only the larger sand particles were seen at the bed surface. On scooping out some sand from the surface, finer sand particles were seen beneath the larger particles. Note that these sand mixes, 1, 2 and 5, had the widest size distributions, with $\sigma_p^* = 0.29$, 0.24 and 0.22, respectively.

6.2 Temperature Non-Uniformity

Although it is appreciated that the bed temperature data is restricted to only four thermocouple locations, it is possible to obtain an estimate of the severity of the temperature non-uniformity within the bed. Since the four thermocouples, B1 to B4, are in the same position for each run, their spread of temperatures can be used to indicate temperature non-uniformity. One way to quantify the spread is through the temperature range, Ω_T, where

$$\Omega_T = \text{Max}[T_{B1} \ldots T_{B4}] - \text{Min}[T_{B1} \ldots T_{B4}] \tag{6.1}$$

Another way is through the standard deviation of the four temperatures at any point in time. For the four temperatures, the standard deviation is calculated as

$$\sigma_T = \sqrt{\frac{\sum_{i=1}^{4}(\bar{T}_B - T_{Bi})^2}{4}} \tag{6.2}$$

where $\bar{T}_B$ is the average of B1, B2, B3 and B4. Figure 6.15 shows the temperature range plotted over time for Runs 5, 10 and 11. Figure 6.16 shows the temperature standard deviation plotted over time for the same runs.

While temperature range and standard deviation adequately represent the degree of temperature uniformity, the temperature range, Ω_T, may be easier to appreciate by the reader. Also, the range is of interest in industrial kilns where it is desired to know how much cooler the center of the bed is. This information can indicate how well the bed material reacts. As such the temperature range is used for most of the subsequent analysis. However, for data analysis the choice is arbitrary, since the range and standard deviation are, in this case, related. Figures 6.17 shows the temperature range divided by the temperature standard deviation for Runs 5, 10 and 11[1]. It can be seen that the range is consistently about 2-2.5 times as large as the standard deviation.

The data on Figures 6.15 and 6.16 is quite typical of that obtained for all runs in that the temperature range, Ω_T, and standard deviation, σ_T, diminish over time as the bed becomes closer to isothermal. The somewhat erratic nature of the curves is caused by small instabilities in the temperature data logging equipment.

In order to compare the degree of temperature non-uniformity in the runs, an average temperature range, $\bar{\Omega}_T$, was calculated over a one minute time interval,

$$\bar{\Omega}_T = \frac{\int_{t_{in}}^{t_{fin}} \Omega_T}{t_{fin} - t_{in}} \tag{6.3}$$

where t_{in} and t_{fin} are the initial and final time. The integral in Equation 6.3 is calculated simply by summing the value of Ω_T at each data point between t_{in} and t_{fin}.

[1]Runs 5, 10 and 11 were chosen arbitrarily

As mentioned in Section 6.1.1 above, temperature data prior to five minutes into each run (or two minutes after rotation) is affected by radiant heat transfer between the hot walls and thermocouples as the bed probe in inserted. Therefore, $t_{in} = 5$ minutes was selected, and so , consequently, $t_{fin} = 6$ minutes. This was used to calculate $\bar{\Omega}_T$ during the earlier part of each run. The same procedure was used to calculate $\bar{\Omega}_T$ between 9 and 10 minutes. By doing this the degree of temperature non-uniformity was quantified for each run, during the initial stages and about mid way through the test. Table 6.4 gives the data for all runs.

To investigate how the spread of the particle size distribution affects temperature non-uniformity, $\bar{\Omega}_T$ is plotted against σ_p^* for runs at 1 rpm on Figure 6.18. Two linear lines of best fit have been drawn through the data points at 5-6 minutes and 9-10 minutes. This has been done in an attempt to identify a general trend, rather than to imply that the trend is linear. From Figure 6.18 one can see that, while there is scatter, the general trend is that as the particle size distribution widens, there is greater temperature non-uniformity, both during the initial stages of the run (5-6 minutes) and mid way through the run (9-10 minutes).

To determine whether the trend was indeed general, a similar plot was made for runs conducted at 2 rpm, see Figure 6.19. In this case the trend is not apparent, $\bar{\Omega}_T$ is greater when $\sigma_p^* = 0.15$ than when $\sigma_p^* = 0.24$, implying greater temperature non-uniformity with particles with a narrower size range. Another way to investigate this is to compare data for all runs after the same number of revolutions. Figure 6.20 shows temperature non-uniformity data for all runs between 2 and 3 revolutions and 6 and 7 revolutions. Note, that this corresponds to 5-6 minutes and 9-10 minutes, respectively, for runs at 1 rpm. By inserting a linear line of best fit through all data points an upward trend, as observed for runs at 1 rpm, is seen. However, the data scatter is extensive which questions the validity of such a trend.

The extent of data scatter can be seen on Figure 6.21, which shows data for all runs with mix 5 ($\bar{d}_p = 1.2$mm, $\sigma_p^* = 0.22$, $n_{RR} = 7.7$). The runs carried out at 1 rpm are all the same and so this data demonstrates the degree of repeatability. The data is spread by approximately 20% and so it is likely that this error range will hold for the data points at

the other speeds. As such this value has been used to construct error bars on Figure 6.21. The same procedure has been applied to the data at 9-10min. From Figure 6.21 it would appear that increasing kiln speed reduces makes the bed temperature more uniform.

6.3 Heat Transfer Rates and Coefficients

Another way in which to analyze the effect of particle size distribution on temperature non-uniformity in the bed is through its effect on heat transfer to the bed. A bed that is closer to isothermal conditions will allow a higher overall rate of heat transfer to it than one that has a cooler center and is warmer closer to the exposed surface and wall. In the latter case, since the temperature difference between the walls and bed surfaces is lower, the driving force for energy transfer is less.

6.3.1 Calculation of Heat Transfer Rates and Coefficients

In order to estimate the heat transfer rate from the wall to the bed, it is assumed that the average temperature of the four bed thermocouples at any time, $\bar{T}_{B1...B4}$, represents the average bed temperature, $\bar{T}_b$. In this way the change in average temperature can be used to calculate the heat flow rate, $Q_{w\to b}$, to the bed as

$$Q_{w\to b} = M_b c_{pb} \frac{\partial \bar{T}_b}{\partial t} \tag{6.4}$$

where

M_b = mass of bed (kg)

$c_{p,b}$ = specific heat capacity of bed (kJ/kg K)

$\frac{\partial \bar{T}_b}{\partial t}$ = rate of temperature change of average of B1 to B4 (degrees K per second)

$\frac{\partial \bar{T}_b}{\partial t}$ is calculated simply by calculating $\frac{\Delta \bar{T}_b}{\Delta t}$ from the discrete data points collected by the data-logger.

Having calculated the heat taken up by the bed, $Q_{w\to b}$, an overall heat transfer coefficient, h_o, can be calculated using

$$h_o = \frac{Q_{w\to b}}{A_b(T_w - T_{bs})} \tag{6.5}$$

In Equation 6.5 T_w is the wall temperature. Section 6.1.2 described that the inside wall

temperatures were measured by thermocouples R1, R2, R4, R5, R7 and R8, see Figure 6.9. The temperatures recorded by these thermocouples were generally similar except for R5, which was consistently higher. No apparent reason for this was discovered but it is unlikely that one region of the refractory surface is much hotter than the rest. As such it can be assumed that the average of R1, R2, R4, R7 and R8 represents the hot wall temperature, T_w.

A_b in Equation 6.5 is the area of the bed surfaces exposed to the wall. To calculate this refer to Figure 4.9. A_b is the straight distance XY plus the arc distance XY multiplied by the length of the furnace.

T_{bs} is the temperature of the bed surface and may be assumed to be the temperature measured by TB4. TB4 is closest to the covered bed area in contact with the wall. However, it also can be assumed to represent the exposed bed surface temperature. This latter assumption is valid if one considers the movement of particles in the cross section, as depicted in Figure 6.22. Particles entering the plug flow region maintain their radial position since motion in this region as a rigid body. Therefore, the temperature recorded by TB4 is likely to be the temperature of particles closest to the exposed bed surface as well.

The above arguments indicate that $T_w = T_{ew} = T_{cw}$ and $T_{bs} = T_{eb} = T_{cb}$. This can be used to calculate the rate of heat transfer from the exposed wall to the bed surface by radiation[2] using

$$Q_{ew \to eb} = \frac{\sigma_{SB}(T_{ew}^4 - T_{eb}^4)}{R_w} \tag{6.6}$$

[2]At the temperatures of the experiment and since there was no gas flow over the bed, heat transfer by conduction and convection is negligible.

where

$$
\begin{aligned}
R_w &= \frac{1-\epsilon_w}{\epsilon_w A_{ew}} + \frac{1}{A_{eb}\mathcal{F}_{eb\to ew}} + \frac{1-\epsilon_b}{\epsilon_b A_{eb}} \\
T_{ew} &= \text{wall temperature in degrees K } (T_w) \\
T_{eb} &= \text{exposed bed temperature in degrees K } (T_{B4}) \\
A_{ew} &= \text{exposed wall area per unit length in m}^2/\text{m} \\
A_{eb} &= \text{exposed bed area per unit length in m}^2/\text{m} \\
\mathcal{F} &= \text{view factor}
\end{aligned}
$$

In this expression Kirchoff's law is assumed, i.e. $\alpha = \epsilon = 1 - \rho$. Also A_{eb} = chord length XY and $A_{ew} = 2\pi r\left(\frac{2\pi-\beta}{2\pi}\right)$, on Figure 4.9.

Finally, the difference between $Q_{w\to b}$ and $Q_{ew\to eb}$ must be the rate of heat flow between the covered wall and covered bed, $Q_{cw\to cb}$. $Q_{ew\to eb}$ and $Q_{cw\to cb}$ can then be used to calculate their respective heat transfer coefficients, $h_{ew\to eb}$ and $h_{cb\to cw}$.

$$h_{ew\to eb} = \frac{Q_{ew\to eb}}{A_{eb}(T_w - T_{eb})} \tag{6.7}$$

$$h_{cw\to cb} = \frac{Q_{cw\to cb}}{A_{cb}(T_w - T_{cb})} \tag{6.8}$$

where

$$
\begin{aligned}
A_{eb} &= \text{straight distance XY on Figure 4.9 mutiplied by furnace length (m}^2) \\
A_{cb} &= \text{arc distance XY on Figure 4.9 mutiplied by furnace length (m}^2) \\
T_w &= \text{wall temperature in degrees K} \\
T_{eb} &= \text{exposed bed temperature in degrees K } (T_{B4}) \\
T_{cb} &= \text{covered bed temperature in degrees K } (T_{B4})
\end{aligned}
$$

Another quantity that has been calculated is the ratio of the heat transferred through

the covered bed surface and exposed bed surface, Ψ, where

$$\Psi = \frac{Q_{cw \to cb}}{Q_{ew \to eb}} \tag{6.9}$$

6.3.2 Results Obtained

The above analysis has been carried out for all runs. Therefore, for every run a plot of the heat rate to the bed, $Q_{w \to b}$, the overall heat transfer coefficient, h_o, the exposed wall to exposed bed heat transfer coefficient, $h_{ew \to eb}$, the covered wall to covered bed heat transfer coefficient, $h_{cw \to cb}$, and the ratio of heat transferred across the covered bed surface and exposed bed surface, Ψ, have been made. These plots are contained in Appendix F. To highlight the trends observed, Runs 4, 5 and 8 will be used as examples.

Figure 6.23 shows the heat rate to the bed, $Q_{w \to b}$, and the temperature driving coefficient, $T_w - T_{bs}$, for Run 5. It can be seen that, as expected, the heat rate to the bed is initially high but tapers away towards the end of the test as the temperature driving force (difference between T_w and T_b) diminishes. The heat rate to the bed and temperature driving force profile for Run 4 is similar, see Figure 6.24. This trend was found in all runs.

The overall heat transfer coefficient, h_o, profile, however, was not always similar. In Run 5, it was relatively constant, see Figure 6.25. In Run 4, Figure 6.26 it followed a wave-like trend, gradually rising, falling and rising again. Overall it was found that the trend for this curve was different from one run to the next. It should be noted that during the final minutes of the plot, while the bed temperature is closer to isothermal conditions, it also is similar to the wall temperature. Therefore, slight errors in the thermocouple readings manifest into large errors in the value of the heat transfer coefficients. As such, in some runs, such as Run 4, the overall heat transfer coefficient becomes very large and/or negative.

The ratio between the heat flow across the covered bed surface and exposed bed surface, Ψ for Run 5 is shown in Figure 6.27. While the profiles were slightly different for all runs, Ψ, was always more than 1.0 indicating that more heat is transferred across the covered bed surface. Table 6.4 gives the average values of Ψ between 5-6 minutes and 2-3 revolutions for all runs. The mechanism for heat transfer across the covered bed surface is

radiation and conduction between the covered wall surface and the sand particles adjacent to it. Since the covered wall area is much less than the exposed wall area, its resistance to radiative heat exchange is greater. However, since the heat rate between the covered wall and covered bed is higher, then conduction heat transfer must be significant. As such, the covered wall to covered bed heat transfer coefficient must be a function of both radiation and conduction.

The rate of heat transfer across the covered bed and exposed bed surfaces was used to calculate the respective heat transfer coefficients. As an example Figure 6.28 shows the profile of the covered wall to covered bed heat transfer coefficient and the exposed wall to exposed bed heat transfer coefficient.

Prior to further analysis with heat transfer coefficients, it is worth determining the sensitivity of the results to input parameters. The bed emissivity was taken to be 0.9, as quoted for sand in Incopera and Dewitt (1981). However, since the bed is granular, the effective emissivity may be larger. This is because any radiation reflecting off the bed particles would most likely be directed towards another particle. Therefore, the bed absorptivity is closer to 1.0 and consequently, through Kirchoff's law, the emissivity would also be 1.0. Also, the wall emissivity was taken as 0.87, as quoted for silicon carbide (the major constituent of the refractory) in Incopera and Dewitt (1981). However, the emissivities for other refractories are closer to 0.75. Calculations with a bed emissivity of 1.0 and refractory emissivity of 0.75 were carried out using the data for Run 5. Figure 6.29 shows the effect on the covered bed to covered wall heat transfer ratio. It can be seen that the change is some 5-10% in either case.

For all analyses bed depth was constant and the depth was measured to be 100mm. To investigate how sensitive the results are with bed depth the heat rate to the bed and overall heat transfer coefficient was calculated for a 110mm bed also. Data for Run 5 was again used and the results are given in Figure 6.30. A small change can be seen.

The sensitivity analysis indicates that the results are only mildly affected by input data, other than temperatures.

6.3.3 Effect of Particle Size Distribution

As in the case of the analysis of temperature non-uniformity, Section 6.2, the heat transfer coefficients and heat rates in each run were compared by calculating the average values over a one minute period. Also, for similar reasons, the averages over the same time periods, 5-6 and 9-10 minutes and 2-3 and 6-7 revolutions, were used. Table 6.4 gives results for values at 5-6 minutes and 2-3 revolutions for all runs.

Figure 6.31 shows the average overall heat transfer coefficient, $\bar{h}_o$, plotted against the normalized particle size standard deviation, σ_p^*, for all runs. The average heat rate to the bed, $\bar{Q}_{w\to b}$, is plotted in Figure 6.32.

The above results imply that particle size distribution has little effect on overall heat transfer and heat rate to the bed. To further investigate this the final bed temperature after each run was plotted with particle size standard deviation, see Figure 6.33. It would appear that particle size distribution does not influence the final bed temperature either, which agrees with the premise made in the first sentence of this paragraph.

One question that can be asked is whether the temperature uniformity within the bed has an influence on the heat rate to the bed. It would be expected that a well mixed bed of uniform temperature would be a better heat sink. This is because its surface temperatures would be lower than those in a bed with cooler particles in the middle and warmer particles at the surfaces. This would lead to a greater temperature driving force for energy transfer between the heat source, refractory walls in the current case, and bed. Figure 6.34 shows a plot of averaged temperature range, $\bar{\Omega}_T$, and average heat rate to the bed, $\bar{Q}_{w\to b}$. The data points are scattered indicating that no relationship was evident.

The effect of furnace rotational speed was investigated to see how much heat transfer is influenced by it. Figure 6.35 shows the relationship between overall heat transfer coefficient, $\bar{h}_o$, and rotational speed. Figure 6.36 show the shows the relationship between average heat rate to the bed, $\bar{Q}_{w\to b}$, and rotational speed. For the earlier data, between 5 and 6 minutes, increasing rotational speed can be seen to increase heat transfer coefficient and heat rate to the bed. Between 9 and 10 minutes the same trend is not clear.

Increasing rotational speed increases the rate of material mixing within the bed and

consequently the adjective component of heat transfer is higher. As such the data for 5-6 minutes is understandable, increasing rotational speed increases overall heat transfer coefficient and heat rate to the bed. This provides some credibility to the experimental results. Between 9-10 minutes one would expect a similar trend but the reason for not finding it are likely related to the lower temperature driving force, $T_w - T_b$, at that time. Slight errors in the temperature measurements may lead to this.

The error bars on Figures 6.35 and 6.36 were calculated based on the range of data for the runs at 1 rpm, which were the same and so demonstrate repeatability. The error ranges further highlight the wide data scatter.

6.4 Overall Comments

The results provided little evidence of a relationship between particle size distribution and temperature uniformity in the cross-section. Since particle segregation was evident, heat transfer within the bed, therefore, appears to be a function of bed effective thermal diffusivity (due to effective conductivity and advective transfer) rather than overall particle flow and re-arrangement.

Prior to making such a statement, however, other reasons for not finding a relationship between particle size distribution and temperature uniformity should be considered. It is possible that during each test particle motion was in a transient mode and segregation had not yet established. This would mean that the bulk particle flow in all runs was similar, leading to similar heat transfer rates.

However, pertinent data from each test was obtained within 20 minutes, which equates to 17 revolutions at 1 rpm, since the furnace was not rotated for the first 3 minutes. Work done on the kinetics of segregation indicates that transverse mixing is, in fact, a fast process. The work of Rogers and Clements (1972) indicated that segregation was well developed after 10 revolutions but Nityanand, Manley, and Henein (1986) found it to be faster, within 1 revolution. The former workers did not take data prior to 10 revolutions since their tests were conducted at higher rotational speeds. Since the current tests were conducted for 17 revolutions, it is likely that the bed was segregated for a significant part

of the test and so it is unlikely that the kinetics of segregation account for not finding a relationship between particle size distribution and temperature uniformity.

If the rate of particle mixing in the active layer is so high that the active layer is effectively isothermal, then all material entering the plug flow region is at the same temperature. Any temperature difference in the plug flow region would then only occur due to radial heat diffusion. This would make all of the results similar. However, since material in the plug flow region remains there for no more than 30 seconds before re-entering the active layer, the temperature of B1 should be higher than the temperature of B4 30 seconds earlier. This was not found to be the case and so an isothermal active layer could not explain the results.

If indeed particle size distribution does not affect temperature non-uniformity within the bed, then an explanation of phenomena that lead to the notion that it does is warranted. In industry it was observed that finer particles of lime remained uncalcined (Sunnergren 1979; Von Wedel 1973). Material flow studies, e.g. (Henein 1980), identified that finer particles remained in the center of the bed, creating the so called "kidney". From this an inference was made that the segregation of the finer particles prevented them from traveling to the exposed bed surface and receiving heat from the walls and free-board. The findings of the current study imply that a core of segregated fine particles may not create a cold center, but rather, a cold core is a result of poor heat transfer through the bed. Naturally, in a lime kiln for example, the finer particles are in the middle and hence would remain uncalcined if the bed core was cold

The heat transfer analysis, Section 6.3, also showed no relationship with particle size distribution. The lack of a relationship between the degree of temperature uniformity, $\bar{\Omega}_T$, and average heat rate to the bed, $\bar{Q}_{b\to w}$ is particularly interesting. It implies that transverse heat transfer to the bed may be independent of heat transfer within the bed. Therefore, a one-dimensional model of a kiln that only considers overall heat transfer between the free-board and bed can provide useful information about kiln performance. Analysis of temperature gradients within the bed can be carried out independently which lends credibility to pseudo three-dimensional models such as Boateng and Barr (1996b).

In experiments like this at such high temperatures, errors are inevitable. The experi-

mental procedure attempted to minimize these but some of the errors were:

- Differences in initial hot refractory temperature between each run.
- Differences in the time the sand bed was stationary inside the furnace prior to rotation.
- Disruption of particle flow by the bed probe, which could have enhanced particle mixing.

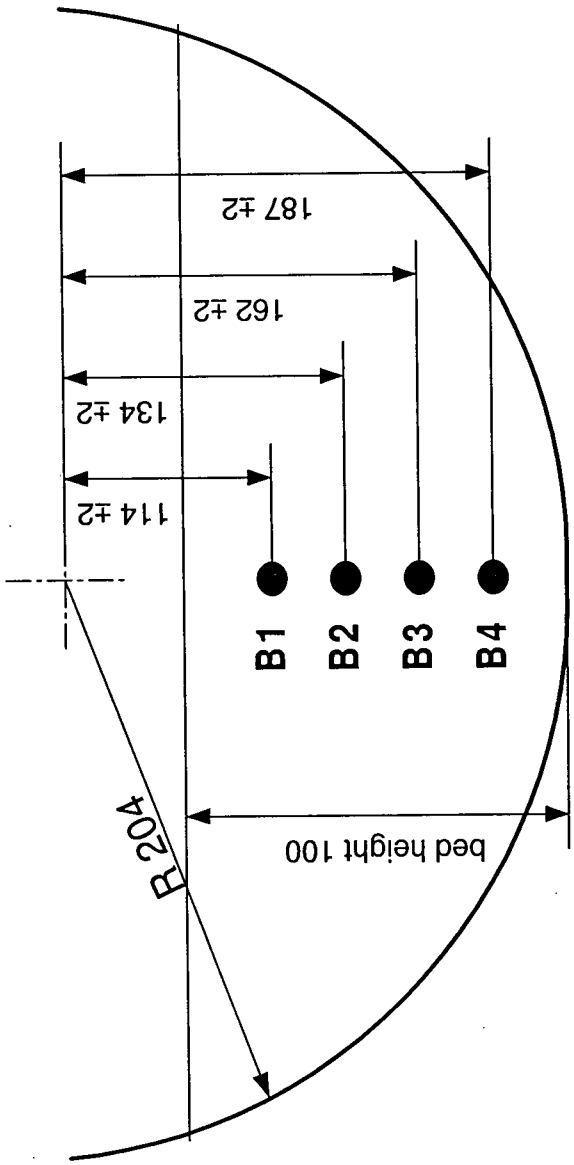

Figure 6.1: Location of Thermocouples in Bed

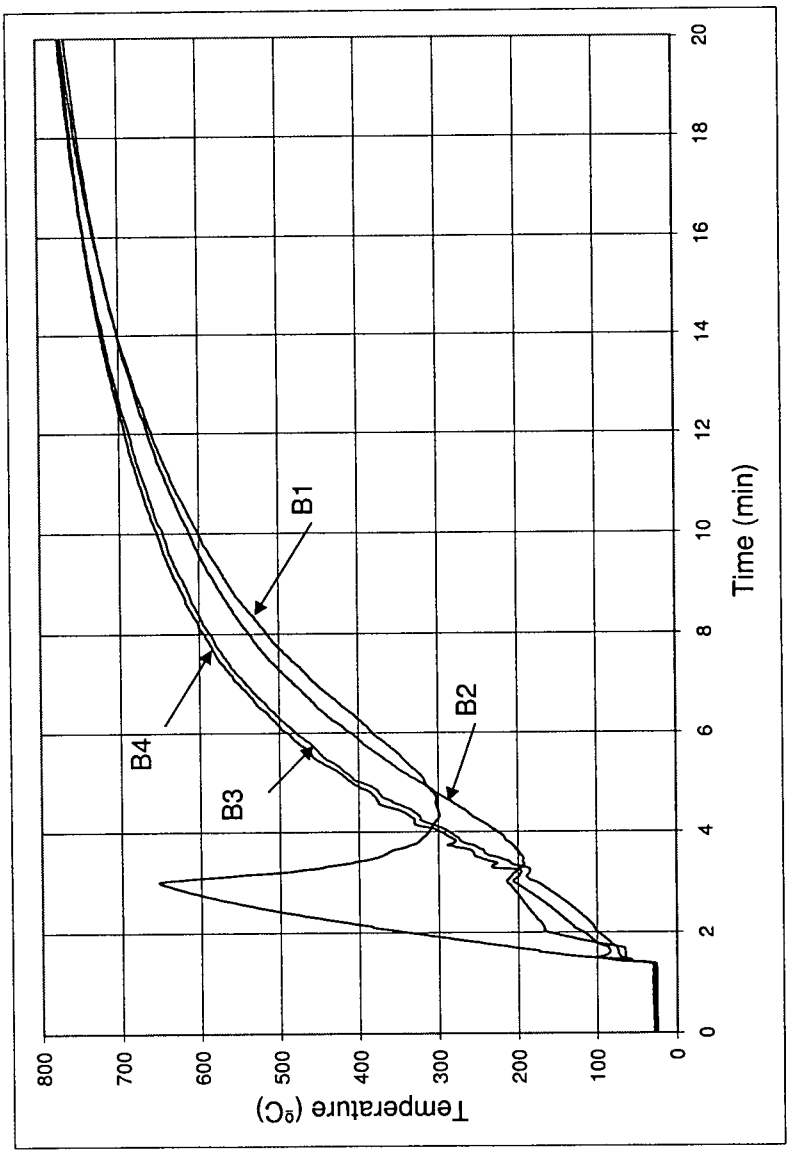

Figure 6.2: Run 5 Bed Temperature History. Mix 2 at 1 rpm ($\bar{d}_p = 1.9$mm, $\sigma_p^* = 0.26$, $n_{RR} = 7.3$)

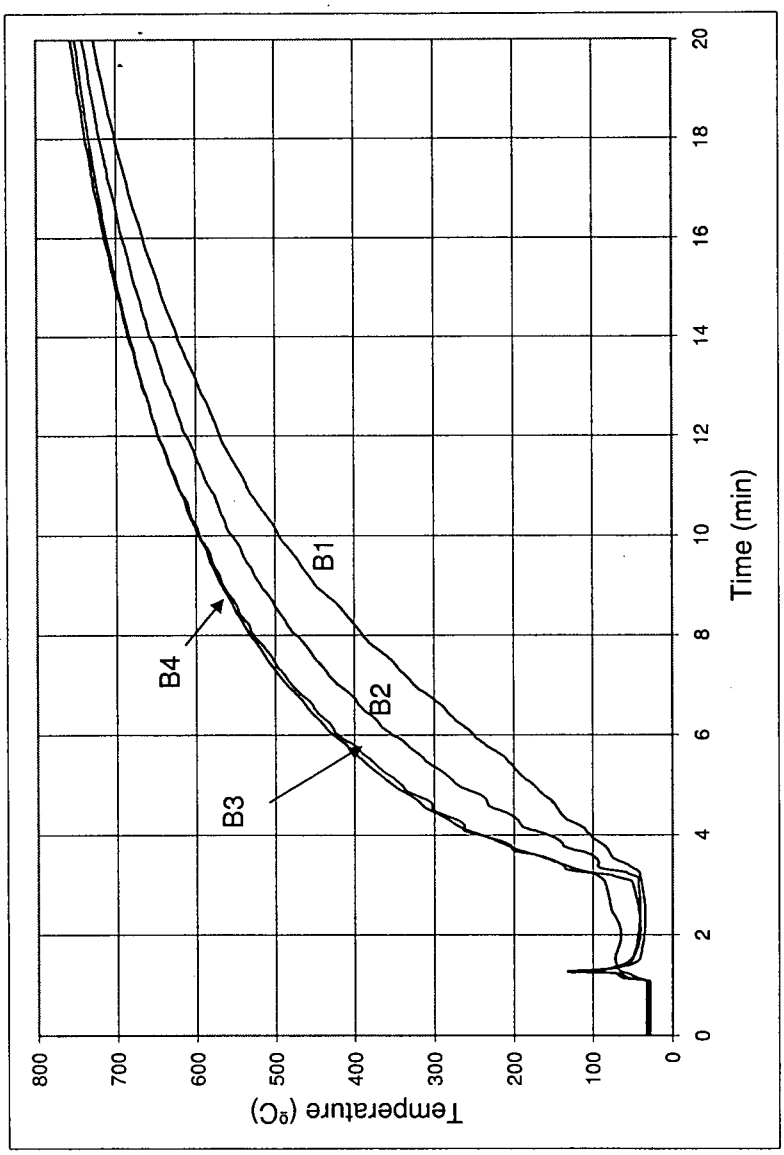

Figure 6.3: Run 8 Bed Temperature History. Mix 5 at 1 rpm ($\bar{d}_p = 1.2$mm, $\sigma_p^* = 0.22$, $n_{RR} = 7.7$)

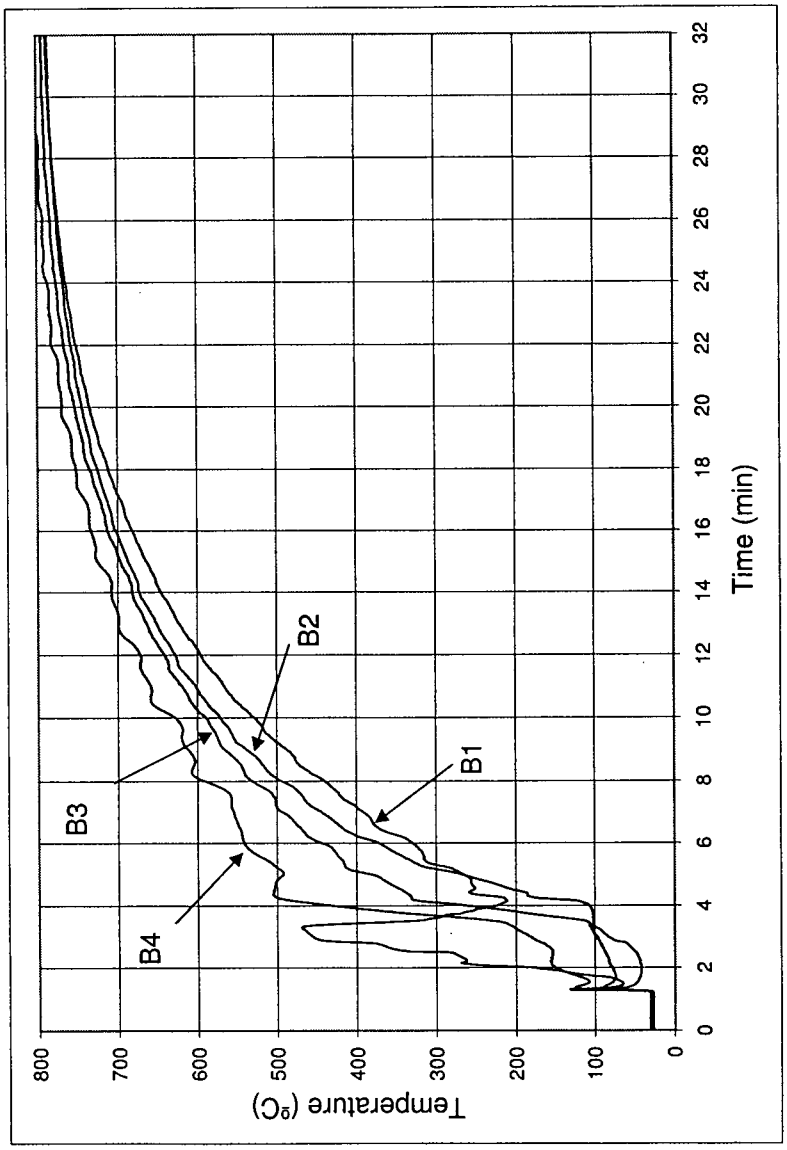

Figure 6.4: Run 15 Bed Temperature History. Mix 5 at 0.43 rpm ($\bar{d}_p = 1.2$mm, $\sigma_p^* = 0.22$, $n_{RR} = 7.7$)

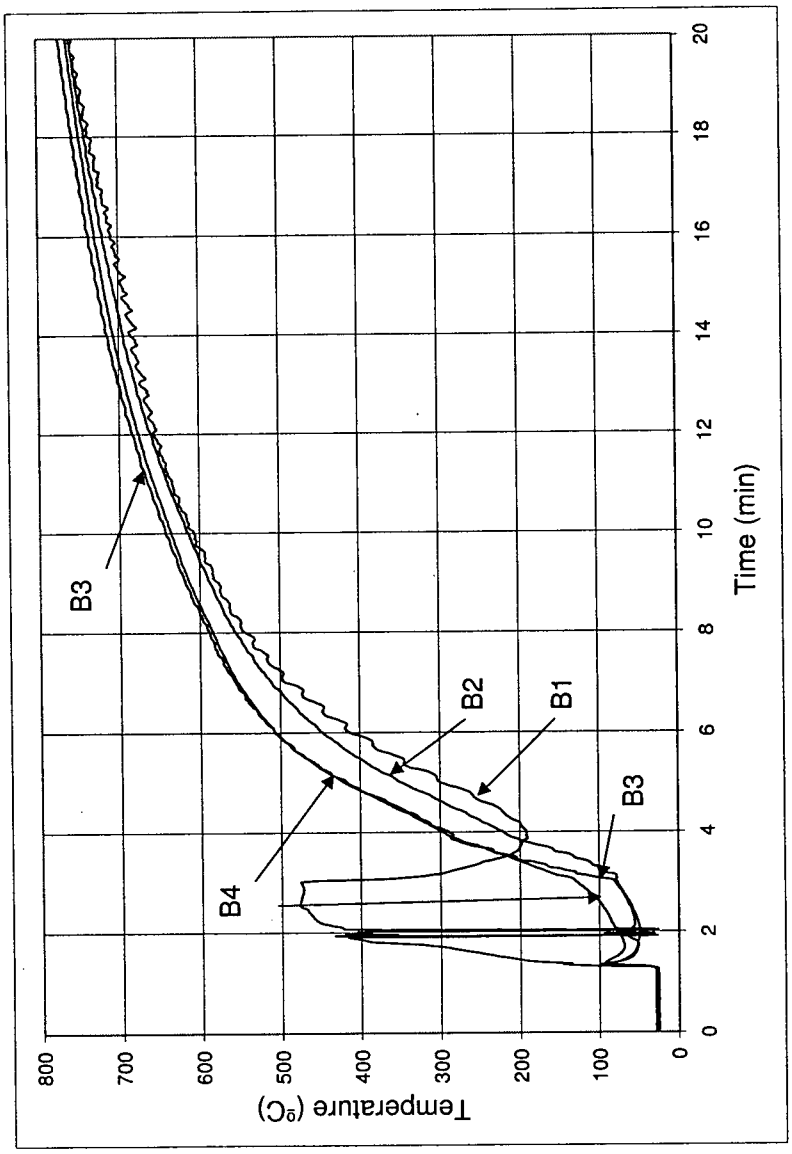

Figure 6.5: Run 9 Bed Temperature History. Mix 5 at 3 rpm ($\bar{d}_p = 1.2$mm, $\sigma_p^* = 0.22$, $n_{RR} = 7.7$)

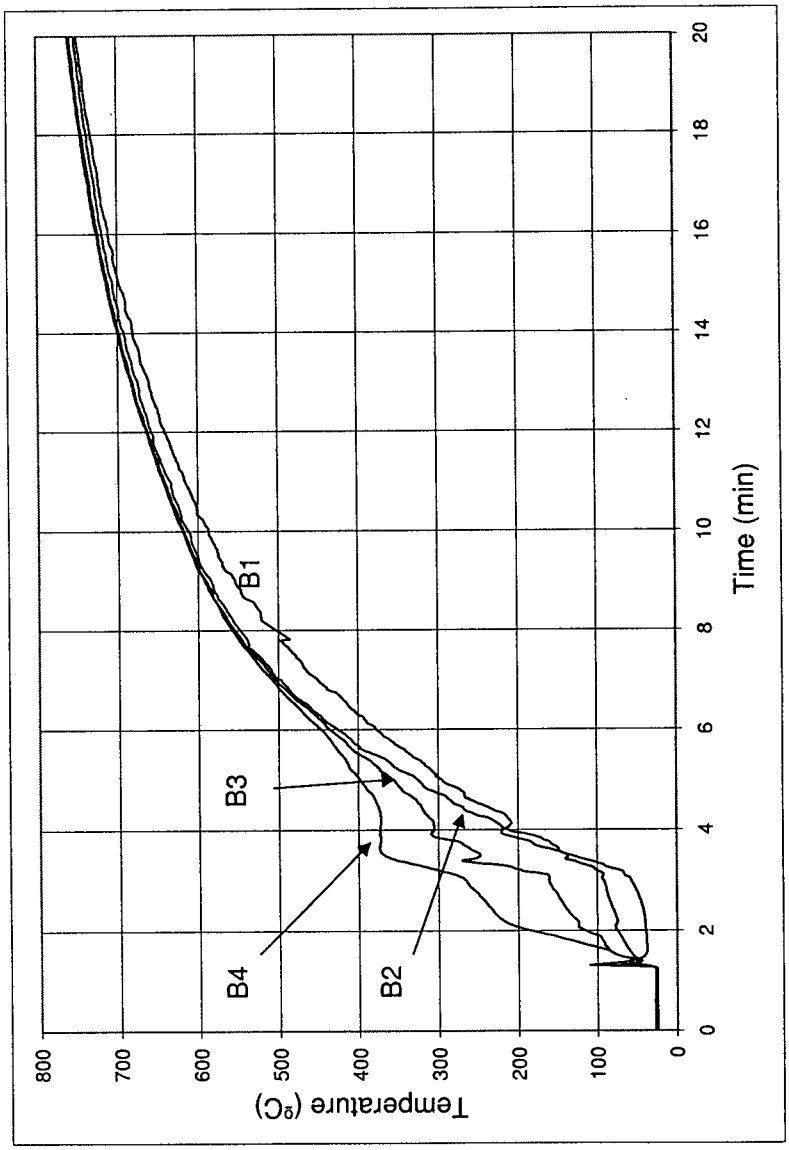

Figure 6.6: Run 11 Bed Temperature History. Mix 4 at 1 rpm ($\bar{d}_p = 3.0$mm, $\sigma_p^* = 0.09$, $n_{RR} = 15.5$)

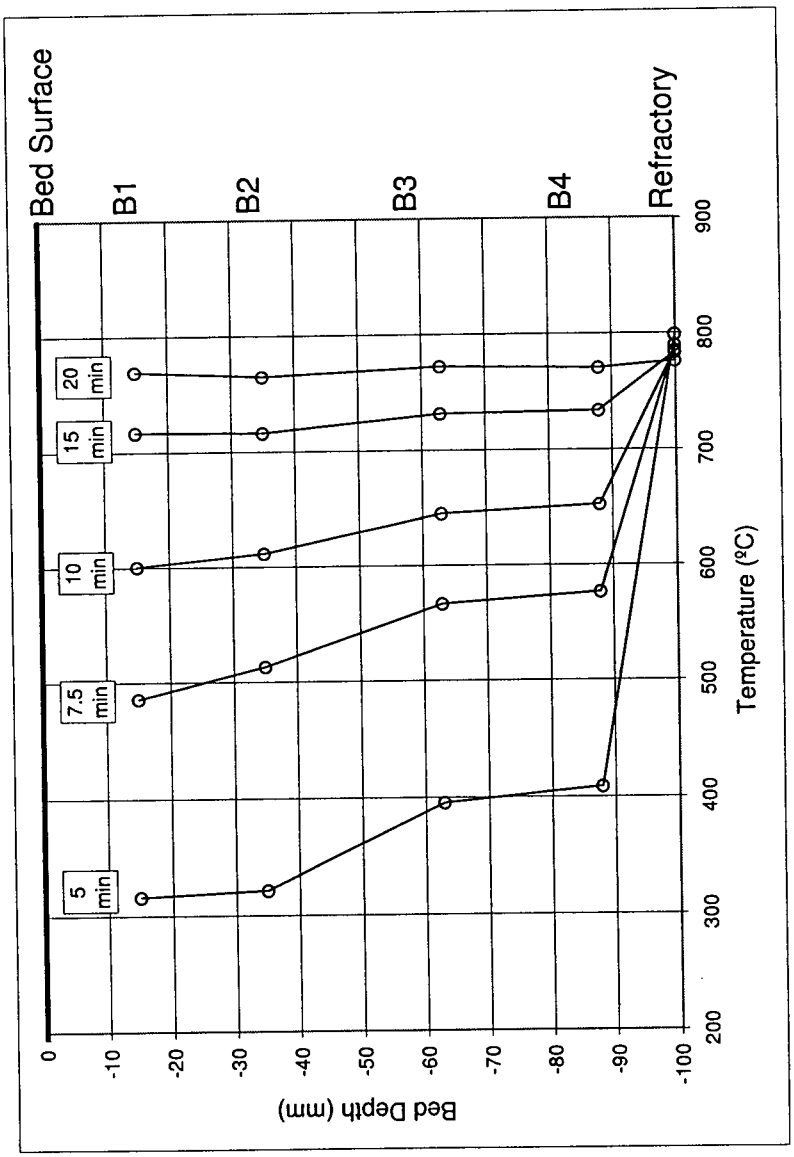

Figure 6.7: Run 5 Bed Temperature Profiles. Mix 2 at 1 rpm ($\bar{d}_p = 1.9$mm, $\sigma_p^* = 0.26$, $n_{RR} = 7.3$)

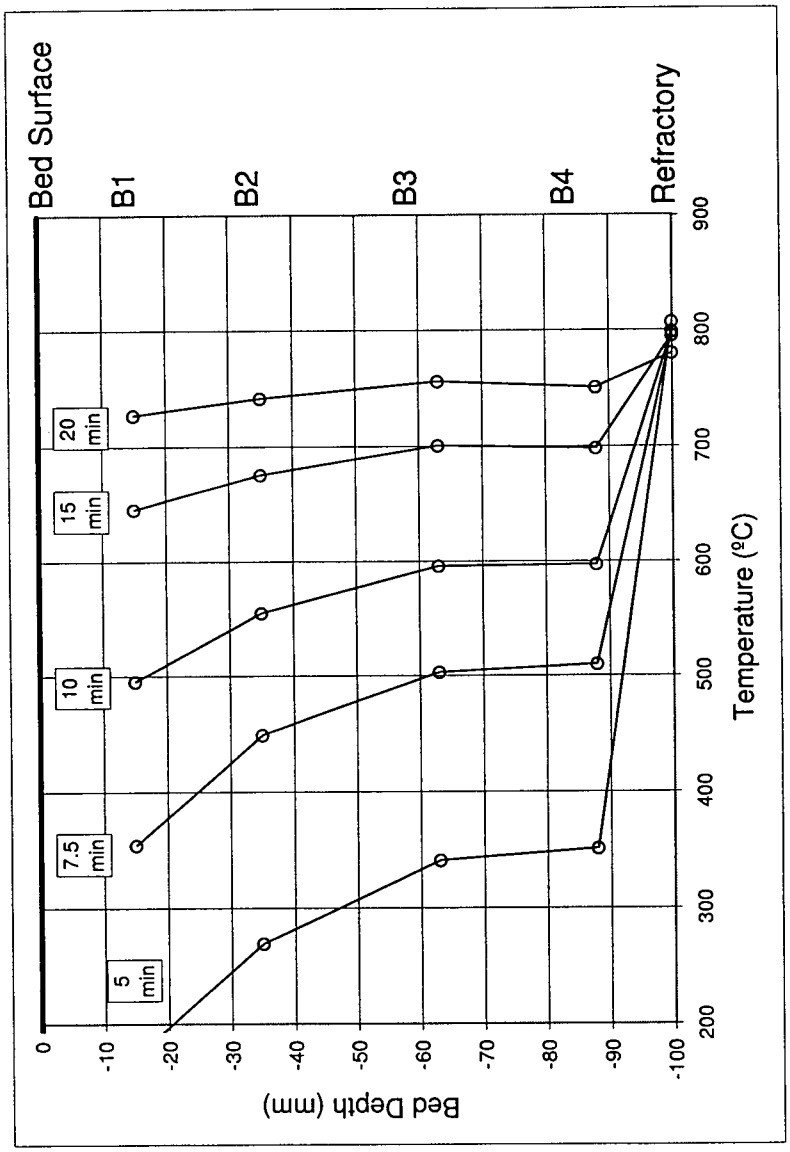

Figure 6.8: Run 8 Bed Temperature Profiles. Mix 5 at 1 rpm ($\bar{d}_p = 1.2$mm, $\sigma_p^* = 0.22$, $n_{RR} = 7.7$)

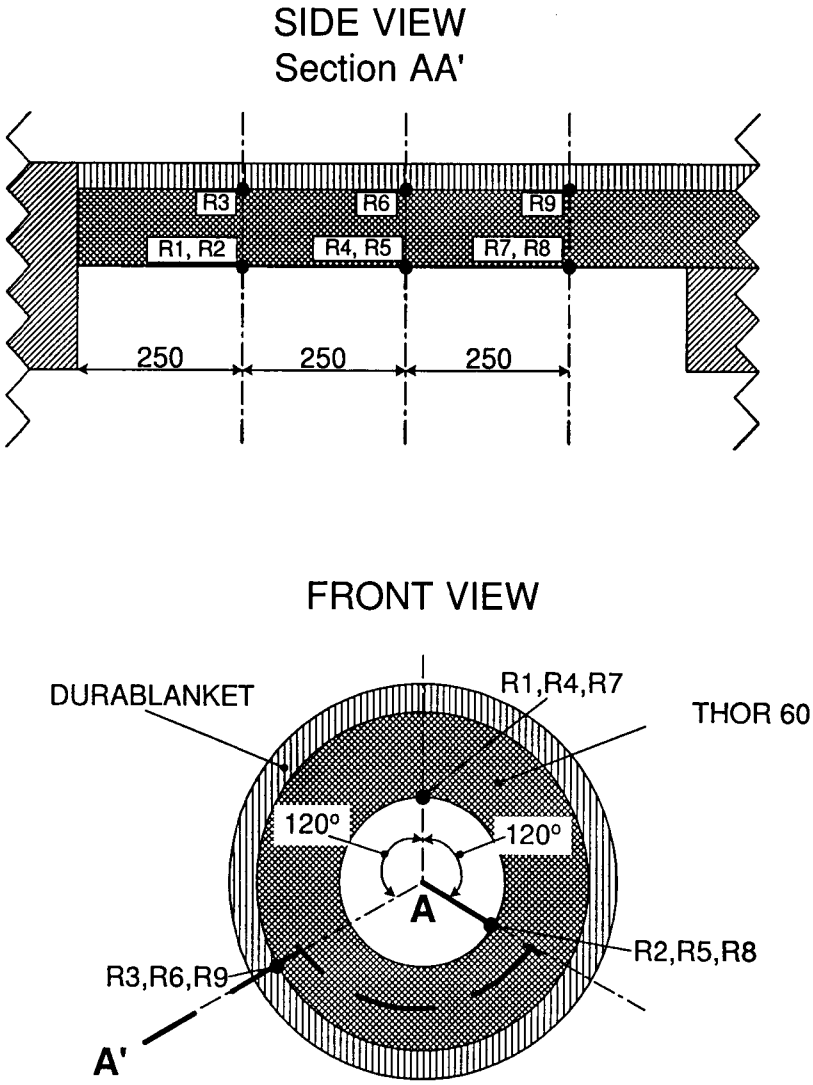

Figure 6.9: Location of Thermocouples in Refractory

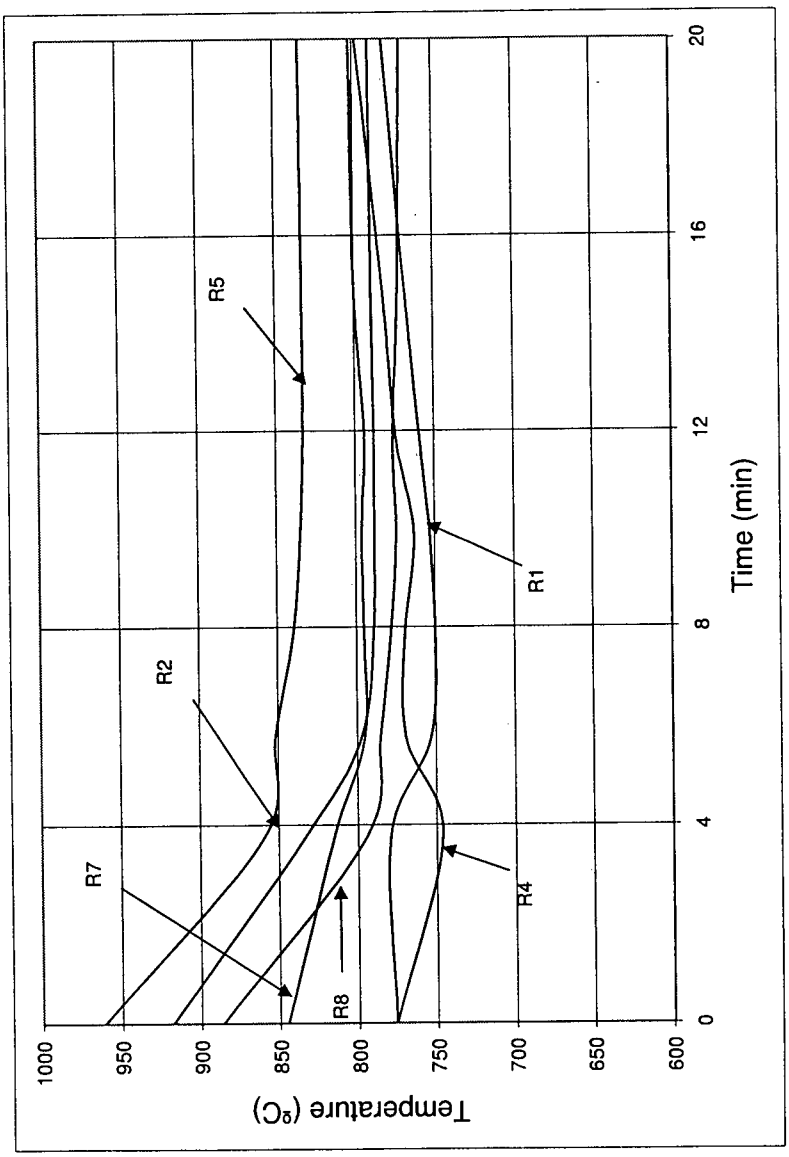

Figure 6.10: Hot Face Refractory Temperature History of Furnace For Run 5 (Mix 2 at 1 rpm, $\bar{d}_p = 1.9$mm, $\sigma_p^* = 0.26$, $n_{RR} = 7.3$)

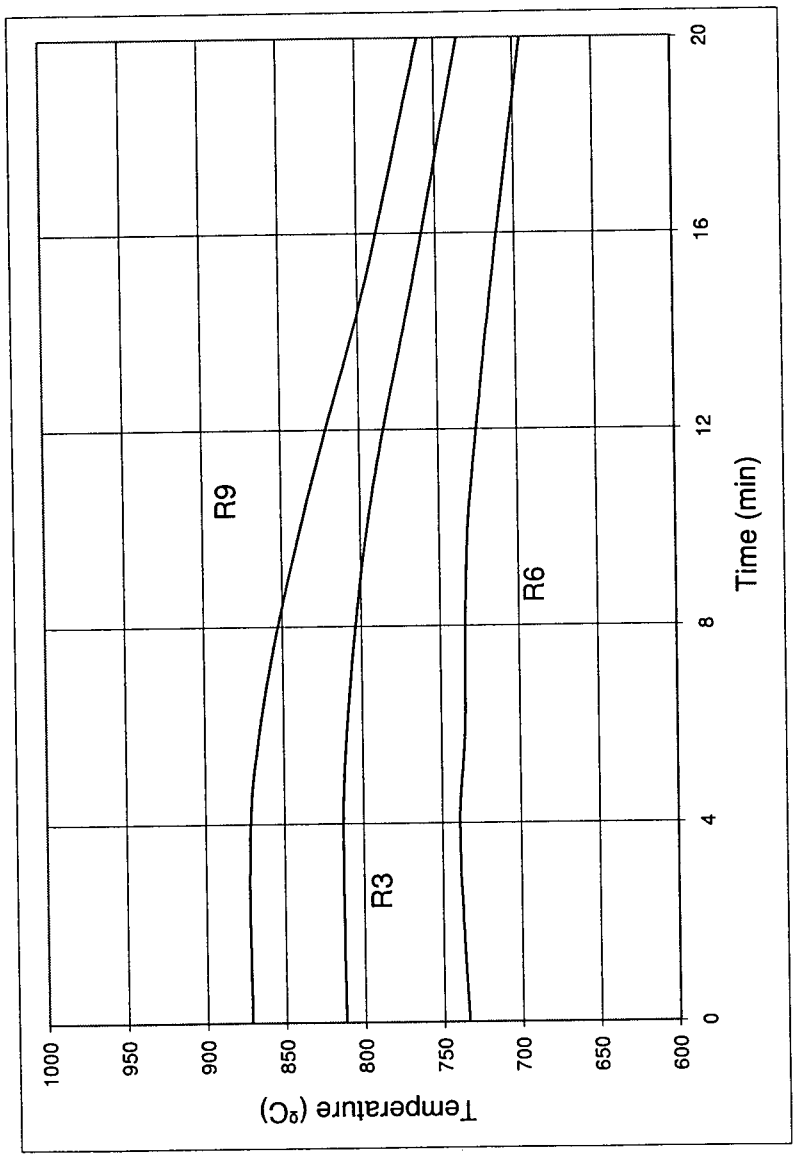

Figure 6.11: Interface Refractory Temperature History of Furnace For Run 5 (Mix 2 at 1 rpm, $\bar{d}_p = 1.9$mm, $\sigma_p^* = 0.26$, $n_{RR} = 7.3$)

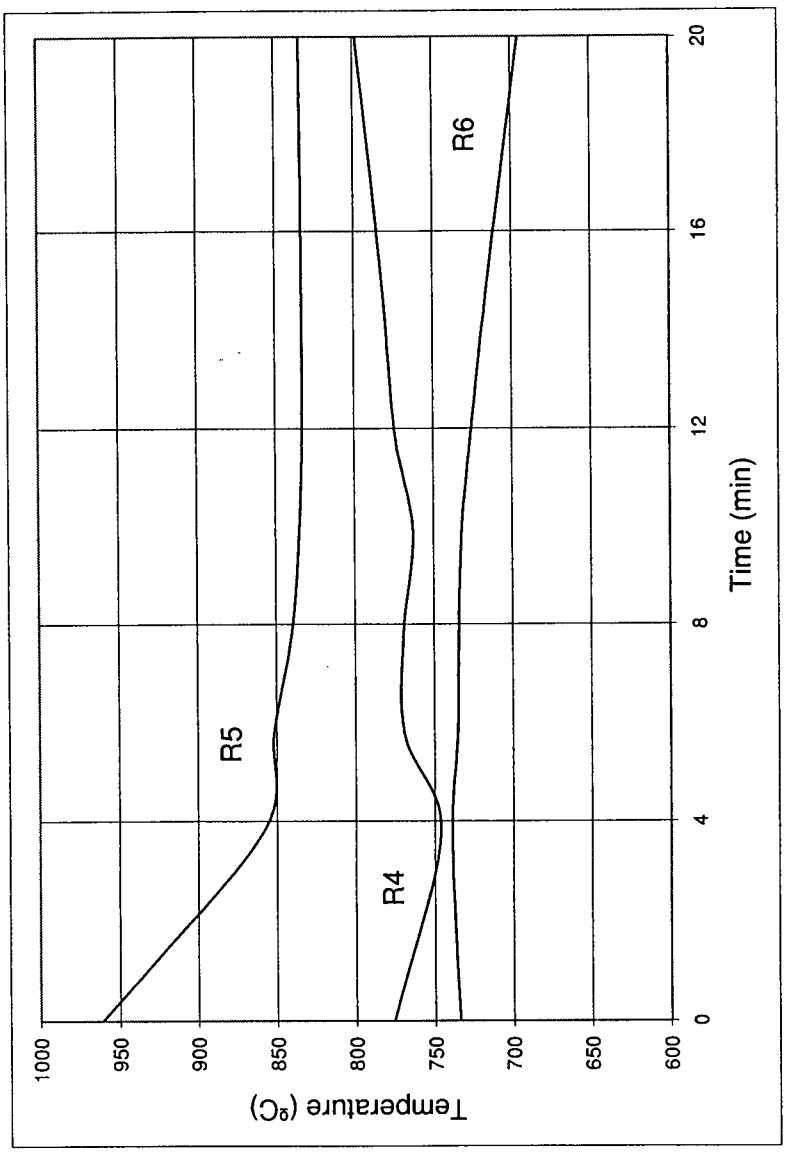

Figure 6.12: Refractory Temperature History at Center of Furnace For Run 5 (Mix 2 at 1 rpm, $\bar{d}_p = 1.9$mm, $\sigma_p^* = 0.26$, $n_{RR} = 7.3$)

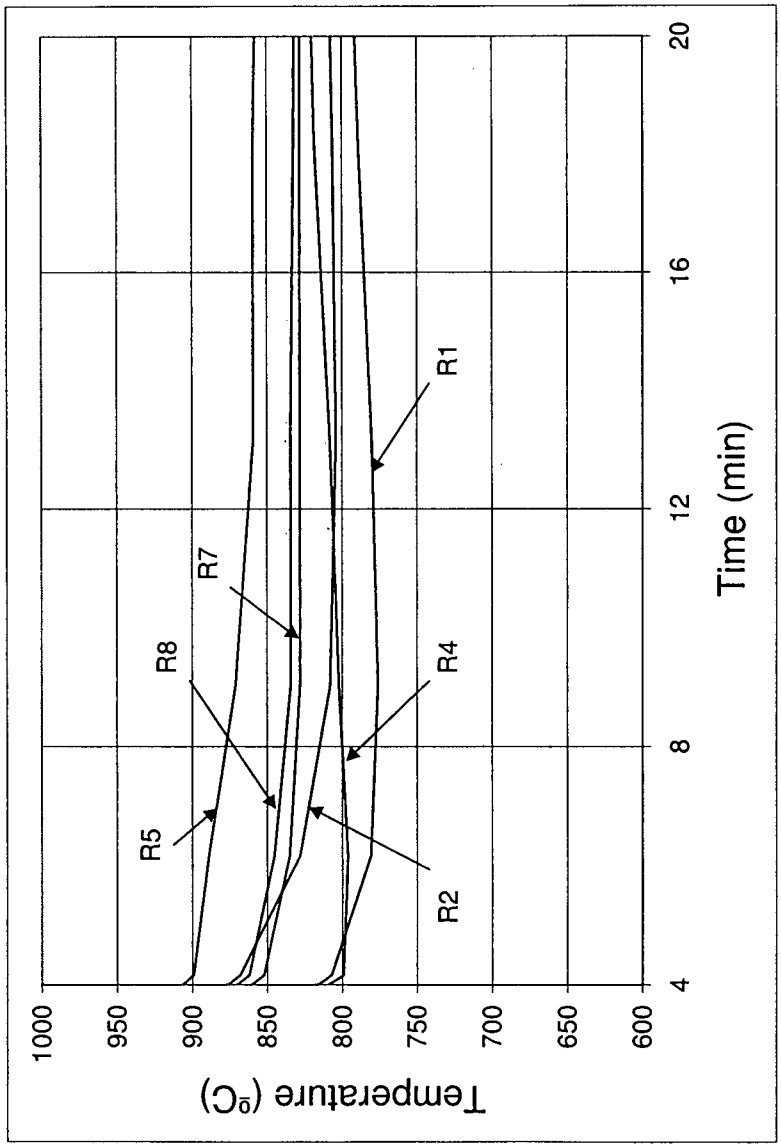

Figure 6.13: Hot Face Refractory Temperature History of Furnace For Run 14 (Mix 5 at 1 rpm, $\bar{d}_p = 1.2\text{mm}$, $\sigma_p^* = 0.22$, $n_{RR} = 7.7$)

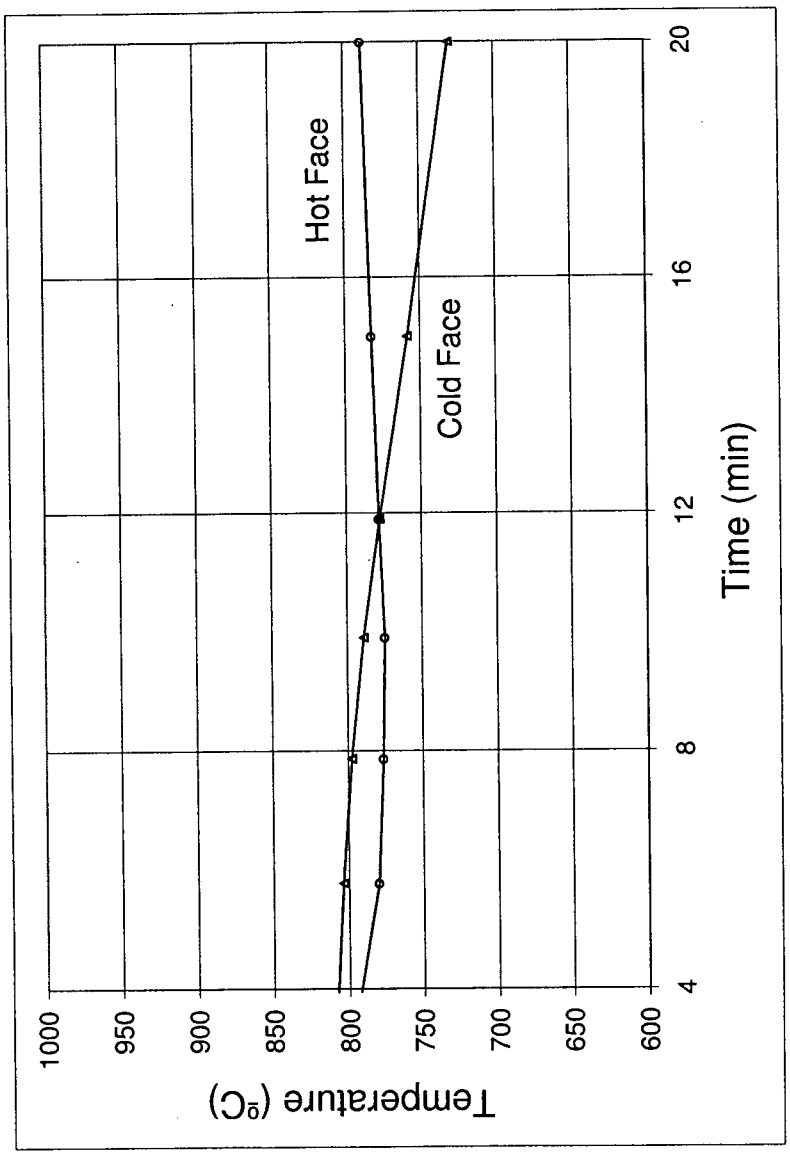

Figure 6.14: Hot Face and Interface Refractory Temperature History at Center of Furnace For Run 5, As used in Heat Transfer Analysis. (Mix 2 at 1 rpm, $\bar{d}_p = 1.9$mm, $\sigma_p^* = 0.26$, $n_{RR} = 7.3$)

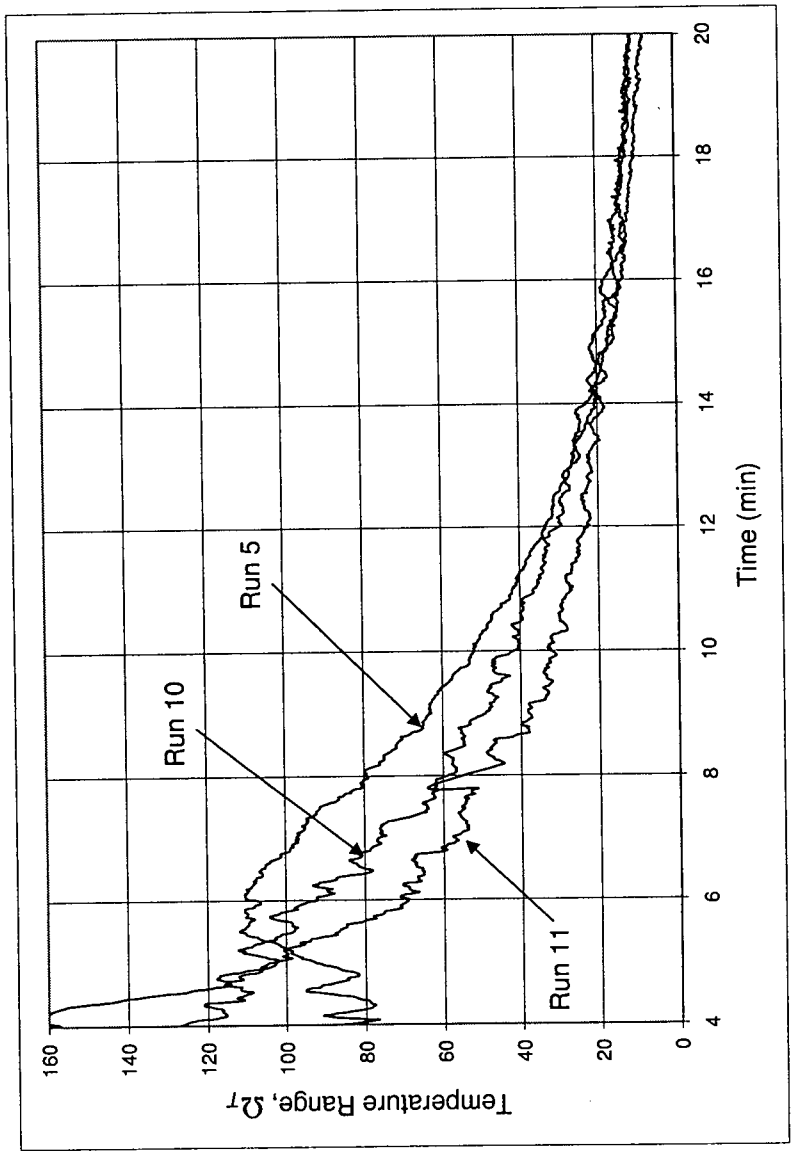

Figure 6.15: Temperature Range of Bed Thermocouples B1-B4 for Runs 5, 10 and 11

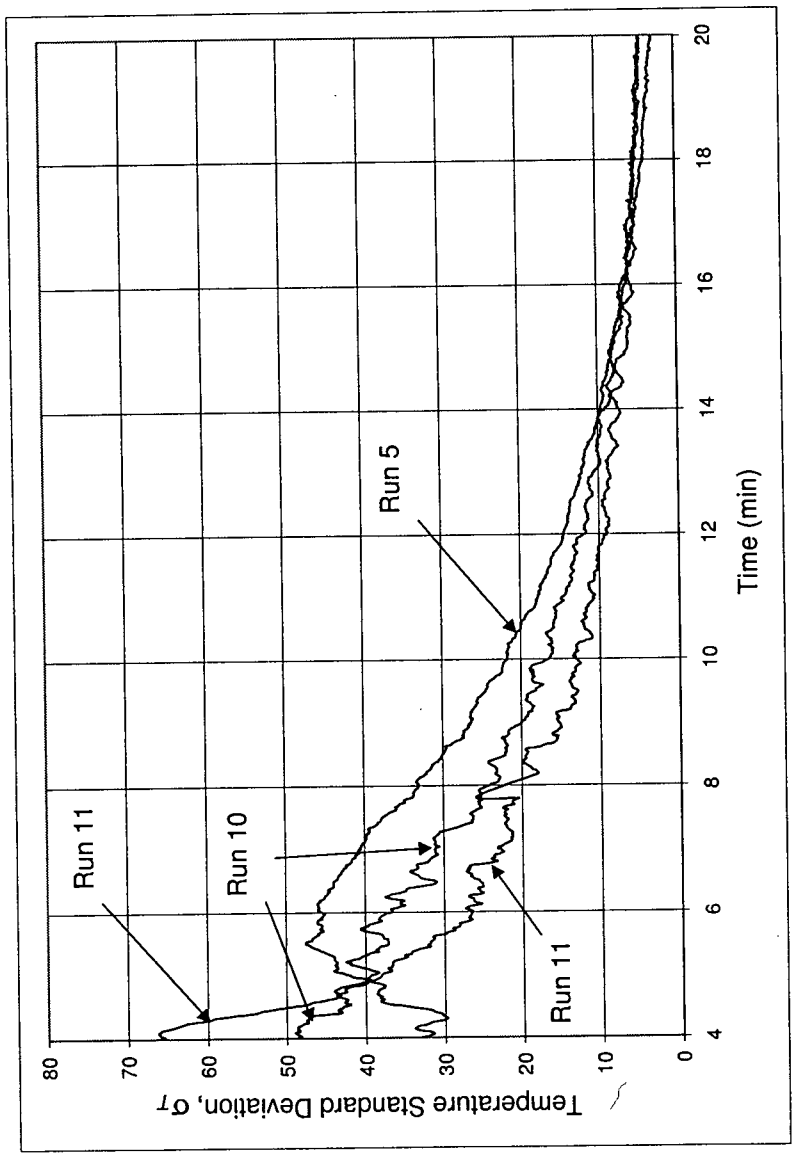

Figure 6.16: Temperature Standard Deviation of Bed Thermocouples B1-B4 for Runs 5, 10 and 11

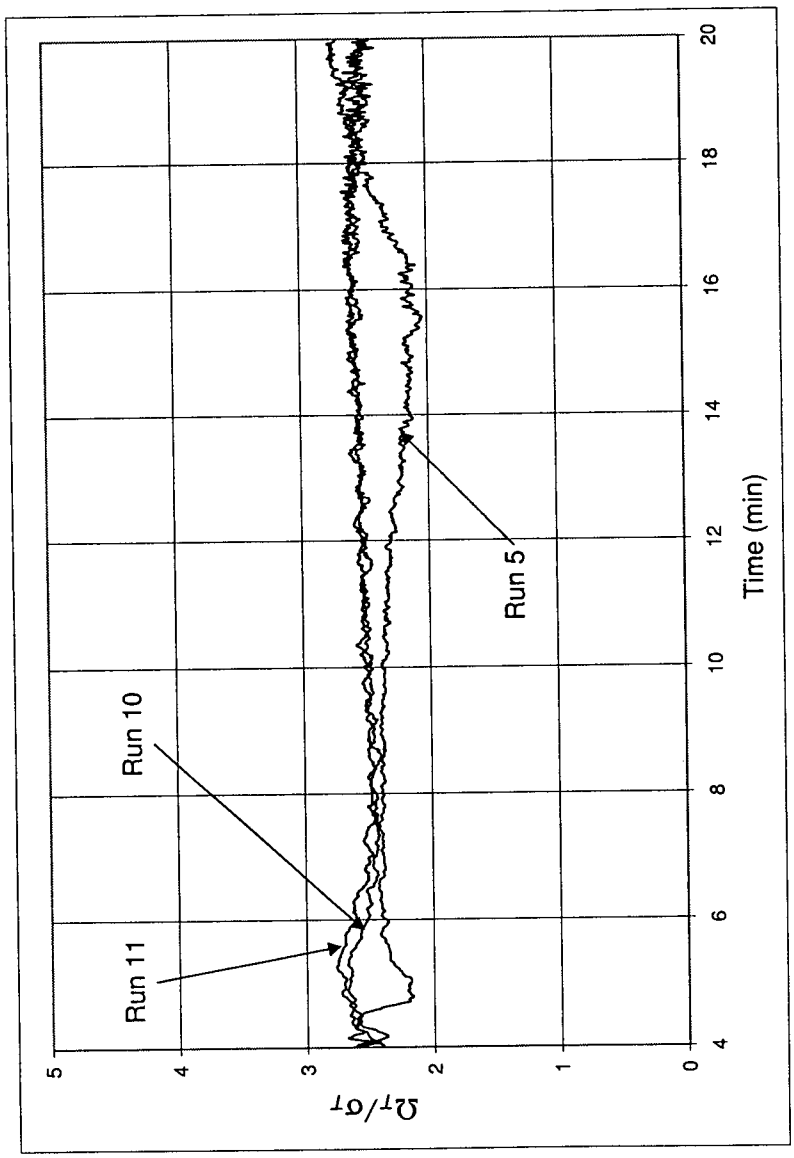

Figure 6.17: Temperature Range Divided by Temperature Standard Deviation of Bed Thermocouples B1-B4 for Runs 5, 10 and 11

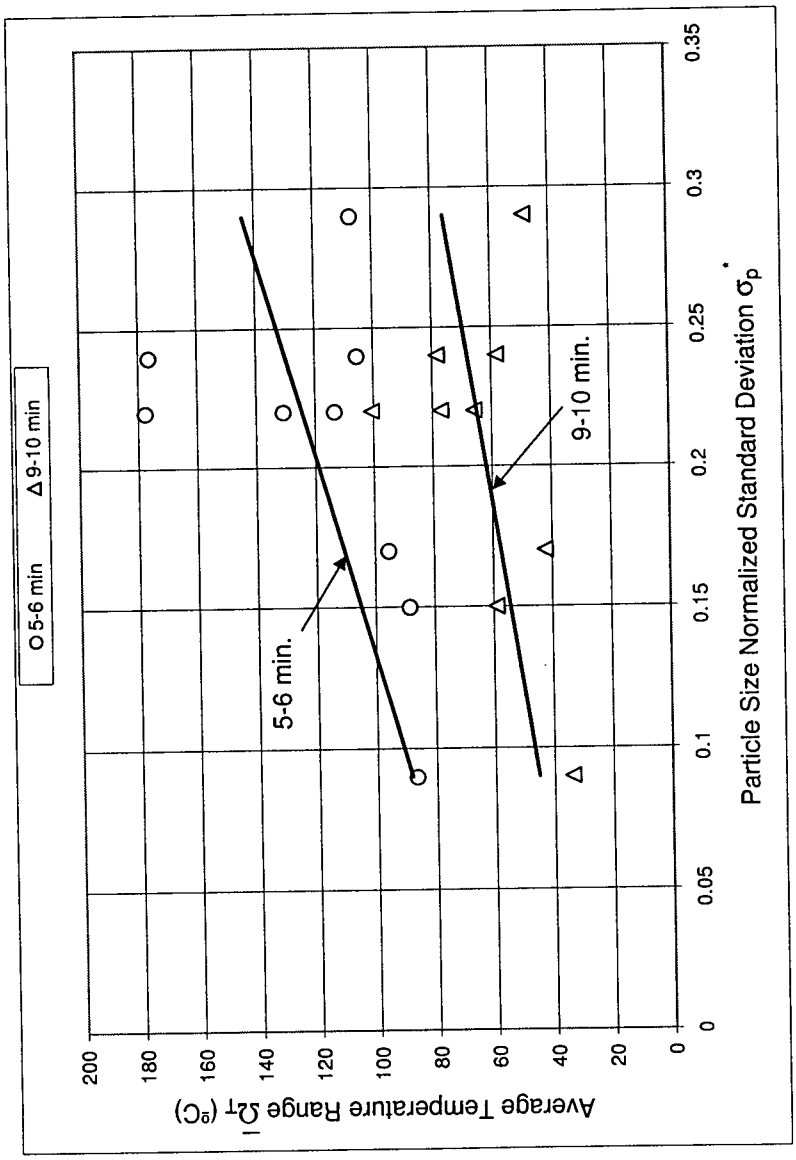

Figure 6.18: Effect of Particle Size Distribution on Degree of Temperature Non-Uniformity at 1rpm

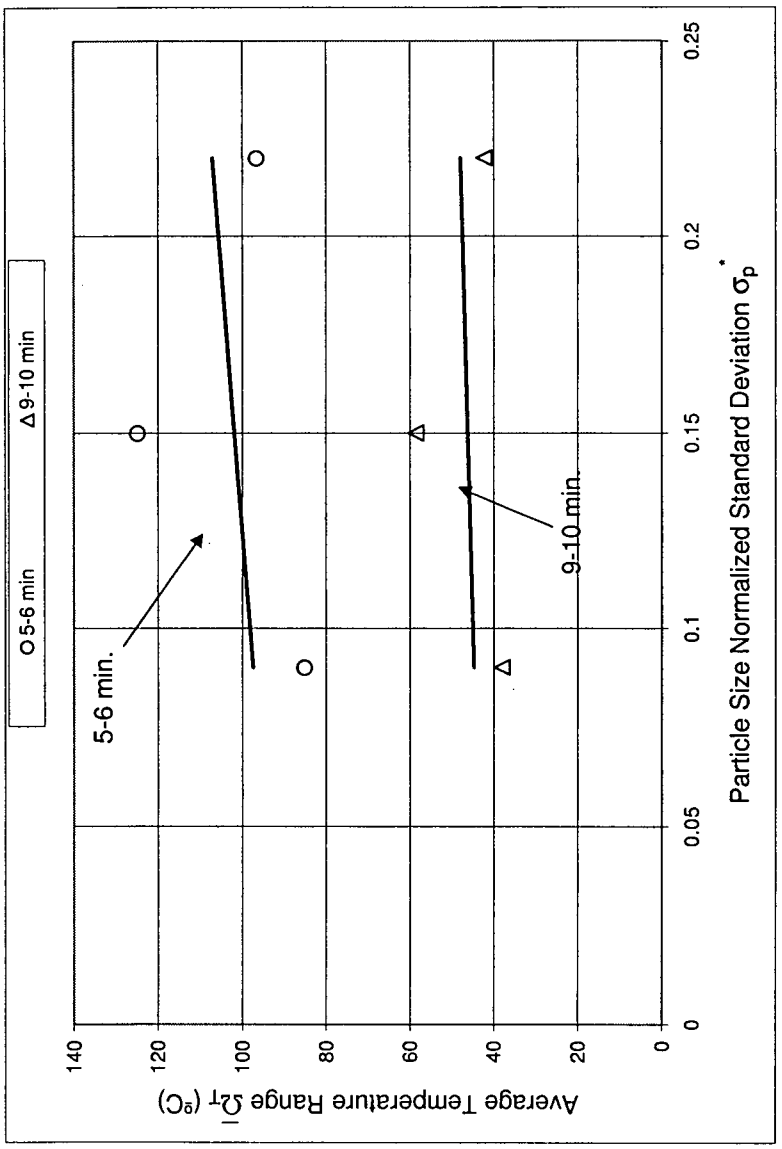

Figure 6.19: Effect of Particle Size Distribution on Degree of Temperature Non-Uniformity at 2rpm

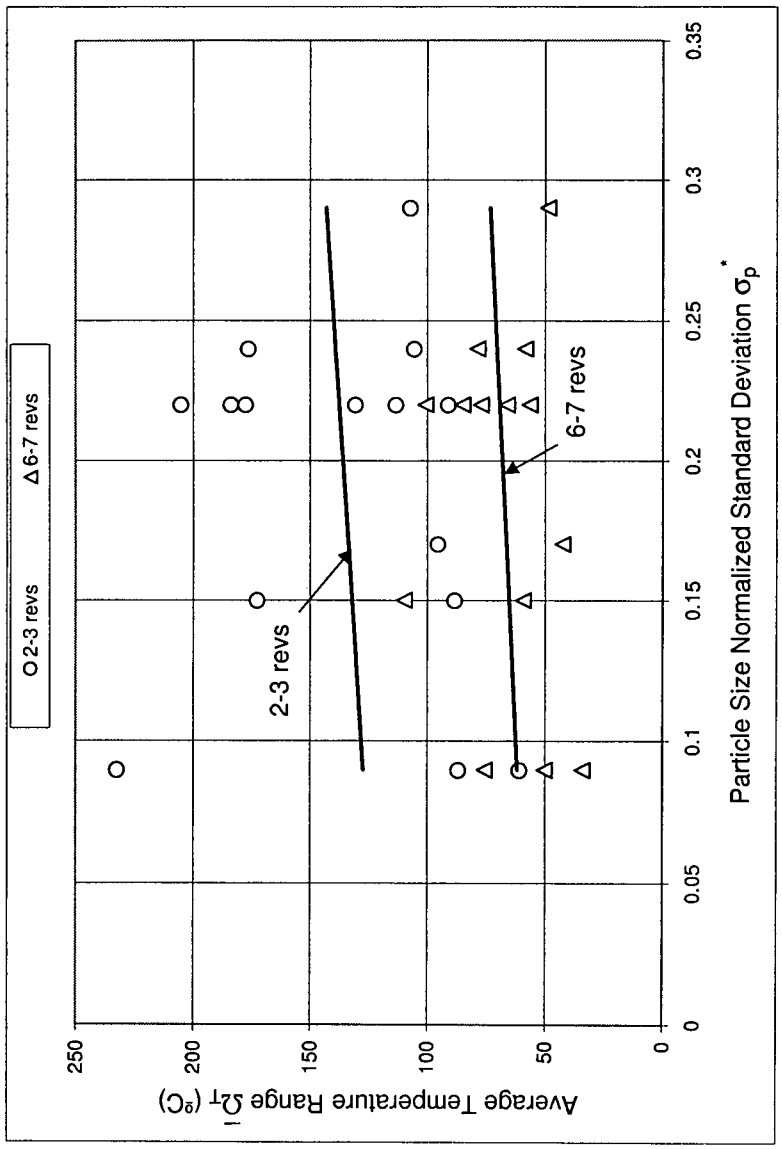

Figure 6.20: Effect of Particle Size Distribution on Degree of Temperature Non-Uniformity. All runs

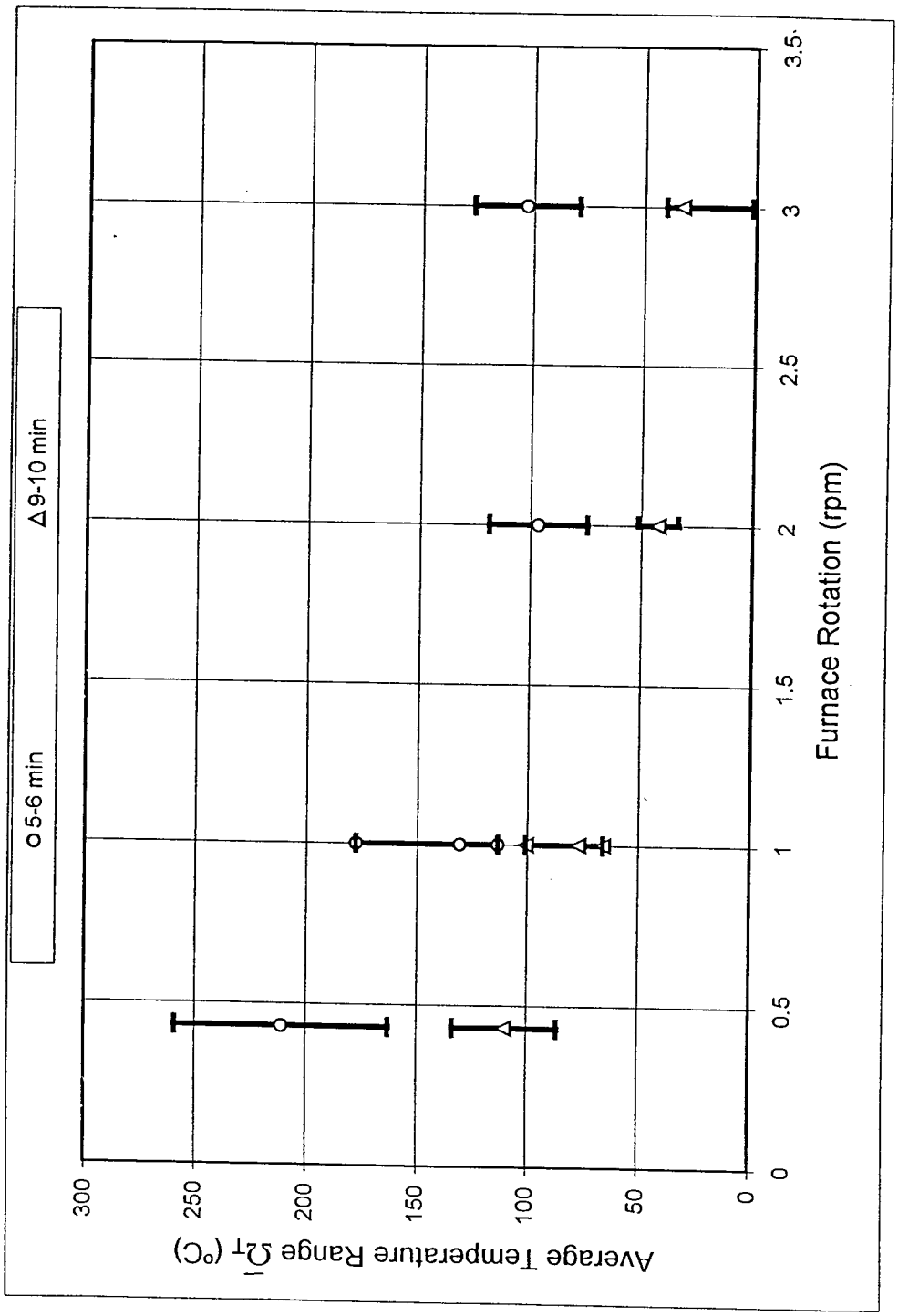

Figure 6.21: Effect of Furnace Rotation on Temperature Non-Uniformity for Runs with Mix 5. ($\bar{d}_p = 1.2$mm, $\sigma_p^* = 0.22$, $n_{RR} = 7.7$)

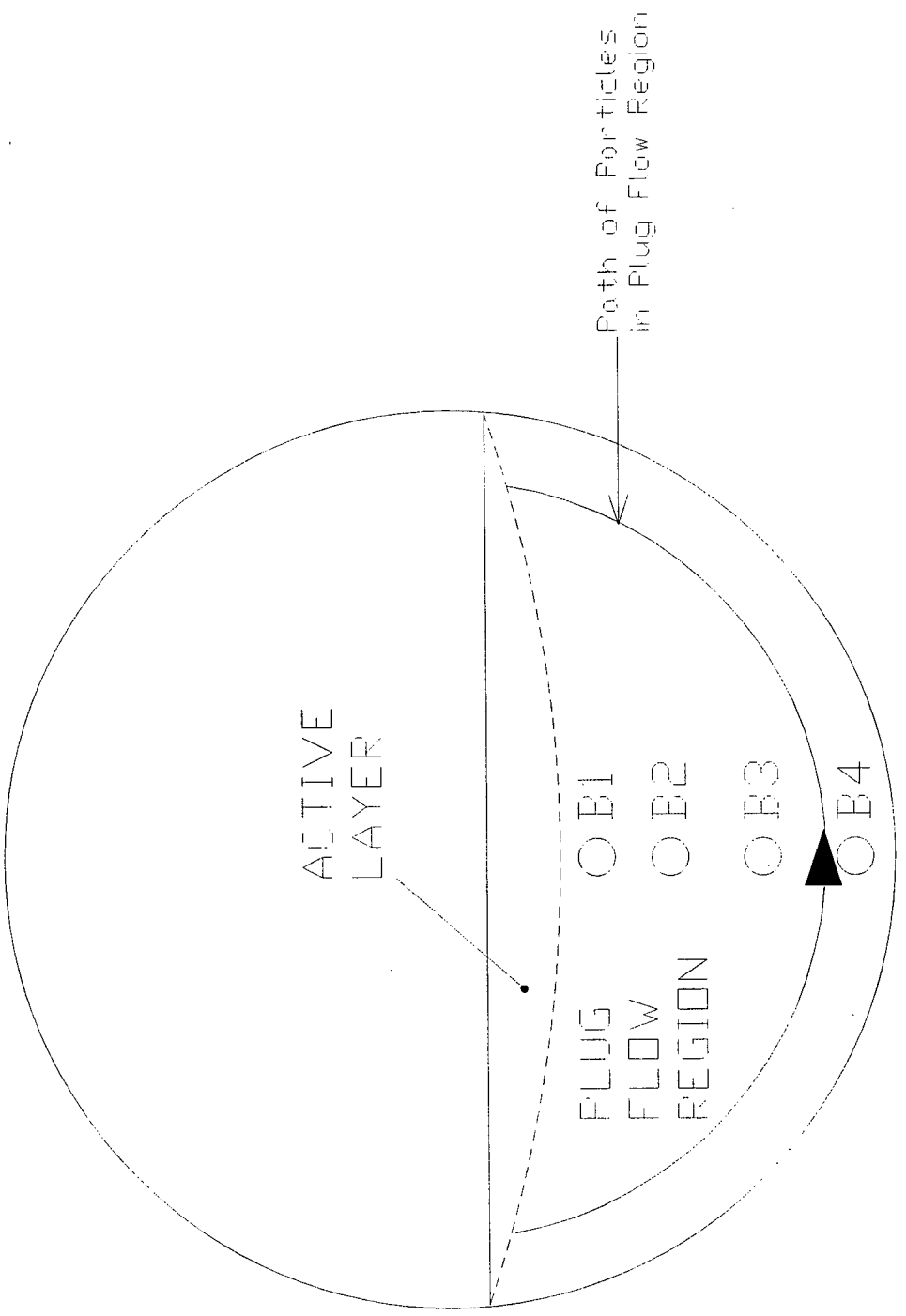

Figure 6.22: Path of Particles in Cross Section

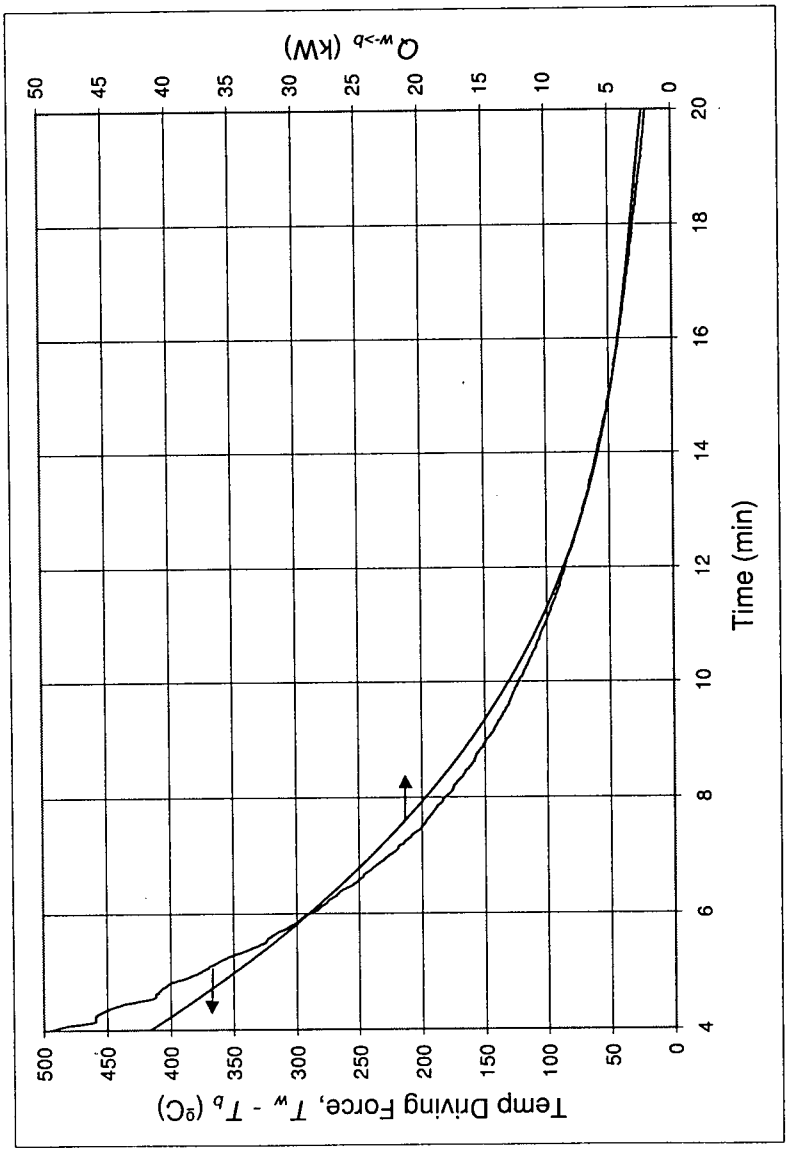

Figure 6.23: Heat Rate to Bed and Temperature Driving Force For Run 5. (Mix 2, ($\bar{d}_p = 1.9$mm, $\sigma_p^* = 0.24$, $n_{RR} = 7.3$)

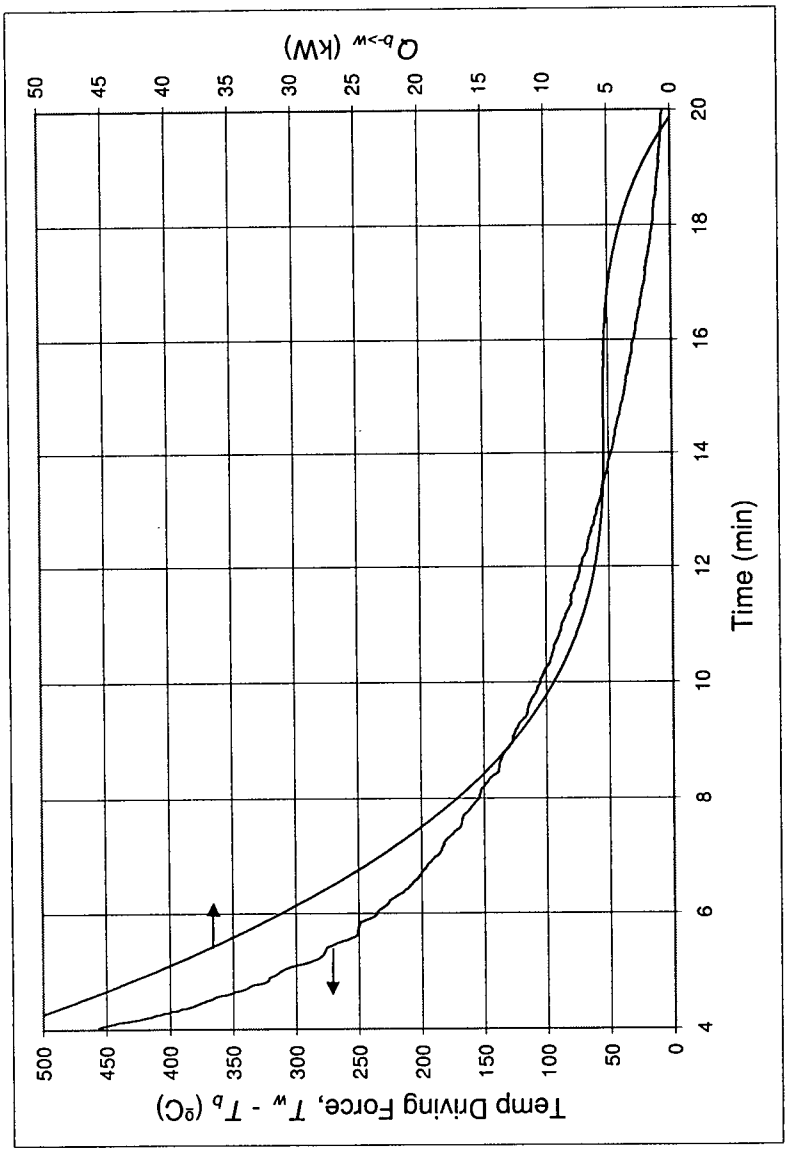

Figure 6.24: Heat Rate to Bed and Temperature Driving Force For Run 4. (Mix 1, ($\bar{d_p} = 1.4$mm, $\sigma_p^* = 0.29$, $n_{RR} = 5.0$)

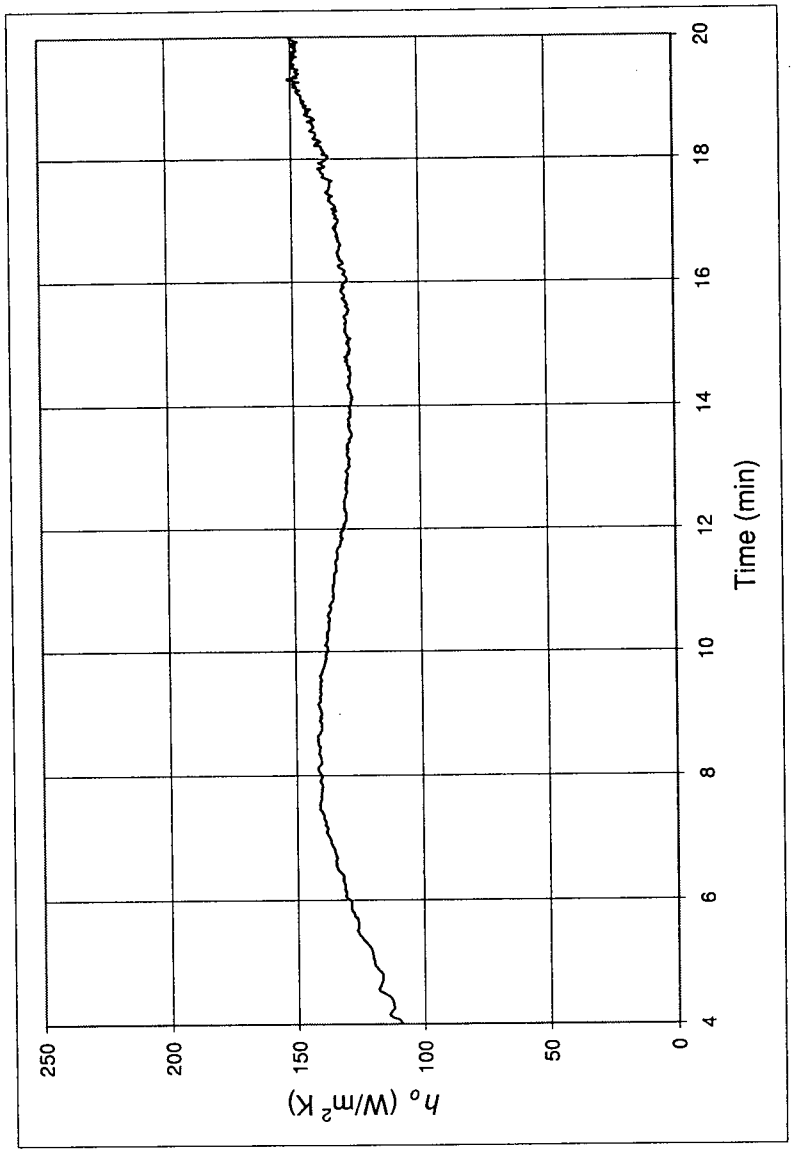

Figure 6.25: Overall Heat Transfer Coefficient For Run 5. (Mix 2, ($\bar{d}_p = 1.2$mm, $\sigma_p^* = 0.22$, $n_{RR} = 7.7$)

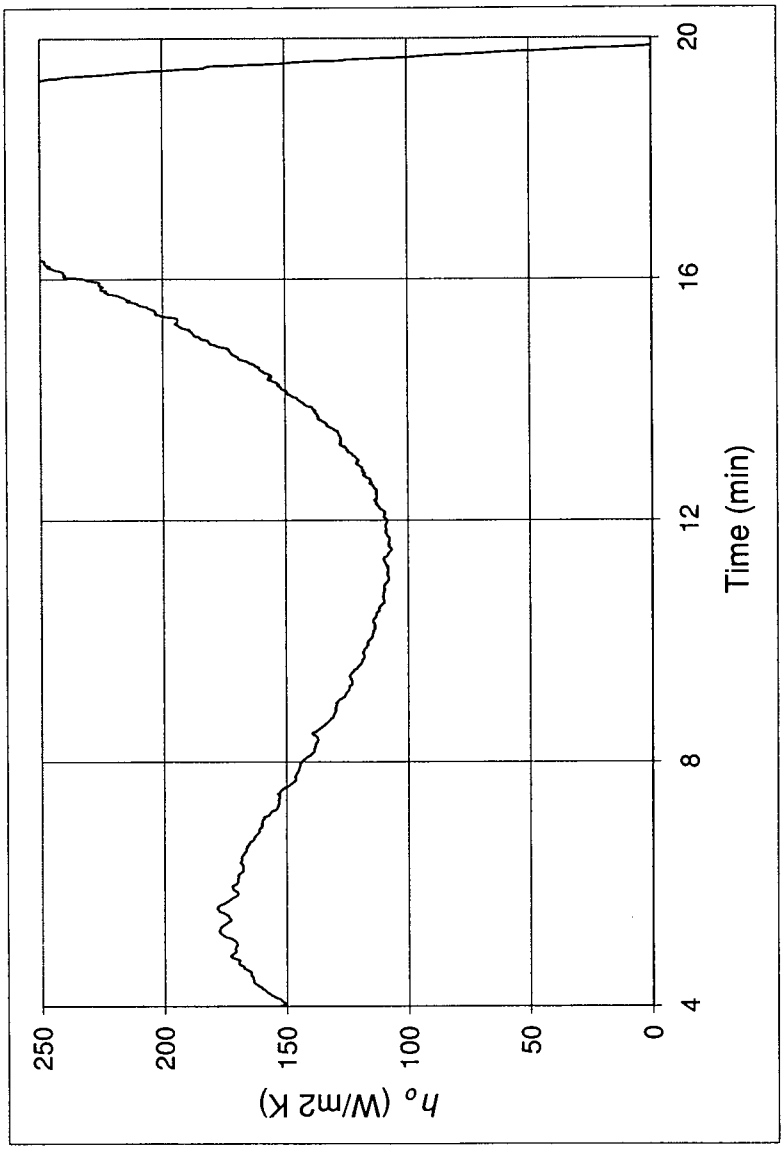

Figure 6.26: Overall Heat Transfer Coefficient For Run 4. (Mix 1, ($\bar{d}_p = 1.4$mm, $\sigma_p^* = 0.29$, $n_{RR} = 5.0$)

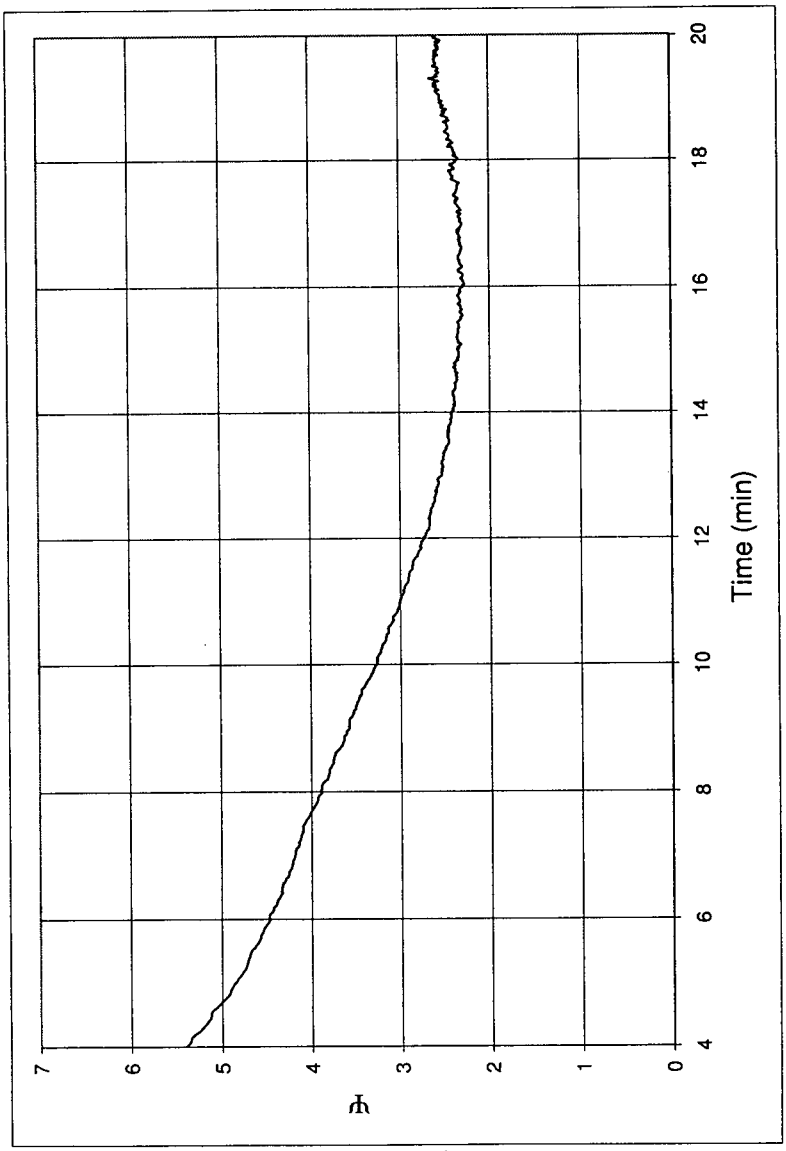

Figure 6.27: Ratio of Heat Flow Across Covered Bed Surface and Exposed Bed Surface For Run 5 ($\bar{d}_p = 1.2$mm, $\sigma_p^* = 0.22$, $n_{RR} = 7.7$)

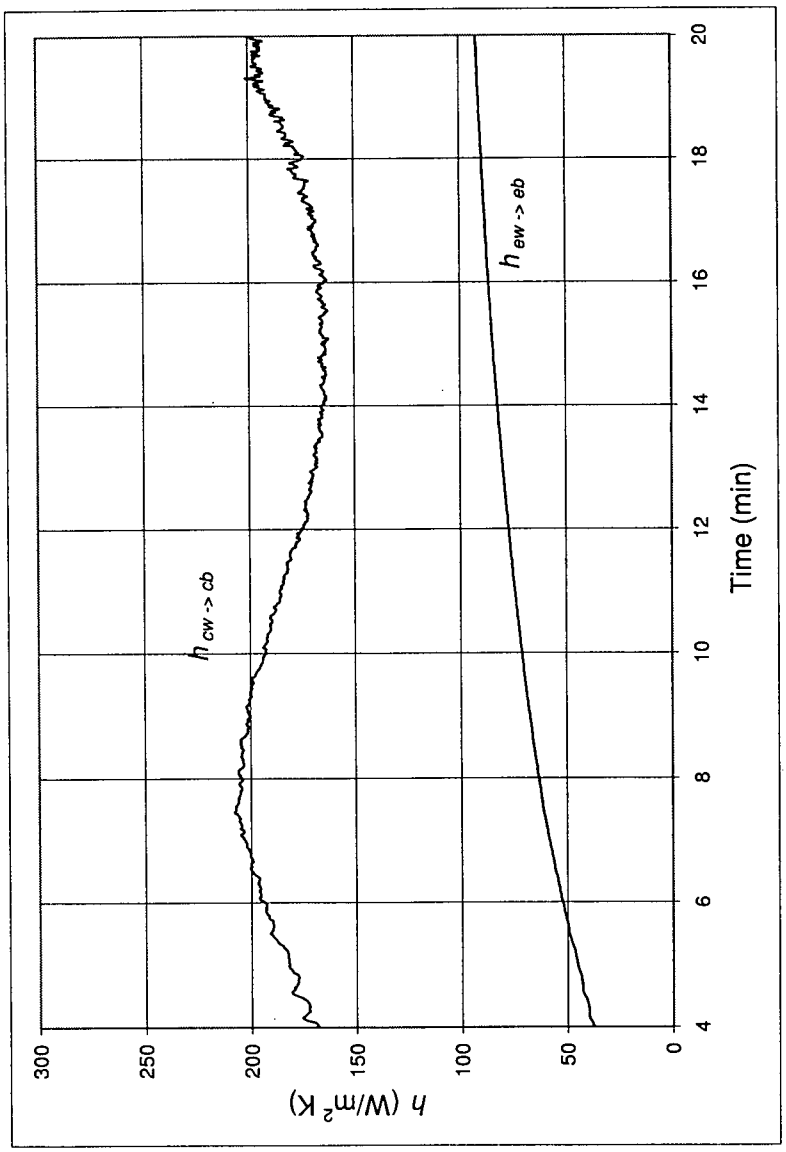

Figure 6.28: Exposed Wall and Covered Wall Heat Transfer Coefficients For Run 5. (Mix 2, ($\bar{d_p} = 1.9$mm, $\sigma_p^* = 0.24$, $n_{RR} = 7.3$)

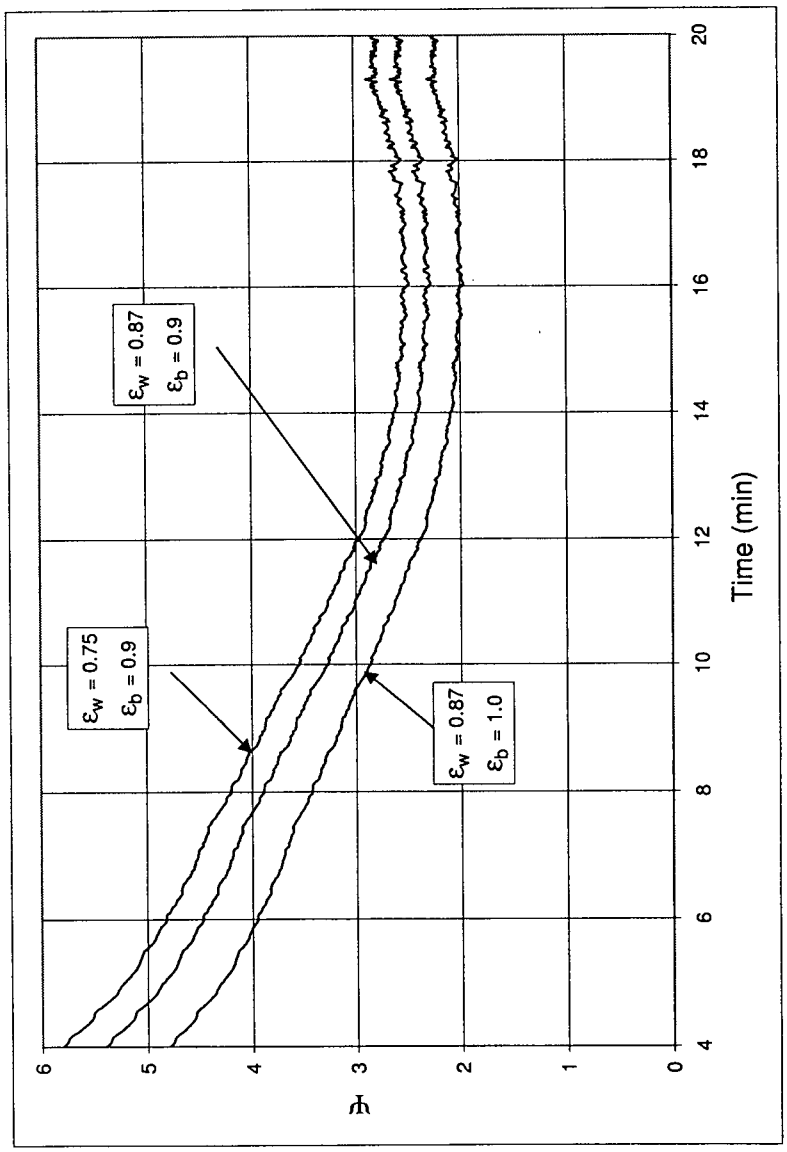

Figure 6.29: Sensitivity of Wall and Bed emissivity on Covered Wall to Covered Bed Heat Transfer Ratio. Run 5 Mix 2 at 1 rpm ($\bar{d_p}$ = 1.9mm, σ_p^* = 0.24, n_{RR} = 7.3)

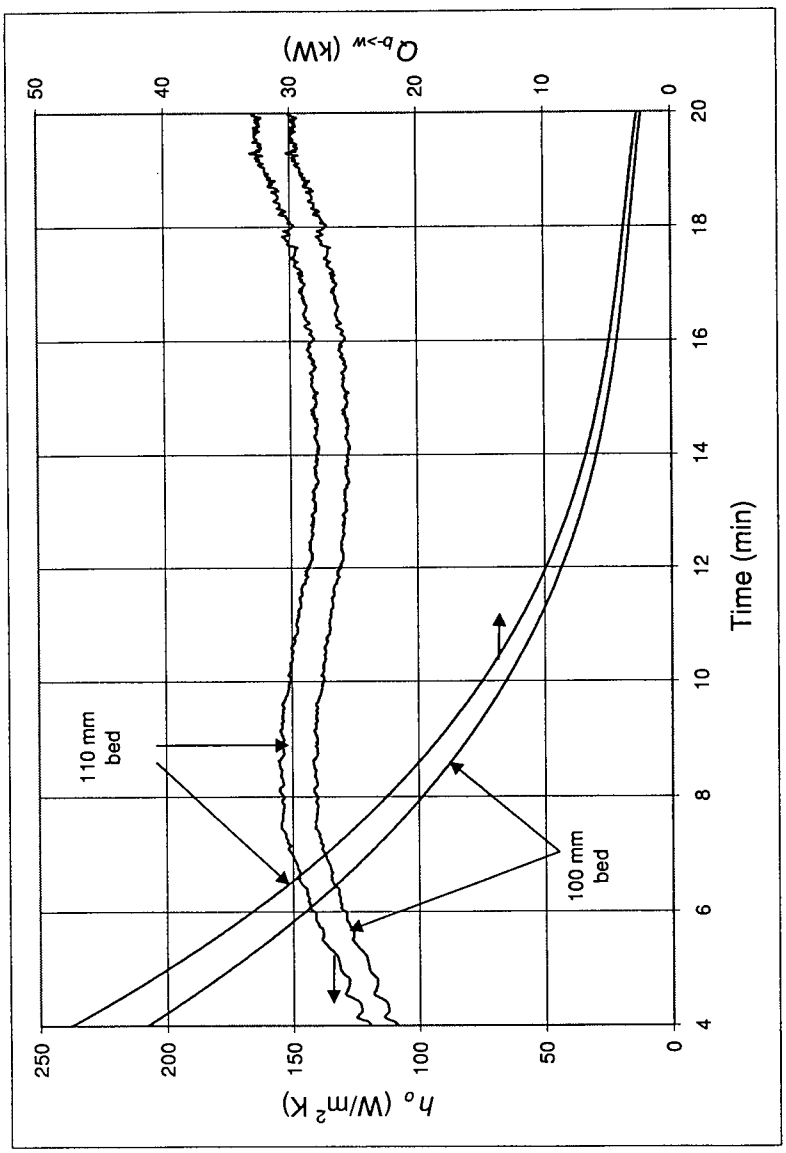

Figure 6.30: Sensitivity of Bed Depth on Overall Heat Transfer Coefficient and Heat Rate to Bed. Run 5 Mix 2 at 1 rpm ($\bar{d}_p = 1.9$mm, $\sigma_p^* = 0.24$, $n_{RR} = 7.3$)

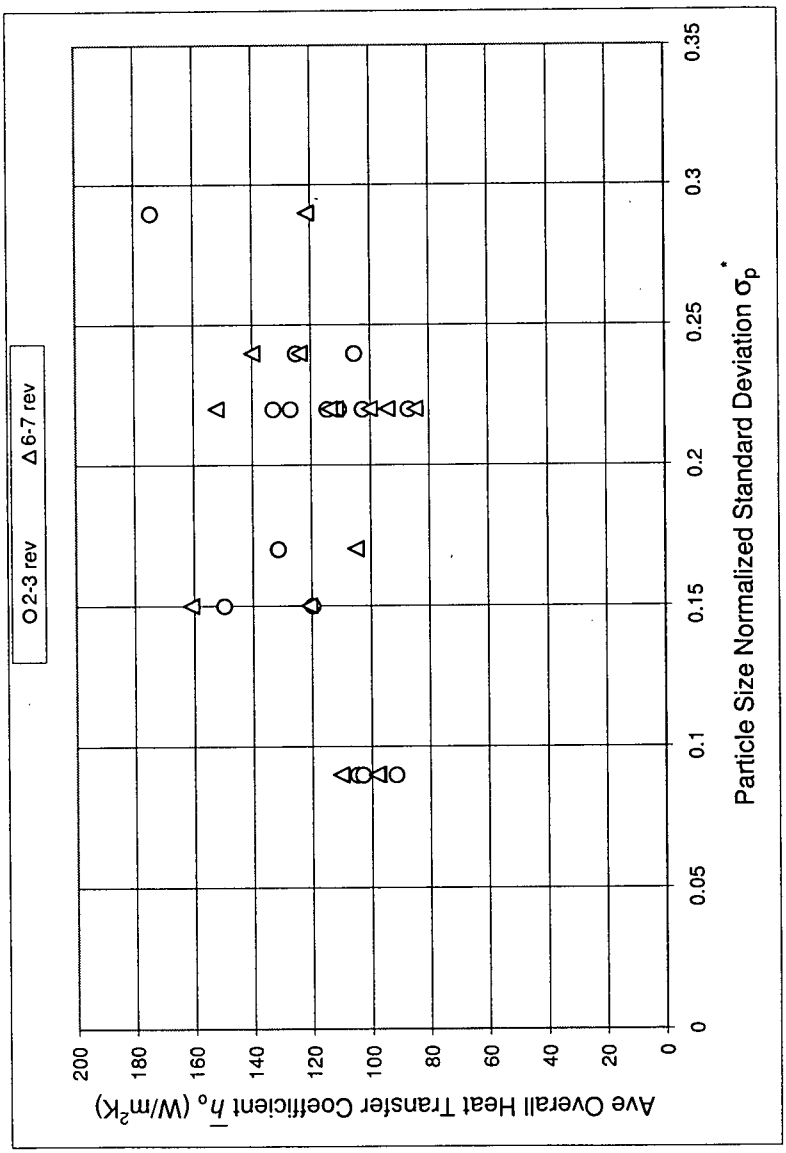

Figure 6.31: Effect of Particle Size Distribution on Overall Heat Transfer Coefficient. All Runs, All Furnace Rotational Speeds

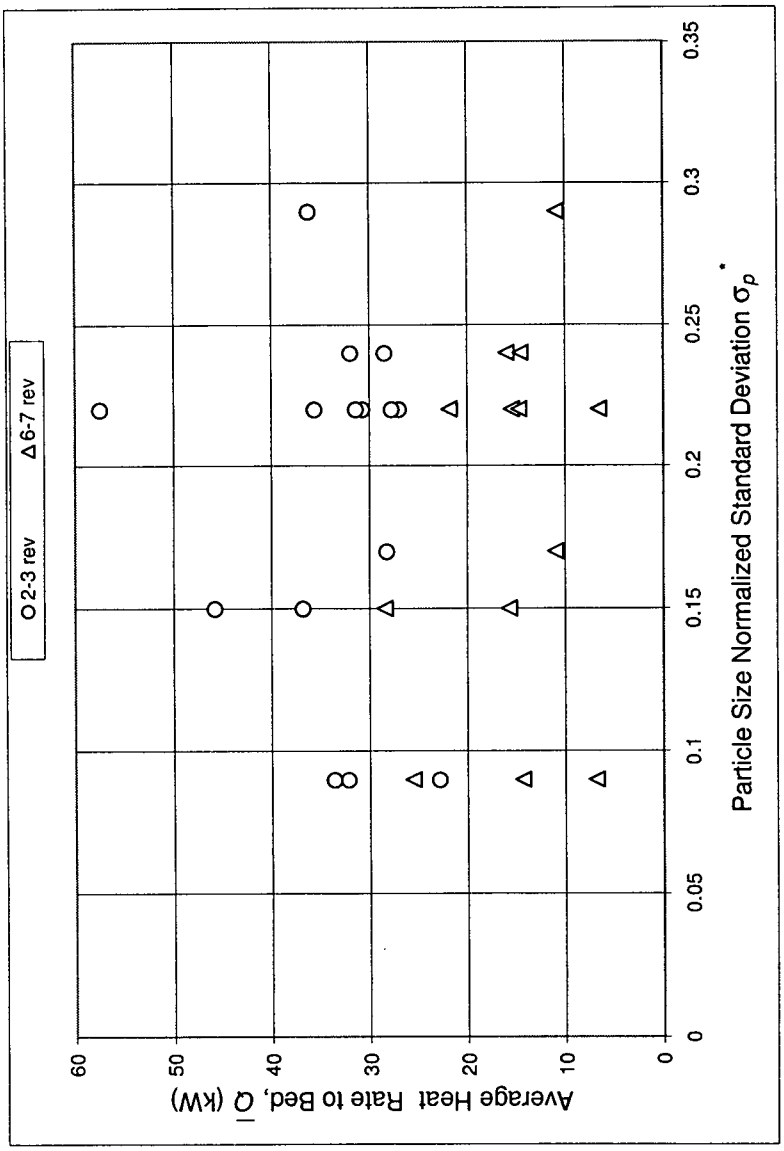

Figure 6.32: Effect of Particle Size Distribution on Heat Rate to Bed. All Runs, All Furnace Rotational Speeds

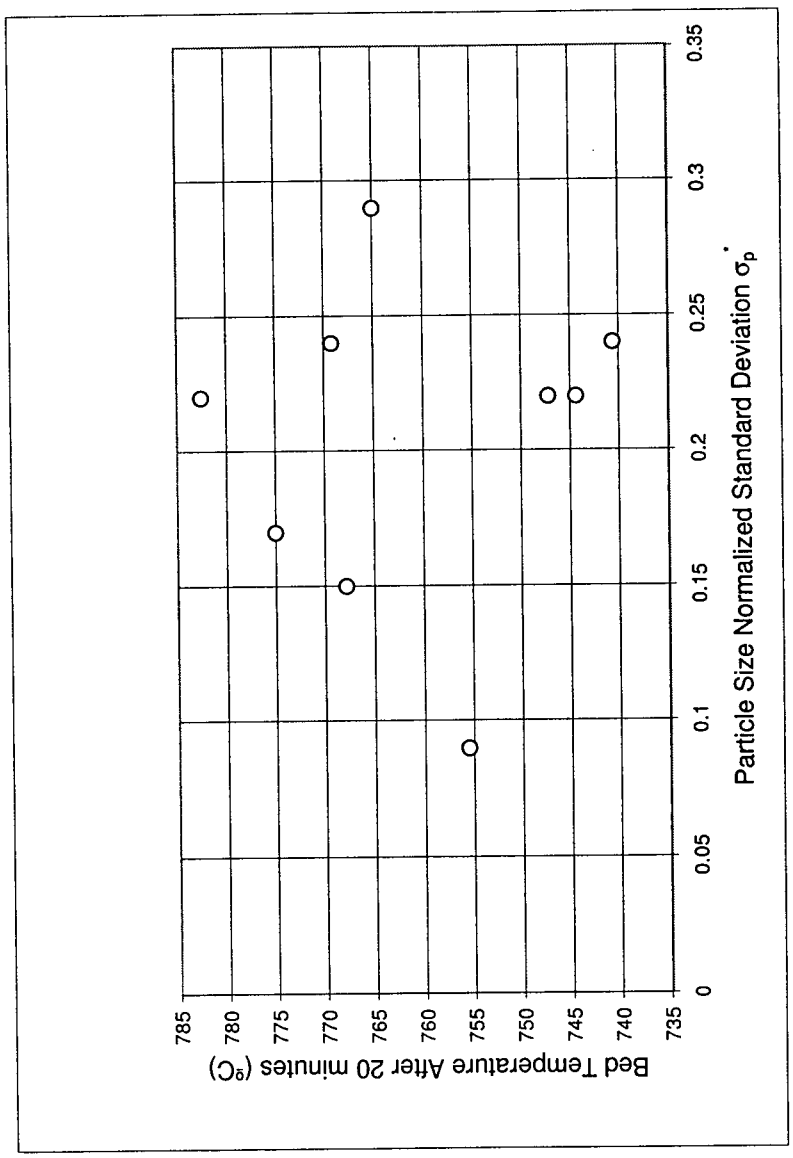

Figure 6.33: Effect of Particle Size Distribution on Final Bed Temperature after 20 minutes. All Runs

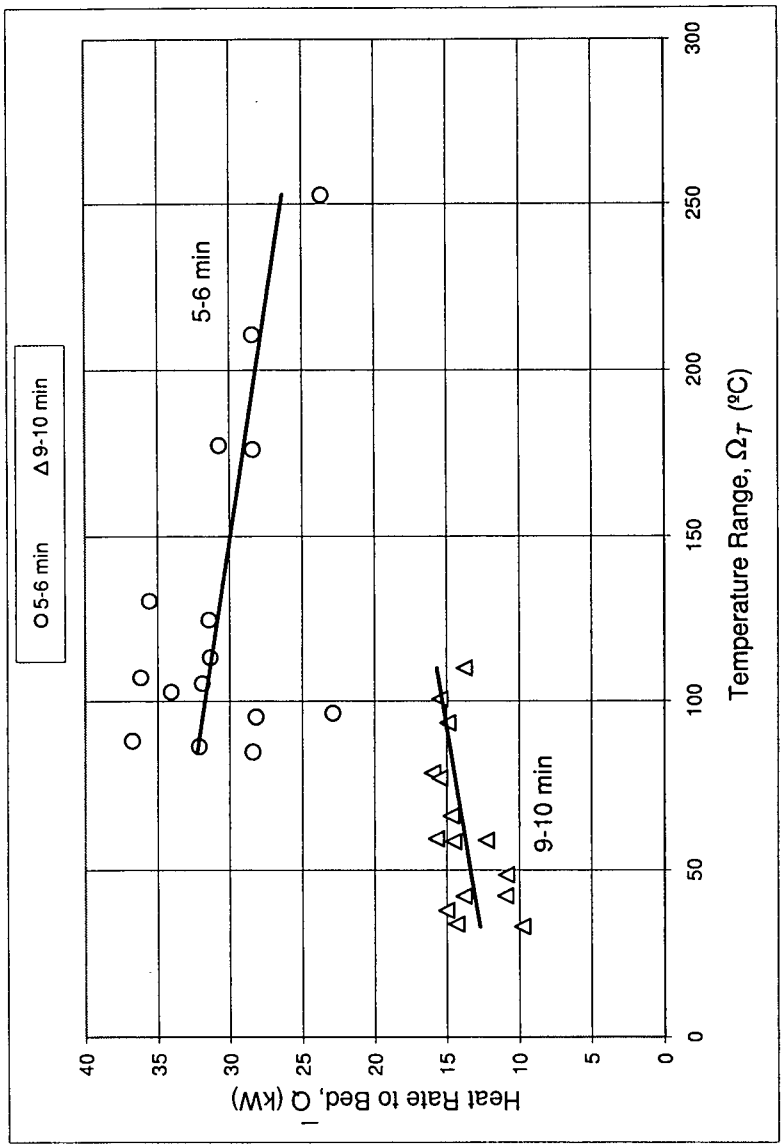

Figure 6.34: Relationship Between Temperature Range and Heat Rate to Bed. All Runs

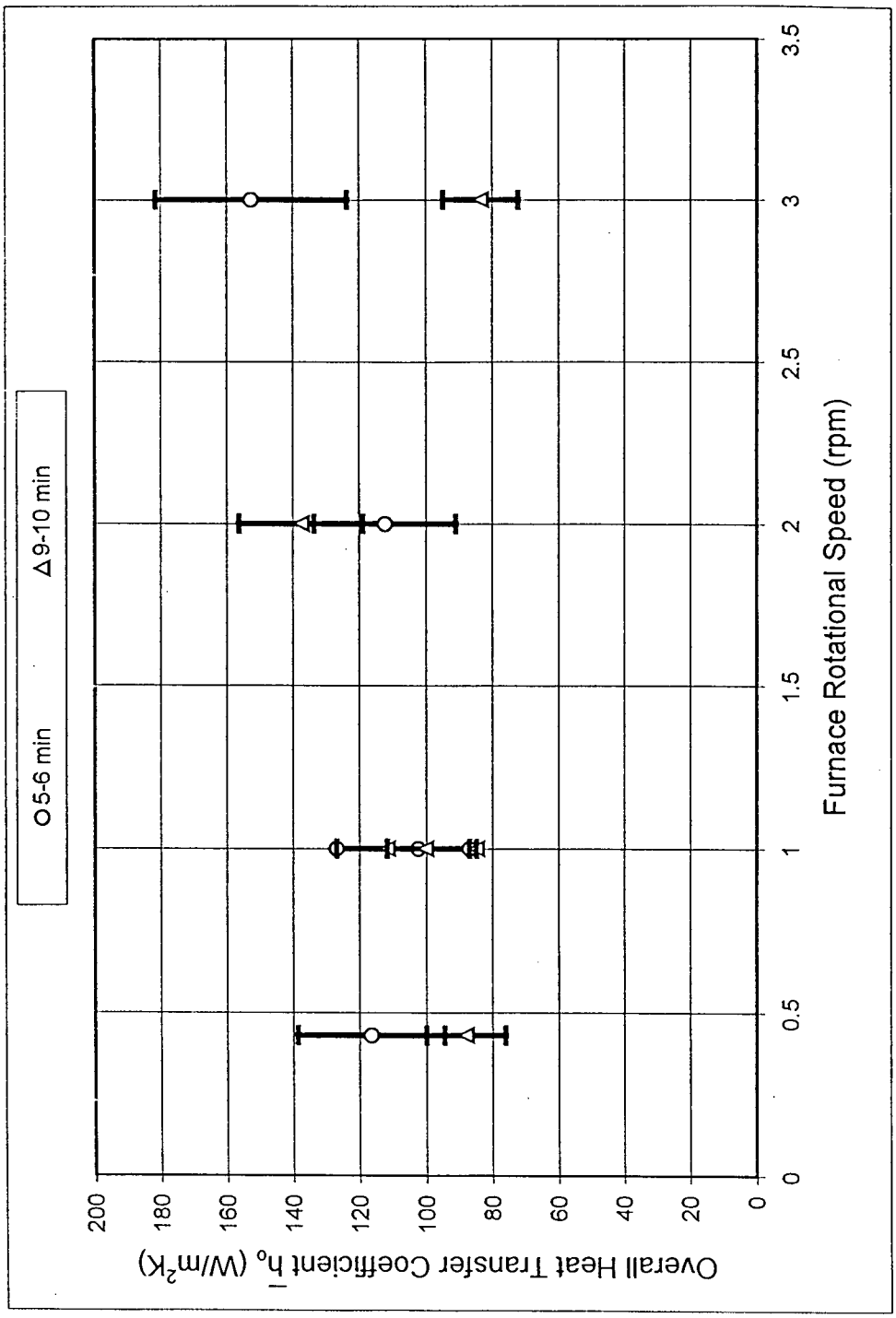

Figure 6.35: Effect of Furnace Rotational Speed on Overall Heat Transfer Coefficient for Runs with Mix 5. ($\bar{d}_p = 1.2$mm, $\sigma_p^* = 0.22$, $n_{RR} = 7.7$)

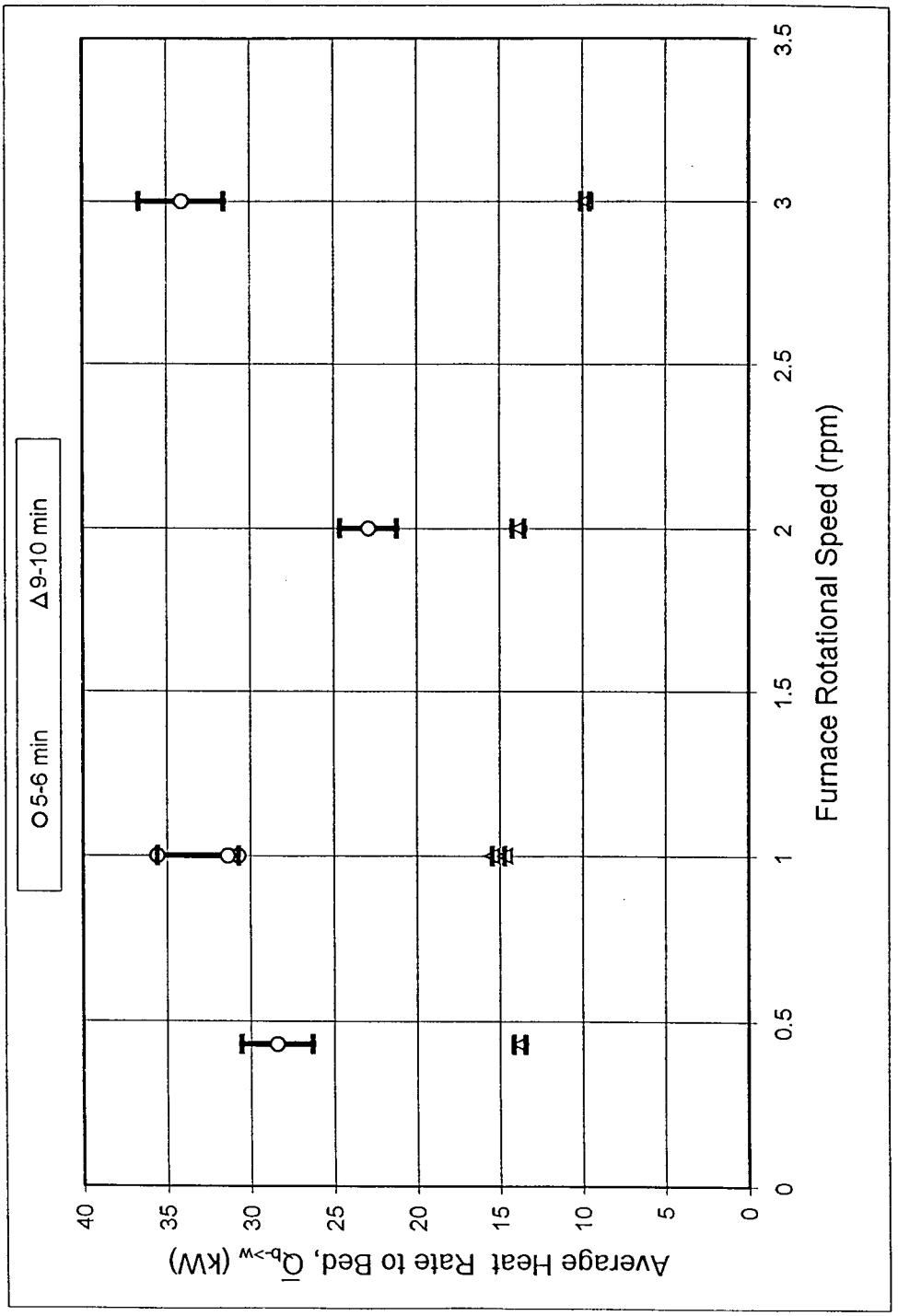

Figure 6.36: Effect of Furnace Rotational Speed on Heat Rate to Bed for Runs with Mix 5. ($\bar{d}_p = 1.2$mm, $\sigma_p^* = 0.22$, $n_{RR} = 7.7$)

Table 6.1: Details of Test Runs

Run	Description	Mix	rpm	Mean Particle Size $\bar{d}_p$ (mm)	Particle Size Standard Deviation σ_p^*	Rosin Rammler Index n_{RR}
1	preliminary run with coarse sand	2	1	1.9	0.24	7.3
2	preliminary run with coarse sand	2	1	1.9	0.24	7.3
3	coarse sand as purchased	2	1	1.9	0.24	7.3
4	50% coarse and 50% fine	1	1	1.4	0.29	5.0
5	coarse sand as purchased	2	1	1.2	0.22	7.7
6	test failed	-	-	-	-	-
7	test failed	-	-	-	-	-
8	fine sand as purchased	5	1	1.2	0.22	7.7
9	fine sand as purchased	5	3	1.2	0.22	7.7
10	coarse sand sieved 2.3-3.3mm	3	1	2.4	0.17	11.7
11	coarse sand sieved 2.8-3.3mm	4	1	3.0	0.9	15.5
12	fine sand sieved 1.2-1.7mm	6	1	1.3	0.15	11.8
13	fine sand as purchased	5	1	1.2	0.22	7.7
14	fine sand as purchased	5	1	1.2	0.22	7.7
15	fine sand as purchased	5	0.43	1.2	0.22	7.7
16	coarse sieved 1.2-1.7mm	4	0.43	3.0	0.09	15.5
17	fine sand as purchased	5	2	1.2	0.22	7.7
18	fine sand sieved 1.2-1.7mm	6	2	1.3	0.15	11.8
19	coarse sand sieved 2.8-3.3mm	4	2	3.0	0.09	15.5

Table 6.2: Measurements of Refractory Thickness During Installation of Thermocouples

Thermocouple	Refractory Thickness (mm)	Blanket Thickness (mm)
R1	67	29
R2	69	28
R4	70	25
R5	65	29
R7	66	29
R8	66	28
Average	67	28

Table 6.3: Sensitivity of Hot Face and Interface Temperatures to Changes in Refractory and Blanket Thickness. Temperatures calculated using 1D model after 120 minutes of Heat at 100kW

Test	Refractory Thickness (mm)	Blanket Thickness (mm)	Hot Face Temp. (°C)	Interface Temp. (°C)	Cold Face Temp. (°C)	Change from as built (°C, [%])
As Built	67	28	1073	869	282	-
1	65	28	1093	897	290	+28 [+3.2]
2	70	28	1045	828	269	-41 [-3.4]
3	67	25	1071	864	303	-5 [-0.5]
4	67	29	1074	870	275	+1 [+0.1]

Table 6.4: Average Values for Temperature Range, Overall Heat Transfer Coefficient and Heat Rate

Run	$\bar{\Omega}_T$ 5-6 min °C	$\bar{h}_o$ 5-6 min W/m^2 K	$\bar{Q}$ 5-6 min kW	$\bar{\Psi}$ 5-6 min	$\bar{\Omega}_T$ 2-3 revs °C	$\bar{h}_o$ 2-3 revs W/m^2 K	$\bar{Q}$ 2-3 revs kW	$\bar{\Psi}$ 2-3 revs
3	176.3	105.2	28.4	4.0	176.3	105.2	28.4	4.0
4	107.2	174.1	36.2	6.2	107.2	174.1	36.2	6.2
5	105.5	124.9	31.9	4.7	105.5	124.9	31.9	4.7
8	177.5	102.4	30.7	3.7	177.5	102.4	30.7	3.7
9	103.0	152.5	34.1	5.3	91.0	132.7	57.5	2.6
10	95.4	131.1	28.2	4.2	95.4	131.1	28.2	4.2
11	86.7	104.7	32.1	3.5	86.7	104.7	32.1	3.5
12	88.3	119.5	36.7	4.7	88.3	119.5	36.7	4.7
13	113.3	86.9	31.3	3.5	113.3	86.9	31.3	3.5
14	130.6	126.8	35.6	4.0	130.6	126.8	35.6	4.0
15	210.8	116.4	28.4	3.1	205.2	114.3	27.0	3.0
16	252.8	106.3	23.6	3.1	232.3	102.9	22.8	3.0
17	96.5	112.2	22.9	3.0	183.8	110.4	27.7	3.1
18	124.8	164.8	31.4	4.6	172.6	149.7	45.8	5.3
19	85.0	103.7	28.4	3.8	60.7	91.5	33.6	3.8

Chapter 7

Conclusions and Recommendations

7.1 Conclusions

In this study high temperature heat transfer in the cross-section of a particulate bed in a rotary furnace has been investigated through experimentation. A refractory lined batch furnace (I.D. = 400mm, Length = 900mm) was designed and manufactured. It was heated using a gas flame and, when the walls reached 1100°C, the gas flame was extinguished and the furnace was charged with sand and rotated. The energy in the walls was used to heat the sand bed. The wall temperature was monitored using thermocouples embedded in it and the temperature rise of the sand bed was monitored using a probe with four thermocouples located at different radial locations. The duration of each test run was about 20 minutes. The wall and bed temperature values allowed the rate of heat transfer from the wall to the bed to be calculated. The four temperatures in the bed itself also allowed one to determine the heat uptake by the bed and to quantify the degree of temperature uniformity. Such experiments have not been reported in the literature and so the first objective of this study was successfully met.

In lime kilns it has been reported that when the particulate feed has a wide size distribution, the fine particles may remain unreacted. It is suspected that since the fines segregate to the center of the bed, they are shielded from the hot free-board gases, that is, segregation hinders cross sectional heat transfer. To investigate this, six sand mixes with varying size distributions were tested in this study. The size distribution was quantified by measuring the particle size mean and standard deviation. The uniformity of the bed temperature was quantified by calculating the range of temperatures recorded by the four bed thermocouples.

Most of the runs were carried out with a rolling bed. The rotational speed was 1 rpm or greater and the fill was approximately 20% of the cross-sectional area. The bed temperature profiles were similar in all cases. The uppermost thermocouple, which is closest

to the exposed surface of the bed, was always the coolest and the lowest thermocouple, closest to the refractory walls, was the warmest. This implied that the upper thermocouple was in the cold core of the bed, below the active layer. This thermocouple was only 15 mm from the bed surface. While it would have been useful to have the active layer temperature, an additional thermocouple would have over agitated the sand particles and so affected the results.

The bed temperature profiles were generally smooth in nature. Two runs were carried out with a slumping bed, with a rotational speed of about 0.4 rpm. In these runs a step wise temperature rise was observed, which corresponds with the mixing nature of such bed motion. This result provides confidence that the probe and instrument set up was able to respond adequately to temperature changes within the bed.

The refractory hot face temperature was found to be relatively constant for the duration of all of the tests. This indicated that the refractory was able to hold sufficient energy for heating the bed to the required temperatures. Also, its conductivity was high enough so that the rate of energy transfer to the hot face, and ultimately the bed, ensured that the required bed temperatures were achieved. Therefore, the furnace was meeting its design objectives.

In all runs it was found that the spread of the temperatures in the bed was between 100-200°C initially. After about 20 minutes the bed was virtually isothermal. Since the four bed thermocouples were always located at the same position and the furnace fill was constant, the spread of these four temperatures was used to make comparisons between the runs. The average spread between 5 and 6 minutes was selected. A plot of this value with particle size distribution demonstrated a somewhat random relationship. This would imply that, for the ranges studied, the particle size range has minimal effect on temperature gradients. At 1 rpm the temperature spread within the bed increased as particle size distribution increased, but there was considerable data scatter and insufficient data points at all size distributions. Further tests at 1 rpm with the existing sand mixes and sand mixes with wider and narrower size ranges should to be carried out to confirm this finding.

By making the assumption that the average of the four bed temperatures indicated

average bed temperature the heat rate to the bed was calculated. Furthermore, by assuming that the average of the hot face thermocouples represented the average hot face temperature, heat transfer coefficients between the wall and bed surface were calculated. The wall to bed overall heat transfer coefficients were in the range 85-175 W/m^2K. The values tended to either remain relatively constant for the duration of the test runs, or their profiles were wave-like. These data represent a significant contribution to the literature since very few studies are available at realistic kiln temperatures and for kiln diameters above 0.25m.

The average values of heat rate to the bed and heat transfer coefficient at 5-6 minutes were compared with particle size distribution and it was found that the latter did not affect the former. This was not surprising considering that temperature uniformity was also not affected by particle size distribution. It was interesting to note, however, that a bed with a wide temperature range (highly non-uniform) did not necessarily result in a lower heat up rate, implying that overall transverse heat transfer may be independent of heat transfer within the bed. Therefore, a one-dimensional model of a kiln that only considers overall heat transfer between the free-board and bed can provide useful information about kiln performance. Analysis of temperature gradients within the bed can be carried out independently which lends credibility to pseudo three-dimensional models such as Boateng and Barr (1996a).

The mechanism of heat transfer from the exposed wall to the exposed bed is radiation. Conduction is negligible since particles at the exposed bed surface are not in contact with the walls. Also there was no gas flow and so convection is also negligible. The rate of heat transfer was, therefore, calculated using radiation theory. Since the overall rate of heat transfer to the bed was calculated also, the difference between these two values was the covered wall to covered bed heat flowrate. The ratio of heat transferred from the covered wall to covered bed and from the exposed wall to exposed bed surface was, therefore, also determined. It was discovered that the rate of heat transferred across the covered bed surface was between 3 and 6 times as much as the rate across the exposed bed surface, especially during the initial stages of the test runs. This result highlights the importance of conduction between the covered wall and bed particles adjacent to it.

In general it was found that particle size distribution has little or no impact on thermal gradients within the bed or overall heat transfer to the bed. One possible reason for this finding is that segregation had not established during the tests, so that the particle flow was the same in all runs. Another is that the active layer was so intensely mixed that it was effectively isothermal, and so radial temperature gradients were due only to thermal diffusion in the plug flow region. Both of these were negated for reasons described in the discussion. As such, for the size ranges tested, particle size range had little impact on the transverse heat transfer.

This study has reported a substantial quantity of heat transfer data within the bed at temperatures close to those found in industrial rotary kilns. Such data has not been available for general use in the past. Use of this data can be made for the purposes of validating mathematical models. As such, this constitutes one of the recommendations.

7.2 Recommendations For Future Work

Based on the findings of the current study the following work is recommended:

- Further tests at 1 rpm with the existing sand mixes and sand mixes with a wider size distribution should be carried out. This will confirm whether there is a relationship between size distribution and temperature non-uniformity.

- The data reported should be used to validate either existing two-dimensional models or to develop new ones. Such models give a clear picture of the temperature profile in the cross-section of the bed and, hence, can provide greater insight into the heat transfer characteristics. Once validated, such models can be modified and applied to industrial kilns

- An appropriate bed model requires a knowledge of the material flow profile, in particular the size, shape and location of the active layer. A novel technique has been developed at the University of Birmingham, UK, and described in (Parker, Dijkstra, Martin, and Seville 1997). Such a technique, or indeed any suitable one, should be applied to cold tests using the same materials in the current study to obtain a velocity profile.

- Another unknown in the bed model is the material effective conductivity in the active layer. The effective thermal conductivity in the plug flow region can be determined using models developed for packed beds, e.g. Schotte (1960). In the active layer the effective conductivity is enhanced due to particle mixing. The degree of particle mixing is, therefore, likely to be related to the effective conductivity. As such a profile of the mixing in the active layer, defined perhaps using the granular temperature (Boateng 1993), needs also to be measured. This can then be associated with the effective thermal conductivity enhancement term to develop the effective conductivity profile in the active layer.

Bibliography

Alyaser, A. H., P. V. Barr, and J. K. Brimacombe (1997). Modelling of axi-symmetric flow and combustion in an industrial scale furnace. *5th Annual Conference of Computational Fluid Dynamics Society of Canada*, 23–28.

Barr, P. V. (1986). *Heat Transfer Processes in Rotary Kilns.* Ph. D. thesis, University of British Columbia, Vancouver, BC, Canada.

Barr, P. V. (1999). Emmisabsor - computer subroutine.

Barr, P. V., J. K. Brimacombe, and A. P. Watkinson (1989a). A heat-transfer model for the rotary kiln: Part1. pilot kiln trials. *Metallurgical Transactions B 20B*, 391–402.

Barr, P. V., J. K. Brimacombe, and A. P. Watkinson (1989b). A heat-transfer model for the rotary kiln: Part ii. development of the cross-secton model. *Metallurgical Transactions B 20B*, 403–419.

Baumann, G., I. M. Jánosi, and D. E. Wolf (1994). Particle trajectories and segregation in a two-dimensional rotating drum. *Europhysics Letters 27*(3), 203–208.

Boateng, A. A. (1993). *Rotary Kiln Transport Phenomena: Study of the Bed Motion and Heat Transfer.* Ph. D. thesis, University of British Columbia, Vancouver, BC, Canada.

Boateng, A. A. and P. V. Barr (1996a). Modelling of particle mixing and segregation in the transverse plane of a rotary kiln. *Chemical Engineering Science 51*(17), 4167–4181.

Boateng, A. A. and P. V. Barr (1996b). A thermal model for the rotary kiln including heat transfer within the bed. *Int. J. Heat Mass Transfer 39*(10), 2131–2147.

Bui, R. T., G. Simard, A. Charette, Y. Kocaefe, and J. Perron (1995). Mathematical modeling of the rotary coke calcining kiln. *The Canadian Journal of Chemical Engineering 73*, 534–545.

Carley-Macauly, K. W. and M. B. Donald (1962). Particle mass segregation in a two-dimensional rotating drum. *Chemical Engineering Science 17*, 493–506.

Chapra, S. C. and R. P. Canale (1988). *Numerical Methods For Engineers.* McGraw-Hill, Inc.

Dolgunin, V. N., A. N. Kudy, and A. A. Ukolov (1998). Development of the model of segregation of particles undergoing flow down an inclined chute. *Powder Technology 96*, 221–218.

Gorog, J. P., J. K. Brimacombe, and T. N. Adams (1981). Radiative heat transfer model in rotary kilns. *Metallurgical Transactions B 12B*, 55–70.

Henein, H. (1980). *Bed Behaviour in Rotary Cylinders with Applications to Rotary Kilns.* Ph. D. thesis, University of British Columbia, Vancouver, BC, Canada.

Hottel, H. C. and A. F. Sarofim (1967). *Radiative Heat Transfer.* New York: McGraw-Hill Book Company Inc.

Imber, M. and V. Paschkis (1962). *Int J Heat Mass Transfer 5*, 623.

Incopera, F. P. and D. P. Dewitt (1981). *Fundamentals of Heat Transfer.* John Wiley and Sons, Inc.

Jenkins, B. G. (1998). Modelling - it's plastic, mathematic, stochastic, elastic and fantastic. edited by dong-ke-zhang and nathan, g. *Adelaide International Workshop on Thermal Energy Engineering and the Environment, Adelaide, Australia.*

Jenkins, B. G. and F. D. Moles (1981). Modelling of heat transfer from a large enclosed flame in a rotary kiln. *Trans IChemE 59*, 17–25.

Lun, C. K. K., S. B. Savage, D. J. Jeffrey, and N. Chepurnity (1984). Kinetic theories for granular flow: inelastic particles in couette flow and slightly inelastic particles in a general flowfield. *J. Fluid Mech 140*, 223–256.

Mastorakos, E., A. Massias, C. D. Tsakiroglou, D. A. Goussis, V. N. Burganos, and A. C. Payatakes (1998). Cfd predictions for cement kilns including flame modelling, heat transfer and clinker chemistry. *Applied Mathematical Modelling 23*, 55–76.

McCarthy, J. J., T. Shinbrot, G. Metcalfe, J. E. Wolf, and J. M. Ottino (1996). Mixing of granular materials in slowly rotated containers. *AIChE Journal 42*(12), 3351–3363.

Meakin, P. and R. Jullien (1992). Simple models for two- and three-dimensional particle size segregation. *Physica A 180*, 1–18.

Nityanand, N., B. Manley, and H. Henein (1986). An analysis of radial segregation for different sized spherical solids in rotary cylinders. *Metallurgical Transactions B 17B*, 247–257.

Ollivier-Gooch, C. (1998). *Computational Methods in Transport Phenomena I and II.* Vancouver, BC, Canada: University of British Columbia.

Parker, D. J., A. E. Dijkstra, T. W. Martin, and J. P. K. Seville (1997). Positron emission particle tracking studies of spherical particle motion in rotating drums. *Chemical Engineering Science 52*(13), 2011–2022.

Patankar, S. V. (1980). *Numerical Heat Transfer and Fluid Flow.* Hemisphere Publishing Inc., McGraw-Hill Book Company.

Pollard, B. L. and H. Henein (1989). Kinetics of radial segregation of different sized irregular particles in rotary cylinders. *Canadian Metallurgical Quarterly 17B*(1), 29–40.

Ristow, G. H. (1994). Particle mass segregation in a two-dimensional rotating drum. *Europhysics Letters 28*(2), 97–101.

Rogers, A. R. and J. A. Clements (1971/1972). The examination of segregation of granular materials in a tumbling mixer. *Powder Technology 5*, 157–168.

Roseman, B. and M. B. Donald (1962). Mixing and de-mixing of solid particles, ii - effect of varying the operating conditions of a horizontal drum mixer. *Brit Chem Eng 7*(11), 823–827.

Rosin, P. and E. Rammler (1933). The laws governing the fineness of powdered coal. *The Institute of Fuel*, 29–36.

Savage, S. B. and C. K. K. Lun (1988). Particle size segregation in inclined chute flow of dry cohensionless granular solids. *J. Fluid Mech 189*, 311–335.

Schotte, W. (1960). Thermal conductivity of packed beds. *AIChE Journal 6*(1), 63–67.

Smith, T. F., Z. F. Shen, and J. N. Friedman (1982). Evaluation of coefficients for the weighted sum of gray gases model. *Transactions of the ASME 104*, 602–608.

Sunnergren, C. E. (1979, September). A new mixer for rotary lime kilns. *National Lime Association Operators Meeting, Seattle WA*.

Von Wedel, K. (1973). Beurteilung des drehrohrofens zur erzieling eines kalkes definierter qualitat (an appreciation of the rotary kiln for producing lime of a specified quality). *Zement-Kalk-Gips 26*(3), 110–113.

Williams, J. C. (1976). The segregation of particulate materials. a review. *Powder Technology 15*, 245–251.

Woodle, G. R. and J. M. Munro (1993). Particle motion and mixing in a rotary kiln. *Powder Technology 76*, 241–245.

Yang, L. and B. Farouk (1997). Modeling of solid particle flow and heat transfer inrotary kiln calciners. *Journal of the Air and Waste Management Association 47*, 1189–1196.

Appendix A

Refractory and Insulation Details

12-17-99 10:48P P.02

VRI-Canada

#60-9080 - 196A Street,
Langley, British Columbia,
Canada, V1M 3B4
Tel: (604) 888-8685
Fax: (604) 888-5211

Brand THOR 60
Class CAST/LOW-MOISTURE

PRELIMINARY LABORATORY TEST DATA

Maximum Recommended Temperature, °F - °C	2700 - 1482
Material Required, lb/ft3 - kg/m3	162 - 2600
Water Required to Cast, wt.%	5.5 - 6.0
ASTM Flow Range, %	28 - 36
Abrasion Loss, cm3	
After 1500°F (816°C)	6
After 2000°F (1093°C)	6
Bethlehem Cycling Test, % Strength Loss Samples Fired @2000°F (1093°C) & Cycled 5X @2000°F (1093°C)	0.0
Thermal Conductivity, BTU-in/ft2 °F hr	
@ 392°F (200°C)	45.2
@ 752°F (400°C)	40.9
@ 1112°F (600°C)	41.3 } 5.9 w/mk.
@ 1472°F (800°C)	41.2 }

TEST TEMP. (°F)	BULK DENSITY (lb/ft3)	TOTAL LINEAR CHANGE (%)	MODULUS OF RUPTURE (lb/in2)	HOT MOR @ TEMP. (lb/in2)	COLD CRUSHING STRENGTH (lb/in2)	APPARENT POROSITY (%)
230	165	---	2400	----	----	13
1500	162	-0.2	----	4900	15000	18
2000	162	---	----	5500	----	17
2500	161	---	----	200	----	14
(°C)	(kg/m3)	(%)	(MPa)	(MPa)	(MPa)	(%)
110	2640	---	17	---	---	13
816	2600	-0.2	---	34	103	18
1093	2600	---	---	38	---	17
1371	2580	---	---	1.4	---	14

CHEMICAL ANALYSIS CALCINED BASIS, wt.%

SiC	59.0	SiO2	14.4	CaO	2.7
Al2O3	23.4	Fe2O3	0.1	Na2O	0.2

The data given above are based on averages of the results of a small number of test specimens made under controlled conditions in the laboratory and are determined by standard ASTM procedures where applicable. Variation from the above results may occur in individual tests and in actual plant production. These results cannot be taken as minima or maxima for specification purposes.

03/95

NARCO CANADA INC.

Brand **Plicast LWI-24R** Quality Number: 1266

This is a medium weight insulating castable formulated with a decreased iron content. Typical uses include petrochemical heater walls and roofs; regenerator linings in FCCU processes; and walls and arches in heat treating furnaces.

TYPICAL TEST DATA

Maximum Recommended Temperature, °F - °C	Up to 2500 - 1371
Pyrometric Cone Equivalent, P.C.E.	15-16
Material Required, lb/ft³ – kg/m³	85 - 1362
Water Required to Temper, wt.%	26.1
Setting characteristics	Hydraulic
Minimum time before firing	24 hours
Average storage life	12 months

Tested after firing at test temperature					Data at temperature	
TEST TEMP. (°F)	TOTAL BULK DENSITY (lb/ft³)	LINEAR CHANGE (%)	MODULUS OF RUPTURE (lb/in²)	COLD CRUSHING STRENGTH (lb/in²)	THERMAL CONDUCT. (BTU-in/h/ft²/F)	HOT MOR @ TEMP. (lb/in²)
230	92	-0.1	350	750	2.3	
1000	87	-0.2	300	700	2.6	275
1500	85	-0.3	220	650	2.8	300
2000	85	-0.5	300	650	3.5	300
2500	88	-1.5	500	1800		225
(°C)	(g/cm³)	(%)	(MPa)	(MPa)	(W/m-K)	(MPa)
110	1.47	-0.1	2.4	5.2	0.33	
538	1.39	-0.2	2.1	4.8	0.37	1.9
816	1.36	-0.3	1.5	4.5	0.40	2.1
1093	1.36	-0.5	2.1	4.5	0.50	2.1
1371	1.41	-1.5	3.4	12.4		1.6

CHEMICAL ANALYSIS, dried basis, wt.%

SiO_2	47.56	CaO	9.32
Al_2O_3	37.45	MgO	0.16
Fe_2O_3	0.79	Na_2O-K_2O	2.12
TiO_2	0.62	L.O.I.	0.19

The data given above are based on averages of test results on samples selected from routine plant production, by standard A.S.T.M. procedures where applicable. Variation from the above data may occur in individual tests. These results cannot be taken as minima or maxima for specification purposes.

A Member of The DIDIER Veitsch Radex Group

11/97

19427 - 92 AVENUE. SURREY. B.C. CANADA V4N 4G6 TELEPHONE: (604) 888-8685 FAX: (604) 888-5211

Typical Physical Properties

	Duraback®	Durablanket® S	Durablanket HP-S	Durablanket 2600
Color	White	White	White	White
Temperature Grade*	982°C (1800°F)	1260°C (2300°F)	1260°C (2300°F)	1430°C (2600°F)
Melting Point	1648°C (3000°F)	1760°C (3200°F)	1760°C (3200°F)	1760°C (3200°F)
Fiber Diameter	2-4 microns (mean)	2.5-3.5 microns (mean)	2.5-3.5 microns (mean)	3.5 microns (average)
Specific Heat @ 1093°C (2000°F)	1130 J/kg °C (0.27 Btu/lb °F)	1130 J/kg °C (0.27 Btu/lb °F)	1130 J/kg °C (0.27 Btu/lb °F)	1130 J/kg °C (0.27 Btu/lb °F)
Specific Gravity	2.73 g/cm³	2.73 g/cm³	2.73 g/cm³	2.73 g/cm³
Average Tensile Strength (ASTM 686-76)	—	5.5 lb/in² @ 4 PCF 9.9 lb/in² @ 6 PCF 12.5 lb/in² @ 8 PCF	—	—
Available Density kg/m³ (lb/ft³)	64 (4)	64, 96, 128 (4, 6, 8)	64, 96, 128 (4, 6, 8)	96, 128 (6, 8)

Typical Chemical Analysis

	PH Blanket	Moist Pak-D®	Fibermat™ Blanket	Fibermax® Mat
Al_2O_3	44%	34.5%	31-35%	72%
SiO_2	51%	62.8%	50-54%	27%
ZrO_2	5%	—	5%	—
Fe_2O_3	—	0.64-0.80%	1.3%	0.02%
TiO_2	—	0.54-1.37%	1.7%	0.001%
MgO	—	—	**0.5%	0.05%
CaO	—	—	≤7.5%	0.05%
Na_2O_3	—	—	—	0.10%
Alkali	—	0.23%	—	—
Leachable Chlorides	<10 ppm	—	<10 ppm	11 ppm
Other Inorganics	—	—	—	—

Typical Physical Properties
PH Blanket

Color:	Tan
Temperature Grade*:	1260°C (2300°F)
Melting Point:	1790°C (3260°F)
Fiber Diameter:	
PH Fine:	5 microns (mean)
PH Coarse:	13 microns (mean)
Fiber Length:	Up to approximately 254 mm (10")
Density:	96 kg/m³ (6 lb/ft³)
Binder Content:	3-5%

Typical Physical Properties
Moist Pak-D®

Color:	White
Basic Composition:	Alumina-silica
Temperature Grade*:	1093°C (2000°F)
Melting Point:	1790°C (3260°F)
Typical Dry Density:	190-290 kg/m³ (12-18 lb/ft³)
Specific Heat Capacity at 1093°C (2000°F):	1130 J/kg °C (0.27 Btu/lb °F)
Tensile Strength – 6.4 mm (¼"):	Wet = 1.2 x 10^6 N/m² (17 psi) Dry = 3.5 x 10^5 N/m² (50 psi)
Hot Gas Erosion Resistance:	Test procedure based on British Gas Council Research Comm. GC173 = over 30.5 m/sec (100 ft/sec)

Normal shelf life one year in unopened containers.

*The temperature grade of Fiberfrax® insulation is determined by irreversible linear change criteria, not product melting point.
**MgO and other trace inorganics.

Form C-1421
Effective 9/99

Printed in USA

Typical Physical Properties
Fibermat™ Blanket

Color:	White
Temperature Grade*:	760°C (1400°F)
Fiber Diameter:	2.5-3.5 microns (mean)
Specific Gravity:	2.73 g/cm³
Nominal Weight:	½" thickness = 3.7 oz/ft²
	1" thickness = 7.3 oz/ft²
	2" thickness = 14.7 oz/ft²
Tensile Strength (ASTM 686-76):	7-10 psi (typical)

Typical Physical Properties
Fibermax® Mat

Color:	White
Temperature Grade*:	1650°C (3000°F)
Melting Point:	1870°C (3400°F)
Fiber Diameter:	2-3.5 microns (mean)
Specific Gravity:	3 g/cm³
Specific Heat Capacity	1246 J/kg °C
at 1093°C (2000°F):	(0.297 Btu/lb °F)
Fiber Surface Area:	7.65 m²/g

Typical Mechanical Properties
Compression Recovery

Percent Compression	Percent Recovery
10	93
30	82
50	71

Duraback®
Durablanket® S
Durablanket HP-S
Durablanket 2600
Thermal Conductivity vs. Mean Temperature (per ASTM C-177)**

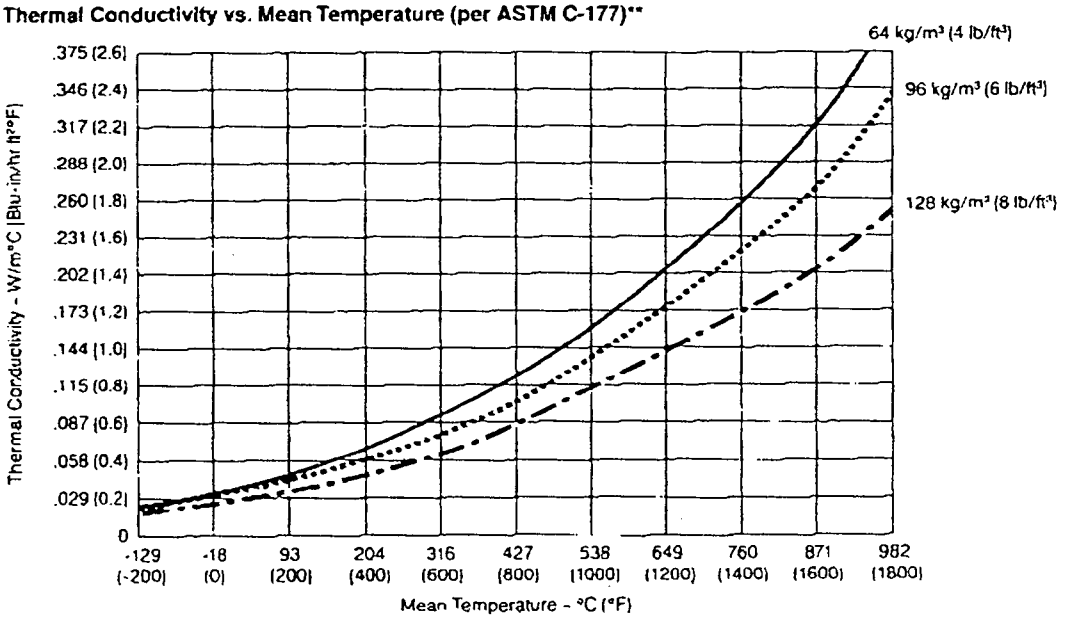

*The temperature grade of Fiberfrax® insulation is determined by irreversible linear change criteria, not product melting point.

For additional information about product performance or to identify the recommended product for your application, please contact the Unifrax Application Engineering Group at 716-278-3899.

Data are average results of tests conducted under standard procedures and are subject to variation. Results should not be used for specification purposes.

**All heat flow calculations are based on a surface emissivity factor of 0.90, an ambient temperature of 27°C (80°F), and zero wind velocity, unless otherwise stated. All thermal conductivity values for Fiberfrax materials have been measured in accordance with ASTM Test Procedure C-177. When comparing similar data, it is advisable to check the validity of all thermal conductivity values and ensure the resulting heat flow calculations are based on the same condition factors. Variations in any of these factors will result in significant differences in the calculated data.

Form C-1421
Effective 9/99

Printed in USA
Page 5 of 8

Appendix B

Engineering Drawings of Furnace and Support

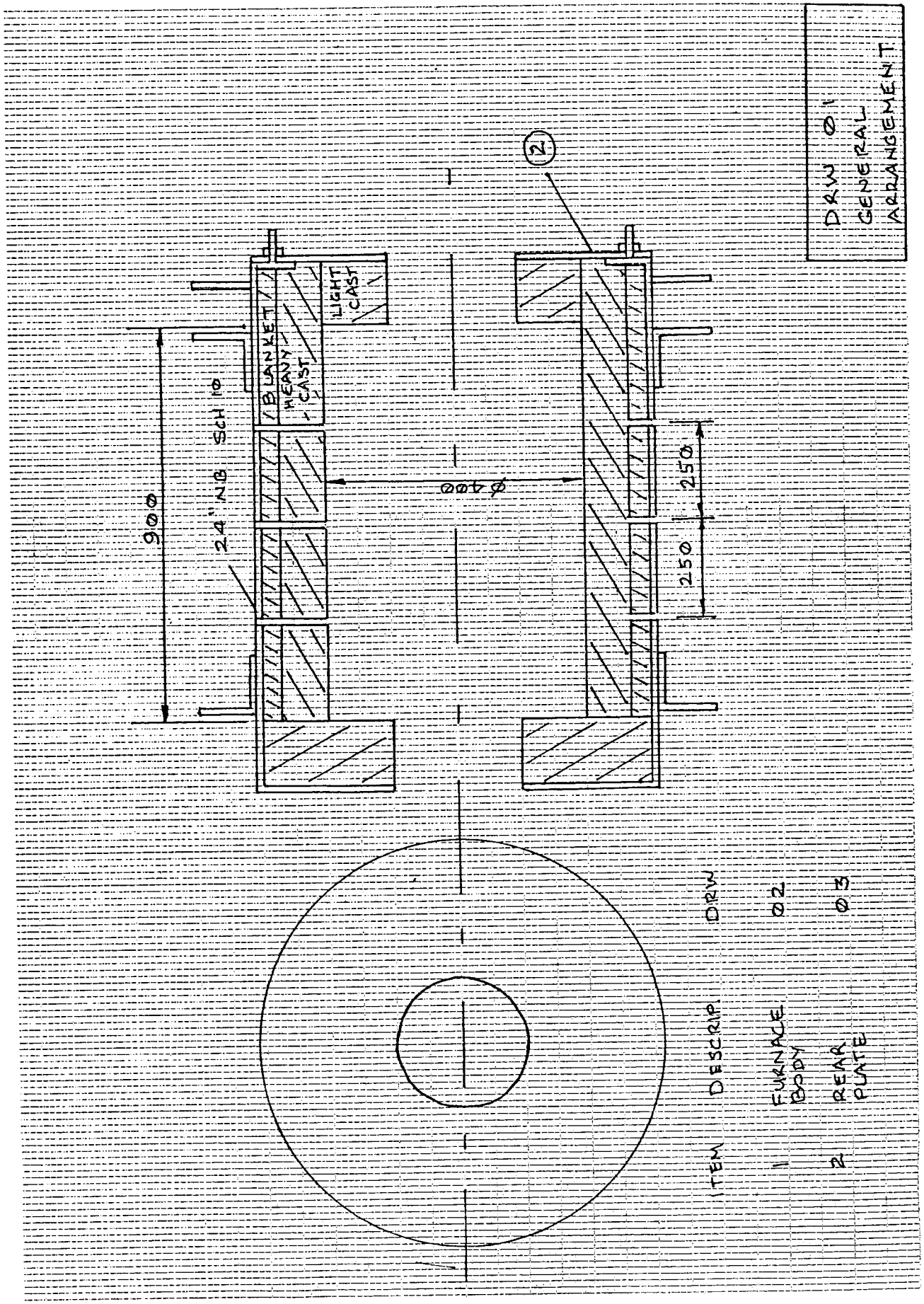
DRW 01
GENERAL ARRANGEMENT
2
BLANKET
HEAVY CAST
LIGHT CAST
24" NB SCH 10
900
ø470
250
250
ITEM DESCRIP. DRW
1 FURNACE BODY 02
2 REAR PLATE 03

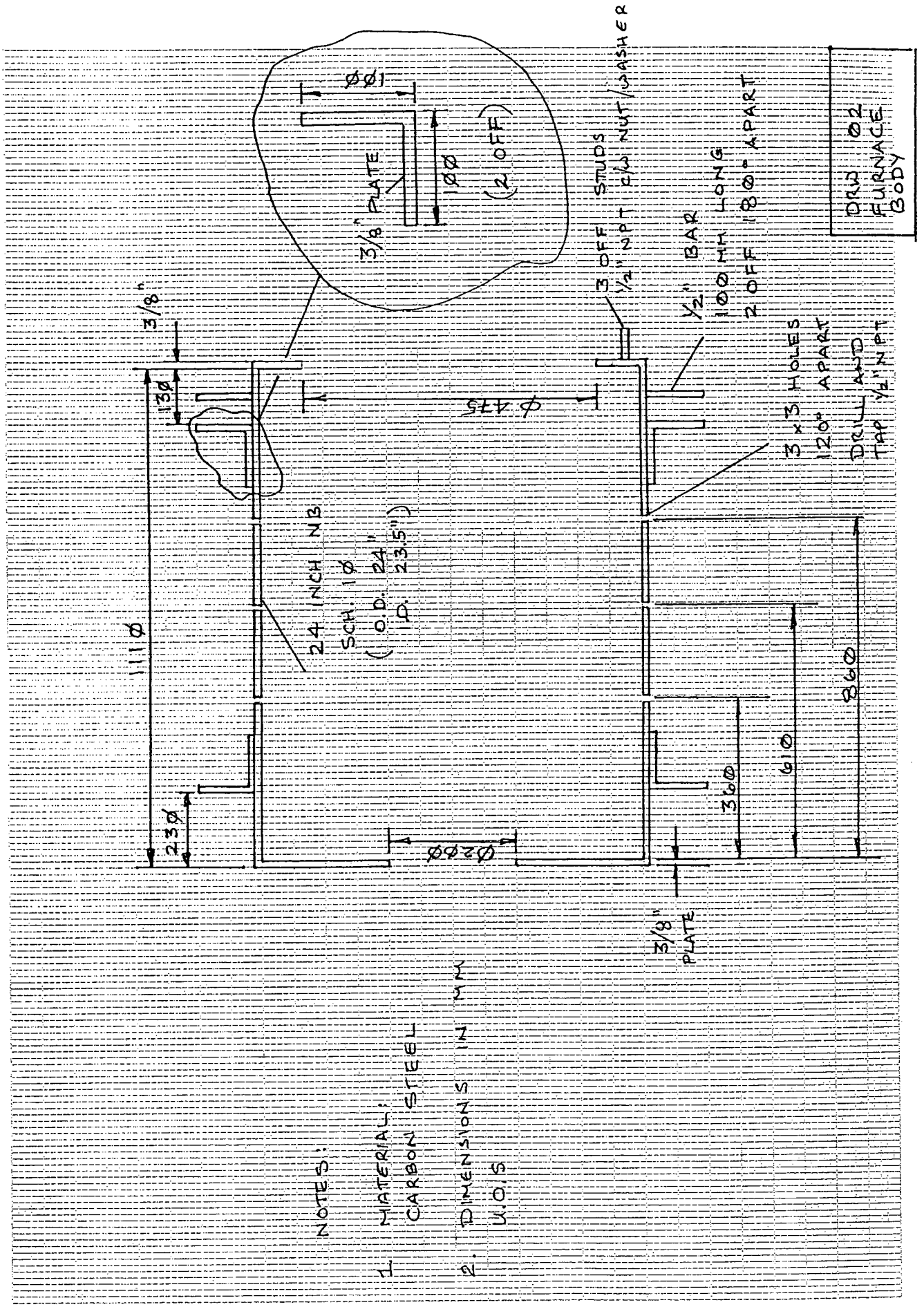
NOTES:
1. MATERIAL: CARBON STEEL
2. DIMENSIONS IN M.M. U.O.S.
ØØ1
3/8" PLATE
ØØ (2 OFF)
3 OFF 1/2" NPT c/w NUT/WASHER STUDS
1/2" BAR 100 mm LONG 2 OFF 180° APART
DRILL AND TAP 1/2" NPT
3 x 3 HOLES 120° APART
DRG 02 FURNACE BODY
3/8"
130
Ø475
24 INCH NB SCH. 10 (O.D. 24" ID 23.5")
1110
230
Ø2ØØ
3/8" PLATE
360
610
860

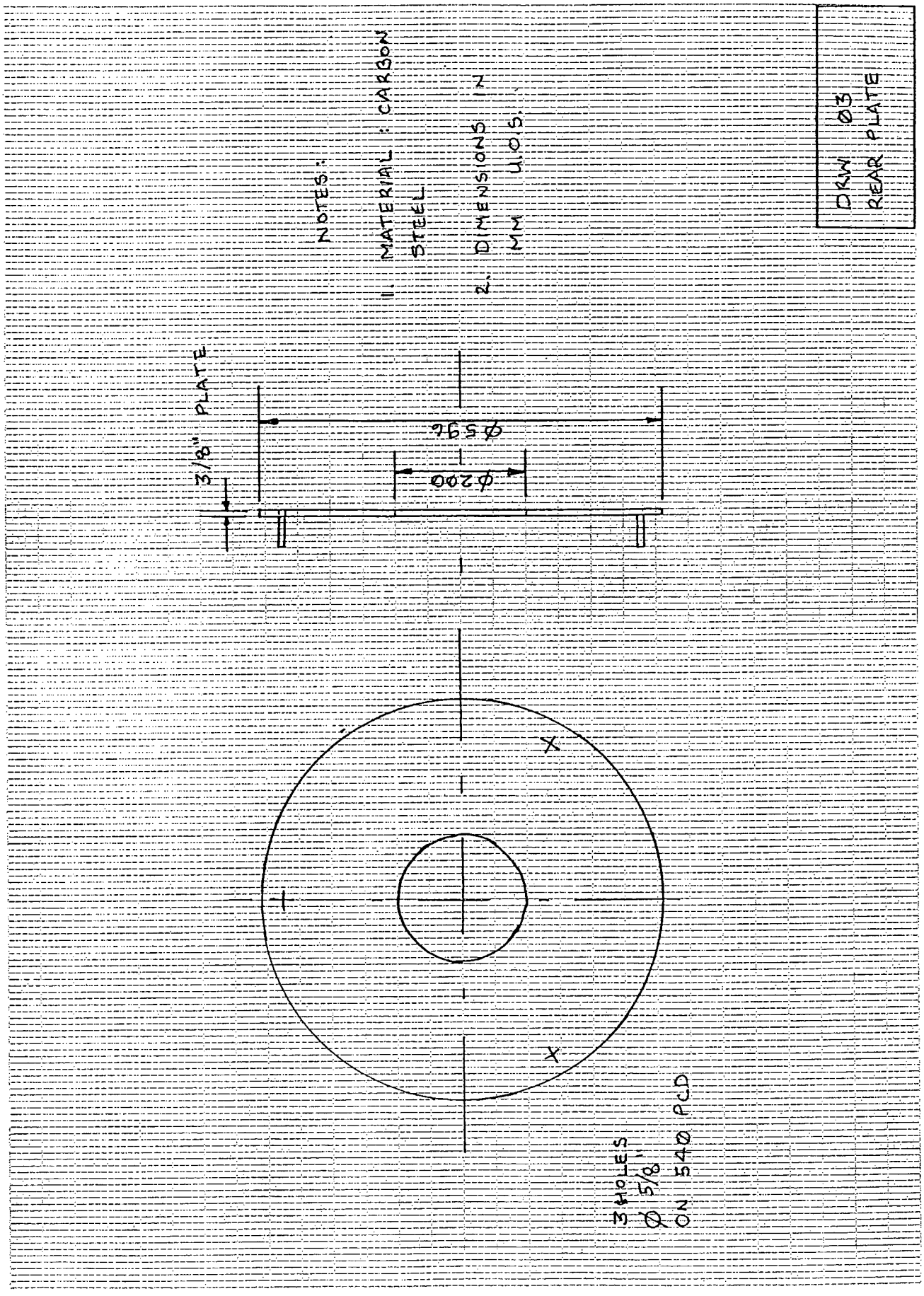
DKW Ø3
REAR PLATE
NOTES:
1. MATERIAL: CARBON STEEL
2. DIMENSIONS IN MM UNLESS
3/8" PLATE
Ø596
Ø200
X
X
3 HOLES Ø 5/8" ON 540 PCD

Appendix C

Specifications of Instrumentation

1. Thermocouple cable
2. Rotary Selector Switch
3. Portable Temperature Indicator
4. Signal Conditioning Board
5. Data Acquisition Board

Thermocouple Wire
Duplex Insulated

MADE IN USA

K Duplex Insulated
CHROMEGA®-
ALOMEGA®
Duplex
ANSI Type K

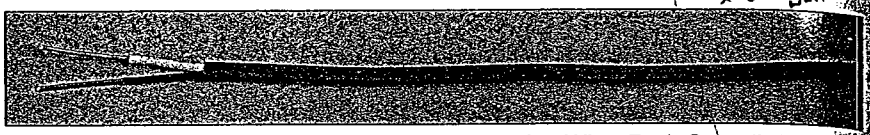

ANSI Color Code: Positive Wire, Yellow; Negative Wire, Red; Overall, Brown

OMEGA Engineering does not use reprocessed Teflon or PVC in manufacturing of thermocouple wire

Insulation	AWG No.	Model Number	Price 1000'	Type Wire	Insulation: Conductor	Insulation: Overall	Max. Temp °F	Max. Temp °C	Nominal Size	Wt.† lb/1000'
Ceramic	14	XC-K-14	$2695	Solid	Nextel Ceramic	Nextel Ceramic	2000	1090	.140 x .200	38
	20	XC-K-20	1425	Solid	Nextel Ceramic	Nextel Ceramic	1800	980	.135 x .190	16
	20	XT-K-20	1275	Solid	Nextel Ceramic	Nextel Ceramic	1800	980	.105 x .155	15
	20	XL-K-20	1200	Solid	Nextel Ceramic	Nextel Ceramic	1800	980	.095 x .135	14
	24	XC-K-24	995	Solid	Nextel Ceramic	Nextel Ceramic	1600	870	.115 x .175	12
	24	XT-K-24	895	Solid	Nextel Ceramic	Nextel Ceramic	1600	870	.088 x .132	11
	24	XL-K-24	845	Solid	Nextel Ceramic	Nextel Ceramic	1600	870	.078 x .116	10
	14	XS-K-14	1875	Solid	Silfa Silica	Silfa Silica	1900	1038	.140 x .200	35
	20	XS-K-20	1050	Solid	Silfa Silica	Silfa Silica	1800	980	.105 x .155	12
	24	XS-K-24	825	Solid	Silfa Silica	Silfa Silica	1600	870	.088 x .132	10
High Temp. Glass**	20	HH-K-20	492	Solid	High Temp. Glass	High Temp. Glass	1300	704	.060 x .105	9
	24	HH-K-24	348	Solid	High Temp. Glass	High Temp. Glass	1300	704	.055 x .090	5
Glass	20	GG-K-20	410	Solid	Glass Braid	Glass Braid	900	482	.060 x .095	9
	20	GG-K-20S	600	7 x 28	Glass Braid	Glass Braid	900	482	.060 x .100	9
	24	GG-K-24	290	Solid	Glass Braid	Glass Braid	900	482	.050 x .080	5
	24	GG-K-24S	395	7 x 32	Glass Braid	Glass Braid	900	482	.050 x .085	5
	26	GG-K-26	270	Solid	Glass Braid	Glass Braid	900	482	.045 x .075	4
	28	GG-K-28	230	Solid	Glass Braid	Glass Braid	900	482	.045 x .070	3
	30	GG-K-30	240	Solid	Glass Wrap	Glass Braid	900	482	.045 x .070	3
	36	GG-K-36	320	Solid	Glass Wrap	Glass Braid	900	482	.045 x .070	2
Teflon® Glass	30	TG-K-30	530	Solid	PFA	Glass Braid	500	260	.034 x .047	2
	36	TG-K-36	590	Solid	PFA	Glass Braid	500	260	.028 x .038	2
	40	TG-K-40	650	Solid	PFA	Glass Braid	500	260	.026 x .035	2
Teflon® Neoflon® PFA (High Performance)	20	TT-K-20	495	Solid	PFA	PFA	500	260	.068 x .116	11
	20	TT-K-20S	755	7 x 28	PFA	PFA	500	260	.073 x .126	11
	22	TT-K-22S	735	7 x 30	PFA	PFA	500	260	.065 x .133	9
	24	TT-K-24	370	Solid	PFA	PFA	500	260	.056 x .093	6
	24	TT-K-24S	515	7 x 32	PFA	PFA	500	260	.063 x .102	6
	30	TT-K-30*	335	Solid	PFA	PFA	500	260	.022 x .038	2
	36	TT-K-36*	375	Solid	PFA	PFA	500	260	.017 x .028	2
	40	TT-K-40*	500	Solid	PFA	PFA	500	260	.015 x .024	2
Teflon® Neoflon® FEP	20	FF-K-20	490	Solid	FEP	FEP	392	200	.068 x .116	11
	24	FF-K-24	350	Solid	FEP	FEP	392	200	.056 x .092	6
Polymers	24	PR-K-24	230	Solid	Polyvinyl	(Rip Cord)	221	105	.050 x .086	5
	20	KK-K-20	1055	Solid	Kapton	Kapton*	600	315	.057 x .103	11
	24	KK-K-24	735	Solid	Kapton	Kapton	600	315	.045 x .079	6

†Weight of spool and wire rounded up to the next highest lb., does not include packing material
**Overall color: clear **Has color tracer*
Wire available with special limits of error, consult Sales for pricing and availability

Discount Schedule
1000 ft spools only
3-4 . . . 10%
5-9 . . . 15%
10-19 . . . 20%

Spool Pricing

1. Determine price per 1000 ft. spool
2. Look up price category for the standard lengths available:

25 ft. = $\frac{\text{Price per 1000'}}{1000}$ x 2.5

50 ft. = $\frac{\text{Price per 1000'}}{1000}$ x 2

100 ft. = $\frac{\text{Price per 1000'}}{1000}$ x 1.75

200 ft. = $\frac{\text{Price per 1000'}}{1000}$ x 1.5

500 ft. = $\frac{\text{Price per 1000'}}{1000}$ x 1

1000 ft. = Price per 1000' (Net)

3. To determine total cost, use established price. category (from step 2) times total length Round price to nearest dollar.
4. Examples:

Wire Type: EXPP-J-14 @ 555/1000'	
50 ft.	EXPP-J-14 @ $.555/ft x 2 = $1.11/ft. (**$55.50** per 50 ft. spool)
100 ft.	EXPP-J-14 @ .555/ft x 1.75 = .97/ft. (**$97.00** per 100 ft. spool)
150 ft.	EXPP-J-14 @ .555/ft x 1.75 = .97/ft. (**$146.00** per 150 ft. lot) *Note: Customer will receive one 100 ft. spool and one 50 ft. spool*
200 ft.	EXPP-J-14 @ .555/ft x 1.5 = .83/ft. (**$167.00** per 200 ft. spool)
300 ft.	EXPP-J-14 @ .555/ft x 1.5 = .83/ft. (**$250.00** per 300 ft. lot) *Note: Customer will receive one 200 ft. spool and one 100 ft. spool*
500 ft.	EXPP-J-14 @ .555/ft x 1 = .555/ft. (**$278.00** per 500 ft. spool)

Standard Thermocouple and RTD Rotary Selector Switches

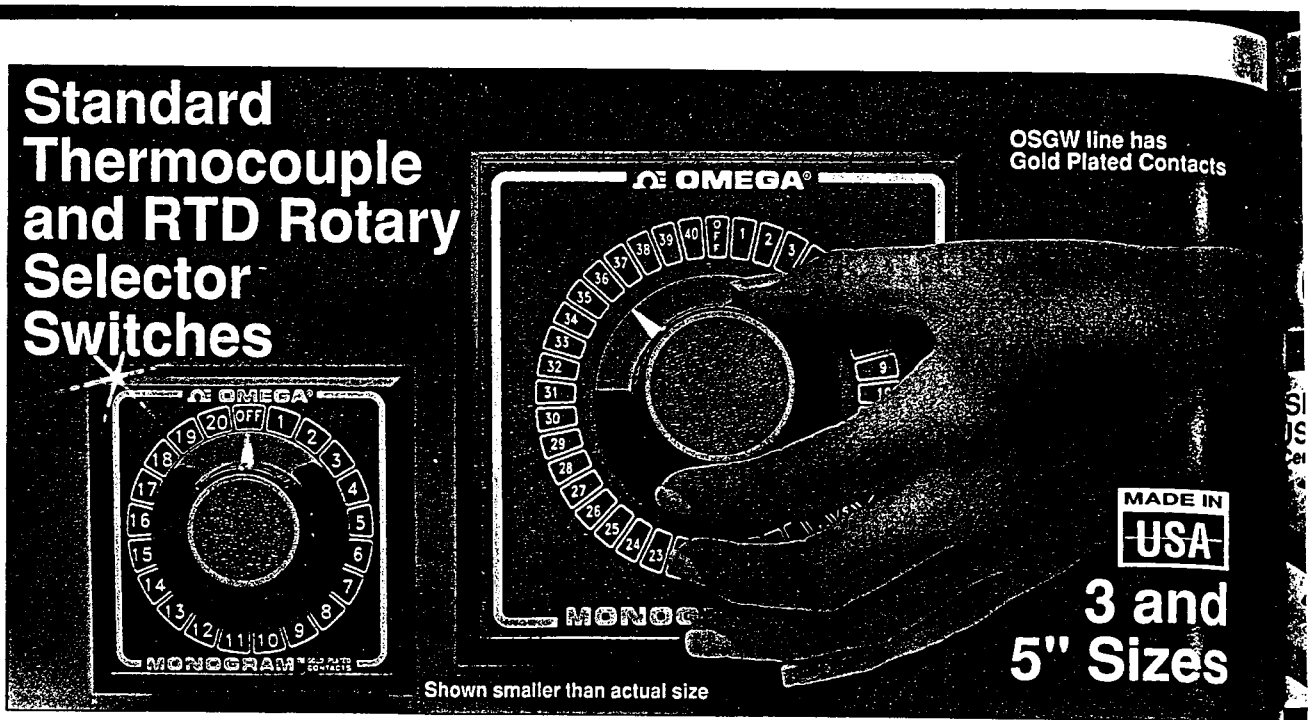

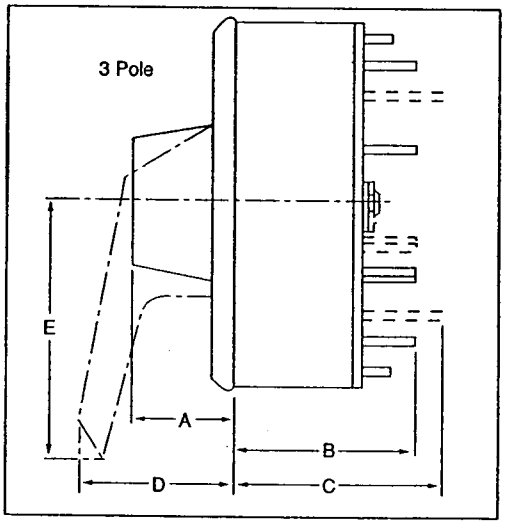

To order with optional pistol grip, add suffix '-PG' to model no. Comes complete with mounting hardware, panel mounting template and instruction manual. Add $6.50 to price.

Ordering Example:** OSWG3-20-PG, 3" (76 mm) switch, 20 positions, gold contacts, with optional pistol grip, $204 + 6.50 = **$210.50.

Insulation Resistance: 20 MΩ at 300 Vdc
Contact Resistance: 0.004 Ω or less
Also Available: Pistol grip handle retrofit kit; specify OSW-PG and switch size, $10.

OSW Switch Dimensions

Switch Size	Dim. A mm (in)	Dim. B* mm (in)	Dim. C mm (in)	Dim. D mm (in)	Dim. E mm (in)	Bezel Size mm (in)
76 mm (3")	28.6 (1⅛")	54 (2⅛")	62 (2⅜")	44.4 (1¾")	66.7 (2⅝")	82.55 (3¼")
127 mm (5")	38.1 (1½")	54 (2⅛")	62 (2⅜")	58.7 (2⅜")	92.07 (3⅝")	133.35 (5¼")

To Order *(Specify Model Number)*

No. of Poles	No. of Positions	Contact Action	Size	Silver Plated Contacts Model No.	Price	Gold Plated Contacts Model No.	Price
2 POLE	2	Break Before Make	3"	OSW3-2	$ 95	OSWG3-2	$142
	3			OSW3-3	97	OSWG3-3	145
	4			OSW3-4	99	OSWG3-4	148
	5			OSW3-5	102	OSWG3-5	153
	6			OSW3-6	104	OSWG3-6	156
	8			OSW3-8	108	OSWG3-8	162
	9			OSW3-9	111	OSWG3-9	166
	10			OSW3-10	113	OSWG3-10	169
	12	Make Before Break	3"	OSW3-12	118	OSWG3-12	177
	14			OSW3-14	122	OSWG3-14	183
	16			OSW3-16	127	OSWG3-16	190
	18			OSW3-18	131	OSWG3-18	196
	20			OSW3-20	136	OSWG3-20	204
	24			OSW5-24	145	OSWG5-24	217
	28		5"	OSW5-28	154	OSWG5-28	231
	30			OSW5-30	158	OSWG5-30	237
	32			OSW5-32	162	OSWG5-32	243
	36			OSW5-36	171	OSWG5-36	256
	40			OSW5-40	185	OSWG5-40	277
3 POLE	6	Make Before Break	127 (5")	OSWT-6	111	OSWGT-6	166
	10			OSWT-10	124	OSWGT-10	186
	12			OSWT-12	131	OSWGT-12	196
	18			OSWT-18	151	OSWGT-18	226
	20			OSWT-20	158	OSWGT-20	237
	24			OSWT-24	168	OSWGT-24	252
	28			OSWT-28	181	OSWGT-28	271
	30			OSWT-30	188	OSWGT-30	282
	32			OSWT-32	195	OSWGT-32	292
	36			OSWT-36	208	OSWGT-36	312
	40			OSWT-40	222	OSWGT-40	333

ANALOG SIGNAL CONDITIONING & EXPANSION

CIO-SSH16 & CIO-SSH16/DST

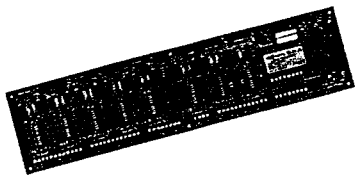

Features

- Adds simultaneous sample & hold front end to A/D board
- 4 channels standard, expandable to 16 channels
- Compatible with CIO-DAS1600 -DAS1400 and -DAS16 families

Analog Input Specifications

Aperture time	175nS avg, 250nS max
Aperture uncertainty	±25 nS
Acquisition time	4 uS
Max sample rate	250 KHz
Droop rate	±100 uV/mS
Input gains	1, 10, 100, 200, 300, 500 600, 700 and 800
Gain selection	Switch selectable. Channels may be at different gains.
Accuracy	0.01% ±1-bit

Channels

4 standard, up to 16 total. Additional channels may be added by purchasing/installing the CIO-SSH-AMP part. Each SSH-AMP adds one channel.

Software Description

Includes *Insta*Cal™, installation, calibration and test software. The CIO-SSH16 is supported by the UniversalLibrary™ for use with the DAS-16, DAS-1600 and DAS-1400 families. UniversalLibrary™ (provides programming language support for all DOS and Windows languages). Also supported by many third party, high-level data acq. programs.

Ordering Information

CIO-SSH16	4 channel SSH board
CIO-SSH16/DST	w/ detachable screw terms.
CIO-SSH-AMP`	1 channel expansion (you may add up to 12 channels)

Interconnect Cables

Standard:	C37FF-# series
Shielded:	C37FFS-5, C37FFS-10

CIO-EXP-32, CIO-EXP-32/DST, CIO-EXP-16 & CIO-EXP-16/DST

Features

- A/D board channel expansion
- 32 channel (EXP-32)
- 16 channel (EXP-16)
- User selectable gains
- On-board CJC sensor

Analog Input Specifications

Channels	32, CIO-EXP-32, differential 16, CIO-EXP-16, differential
Gain weights	1, 10, 100, 200, 300, 500
CJC sensor	+24.4 mV/°C (0V at 0°C)

User Field Configurable Options

Input filters (7 Hz), Open Thermocouple detection, 10Kohm ground reference resistor.

Cascading with the EXP-16 & EXP-32

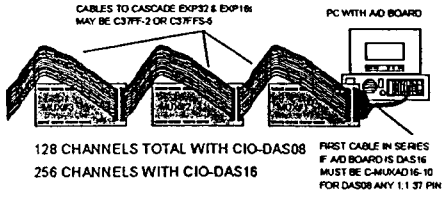

Software Description

Includes *Insta*Cal™, installation, calibration and test software. The CIO-EXP series is supported by the UniversalLibrary™ for use with most A/D boards.

/DST versions provide all field I/O wiring through detachable screw terminals.

Operating Modes

The active EXP-32/16 channel is selected by the host A/D board's digital output. An A/D board analog input must be dedicated to each EXP board.

Interconnect Cables

DAS-800/8 series	C37FF-# series
DAS-1600/1400/16 series	C-EXP2DAS16-10

CIO-EXP-BRIDGE16 & CIO-EXP-BRIDGE16/DST

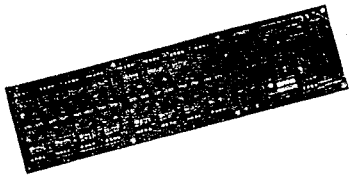

Features

- 16 chan., A/D board expansion
- Ideal strain gauge interface
- On-board Wheatstone bridge circuitry
- User selectable gains

Analog Input Specifications

Channels	16, fully differential
Gains	1, 10, 100, 1000

Field Installable Precision Resistors

It is critical that you use high quality resistors. We offer these values that match many sensors

CIO-EXP-RES-120	120 Ohm, 5ppm, 0.1%
CIO-EXP-RES-350	350 Ohm, 5ppm, 0.1%
CIO-EXP-RES-1000	1000 Ohm, 5ppm, 0.1%

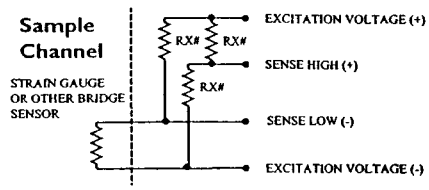

Software Description

Includes *Insta*Cal™, installation, calibration and test software. The CIO-EXP series is supported by the UniversalLibrary™ for use with most A/D boards.

/DST version provides all field I/O wiring through detachable screw terminals.

Operating Modes

The active EXP-BRIDGE16 channel is selected by the host A/D board's digital output. An A/D board analog input must be dedicated to each EXP board.

Interconnect Cables

DAS-800/8 series	C37FF-# series
DAS-1600/1400/16 series	C-EXP2DAS16-10

618-0530 COMPUTER BOARDS INC. 1-450-689-4572 MONTREAL

DAS-8 FAMILY ANALOG I

CIO-DAS08

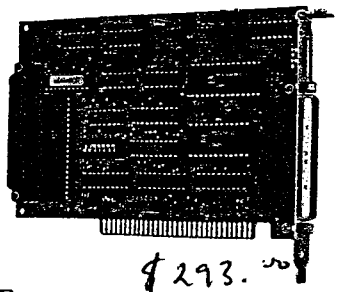

$293.00

Features

- 8 channel single-ended
- 12-bit, 20KHz A/D
- 3 counters
- 31-bits of digital I/O

Analog Input Specifications

Input resolution	12-bits (1 in 4096)
Input ranges:	±10V, ±5V, 0-10V
Range selection	Switch selectable
Max sample rate	20 KHz
Trigger/timing	Int/ext clock and trigger

Digital Input/Output (see pg 53 for family specs)

Number of bits	24-bits CMOS, 3 banks of 8 7-bits TTL, 4 out, 3 in

Software Description
Includes *Insta*Cal™, installation, calibration and test software. Supported by UniversalLibrary™ (provides programming language support for all DOS and Windows languages). Also supported by most third party, high-level data acq. programs.

Channel Expansion and Signal Conditioni
See pages 16 through 20 for options

For more channels	See CIO-EXP-ser
For isolated inputs	See ISO-RACK0
For RTD or bridges	See EXP-GP, RTI or BRIDGE16

Cables / Screw Terminal / Acces Boards
Analog: C37FF-# / CIO-MINI37
Digital: BP-37 & C37FF-# / CIO-MINI37
Expansion: C37FF# / CIO-EXP-series

All CIO-MINI series screw terminal boards now available with detachable screw termin Simply add a /DST suffix to the CIO-MINI number. See our price list (pg 9) for /DST p ing details.

CIO-DAS08/JR/16-AO & CIO-DAS08/JR/16

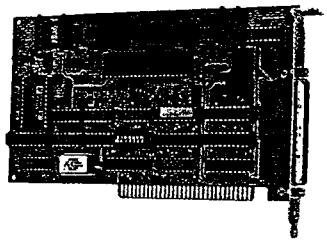

Features

- 8 channel A/D
- 16-bit, 30 sample/sec A/D
- Dual 16-bit D/A (-AO version)
- 16-bit digital I/O
- Ideal education configuration
- See Data Lab Solution

Analog Input Specifications

Input resolution	16-bits (1 in 65536)
Input range	±5V
Max sample rate	30 samples per second

Analog Outputs (-AO version only)

Channels	2, 16-bit resolution
Output range	±5V

Digital Input/Output (see pg 53 for family specs)

Number of bits	16-bits TTL, 8 in, 8 out

Options
The DAS08/JR/16 has no analog outputs, but may be upgraded to the DAS08/JR/16-AO by purchasing/installing the CIO-DUAL-DAC16 chip set.

Software Description
Includes *Insta*Cal™, installation, calibration test software. Supported by UniversalLibrar (provides programming language support fo DOS and Windows languages). Also suppo by most third party, high-level data acq. progra

Teaching Tools
See the Data Lab Solution and computer interface course books shown on page 20

Cables / Screw Terminal Boards
Low cost mating connector kit: DFCON-37
Screw terminal: C37FF-# / CIO-MINI37
Data Lab: C37FF-# / CIO-LAB8-TERM

CIO-DAS08/JR-AO & CIO-DAS08/JR

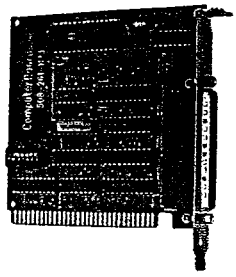

Features

- 8 channel A/D
- 12-bit, 20 KHz A/D
- Dual 12-bit D/A (-AO version)
- 16-bit digital I/O
- Ideal education configuration
- See Data Lab Solution

Analog Input Specifications

Input resolution	12-bits (1 in 4096)
Input range	±5V
Max sample rate	20 KHz

Analog Outputs (-AO version only)

Channels	2, 12-bit resolution
Output range	±5V

Digital Input/Output (see pg 53 for family specs)

Number of bits	16-bits TTL, 8 in, 8 out

Options
The DAS08/JR has no analog outputs, but may be upgraded to the DAS08/JR-AO by purchasing/installing the CIO-DUAL-DAC chip set.

Software Description
Includes *Insta*Cal™, installation, calibration a test software. Supported by UniversalLibrary (provides programming language support for DOS and Windows languages). Also support by most third party, high-level data acq. progran

Teaching Tools
See the Data Lab Solution and computer interface course books shown on page 20

Cables / Screw Terminal Boards
Low cost mating connector kit: DFCON-37
Screw terminal: C37FF-# / CIO-MINI37
Data Lab: C37FF-# / CIO-LAB8-TERM

Exceptional Digital Thermometers

Single and Dual Input Models HH-20 Series

MADE IN USA

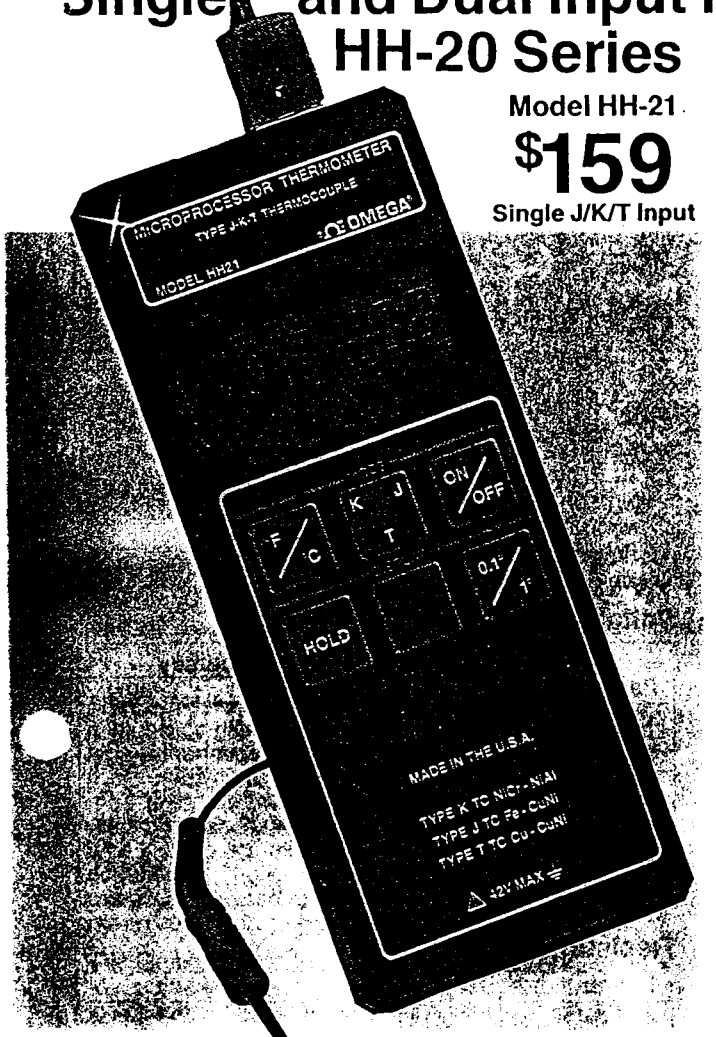

Model HH-21

$159

Single J/K/T Input

The HH-20 series microprocessor-based handheld thermometers offer wide-ranging temperature readings and feature state-of-the-art innovations. An easy to read custom 5-digit LCD readout with trend display and diagnostics, are all standard. The case is drop, splash and dust-proof, and has a built-in tilt stand/handle for bench use or hands-free field measurements.

The HH-21 is a single input unit that accepts J, K and T thermocouple types. From the front panel, the user can select the thermocouple type, display units (C or F), display resolution (0.1° or 1°). The HH-21 also has a display hold function. As with all the HH-20 series units, the HH-21 features exceptionally high accuracy, 0.1% of reading plus 1°F.

The HH-22 and HH-23 accept dual inputs. The HH-22 accepts either J or K thermocouples, while the HH-23 works with J, K or T types. Both models can display T1 (input 1), T2 (input 2), T1-T2 (difference), or scan between T1, T2 and T1-T2. Standard features for both the HH-22 and HH-23 include display hold, Min and Max storage, and trend indication. The Min and Max functions record minimum and maximum values for T2 and T1-T2. Trend indication shows if the displayed input is increasing, decreasing or stable.

When you turn on an HH-20, it remembers what you were doing; the thermocouple type, resolution, and temperature units are stored in non-volatile memory so you don't have to reprogram every time you start-up.

- ✓ Single and Dual Input Models with Display Hold
- ✓ Dual Input Models Feature Trend, Min/Max and Differential Measurements
- ✓ HH-21 and HH-23 Accept J, K and T Inputs
- ✓ HH-22 Accepts J and K Inputs
- ✓ 0.1° Resolution in F and C Over Full Range
- ✓ High 0.1% Reading Accuracy
- ✓ Self-Diagnostics and Retention of User Programming

Model KMQSS-125G-6 miniature transition joint probe sold separately, $24. See section A for the complete selection of OMEGA thermocouple probes.

Each unit supplied with beaded wire probe, transition adaptor, integral tiltstand wrist strap, 9 V battery and manual.

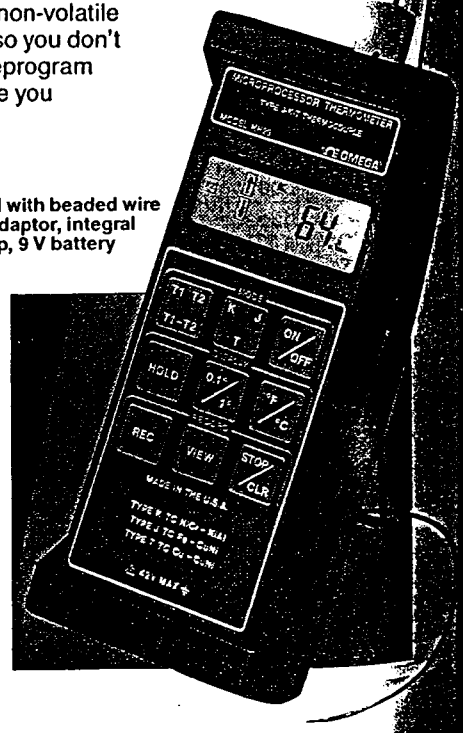

The HH20-H holster provides additional shock protection and a convenient belt clip, $18.

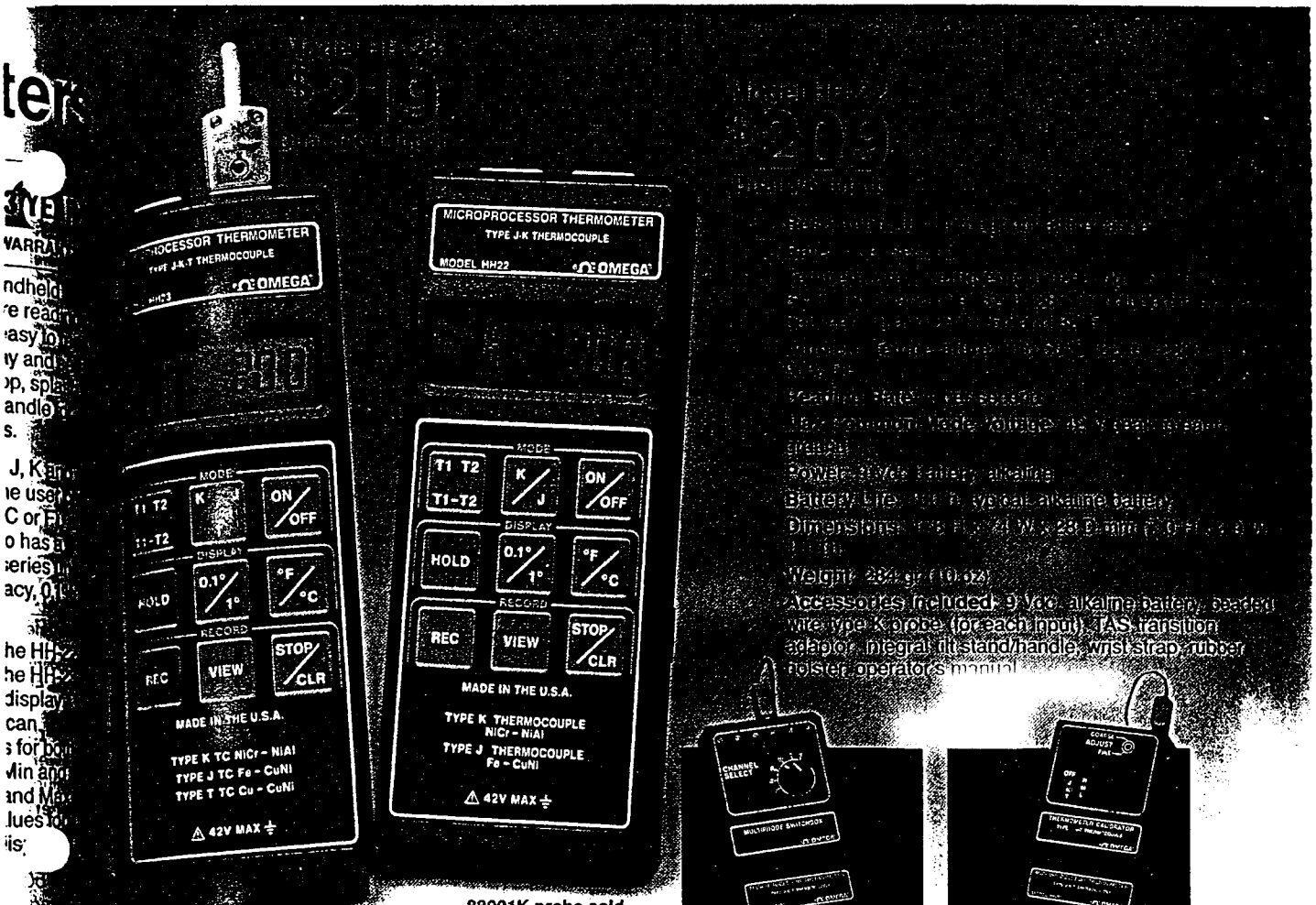

88001K probe sold separately, $110. 88000 series probes shown on pages A-55 through A-68.

Specifications

Display: 5-digit LCD; custom indicators for thermocouple type, °F/°C units, hold, low battery; HH-22 and HH-23 have additional indicators for input (T1, T2, T1-T2, scan), up/down trend arrows, min/max data storage.

Keypad: momentary switches with tactile feedback; on-off, thermocouple type, units, resolution, hold; HH-22 and HH-23 have additional keys for record min/max, view min/max, stop/clear record input type (T1, T2, T1-T2, scan)

Configuration Retention: selected readout, input type, units and resolution retained on power-off

Diagnostics: low battery, open thermocouple, invalid keypad entry, out of range, internal hardware fault

Accuracy: 0.1% rdg + 1°F

Repeatability: 0.2°C for 1 week at constant temperature

Input Ranges:

Type	Range, °F	Range, °C
J	−346 to 1400°F	−210 to 760°C
K	−328 to 2502°F	−200 to 1372°C
T	−328 to 752°F	−200 to 400°C

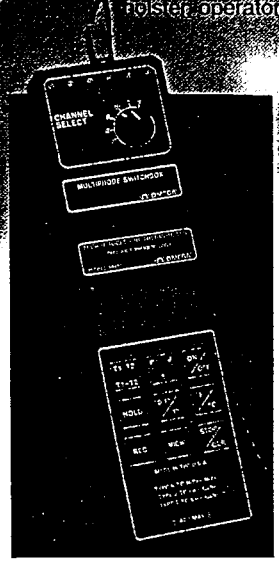

The HH20SW Allows up to 6 Probes, $99. See Page L-9 for Complete Details.

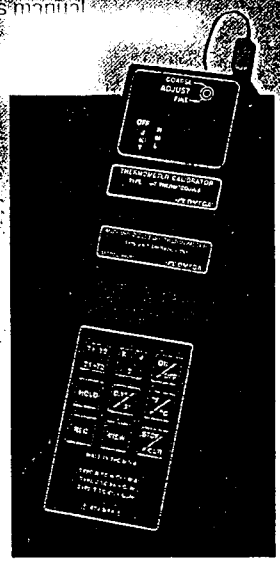

The HH20-CAL Turns a Handheld into a Portable Calibrator, $99. See Page K-48 for Complete Information.

To Order (Specify Model Number)

Model No.	Price	No. of Inputs	Input Types
HH-21	$159	1	J/K/T
HH-22	209	2	J/K
HH-23	219	2	J/K/T

Each unit supplied complete with beaded wire type K probe (for each input), TAS transition adaptor, integral tilt stand/handle, wrist strap, 9 V battery, shock resistant holster and users manual.

Accessories

Model No.	Price	Description
SC-450L	$10	soft carrying case
HH22-AC	50	9 V NiCad Battery with 110 Vac charger for HH-22 or HH-23
MN1604	3	extra alkaline battery.

Appendix D

Sand Details

MATERIAL SAFETY DATA SHEET

SECTION 1 - PRODUCT IDENTIFICATION AND USE

Product Identifier	**TARGET FILTER SAND AND GRAVEL**
Product Use	Filter Medium / Inorganic Filler

Manufacturer	Supplier
Target Products Ltd. 7550 Conrad Street Burnaby BC V5A 2H7	
Emergency Telephone Number (613) 996-6666 (Canutec)	Emergency Telephone Number

SECTION 2 - HAZARDOUS INGREDIENTS

Ingredient	%	CAS Number	LD_{50}	LC_{50}
Crystalline silica	60	14808-60-7	N/A	N/A

SECTION 3 - PHYSICAL DATA

Physical State	Solid		
Odour/Appearance	Grey to yellow crystals, no odour		
Vapour Pressure	N/A	Vapour Density	N/A
Evaporation Rate	N/A	Boiling Point	2230 °C
Freezing Point	1610 °C	pH	6-7
Specific Gravity	2.65	Coeff. Water/Oil Dist.	N/A

SECTION 4 - FIRE AND EXPLOSION DATA

Flammability	Not flammable	Means of Extinction	N/A
Flashpoint	N/A	Upper/Lower Flame. Limit	N/A
Autoignition Temp.	N/A	Hazardous Combustion Products	None

Explosion Data	
Sensitivity to Impact	None
Sensitivity to Static Discharge	None

SECTION 5 - REACTIVITY DATA

Chemical Stability	Stable
Incompatibility with Other Substances	None
Reactivity, and under what conditions	

Silica will dissolve in hydrofluoric acid to give silicon tetrafluoride, a corrosive gas.

NOTE: N/A = Not Applicable

Product Identifier **TARGET FILTER SAND AND GRAVEL**

SECTION 6 - TOXICOLOGICAL PROPERTIES

Route of Entry					
Skin Contact	No	Skin Absorption	No	Eye Contact	No
Inhalation	Yes	Ingestion	No		

Effects of Acute Exposure to Product

No potential acute toxic hazards known.

Effects of Chronic Exposure to Product

Target Industrial Sand 10-20 is screened to remove dust, thus avoiding the problems associated with respirable silica. In blast cleaning operations a dust may be formed which is subject to the following warning:

Excessive inhalation of crystalline silica dust may result in respiratory disease, including silicosis, pneumoconiosis and pulmonary fibrosis. The International Agency for Research on Cancer (IARC) has evaluated in Volume 42, Monographs on the Evaluation of the Carcinogenicity Risk of Chemicals to Humans; Silica and Some Silicates (1987), that there is "sufficient evidence for the carcinogenicity of crystalline silica to experimental animals" and "limited evidence with respect to humans."

Exposure Limits

OSHA PEL: Exposure to airborne crystalline silica shall not exceed an 8-hour time-weighted average limit as stated in 29 CFR 19100.1000 Table Z3 for Mineral Dusts, specifically "Silica: Crystalline: Quartz (respirable)".

Crystalline Quartz (Respirable)	$\frac{250}{\%\ SiO_2 + 5}$ Mppcf	$\frac{10}{\%\ SiO_2 + 2}$ mg/m^3
Quartz (Total Dust)		$\frac{30}{\%\ SiO_2 + 2}$ mg/m^3

ACGIH TLV: Crystalline Quartz
TLV - TWA = 0.1 mg/m^3 (respirable dust).

NIOSH has recommended that the permissible exposure limit be changed to 50 micrograms respirable free silica per cubic meter of air averaged over a work shift of up to 10 hours per day, 40 hours per week.

Irritancy of Product

Individuals with pulmonary and /or respiratory disease, including, but not limited to, asthma and bronchitis, or subject to eye irritation, should be precluded from exposure.

Sensitization to Product	N/A		
Carcinogenicity	NTP No	IARC Monographs Level 2A Grouping	OSHA Regulated No
Teratogenicity	None	Reproductive Toxicity	None
Mutagenicity	None	Synergistic Products	None

Product Identifier	TARGET FILTER SAND AND GRAVEL

SECTION 7 - PREVENTIVE MEASURES

Personal Protective Equipment	
	Use conventional NIOSH approved or equivalent respiratory protection equipment based on considerations of airborne concentration and duration of exposure. For sandblasting use appropriate protective equipment and filtered air supply.
Gloves	Abrasion resistant gloves are essential for sandblasting, and desirable for other industrial situations.
Eye	Use appropriate eye protection to minimize contact with dust. Full protective hood is recommended for sandblasting.
Other	Wear appropriate clothing and footwear for the specific application.
Engineering Controls	
	For blast cleaning operations, use adequate ventilation and dust collection. Do not permit dust to accumulate in work area.
Leak and Spill Procedure	
	If uncontaminated, collect for reuse or disposal. Use dustless procedures. If contaminated, use appropriate method and container for contaminant.
Waste Disposal	
	If uncontaminated, dispose as an inert, non-metallic mineral. If contaminated, use appropriate method for contaminant in accordance with applicable regulation(s).
Handling Procedures and Equipment	
	Avoid creation of respirable dust if possible. Use adequate ventilation and dust collection.
Storage Requirements	
	Store in a dry place.
Special Shipping Information	
	N/A

SECTION 8 - FIRST AID MEASURES

Eyes	Flush with running water. Obtain medical attention if irritation persists.
Gross Inhalation	Remove to fresh air. Give oxygen with artificial respiration as needed. Obtain medical attention for treatment, observation and support as needed.

SECTION 9 - PREPARATION DATE OF MSDS

Prepared By	Target Products Ltd., Quality Control Department
Phone Number	(604) 420-3620
Date	June 16, 2000

The information in this Material Safety Data Sheet relates only to the specific material designated herein and does not relate to use in combination with any other material or in any process. The information given is based on technical data that we believe to be reliable at the time of issue of the MSDS. Because conditions of use are outside our control, it is the responsibility of the user to verify safety data for combinations with other materials, or for use in specific processes, and to verify waste disposal requirements.

MATERIAL SAFETY DATA SHEET

SECTION 1 - PRODUCT IDENTIFICATION AND USE

Product Identifier	**TARGET FILTER SAND**
Product Use	Filter medium, inorganic filler
Manufacturer	Supplier Target Products Ltd. 9503-87 Avenue Morinville, Alberta
Emergency Telephone Number	Emergency Telephone Number (613) 996-6666 (Canutec)

SECTION 2 - HAZARDOUS INGREDIENTS

Ingredient	%	CAS Number	LD_{50}	LC_{50}
Crystalline silica	93	14808-60-7	N/A	N/A

SECTION 3 - PHYSICAL DATA

Physical State	Solid		
Odour/Appearance	White to yellow crystals, no odour		
Vapour Pressure	N/A	Vapour Density	N/A
Evaporation Rate	N/A	Boiling Point	2230 °C
Freezing Point	1610 °C	pH	6-7
Specific Gravity	2.65	Coeff. Water/Oil Dist.	N/A

SECTION 4 - FIRE AND EXPLOSION DATA

Flammability	Not flammable	Means of Extinction	N/A
Flashpoint	N/A	Upper/Lower Flam. Limit	N/A
Autoignition Temp.	N/A	Hazardous Combustion Products	None

Explosion Data	
Sensitivity to Impact	None
Sensitivity to Static Discharge	None

SECTION 5 - REACTIVITY DATA

Chemical Stability	Stable
Incompatibility with Other Substances	None

Reactivity, and under what conditions

Silica will dissolve in hydrofluoric acid to give silicon tetrafluoride, a corrosive gas.

NOTE: N/A = Not Applicable

Product Identifier	TARGET FILTER SAND

SECTION 6 - TOXICOLOGICAL PROPERTIES

Route of Entry					
Skin Contact	No	Skin Absorption	No	Eye Contact	No
Inhalation	Yes	Ingestion	No		

Effects of Acute Exposure to Product

No potential acute toxic hazards known.

Effects of Chronic Exposure to Product

Excessive inhalation of crystalline silica dust may result in respiratory disease, including silicosis, pneumoconiosis and pulmonary fibrosis. The International Agency for Research on Cancer (IARC) has evaluated in Volume 42, Monographs on the Evaluation of the Carcinogenicity Risk of Chemicals to Humans; Silica and Some Silicates (1987), that there is "sufficient evidence for the carcinogenicity of crystalline silica to experimental animals" and "limited evidence with respect to humans."

Exposure Limits

OSHA PEL: Exposure to airborne crystalline silica shall not exceed an 8-hour time-weighted average limit as stated in 29 CFR 19100.1000 Table Z3 for Mineral Dusts, specifically "Silica: Crystalline: Quartz (respirable)".

Crystalline Quartz (Respirable)	$\frac{250}{\%\ SiO_2 + 5}$ Mppcf	$\frac{10}{\%\ SiO_2 + 2}$ mg/m^3
Quartz (Total Dust)		$\frac{30}{\%\ SiO_2 + 2}$ mg/m^3

ACGIH TLV: Crystalline Quartz
TLV - TWA = 0.1 mg/m^3 (respirable dust).

NIOSH has recommended that the permissible exposure limit be changed to 50 micrograms respirable free silica per cubic meter of air averaged over a work shift of up to 10 hours per day, 40 hours per week.

Irritancy of Product

Individuals with pulmonary and /or respiratory disease, including, but not limited to, asthma and bronchitis, or subject to eye irritation, should be precluded from exposure.

Sensitization to Product	N/A		
Carcinogenicity	NTP	IARC Monographs	OSHA Regulated
See "Chronic Exposure"	No	Level 2A Grouping	No
Teratogenicity	None	Reproductive Toxicity	None
Mutagenicity	None	Synergistic Products	None

SECTION 7 - PREVENTIVE MEASURES

Personal Protective Equipment

Use conventional NIOSH approved or equivalent respiratory protection equipment based on considerations of airborne concentration and duration of exposure.
For sandblasting use appropriate protective equipment and filtered air supply.

Gloves — Abrasion resistant gloves are essential for sandblasting, and desirable for other industrial situations.

Eye — Use appropriate eye protection to minimize contact with dust. Full protective hood is recommended for sandblasting.

Other — Wear appropriate clothing and footwear for the specific application.
Clean clothing that has become dusty.

Product Identifier	TARGET FILTER SAND

Section 7, continued

Engineering Controls
Use adequate ventilation and dust collection. Do not permit dust to accumulate in work area.

Leak and Spill Procedure
If uncontaminated, collect for reuse or disposal. Use dustless procedures. If contaminated, use appropriate method and container for contaminant.

Waste Disposal
If uncontaminated, dispose as an inert, non-metallic mineral.
If contaminated, use appropriate method for contaminant in accordance with applicable regulation(s).

Handling Procedures and Equipment
Avoid creation of respirable dust if possible. Use adequate ventilation and dust collection.

Storage Requirements
Store in a dry place.

Special Shipping Information
N/A

SECTION 8 - FIRST AID MEASURES

Eyes	Flush with running water. Obtain medical attention if irritation persists.
Gross Inhalation	Remove to fresh air. Give oxygen with artificial respiration as needed. Obtain medical attention for treatment, observation and support as needed.

SECTION 9 - PREPARATION DATE OF MSDS

Prepared By	Target Products Ltd., Quality Control Department
Phone Number	(604) 420-3620
Date	June 16, 2000

The information in this Material Safety Data Sheet relates only to the specific material designated herein and does not relate to use in combination with any other material or in any process. The information given is based on technical data that we believe to be reliable at the time of issue of the MSDS. Because conditions of use are outside our control, it is the responsibility of the user to verify safety data for combinations with other materials, or for use in specific processes, and to verify waste disposal requirements.

Appendix E

Size Distribution Information For Sand Mixes

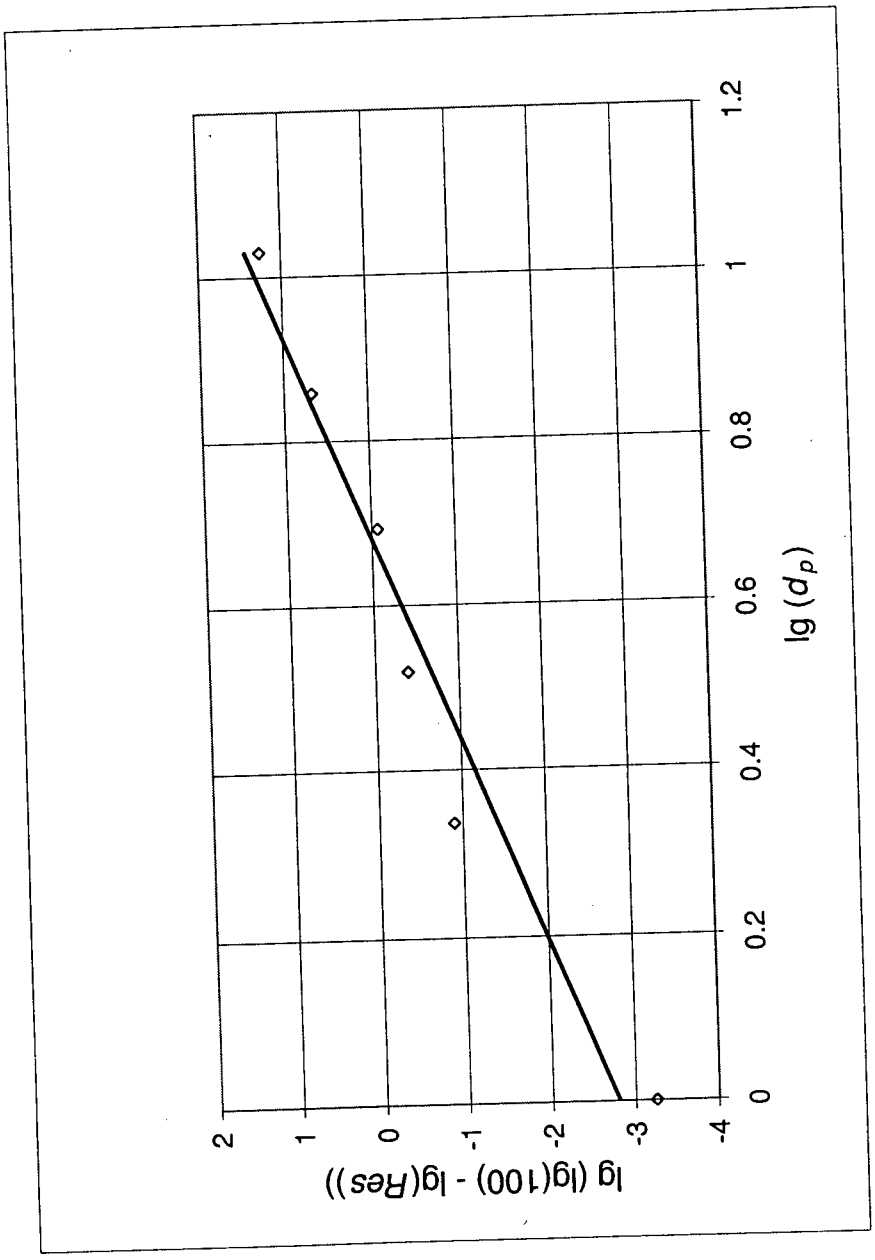

Figure E.1: Rosin-Rammler Distribution for Mix 1, Test 1 ($n_{RR} = 4.1$, $C = 0.95$)

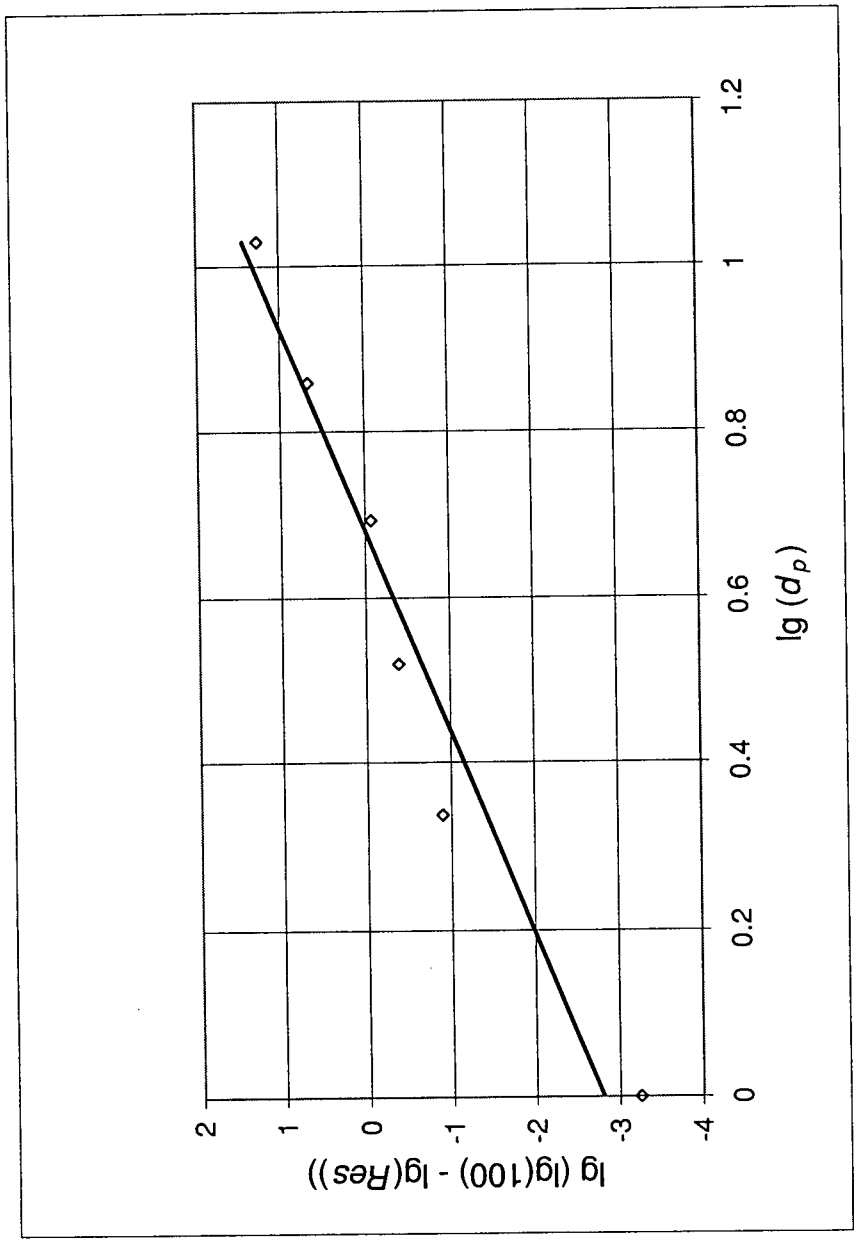

Figure E.2: Rosin-Rammler Distribution for Mix 1, Test 2 ($n_{RR} = 5.8$, $C = 0.95$)

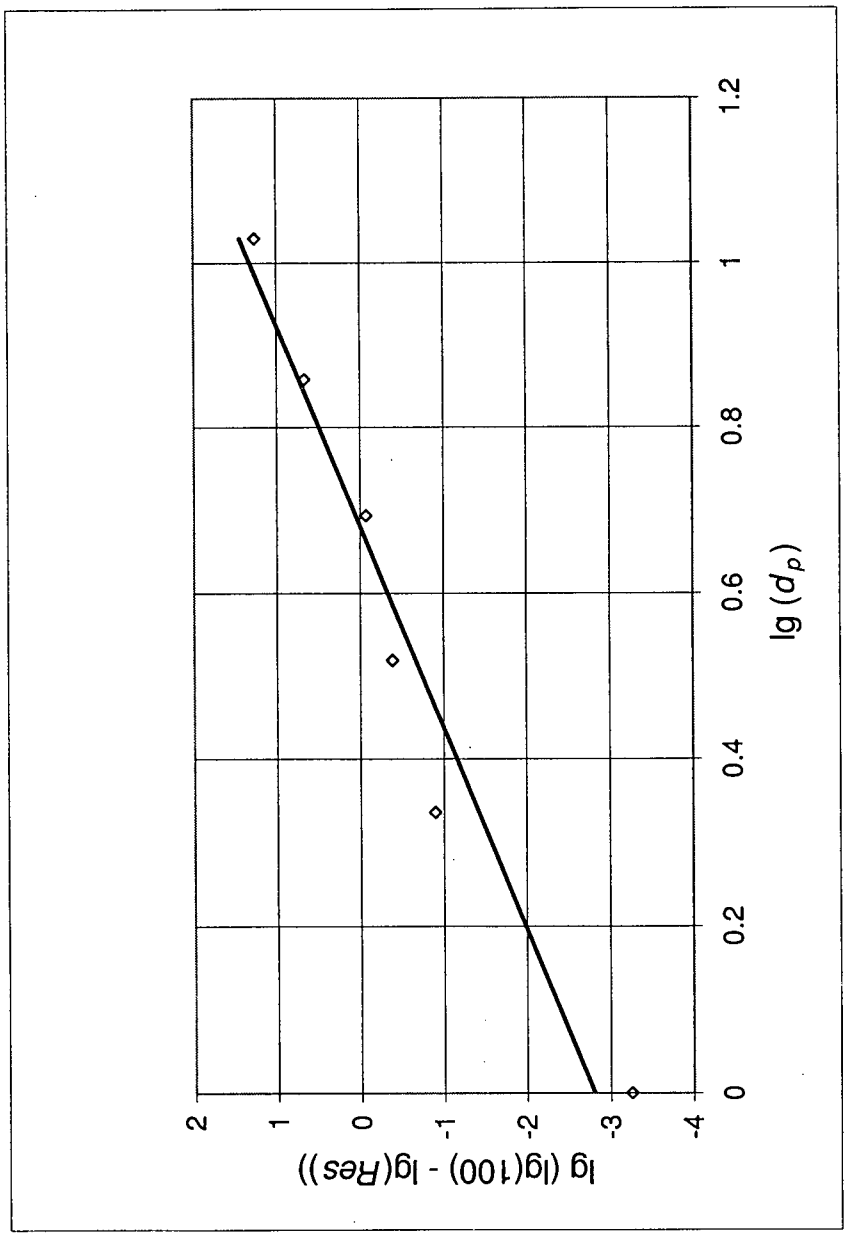

Figure E.3: Rosin-Rammler Distribution for Mix 2, Test 1 ($n_{RR} = 8.1$, $C = 1.00$)

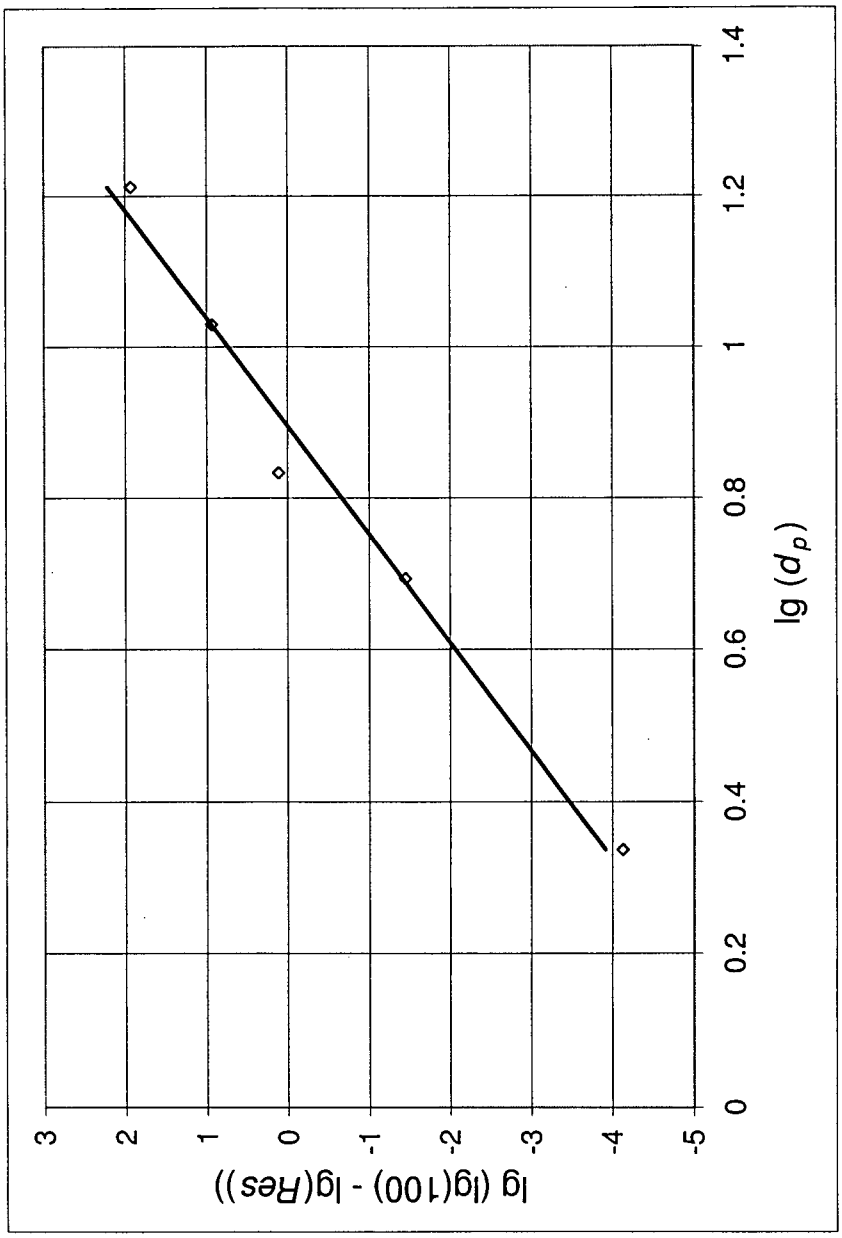

Figure E.4: Rosin-Rammler Distribution for Mix 2, Test 2 ($n_{RR} = 7.0$, $C = 0.98$)

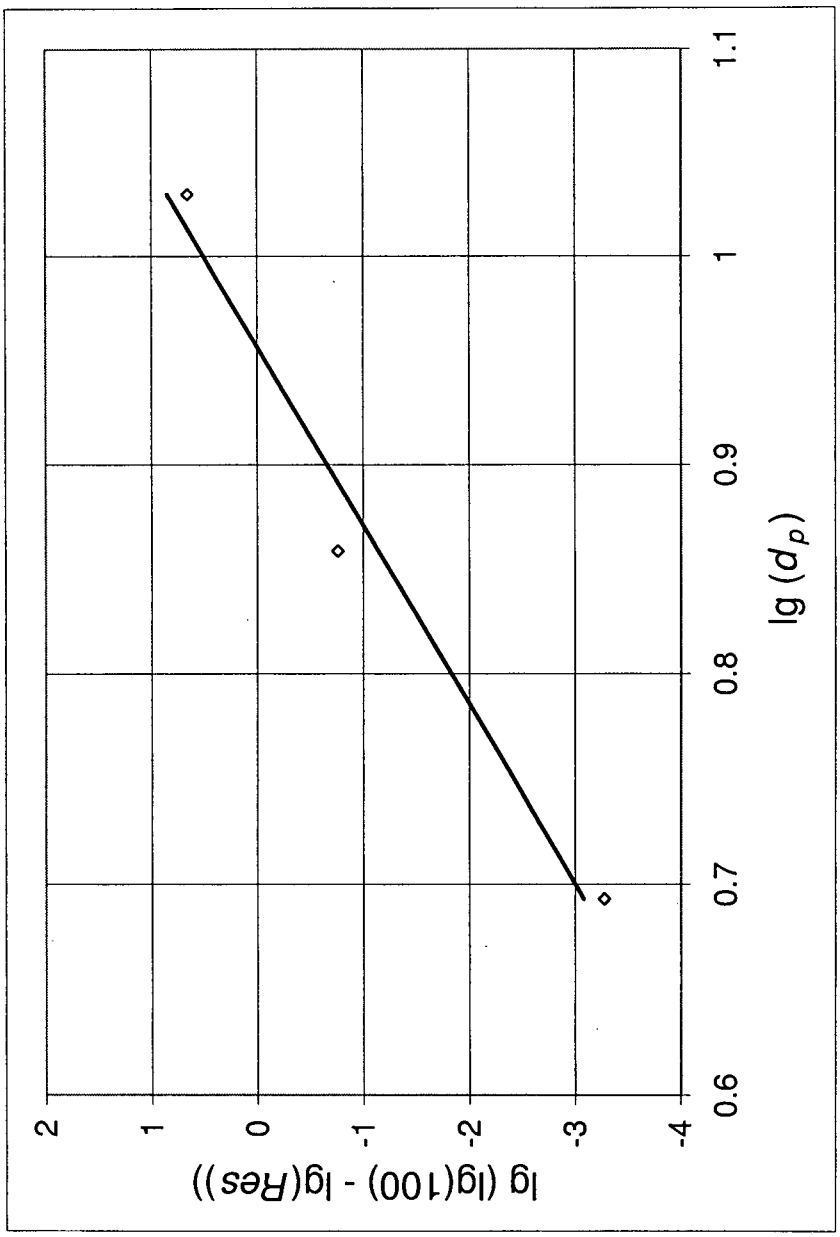

Figure E.5: Rosin-Rammler Distribution for Mix 3 ($n_{RR} = 11.7$, $C = 0.97$)

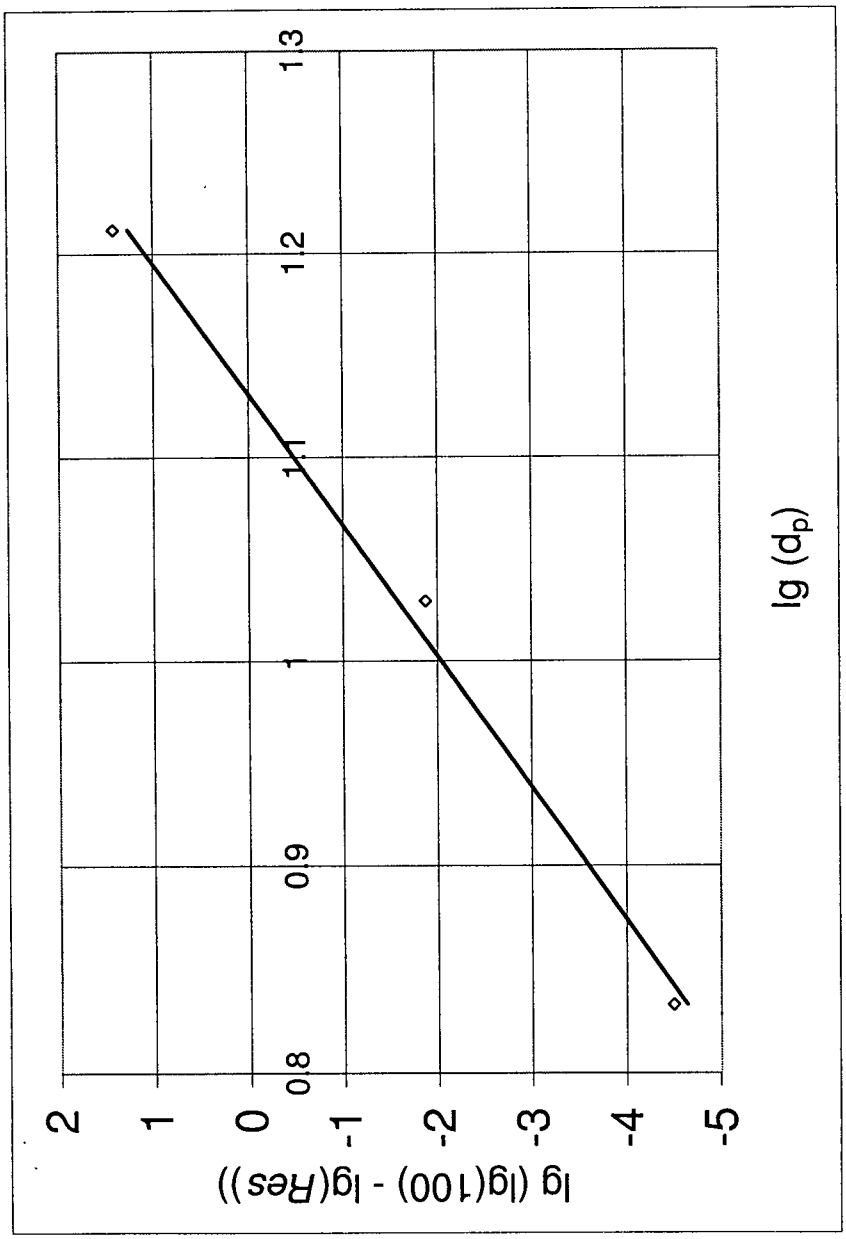

Figure E.6: Rosin-Rammler Distribution for Mix 4 ($n_{RR} = 15.6$, $C = 0.99$)

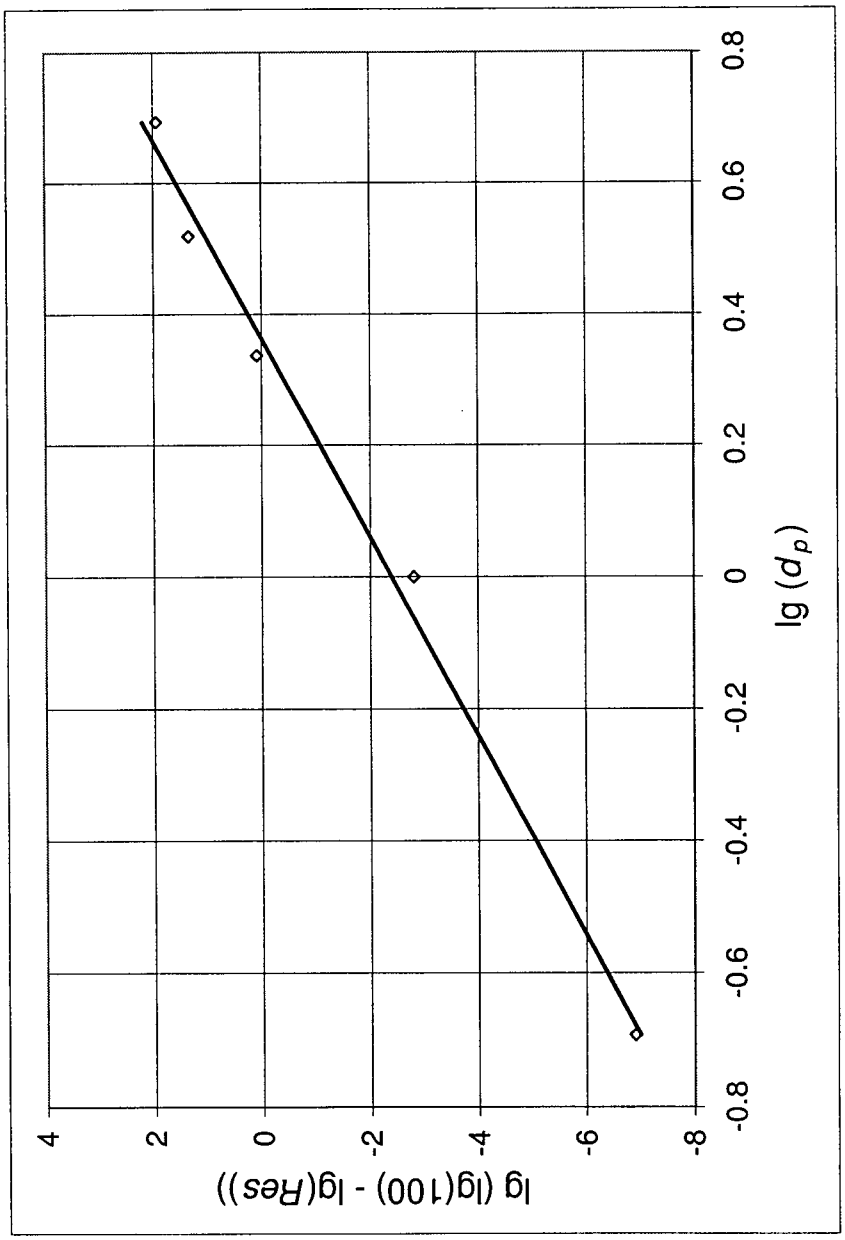

Figure E.7: Rosin-Rammler Distribution for Mix 5, Test 1 ($n_{RR} = 6.6$, $C = 0.99$)

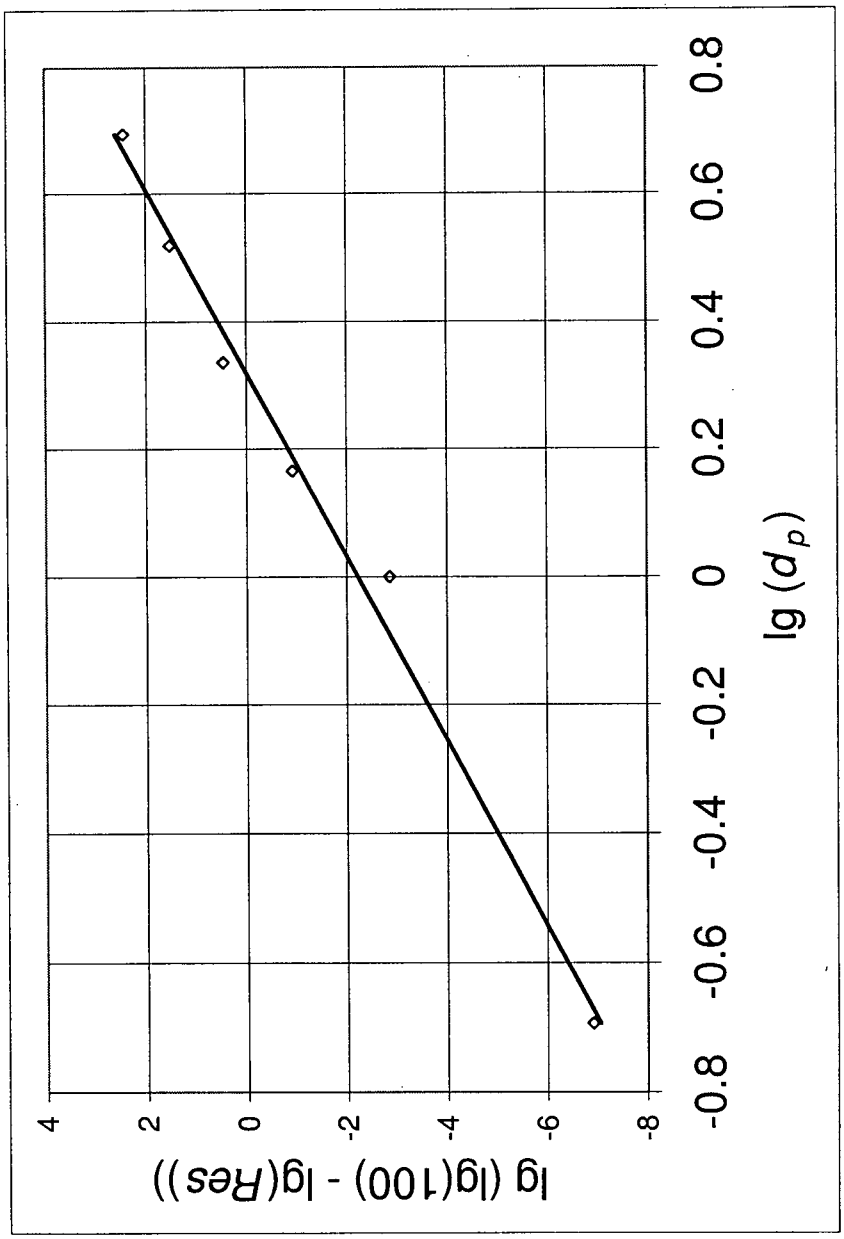

Figure E.8: Rosin-Rammler Distribution for Mix 5, Test 2 ($n_{RR} = 7.0$, $C = 0.99$)

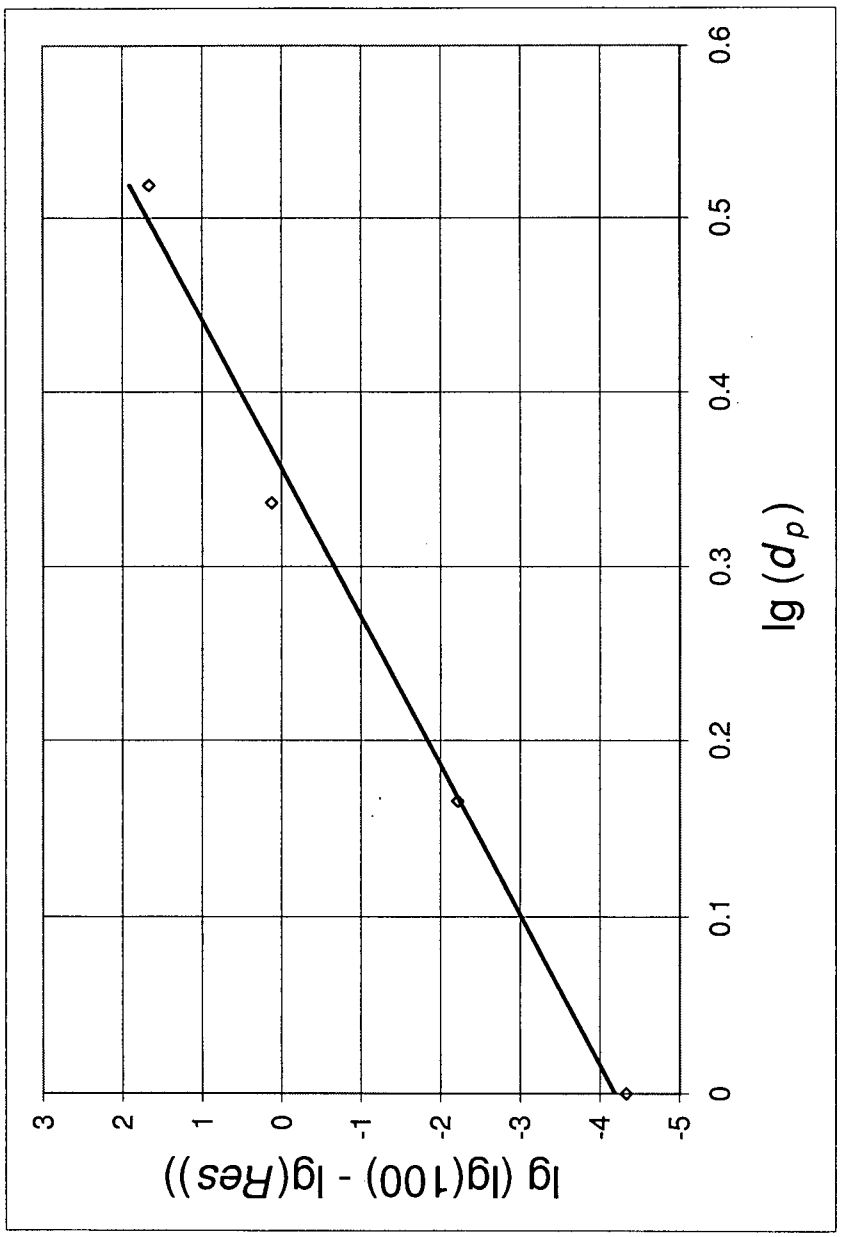

Figure E.9: Rosin-Rammler Distribution for Mix 6 ($n_{RR} = 11.8$, $C = 0.99$)

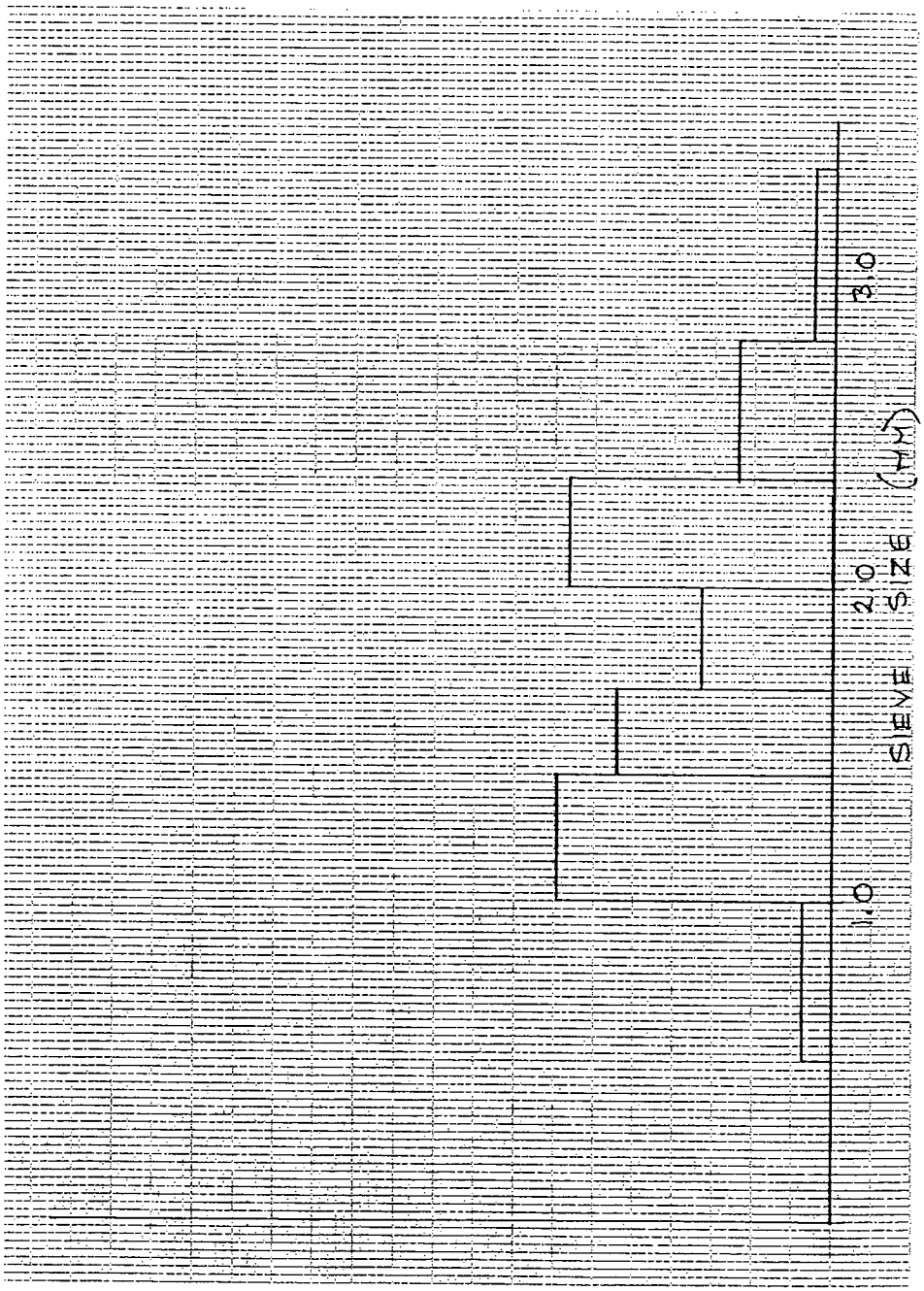

Figure E.10: Size Distribution for Mix 1, Test 1 ($d_p = 1.4$, $\sigma_p^* = 0.33$)

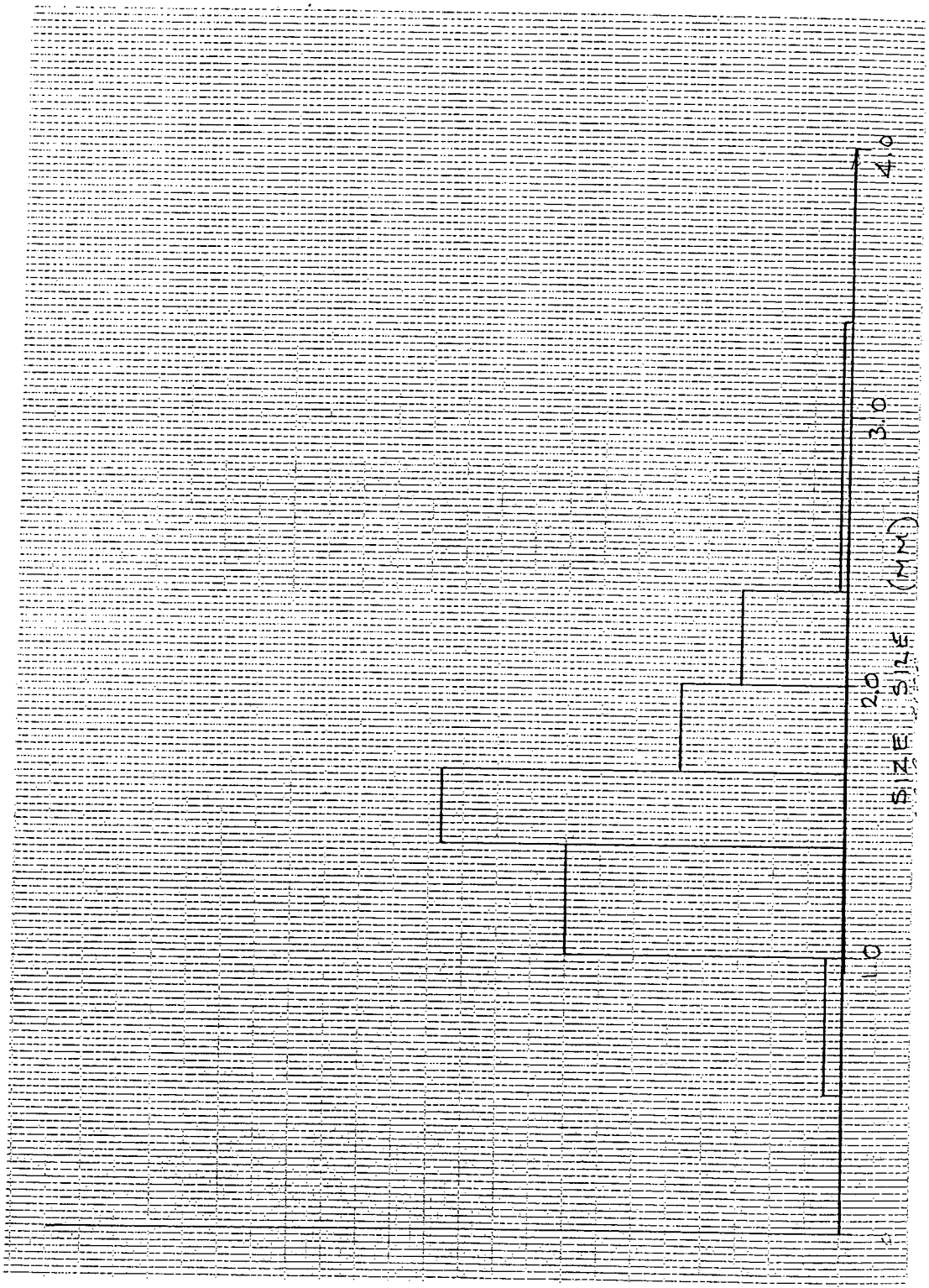

Figure E.11: Size Distribution for Mix 1, Test 2 ($d_p = 1.4$, $\sigma_p^* = 0.25$)

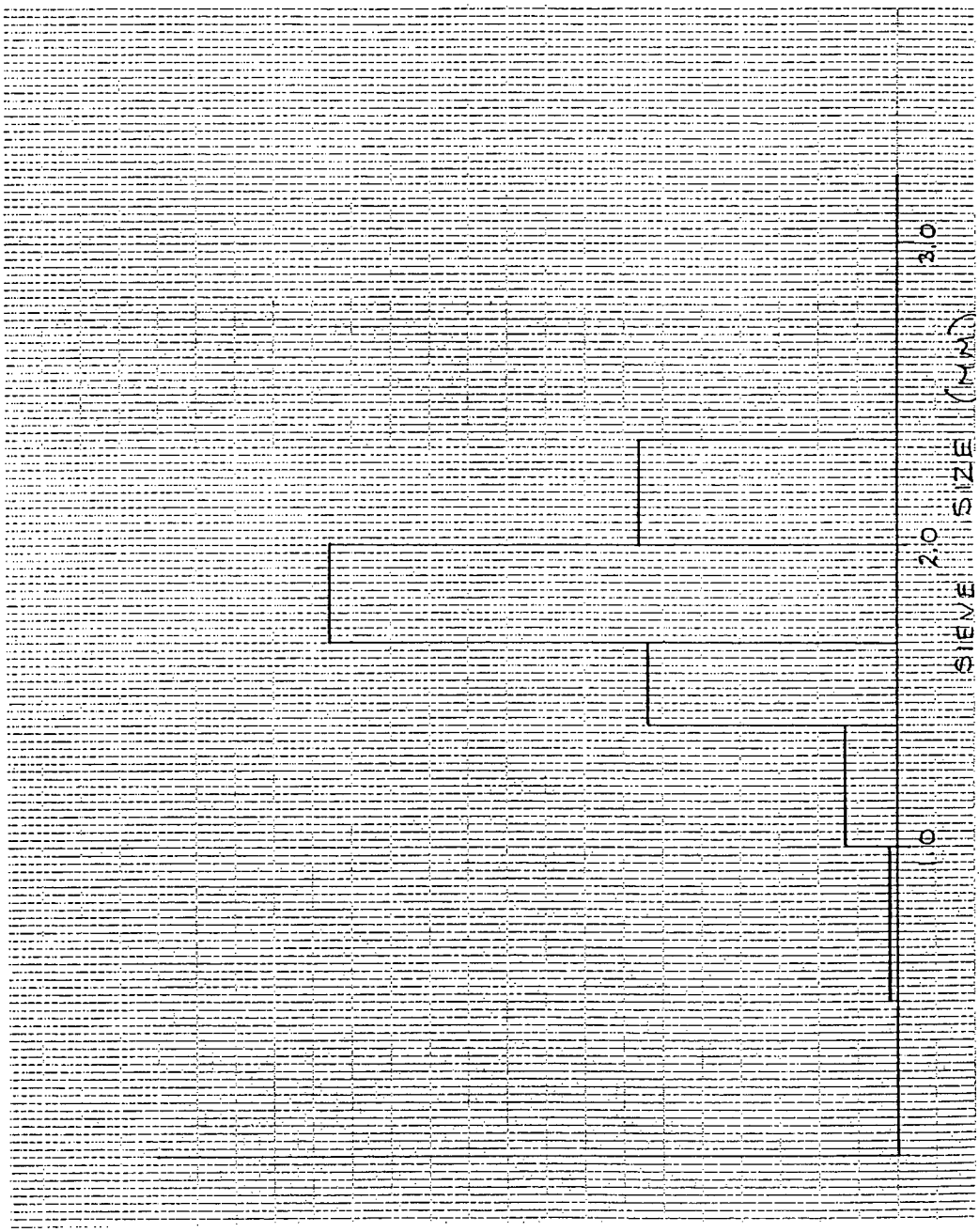

Figure E.12: Size Distribution for Mix 2, Test 1 ($d_p = 1.7$, $\sigma_p^* = 0.22$)

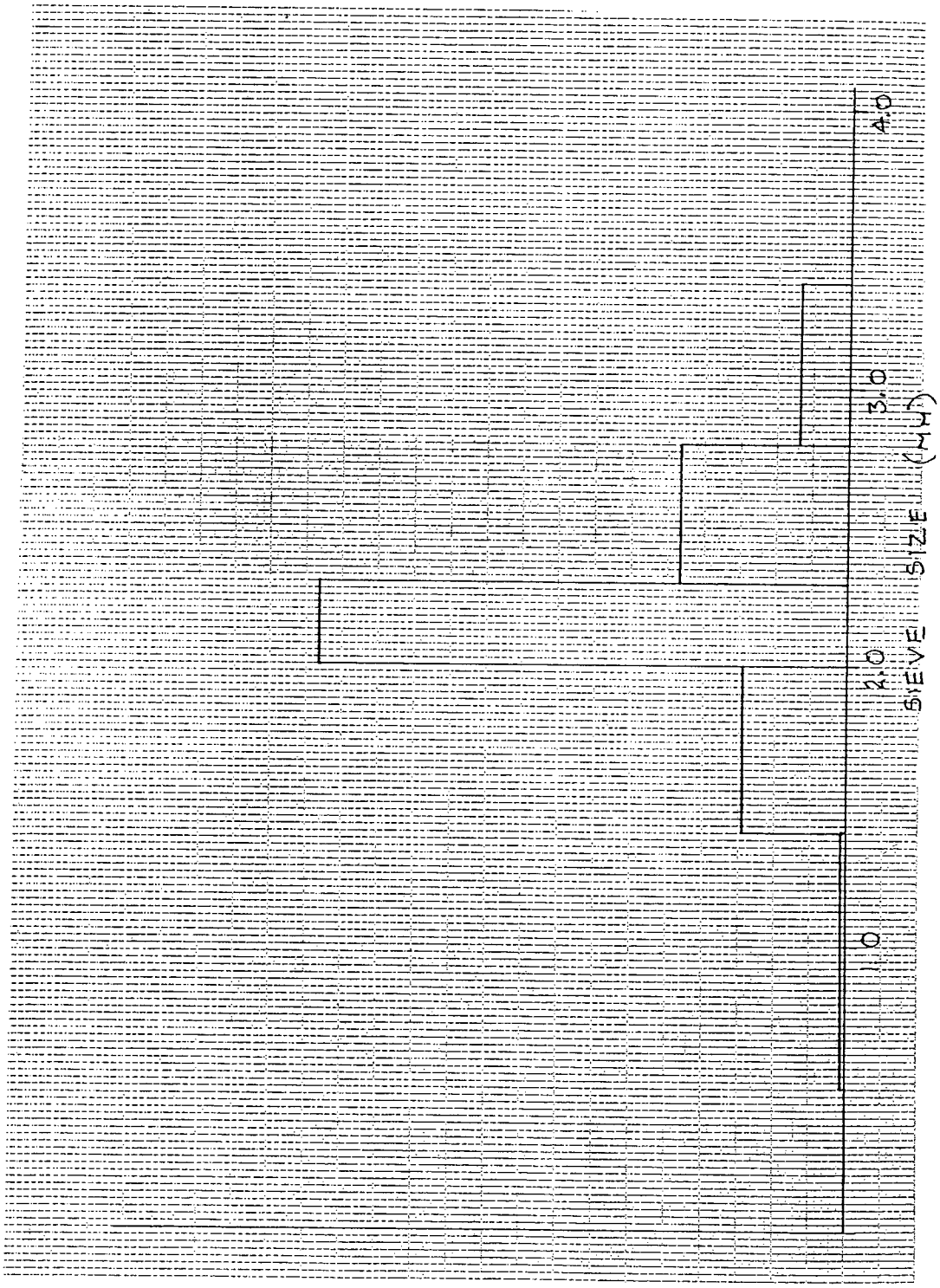

Figure E.13: Size Distribution for Mix 2, Test 2 ($d_p = 2.0$, $\sigma_p^* = 0.26$)

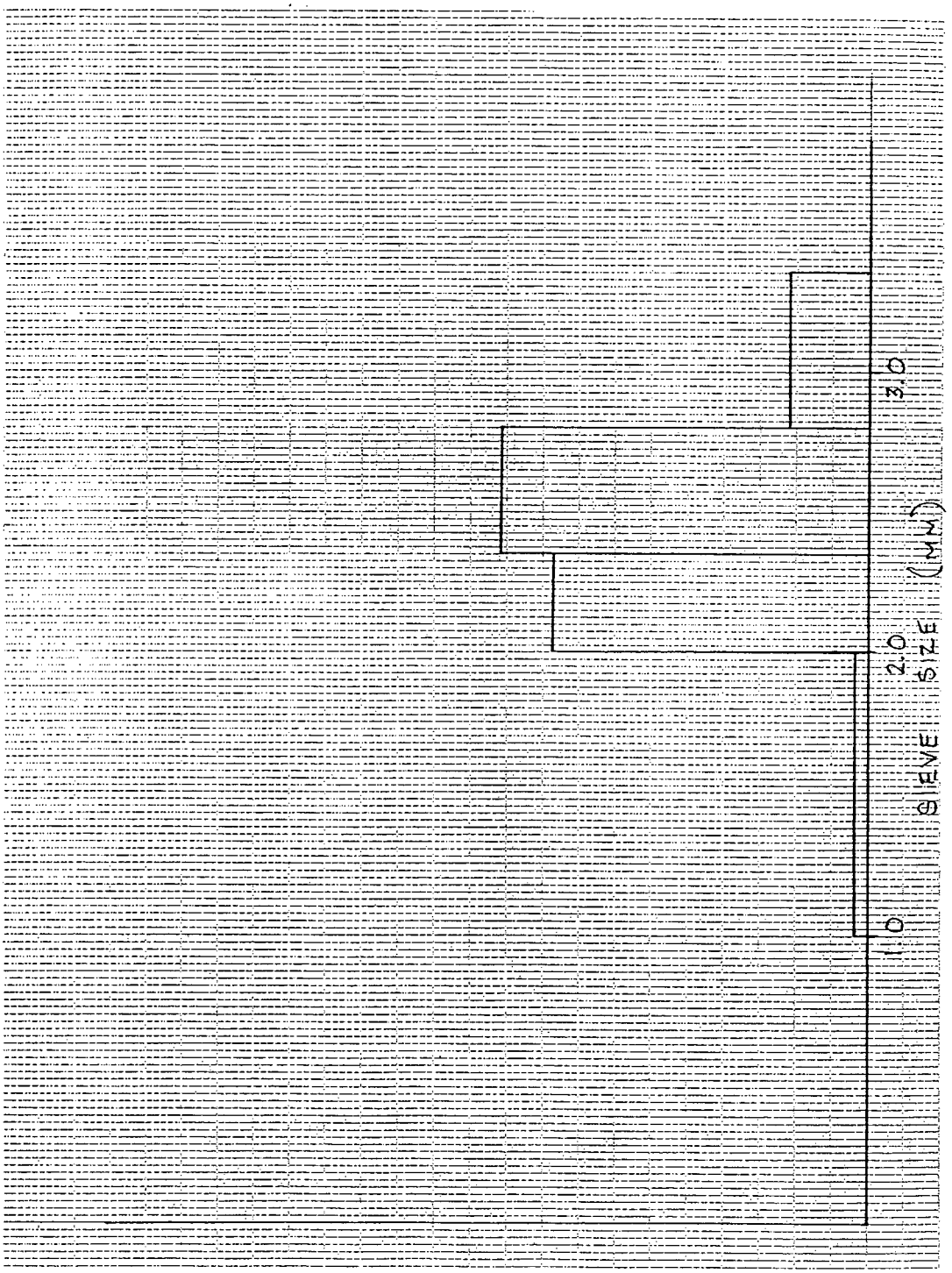

Figure E.14: Size Distribution for Mix 3 ($d_p = 2.4$, $\sigma_p^* = 0.17$)

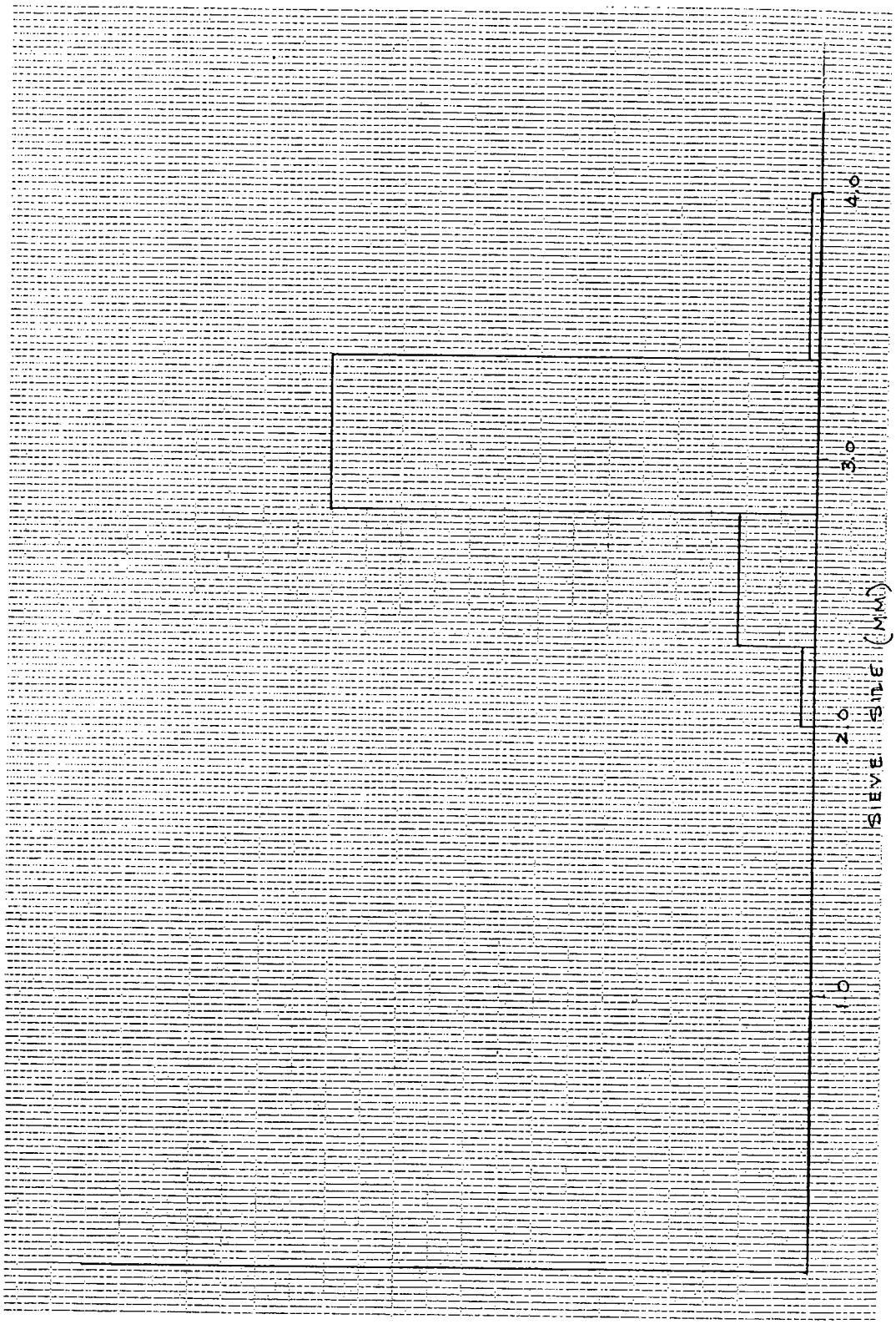

Figure E.15: Size Distribution for Mix 4 ($d_p = 3.0$, $\sigma_p^* = 0.09$)

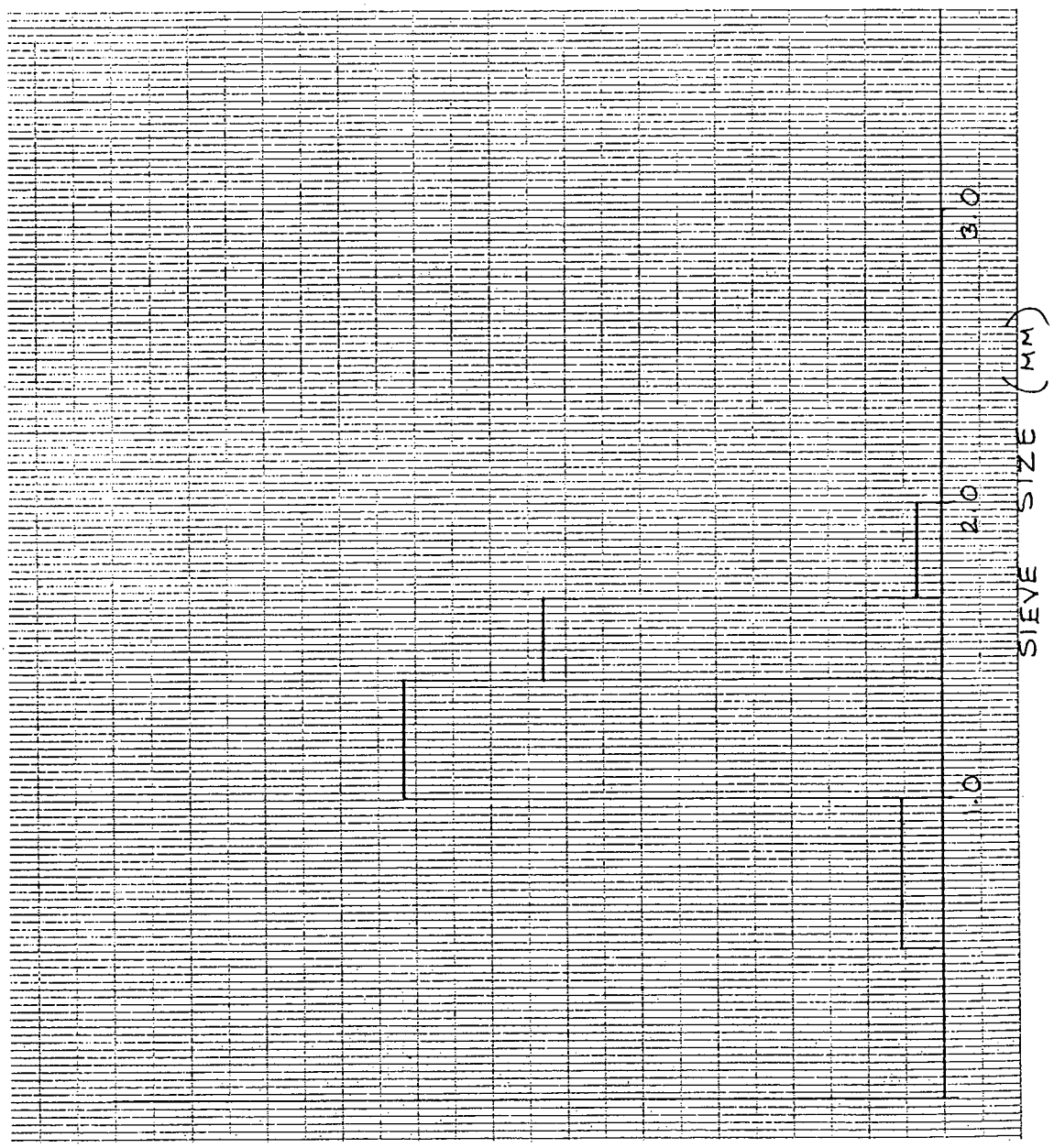

Figure E.16: Size Distribution for Mix 5, Test 1 ($d_p = 1.2$, $\sigma_p^* = 0.22$)

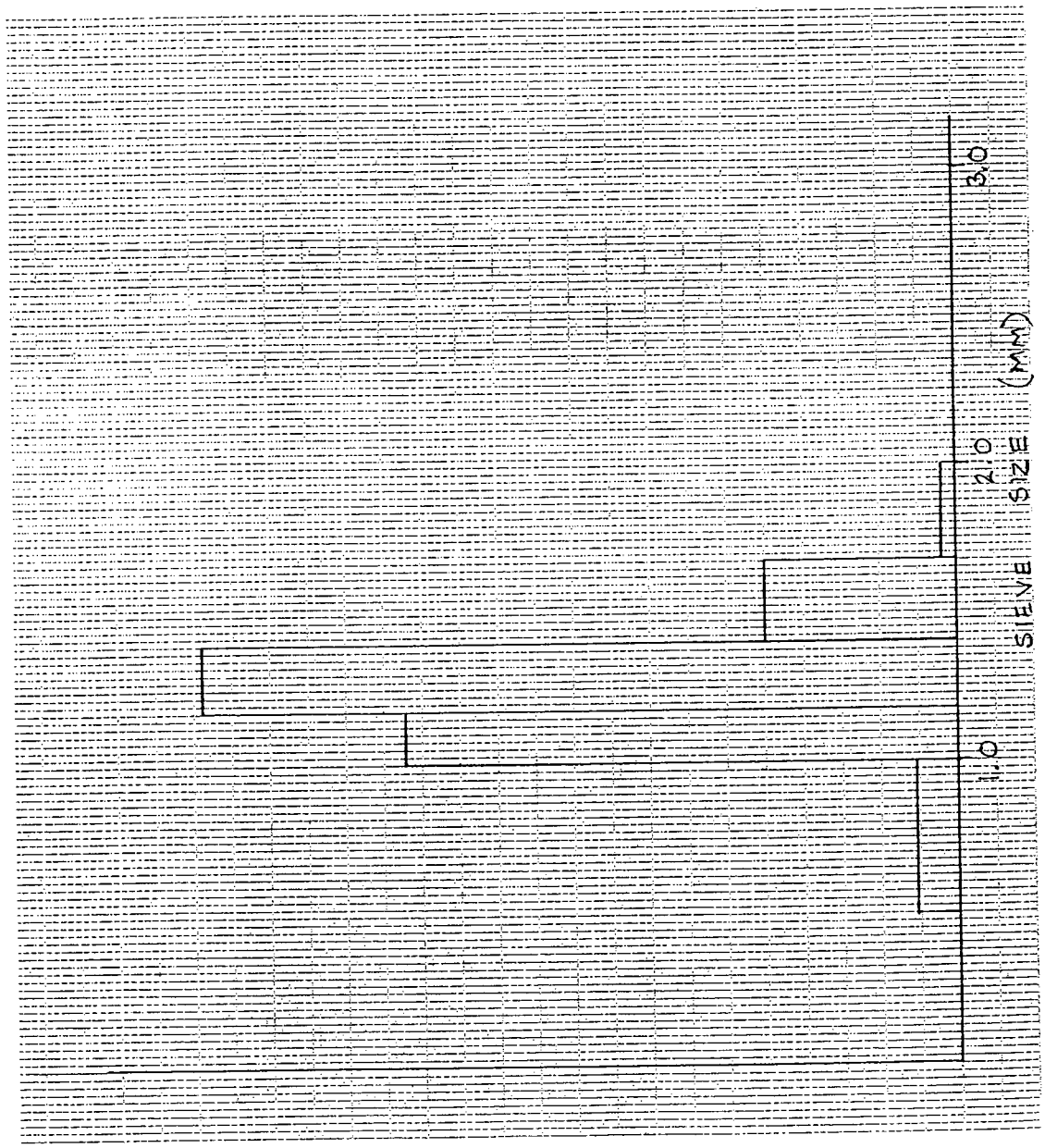

Figure E.17: Size Distribution for Mix 5, Test 2 ($d_p = 1.2$, $\sigma_p^* = 0.21$)

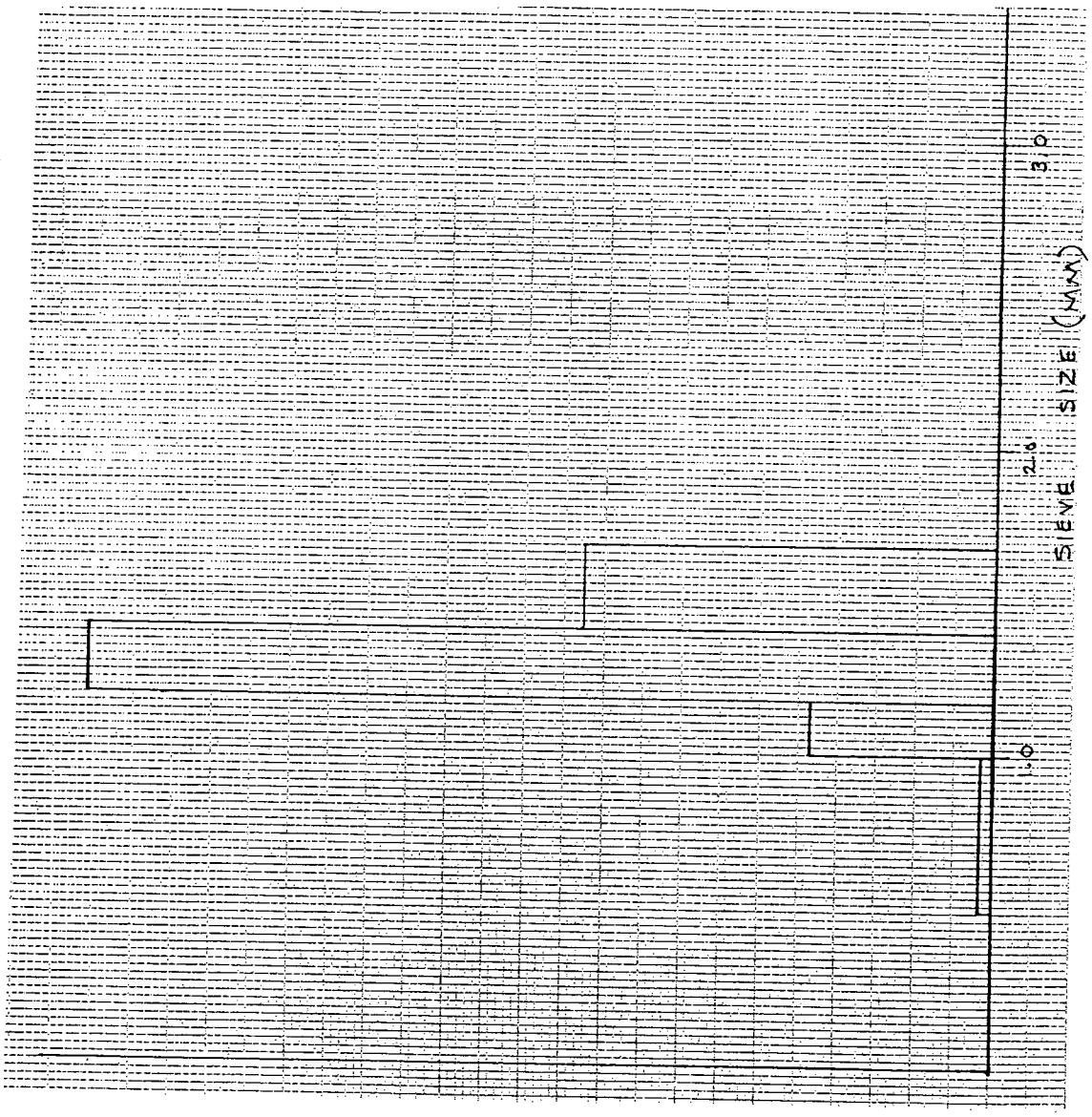

Figure E.18: Size Distribution for Mix 6 ($d_p = 1.3$, $\sigma_p^* = 0.15$)

Appendix F

Results:

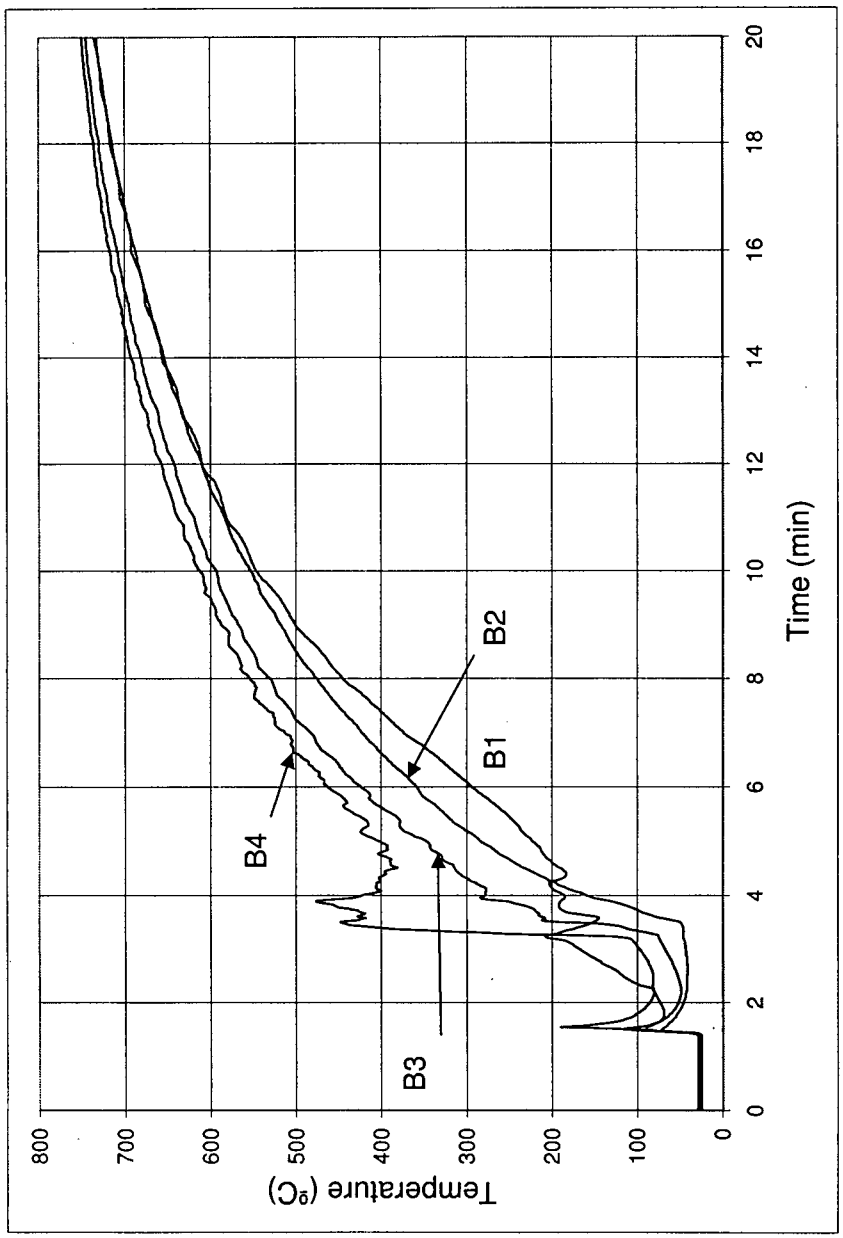

Figure F.1: Run 3 Bed Temperature History. Mix 2 at 1 rpm ($\bar{d}_p = 1.9$mm, $\sigma_p^* = 0.26$, $n_{RR} = 7.3$)

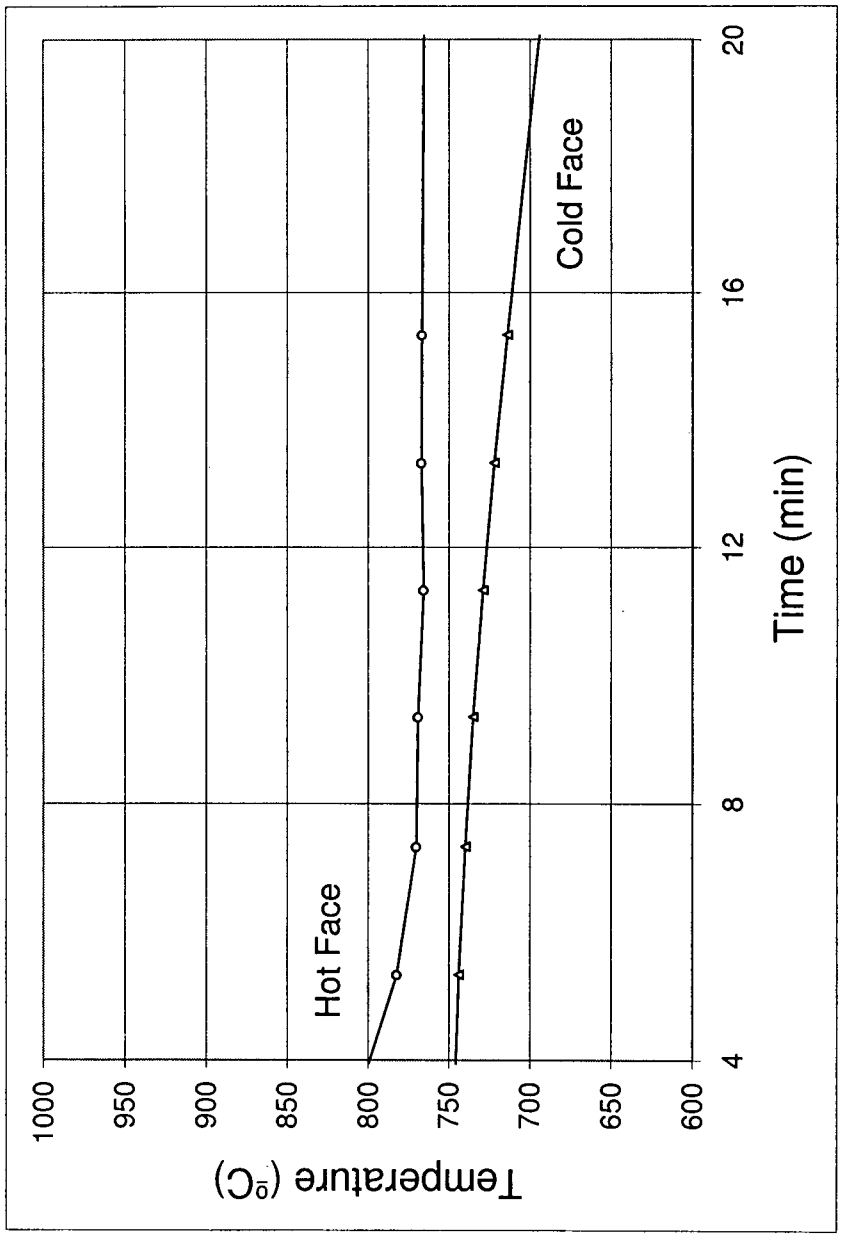

Figure F.2: Run 3 Wall Temperature History. Mix 2 at 1 rpm ($\bar{d_p} = 1.9$mm, $\sigma_p^* = 0.26$, $n_{RR} = 7.3$)

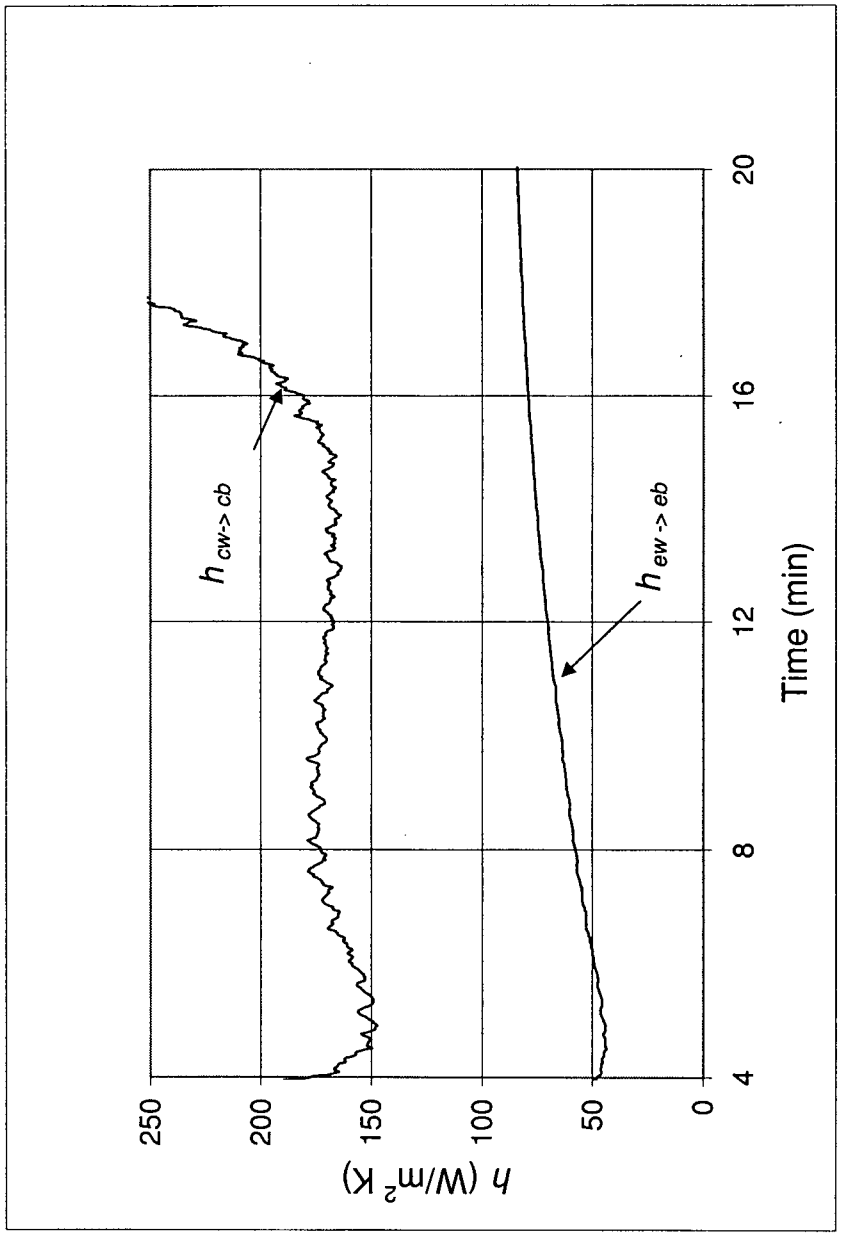

Figure F.3: Run 3 Exposed Wall to Exposed Bed, $h_{ew \to eb}$, and Covered Wall to Covered Bed, $h_{cw \to cb}$, Heat Transfer Coefficients. Mix 2 at 1 rpm ($\bar{d}_p = 1.9$mm, $\sigma_p^* = 0.26$, $n_{RR} = 7.3$)

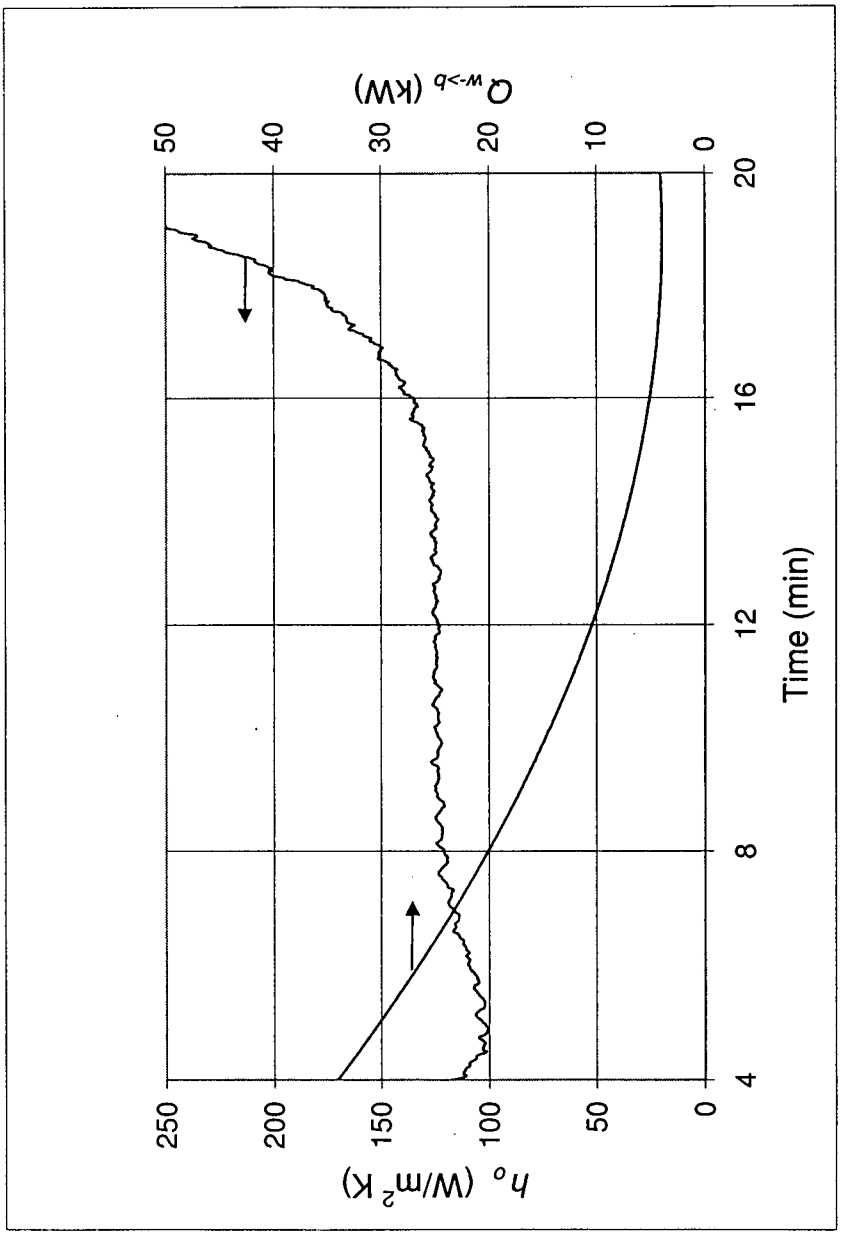

Figure F.4: Run 3 Overall Wall to Bed Heat Transfer Coefficient, h_o, and Heat Flow, $Q_{w\to b}$. Mix 2 at 1 rpm ($\bar{d}_p$ = 1.9mm, σ_p^* = 0.26, n_{RR} = 7.3)

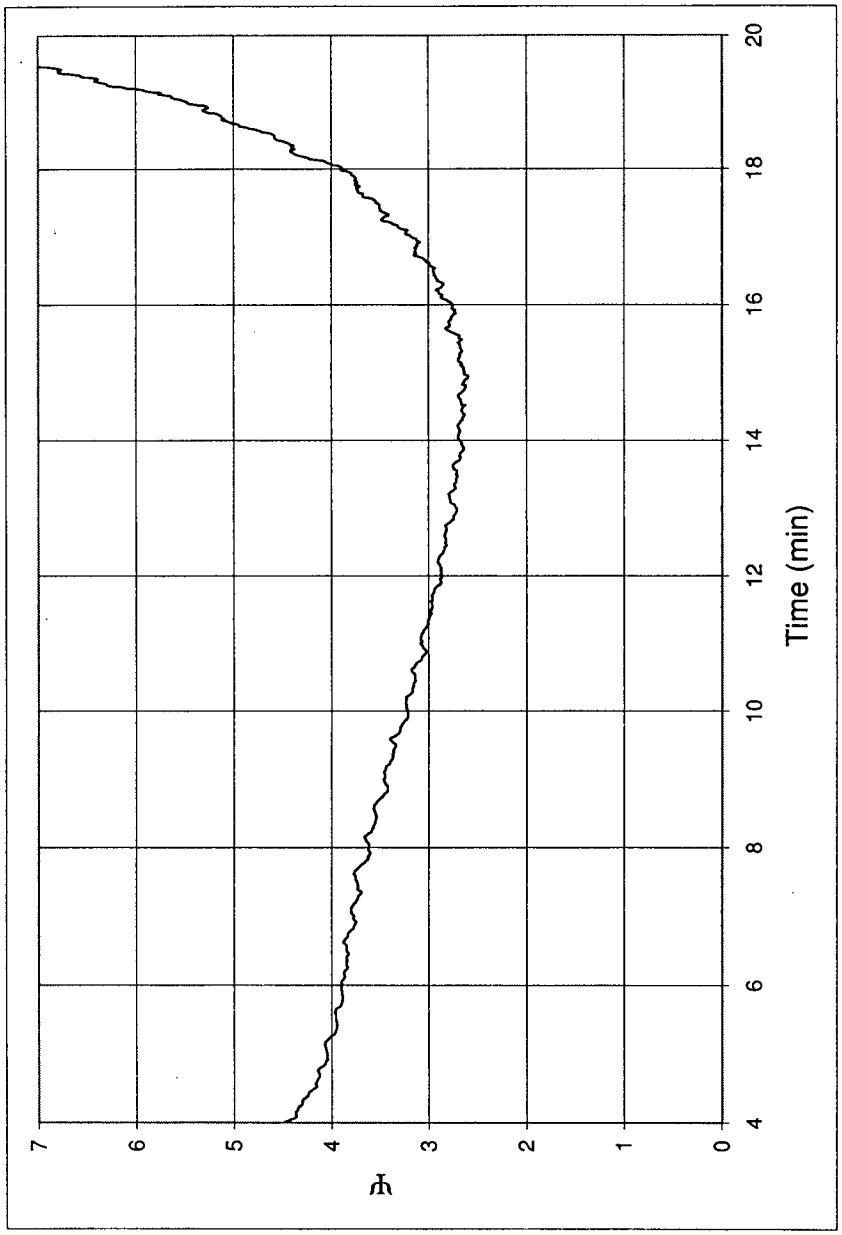

Figure F.5: Run 3 Ratio Between Heat Flow to Covered Wall and Exposed Wall, Ψ. Mix 2 at 1 rpm ($\bar{d}_p = 1.9$mm, $\sigma_p^* = 0.26$, $n_{RR} = 7.3$)

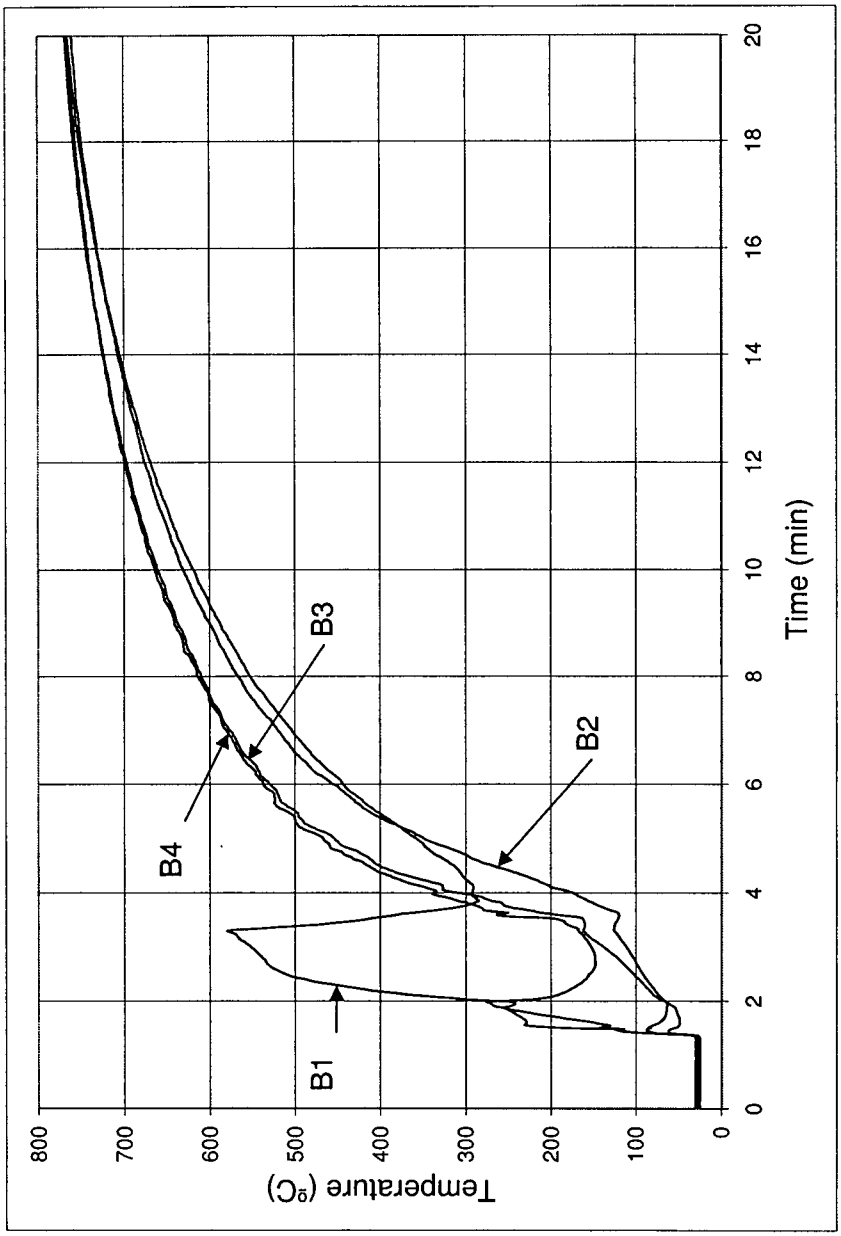

Figure F.6: Run 4 Bed Temperature History. Mix 1 at 1 rpm ($\bar{d}_p = 1.4$mm, $\sigma_p^* = 0.29$, $n_{RR} = 5.0$)

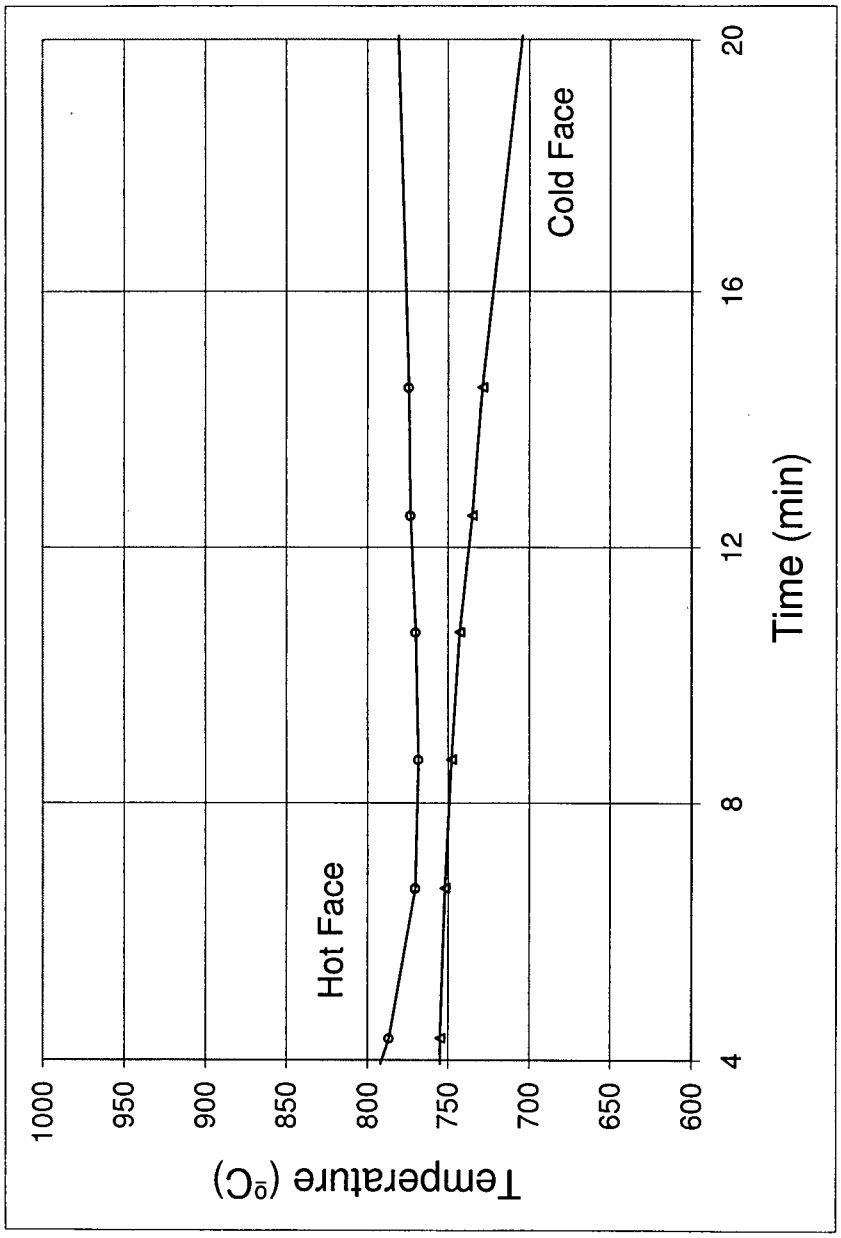

Figure F.7: Run 4 Wall Temperature History. Mix 1 at 1 rpm ($\bar{d}_p = 1.4$mm, $\sigma_p^* = 0.29$, $n_{RR} = 5.0$)

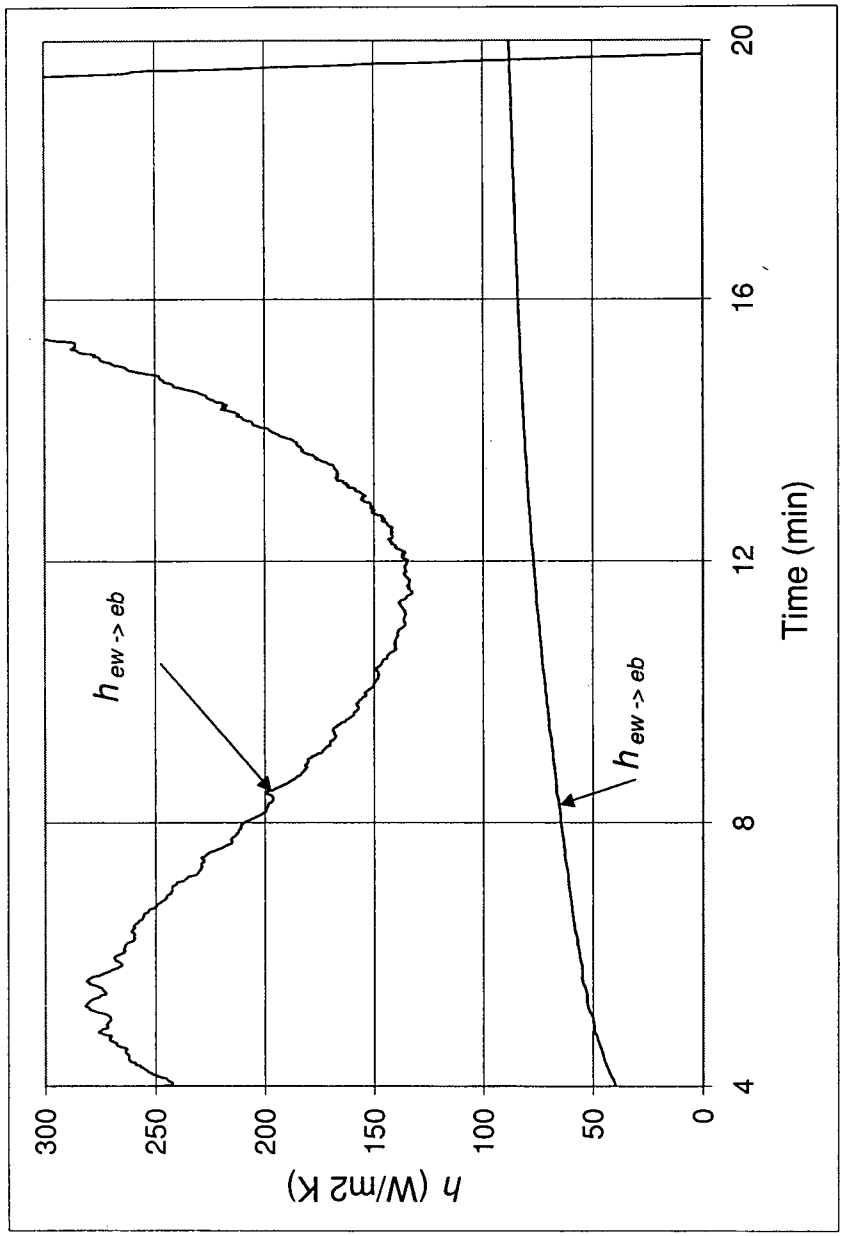

Figure F.8: Run 4 Exposed Wall to Exposed Bed, $h_{ew \to eb}$, and Covered Wall to Covered Bed, $h_{cw \to cb}$, Heat Transfer Coefficients. Mix 1 at 1 rpm ($\bar{d}_p = 1.4$mm, $\sigma_p^* = 0.29$, $n_{RR} = 5.0$)

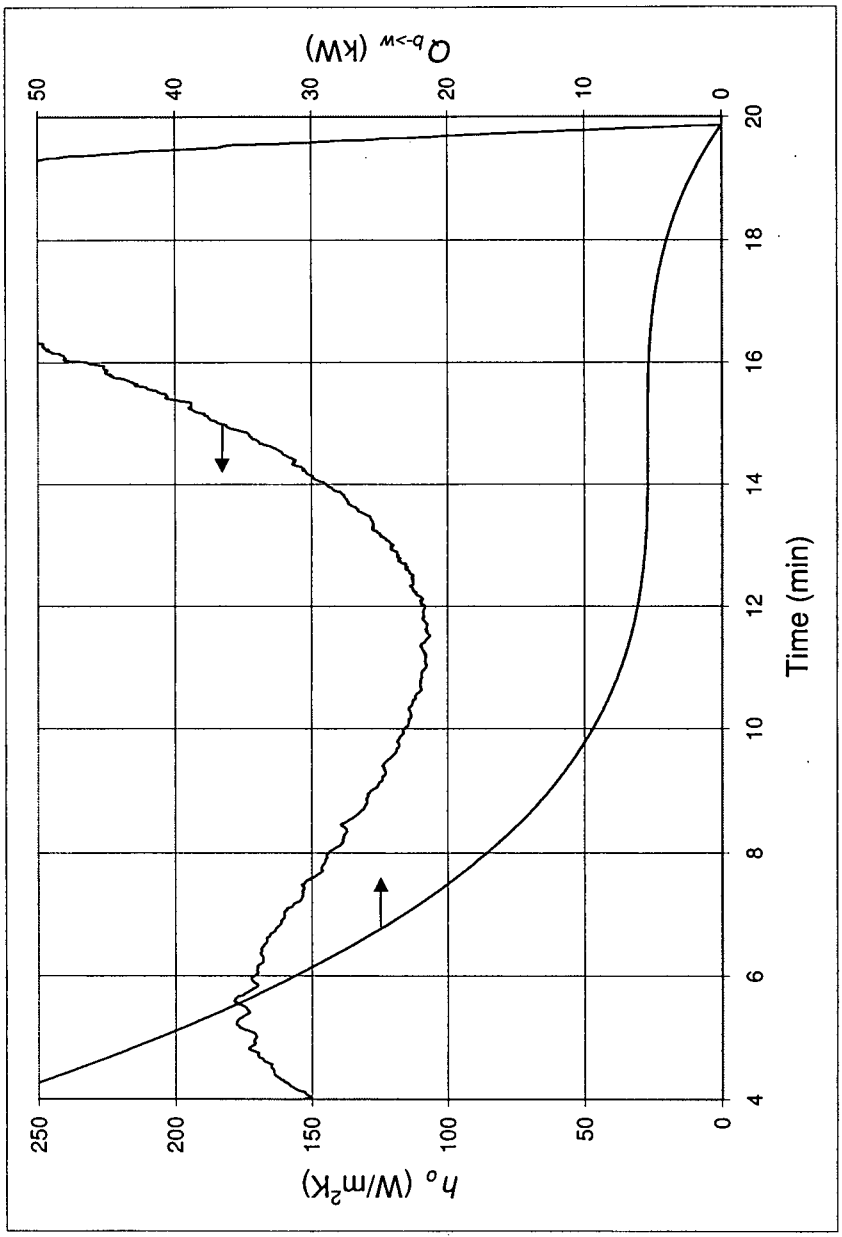

Figure F.9: Run 4 Overall Wall to Bed Heat Transfer Coefficient, h_o, and Heat Flow, $Q_{w \to b}$. Mix 1 at 1 rpm ($\bar{d}_p = 1.4$mm, $\sigma_p^* = 0.29$, $n_{RR} = 5.0$)

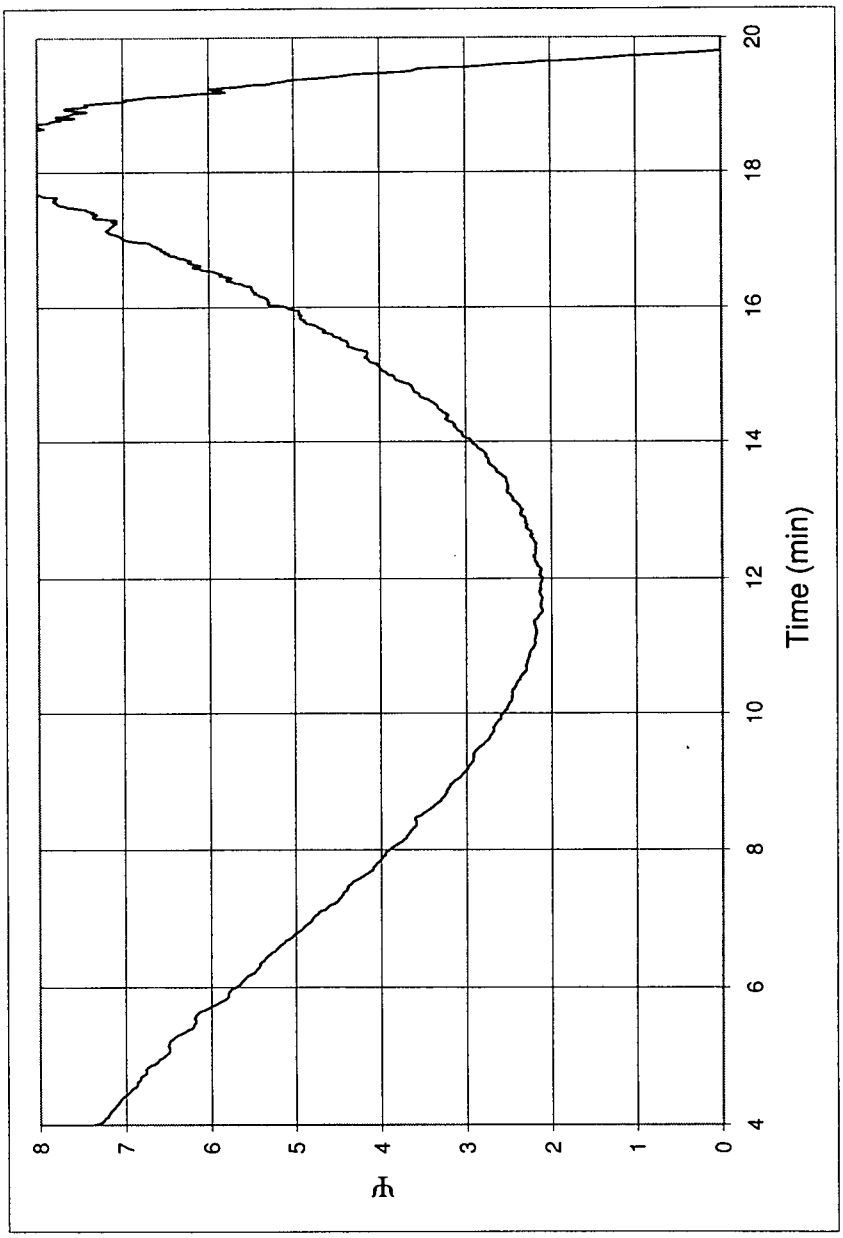

Figure F.10: Run 4 Ratio Between Heat Flow to Covered Wall and Exposed Wall, Ψ. Mix 1 at 1 rpm ($\bar{d}_p = 1.4$mm, $\sigma_p^* = 0.29$, $n_{RR} = 5.0$)

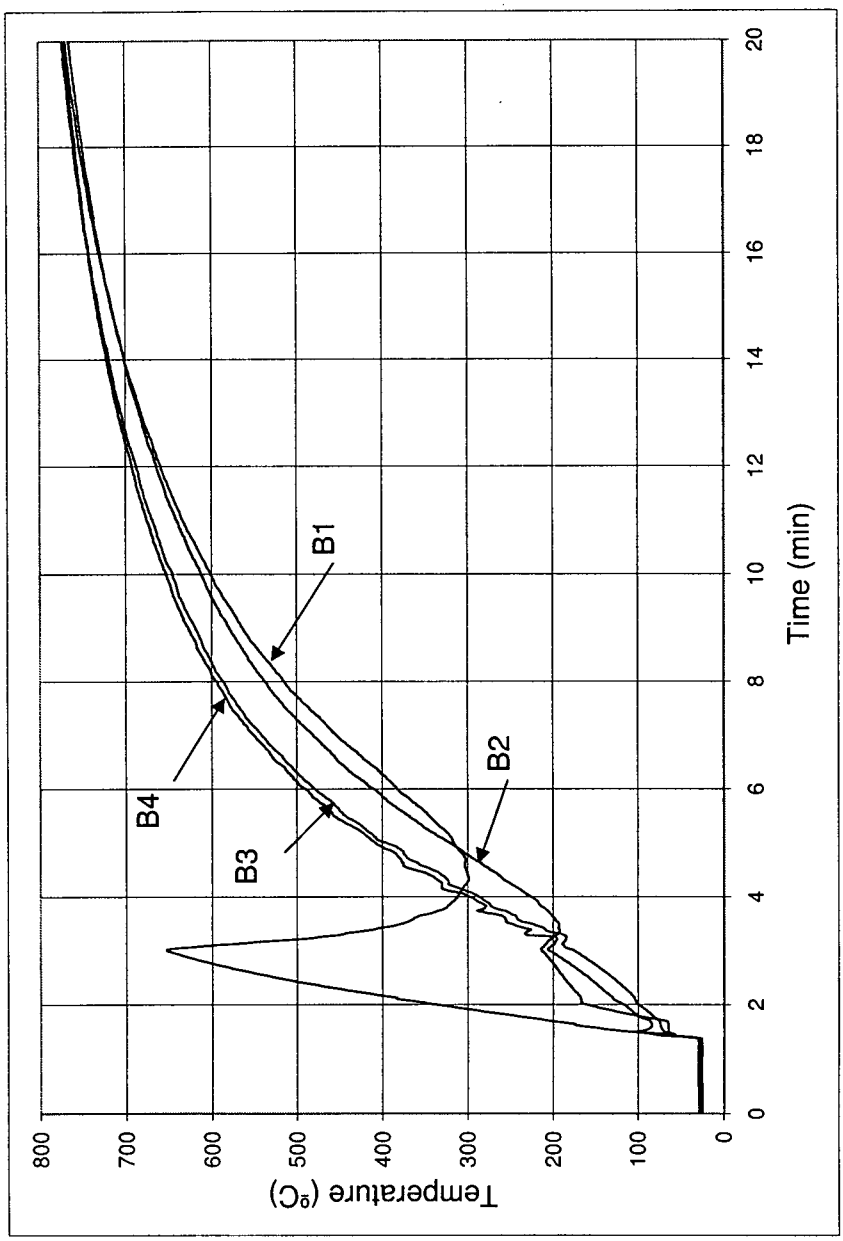

Figure F.11: Run 5 Bed Temperature History. Mix 2 at 1 rpm ($\bar{d}_p = 1.9$mm, $\sigma_p^* = 0.26$, $n_{RR} = 7.3$)

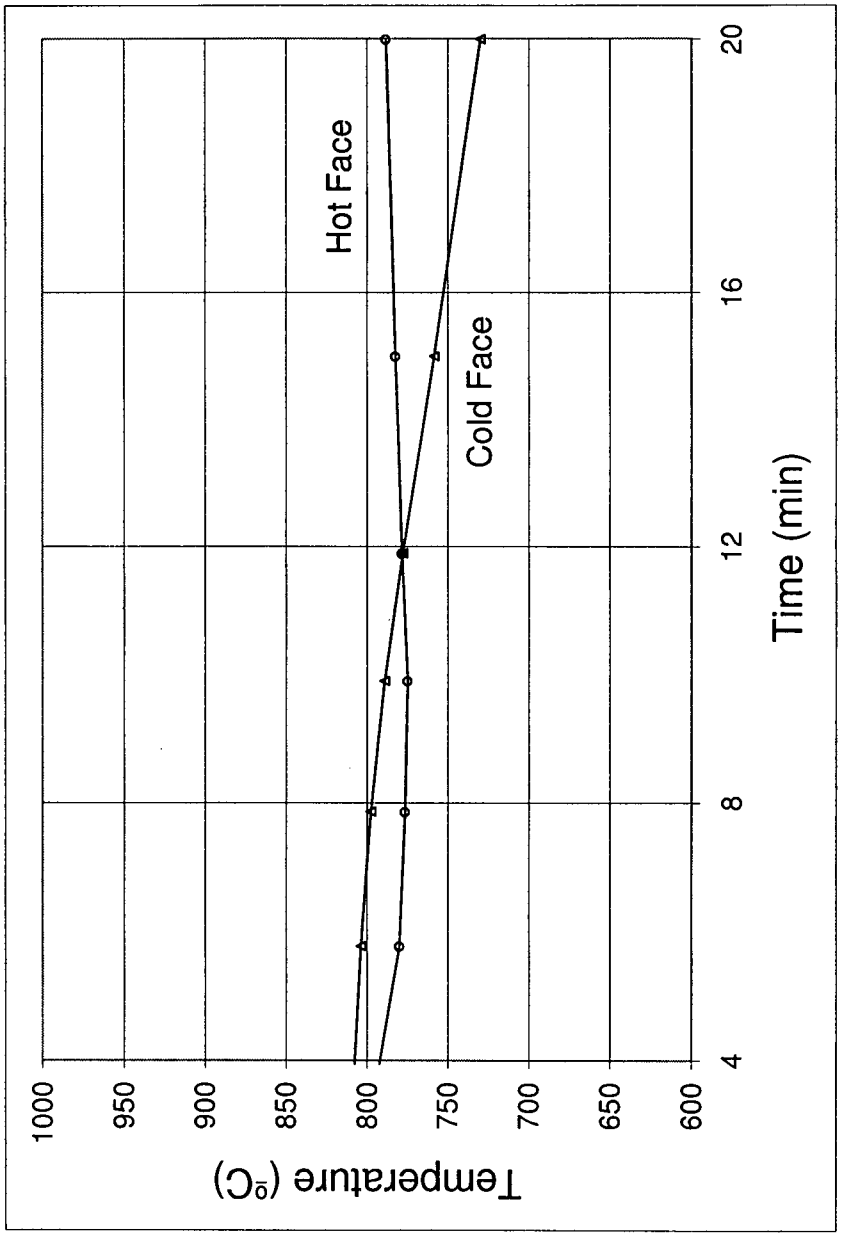

Figure F.12: Run 5 Wall Temperature History. Mix 2 at 1 rpm ($\bar{d}_p = 1.9$mm, $\sigma_p^* = 0.26$, $n_{RR} = 7.3$)

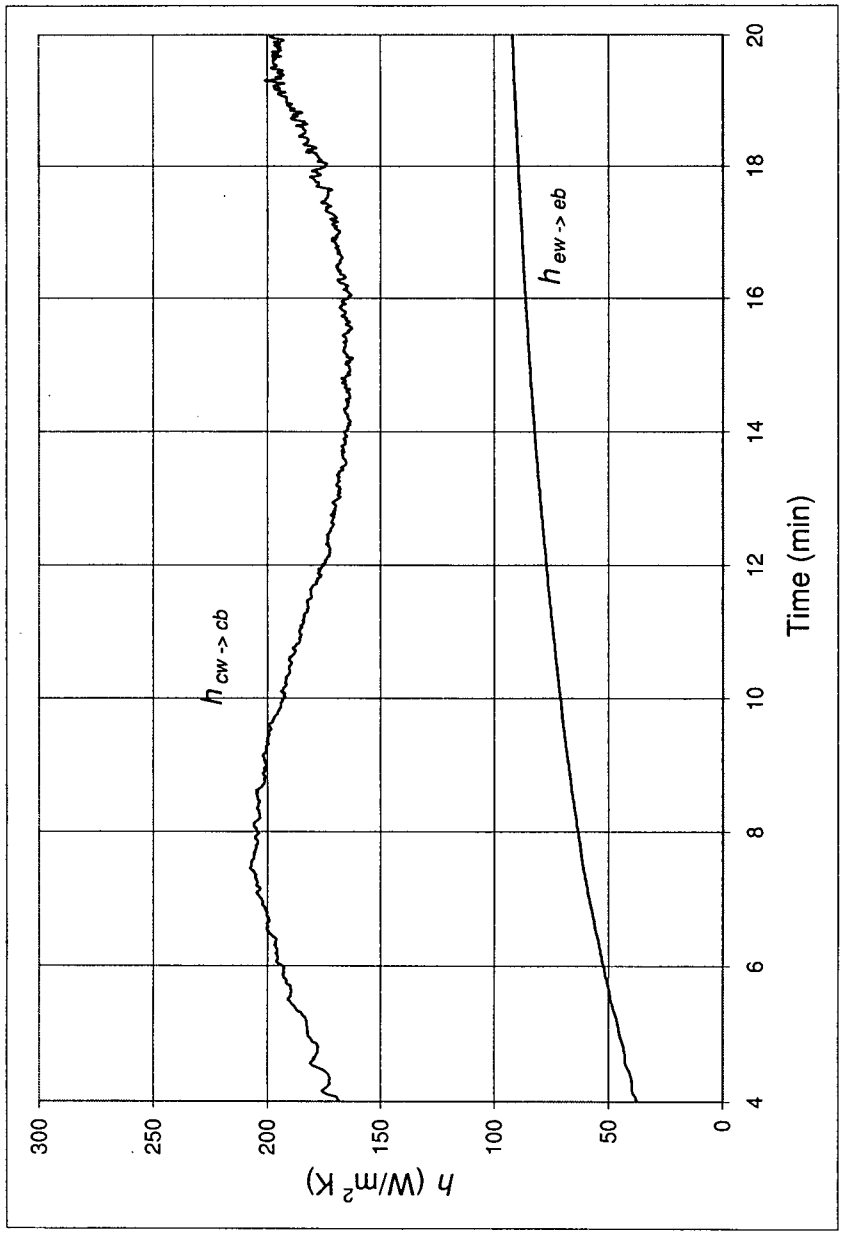

Figure F.13: Run 5 Exposed Wall to Exposed Bed, $h_{ew \to eb}$, and Covered Wall to Covered Bed, $h_{cw \to cb}$, Heat Transfer Coefficients. Mix 2 at 1 rpm ($\bar{d}_p = 1.9$mm, $\sigma_p^* = 0.26$, $n_{RR} = 7.3$)

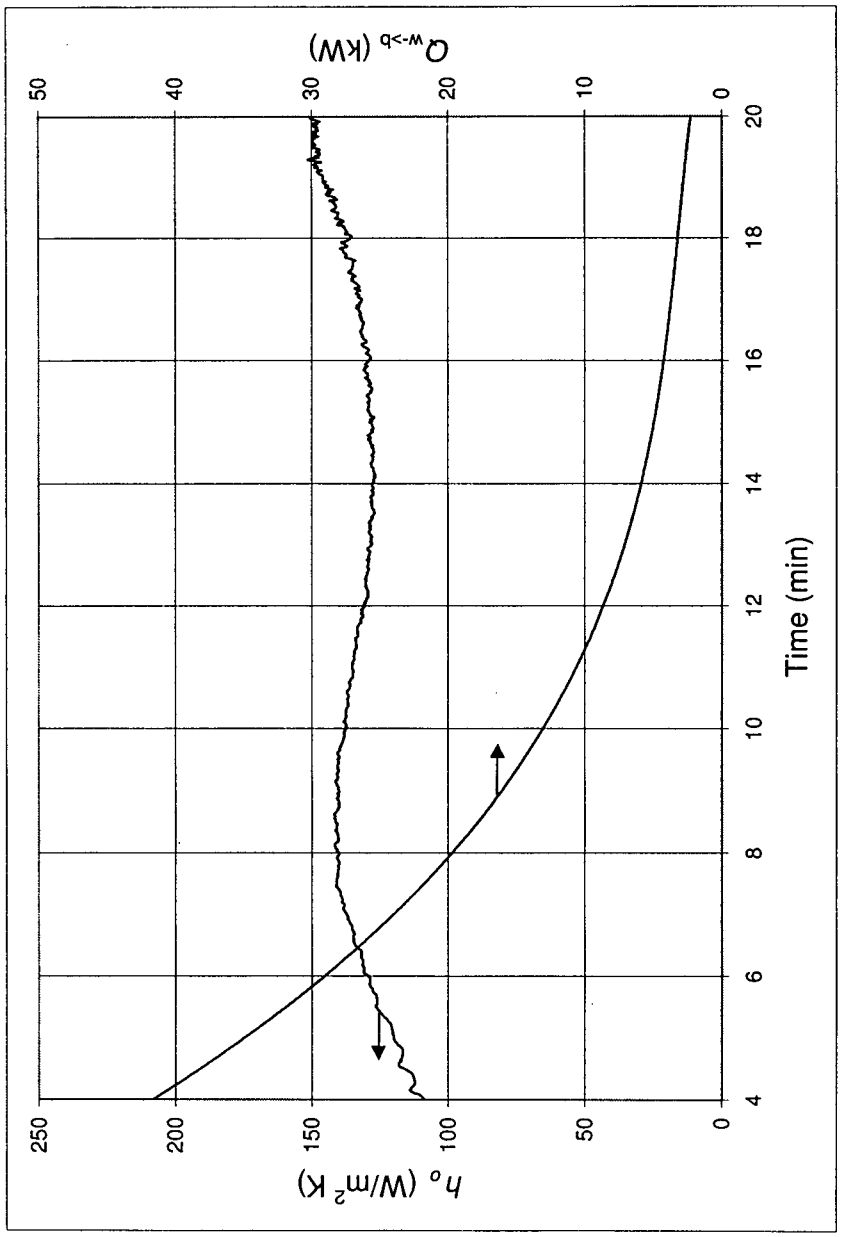

Figure F.14: Run 5 Overall Wall to Bed Heat Transfer Coefficient, h_o, and Heat Flow, $Q_{w\to b}$. Mix 2 at 1 rpm ($\bar{d}_p = 1.9$mm, $\sigma_p^* = 0.26$, $n_{RR} = 7.3$)

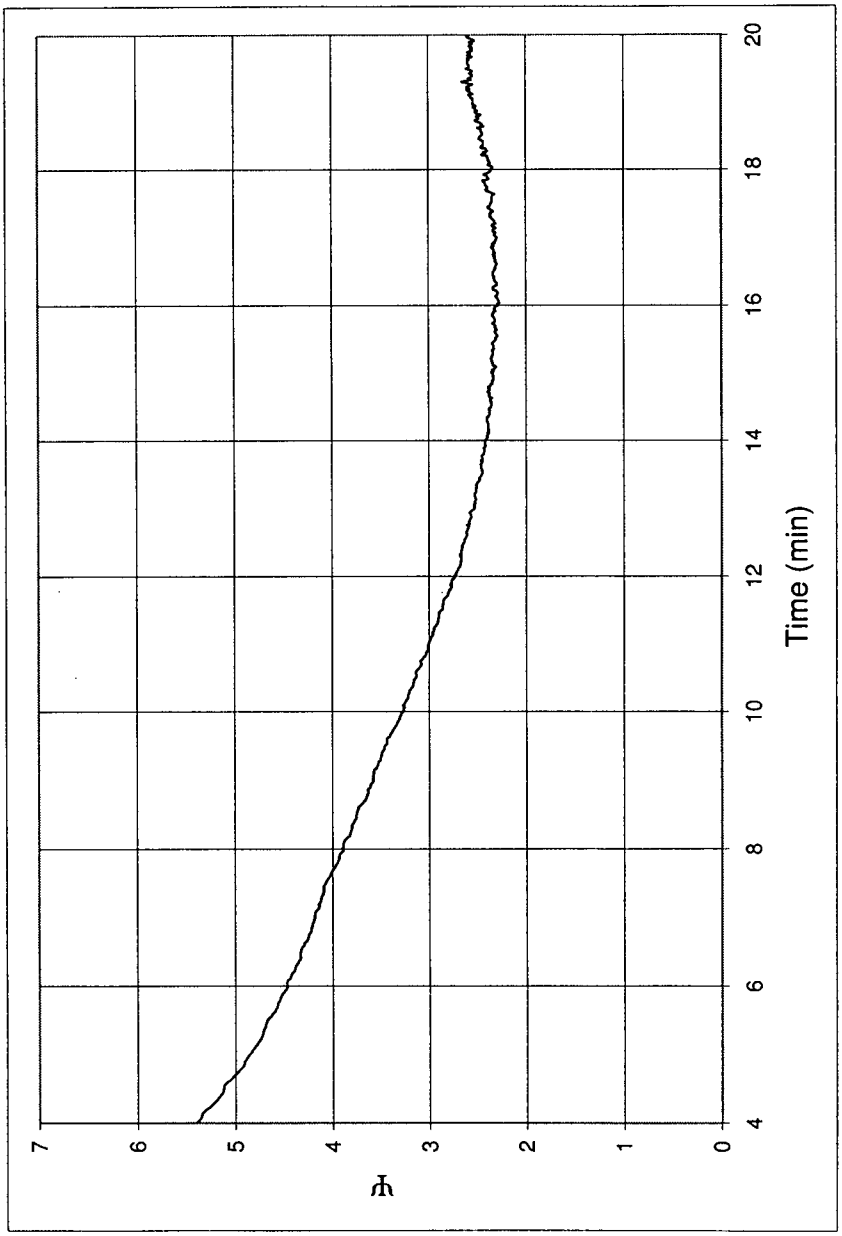

Figure F.15: Run 5 Ratio Between Heat Flow to Covered Wall and Exposed Wall, Ψ. Mix 2 at 1 rpm ($\bar{d}_p = 1.9$mm, $\sigma_p^* = 0.26$, $n_{RR} = 7.3$)

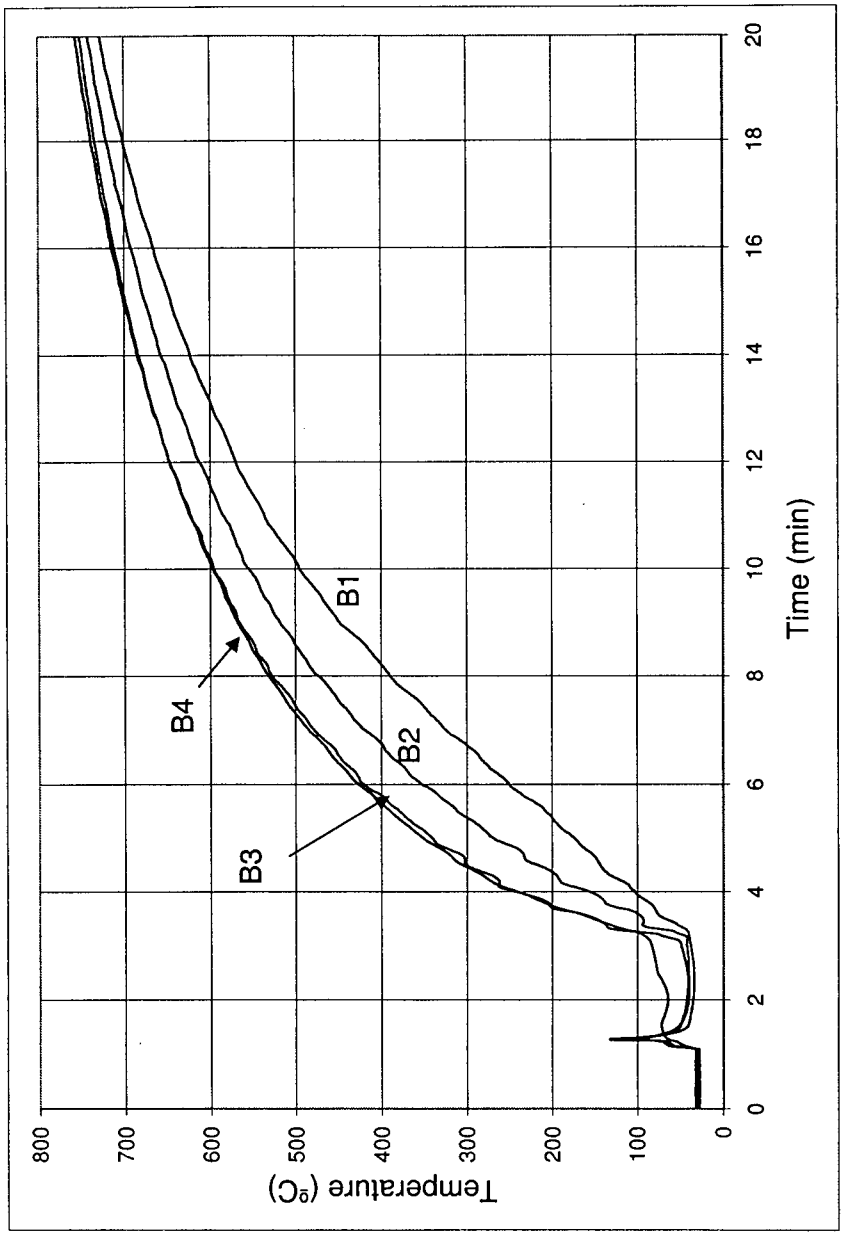

Figure F.16: Run 8 Bed Temperature History. Mix 5 at 1 rpm ($\bar{d_p} = 1.2$mm, $\sigma_p^* = 0.22$, $n_{RR} = 7.7$)

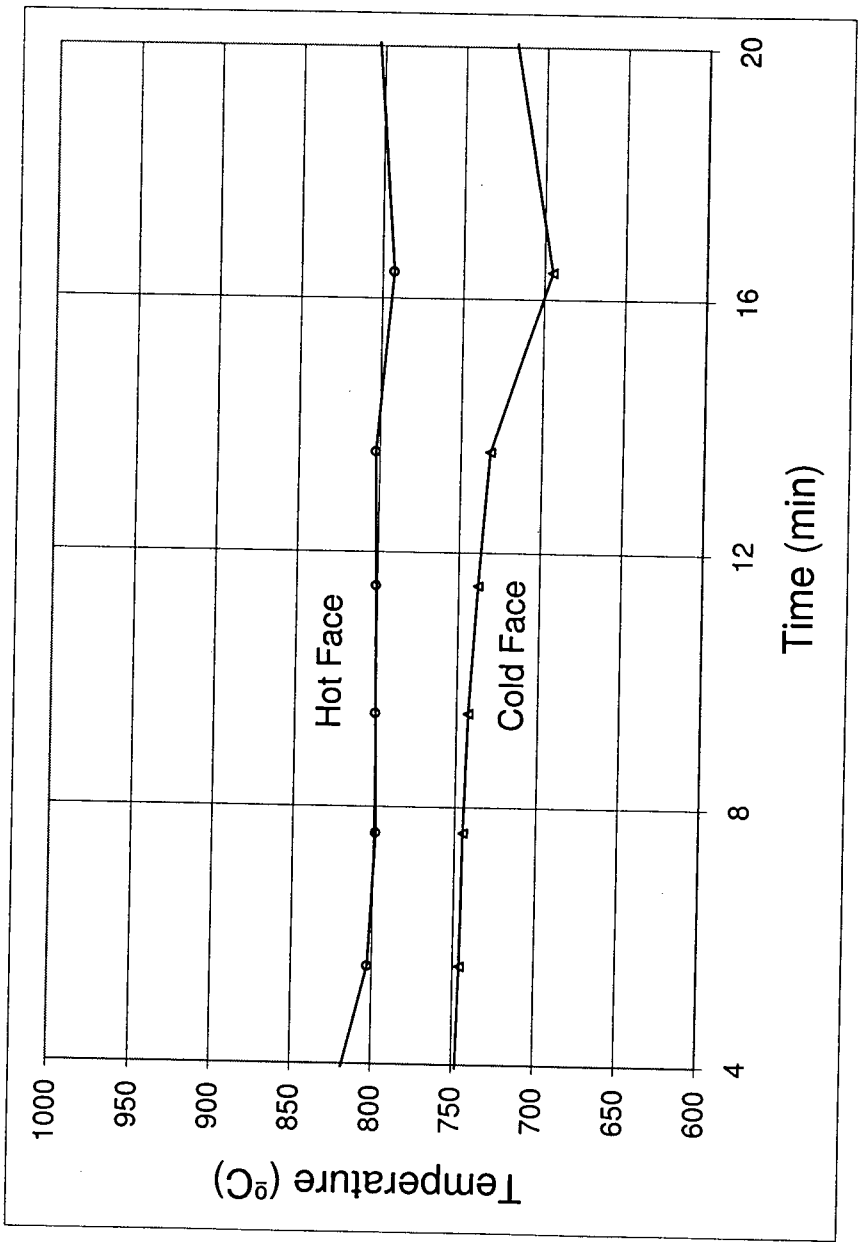

Figure F.17: Run 8 Wall Temperature History. Mix 5 at 1 rpm ($\bar{d}_p = 1.2$mm, $\sigma_p^* = 0.22$, $n_{RR} = 7.7$)

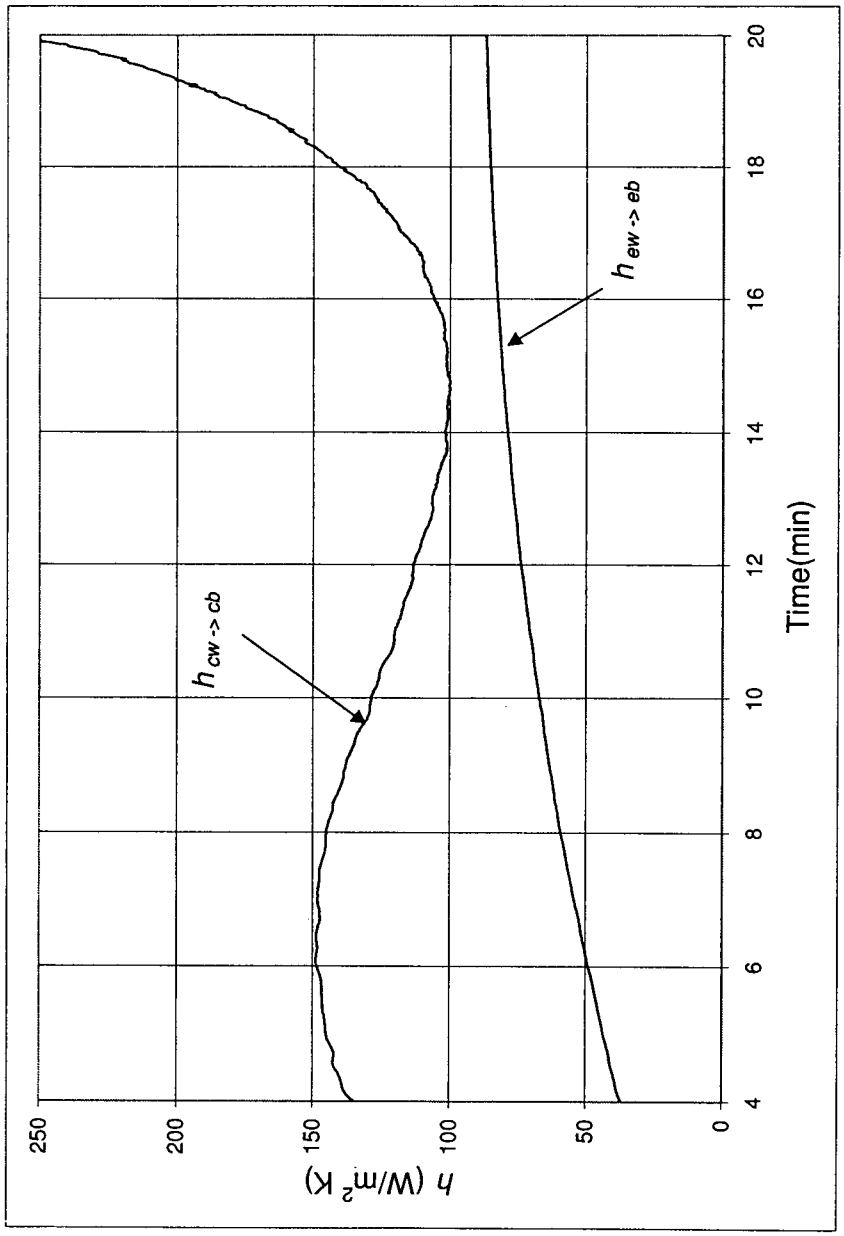

Figure F.18: Run 8 Exposed Wall to Exposed Bed, $h_{ew \to eb}$, and Covered Wall to Covered Bed, $h_{cw \to cb}$, Heat Transfer Coefficients. Mix 5 at 1 rpm ($\tilde{d_p} = 1.2$mm, $\sigma_p^* = 0.22$, $n_{RR} = 7.7$)

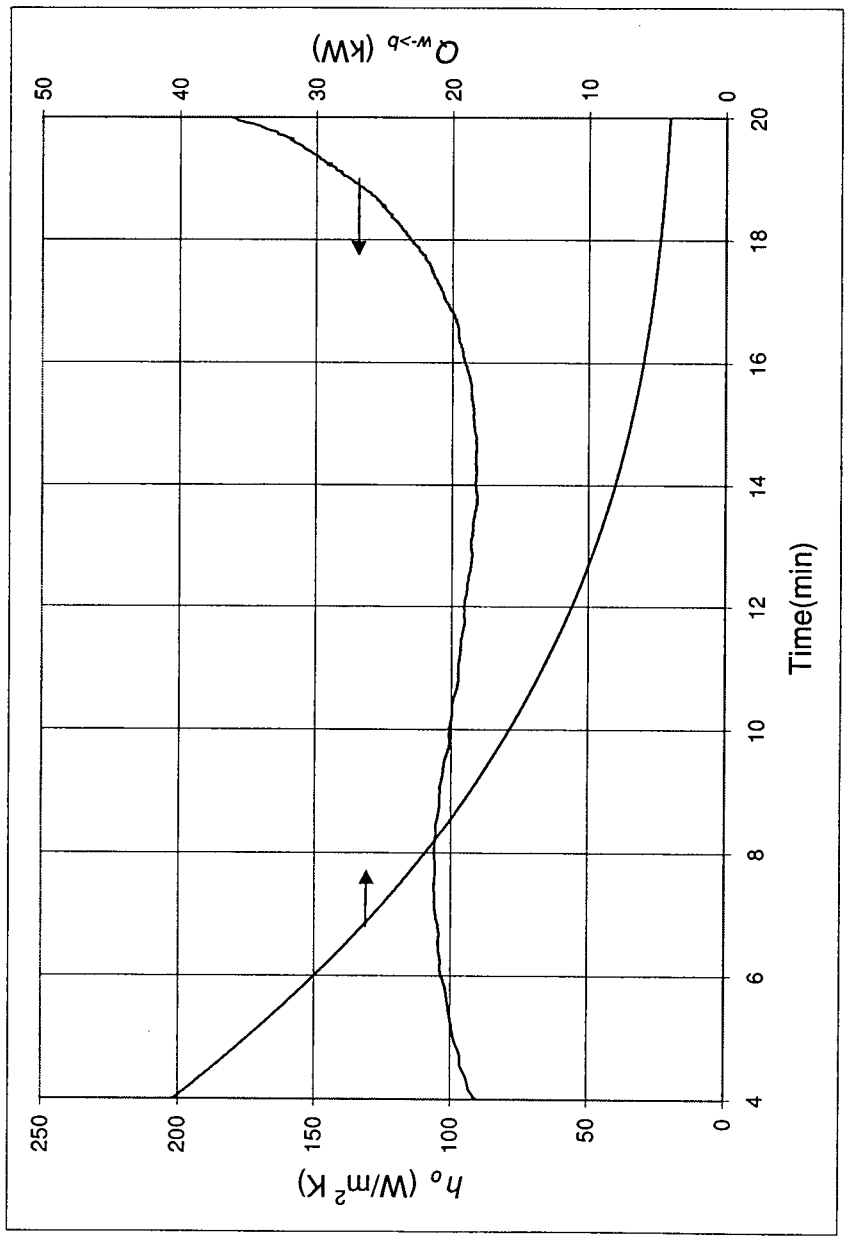

Figure F.19: Run 8 Overall Wall to Bed Heat Transfer Coefficient, h_o, and Heat Flow, $Q_{w\to b}$. Mix 5 at 1 rpm ($\bar{d}_p = 1.2$mm, $\sigma_p^* = 0.22$, $n_{RR} = 7.7$)

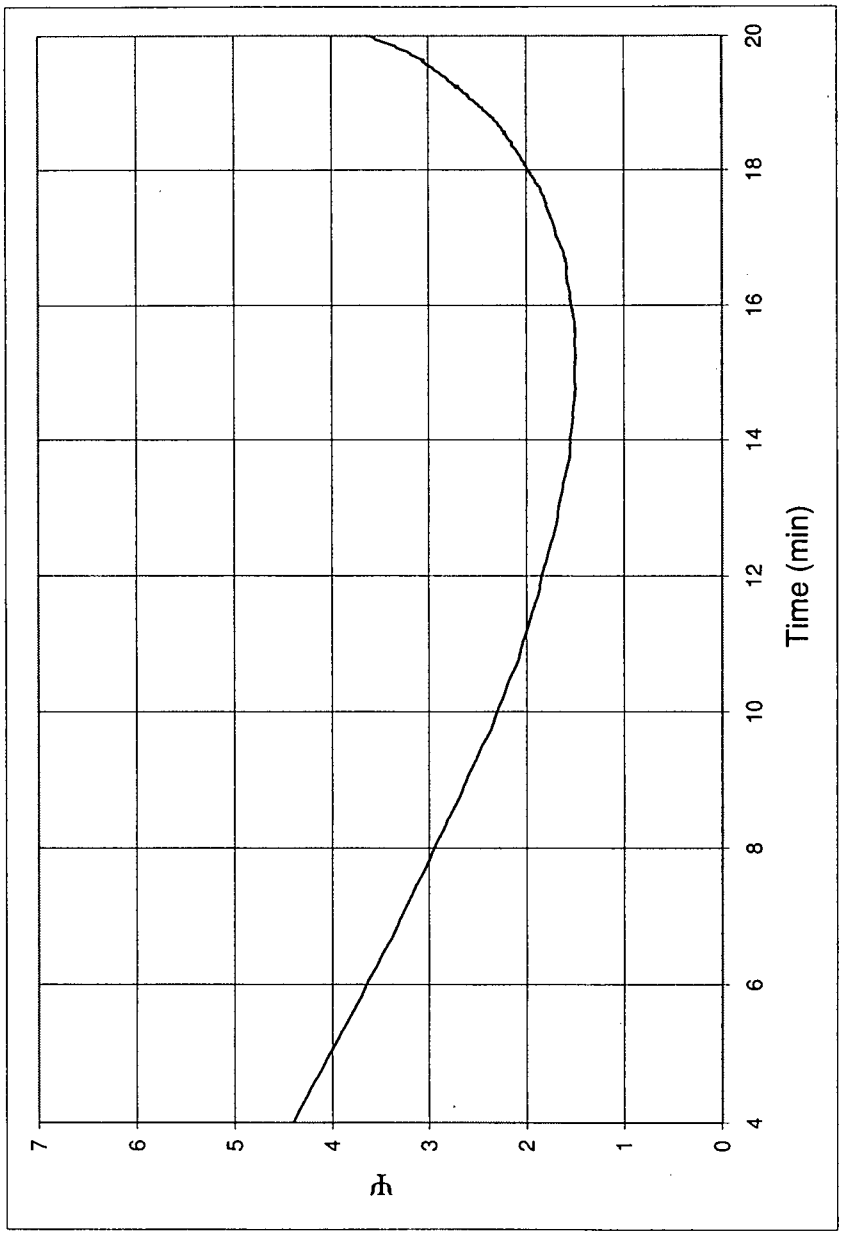

Figure F.20: Run 8 Ratio Between Heat Flow to Covered Wall and Exposed Wall, Ψ. Mix 5 at 1 rpm ($\bar{d}_p = 1.2$mm, $\sigma_p^* = 0.22$, $n_{RR} = 7.7$)

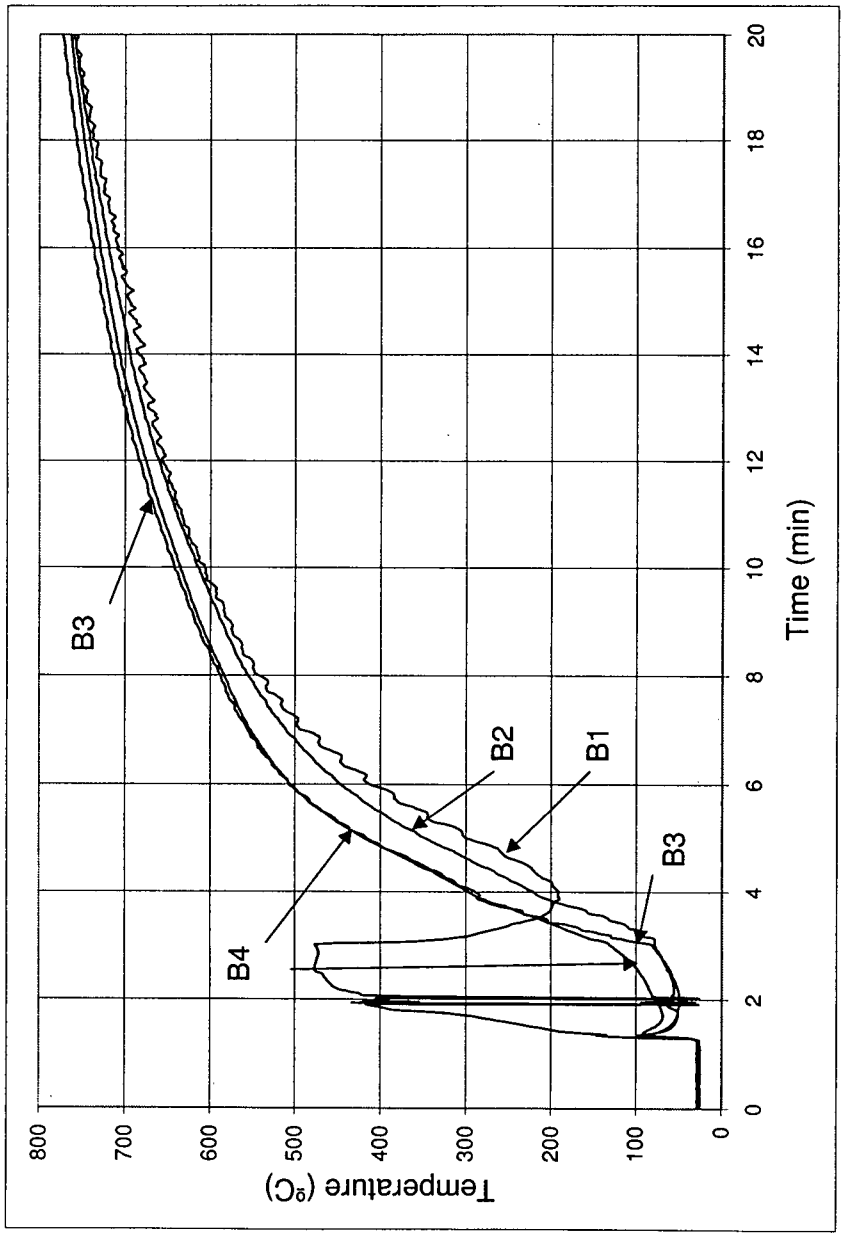

Figure F.21: Run 9 Bed Temperature History. Mix 5 at 3 rpm ($\bar{d}_p = 1.2$mm, $\sigma_p^* = 0.22$, $n_{RR} = 7.7$)

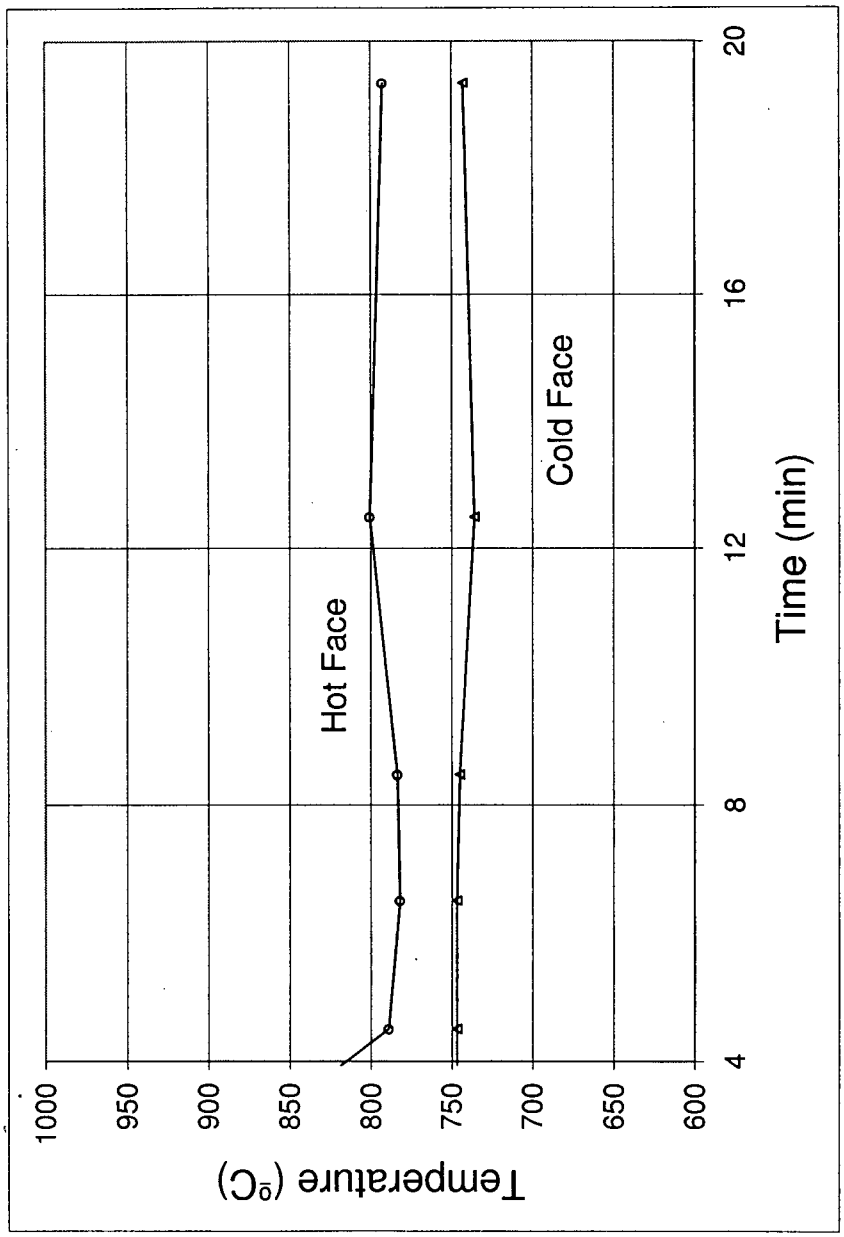

Figure F.22: Run 9 Wall Temperature History. Mix 5 at 3 rpm ($\bar{d_p} = 1.2$mm, $\sigma_p^* = 0.22$, $n_{RR} = 7.7$)

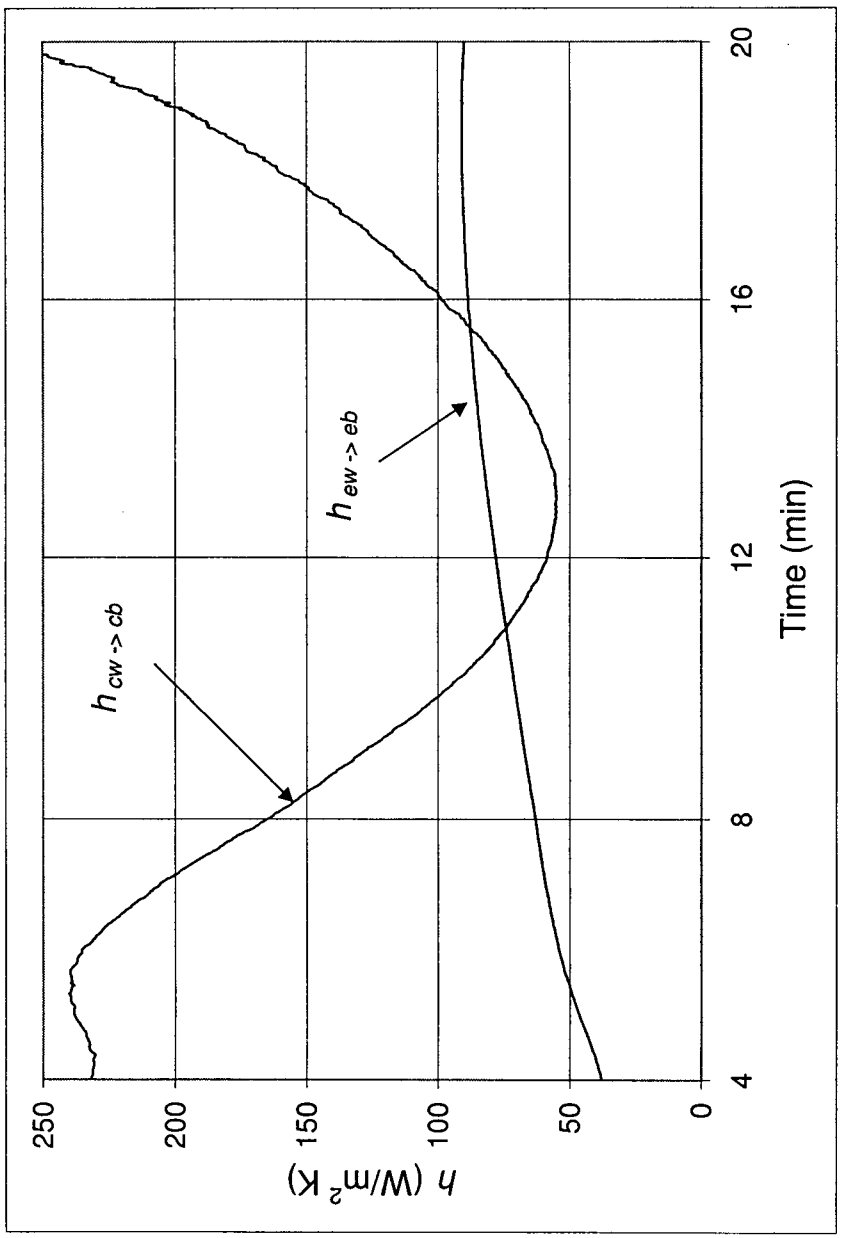

Figure F.23: Run 9 Exposed Wall to Exposed Bed, $h_{ew \to eb}$, and Covered Wall to Covered Bed, $h_{cw \to cb}$, Heat Transfer Coefficients. Mix 5 at 3 rpm ($\bar{d_p} = 1.2$mm, $\sigma_p^* = 0.22$, $n_{RR} = 7.7$)

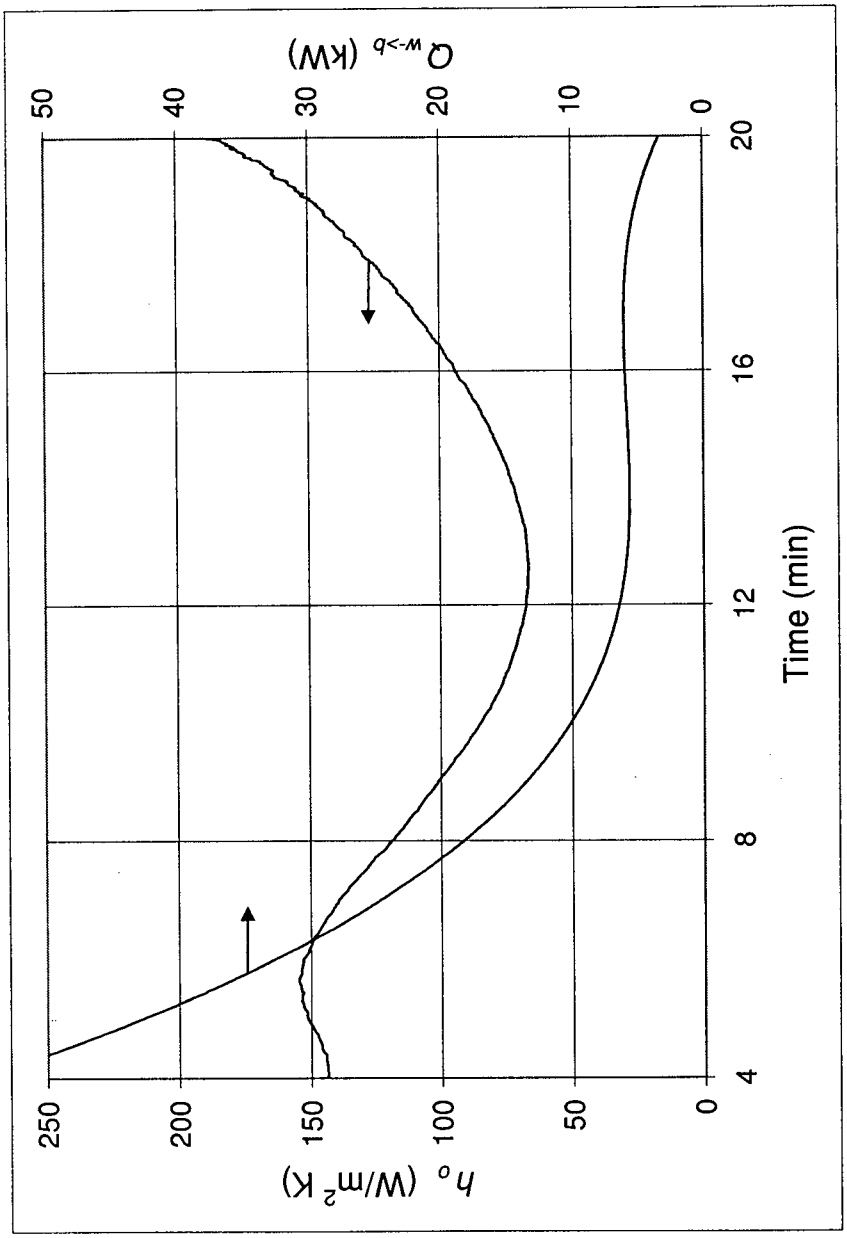

Figure F.24: Run 9 Overall Wall to Bed Heat Transfer Coefficient, h_o, and Heat Flow, $Q_{w\to b}$. Mix 5 at 3 rpm ($\bar{d}_p = 1.2$mm, $\sigma_p^* = 0.22$, $n_{RR} = 7.7$)

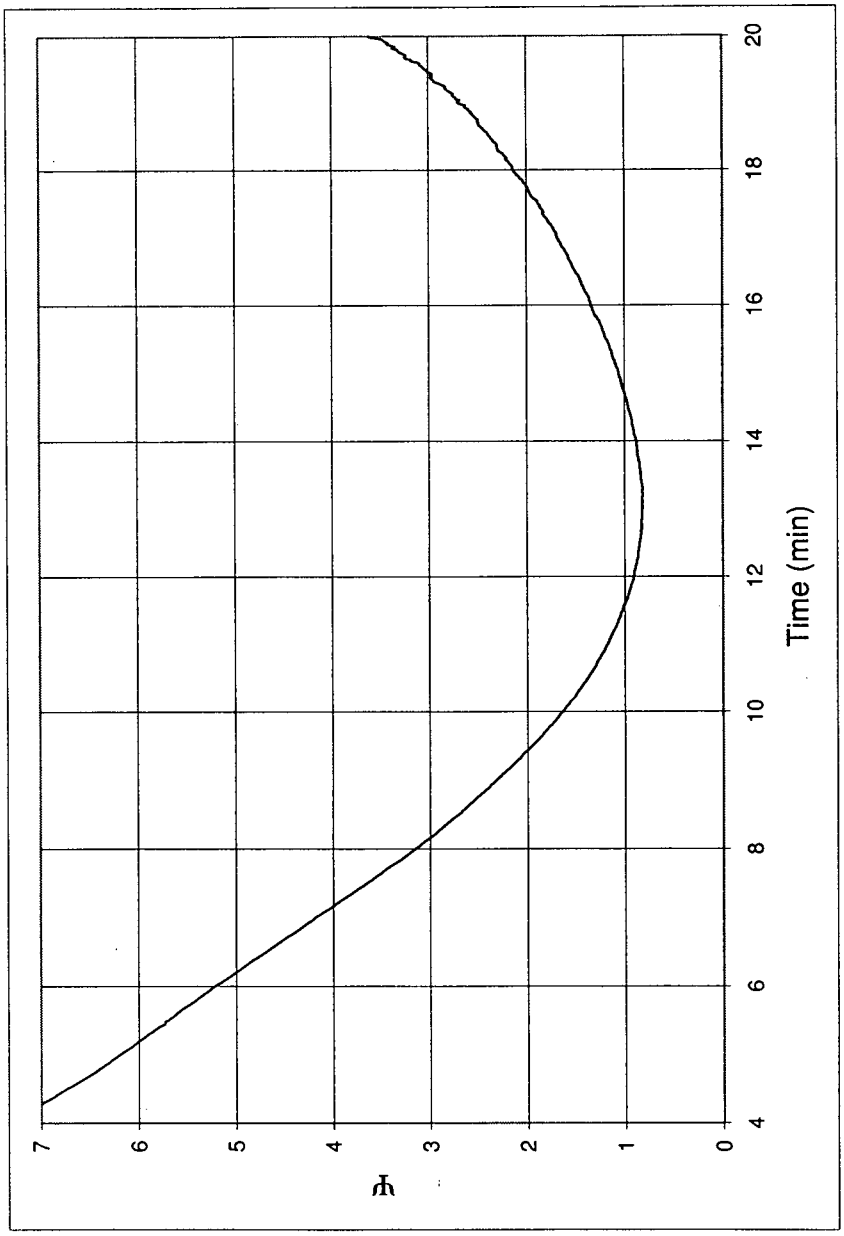

Figure F.25: Run 9 Ratio Between Heat Flow to Covered Wall and Exposed Wall, Ψ. Mix 5 at 3 rpm ($\bar{d}_p = 1.2$mm, $\sigma_p^* = 0.22$, $n_{RR} = 7.7$)

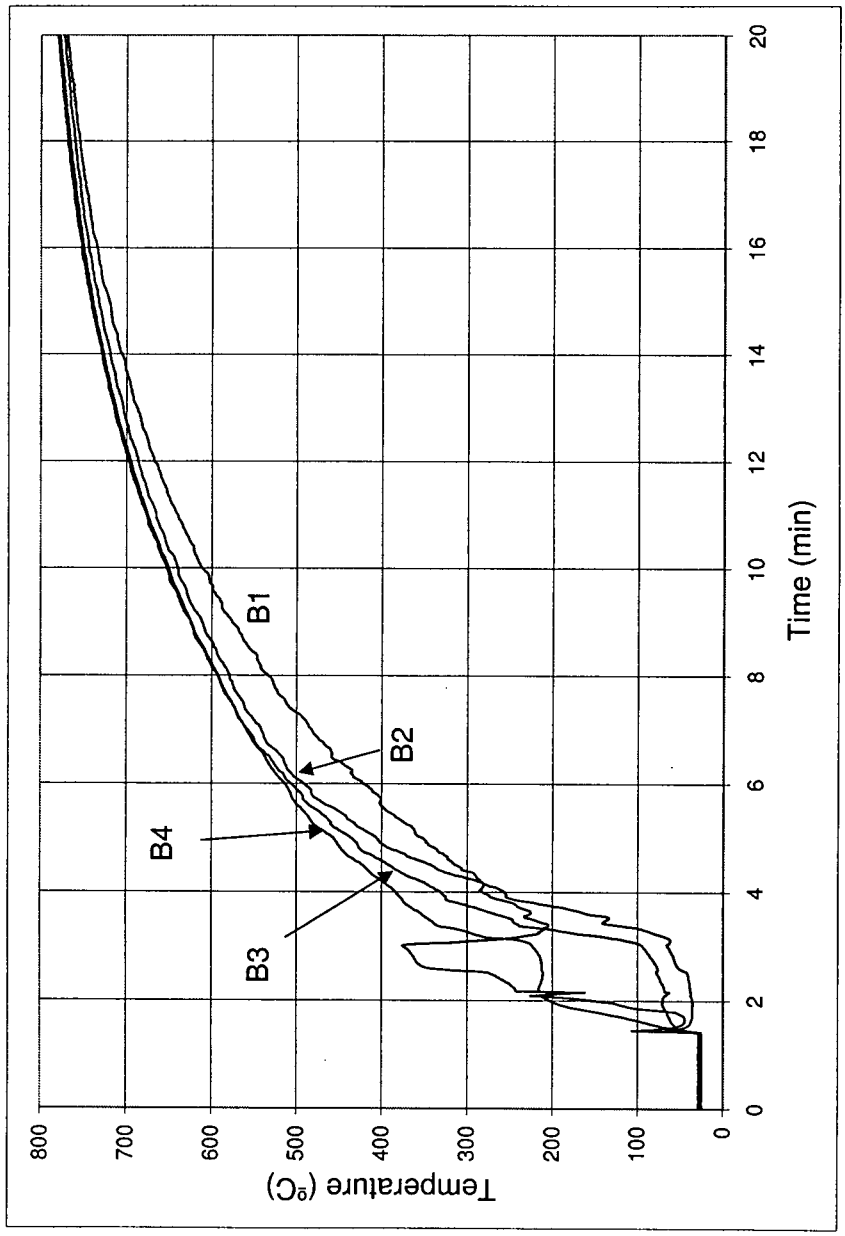

Figure F.26: Run 10 Bed Temperature History. Mix 3 at 1 rpm ($\bar{d}_p = 2.4$mm, $\sigma_p^* = 0.17$, $n_{RR} = 11.7$)

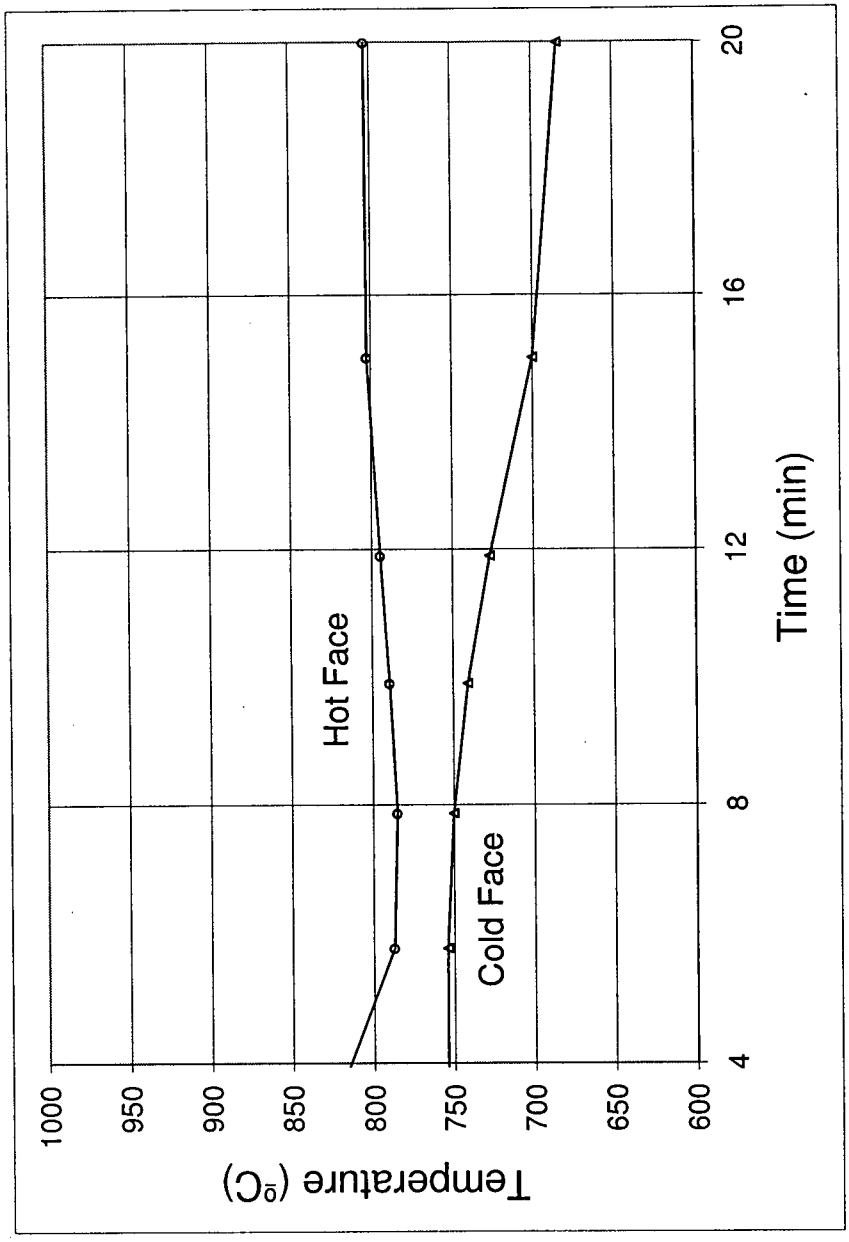

Figure F.27: Run 10 Wall Temperature History. Mix 3 at 1 rpm ($\bar{d}_p = 2.4$mm, $\sigma_p^* = 0.17$, $n_{RR} = 11.7$)

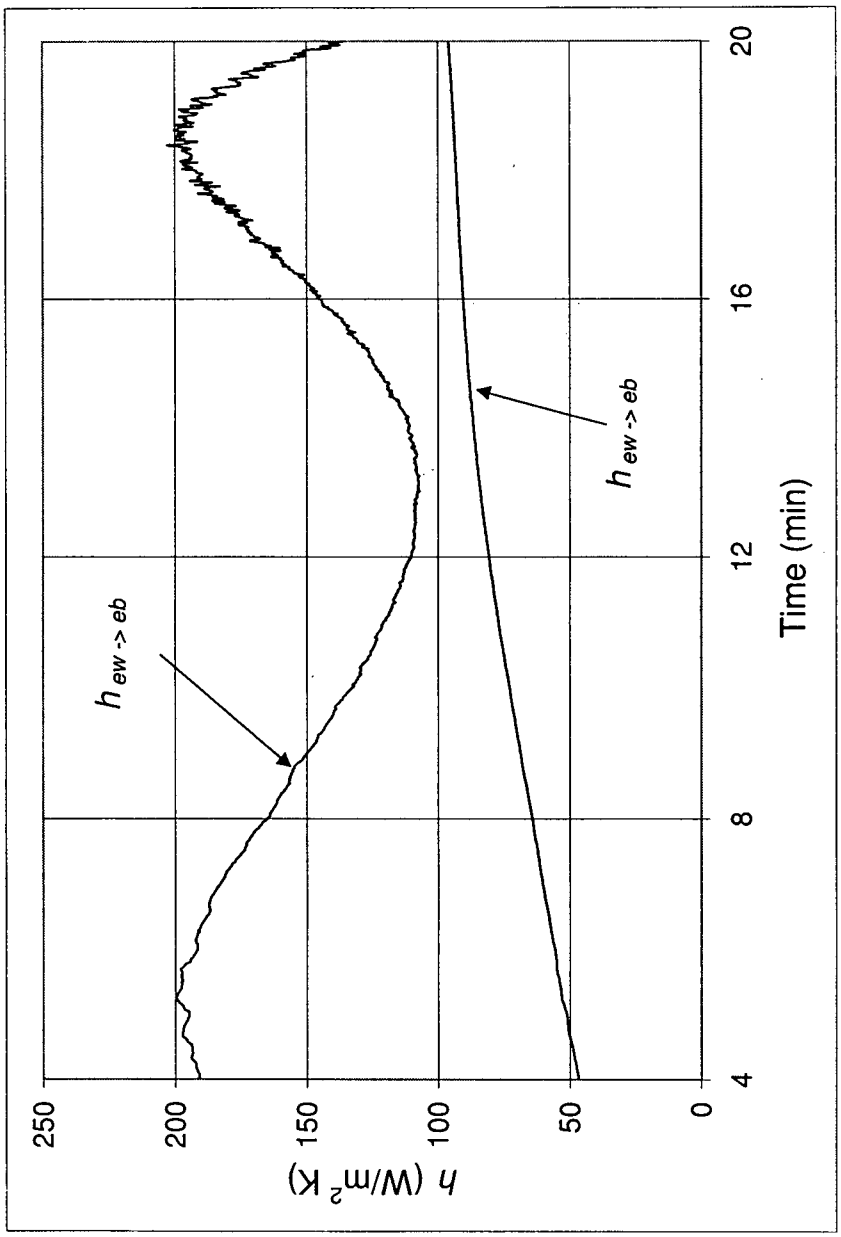

Figure F.28: Run 10 Exposed Wall to Exposed Bed, $h_{ew \to eb}$, and Covered Wall to Covered Bed, $h_{cw \to cb}$, Heat Transfer Coefficients. Mix 3 at 1 rpm ($\bar{d}_p = 2.4$mm, $\sigma_p^* = 0.17$, $n_{RR} = 11.7$)

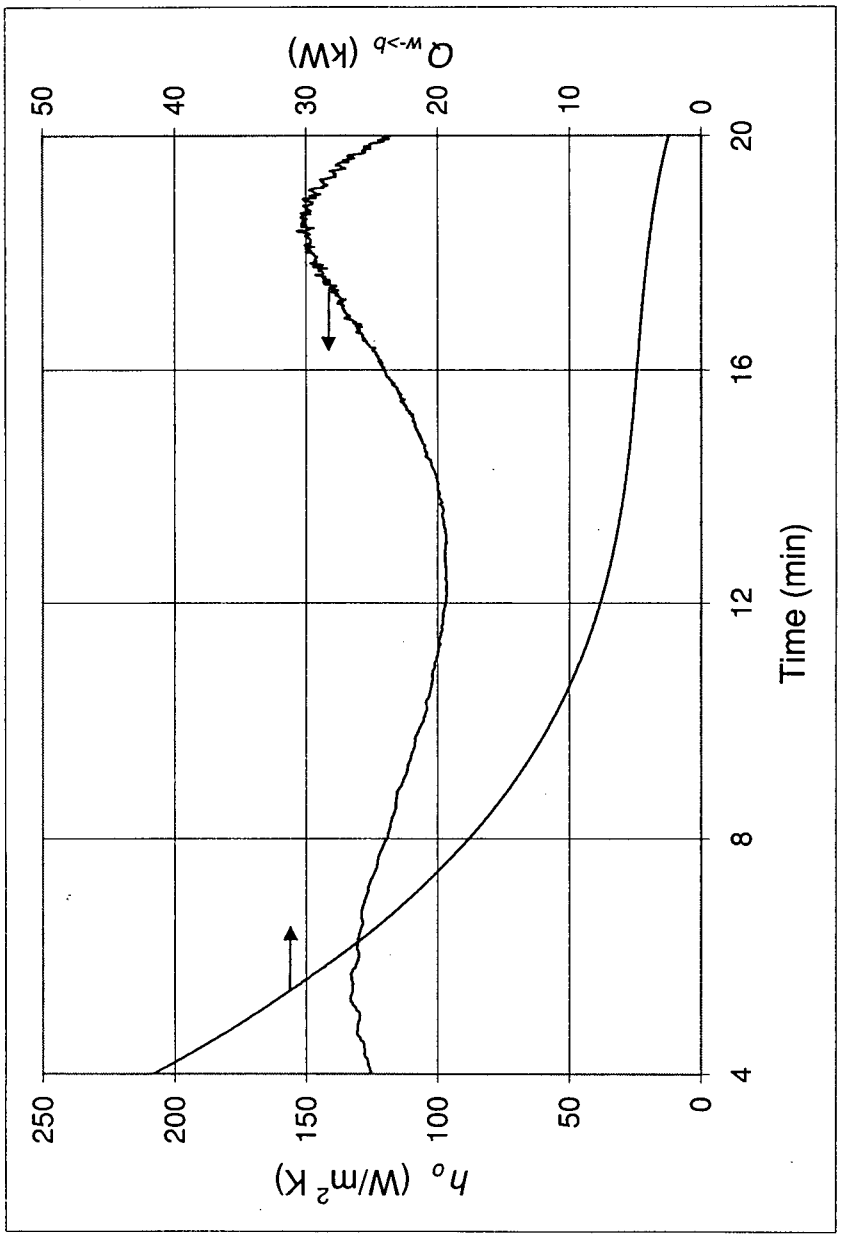

Figure F.29: Run 10 Overall Wall to Bed Heat Transfer Coefficient, h_o, and Heat Flow, $Q_{w\to b}$. Mix 3 at 1 rpm ($\bar{d}_p = 2.4$mm, $\sigma_p^* = 0.17$, $n_{RR} = 11.7$)

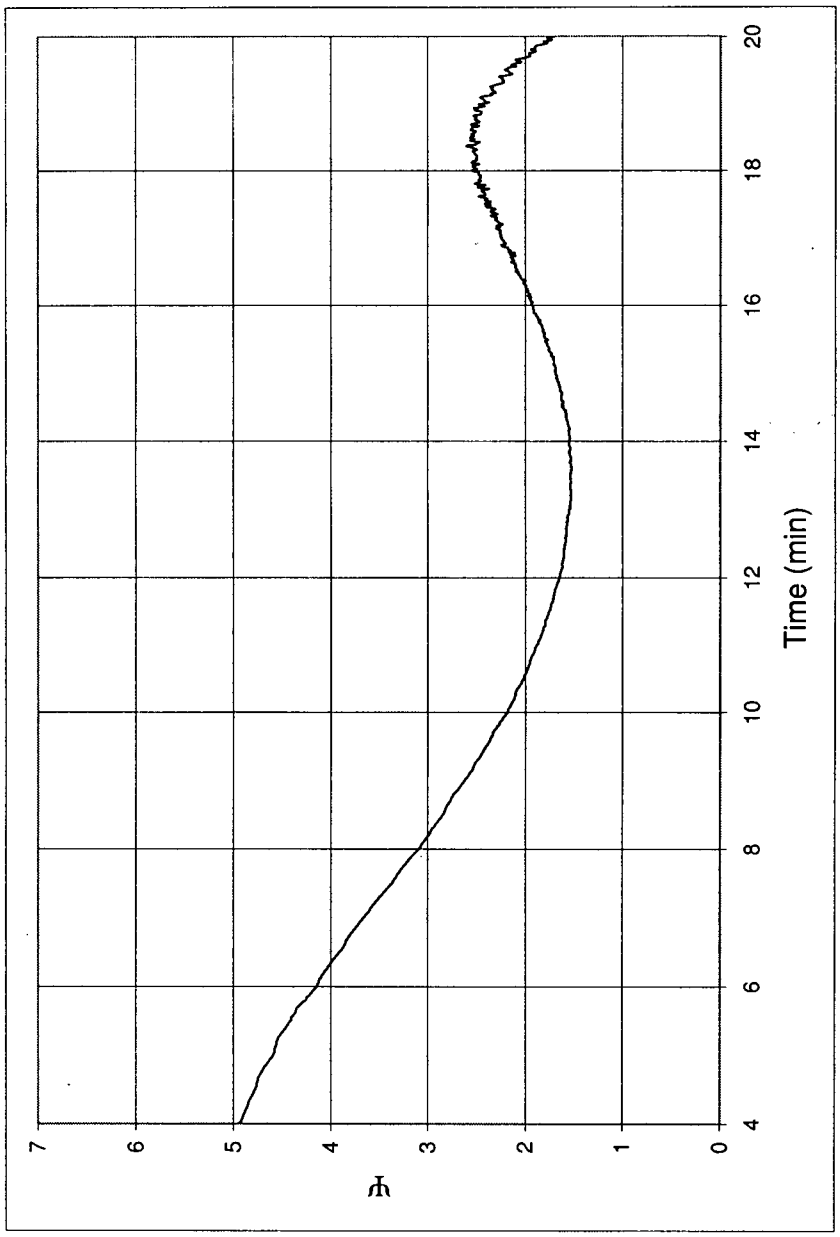

Figure F.30: Run 10 Ratio Between Heat Flow to Covered Wall and Exposed Wall, Ψ. Mix 3 at 1 rpm ($\bar{d_p} = 2.4$mm, $\sigma_p^* = 0.17$, $n_{RR} = 11.7$)

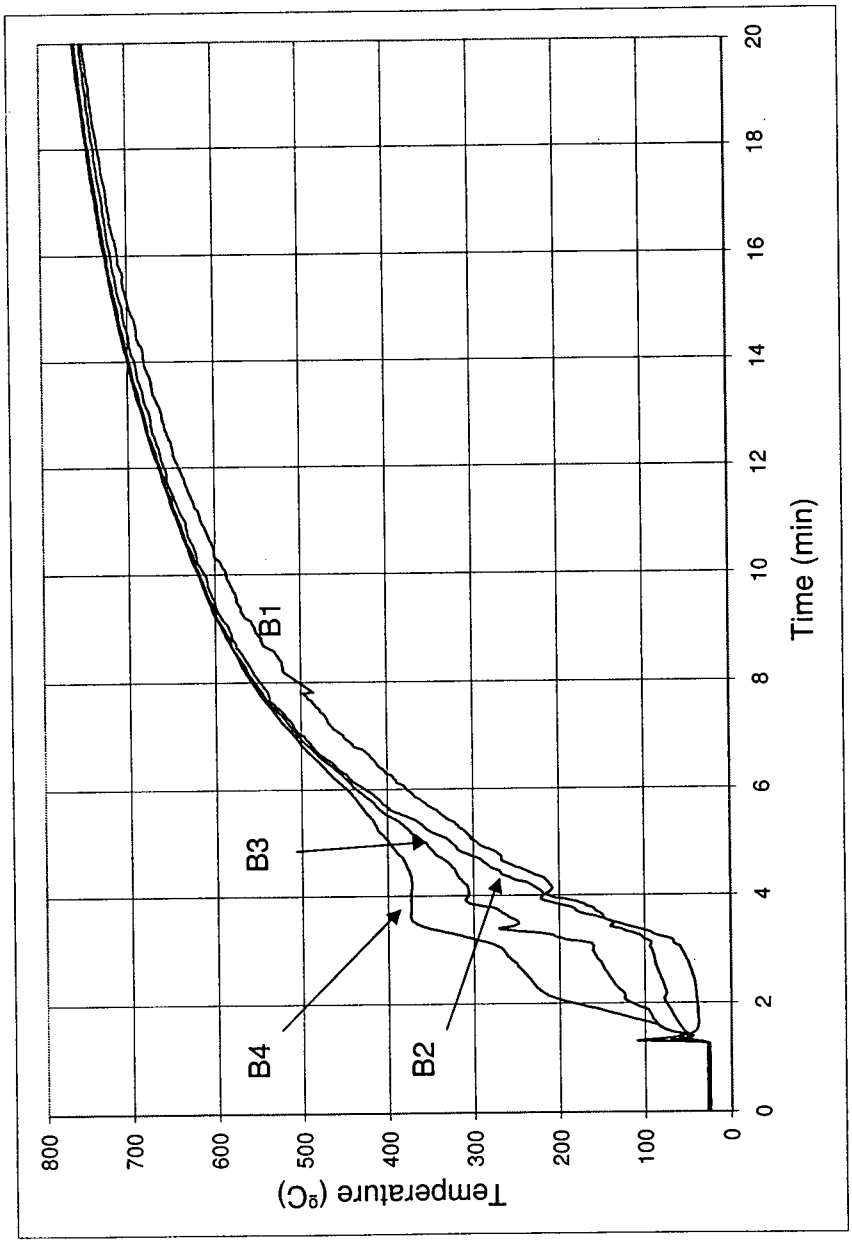

Figure F.31: Run 11 Bed Temperature History. Mix 4 at 1 rpm ($\bar{d_p} = 3.0$mm, $\sigma_p^* = 0.09$, $n_{RR} = 15.5$)

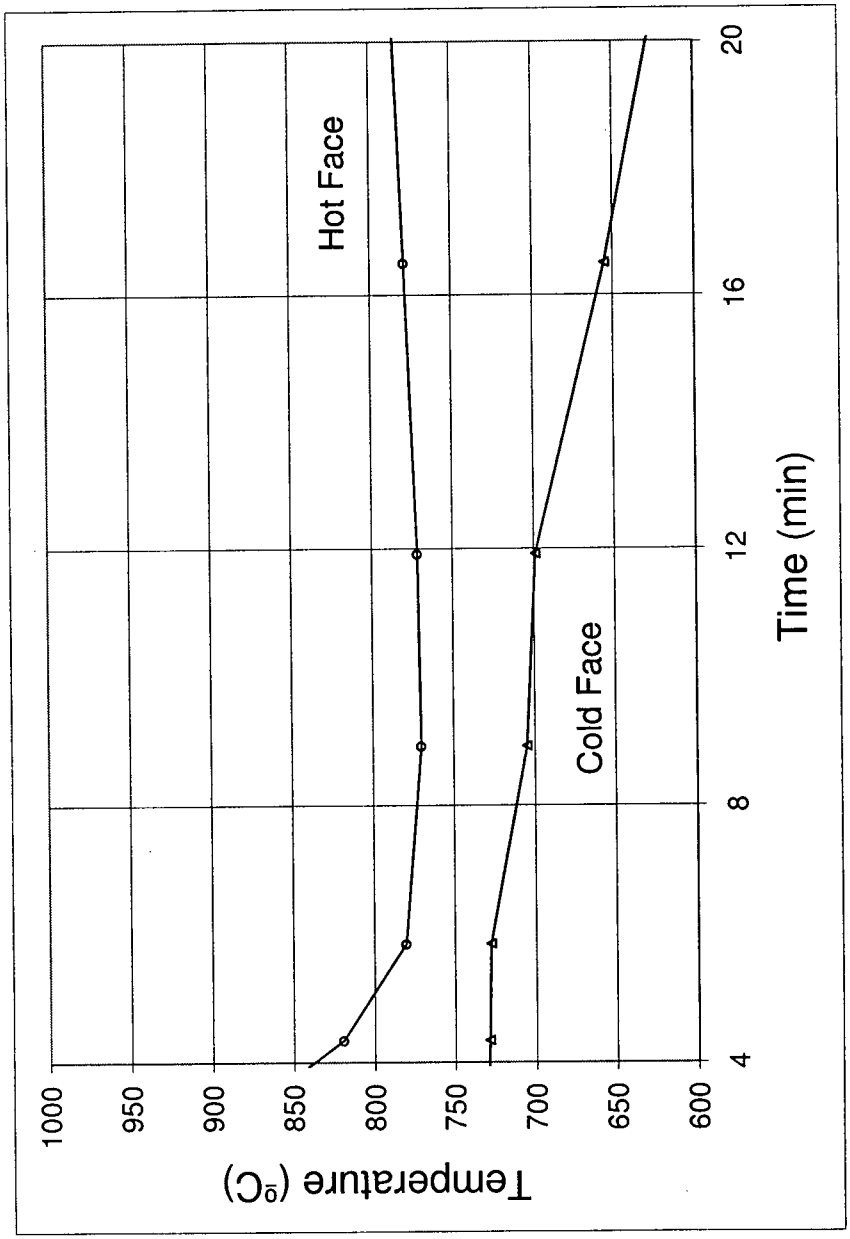

Figure F.32: Run 11 Wall Temperature History. Mix 4 at 1 rpm ($\bar{d}_p = 3.0$mm, $\sigma_p^* = 0.09$, $n_{RR} = 15.5$)

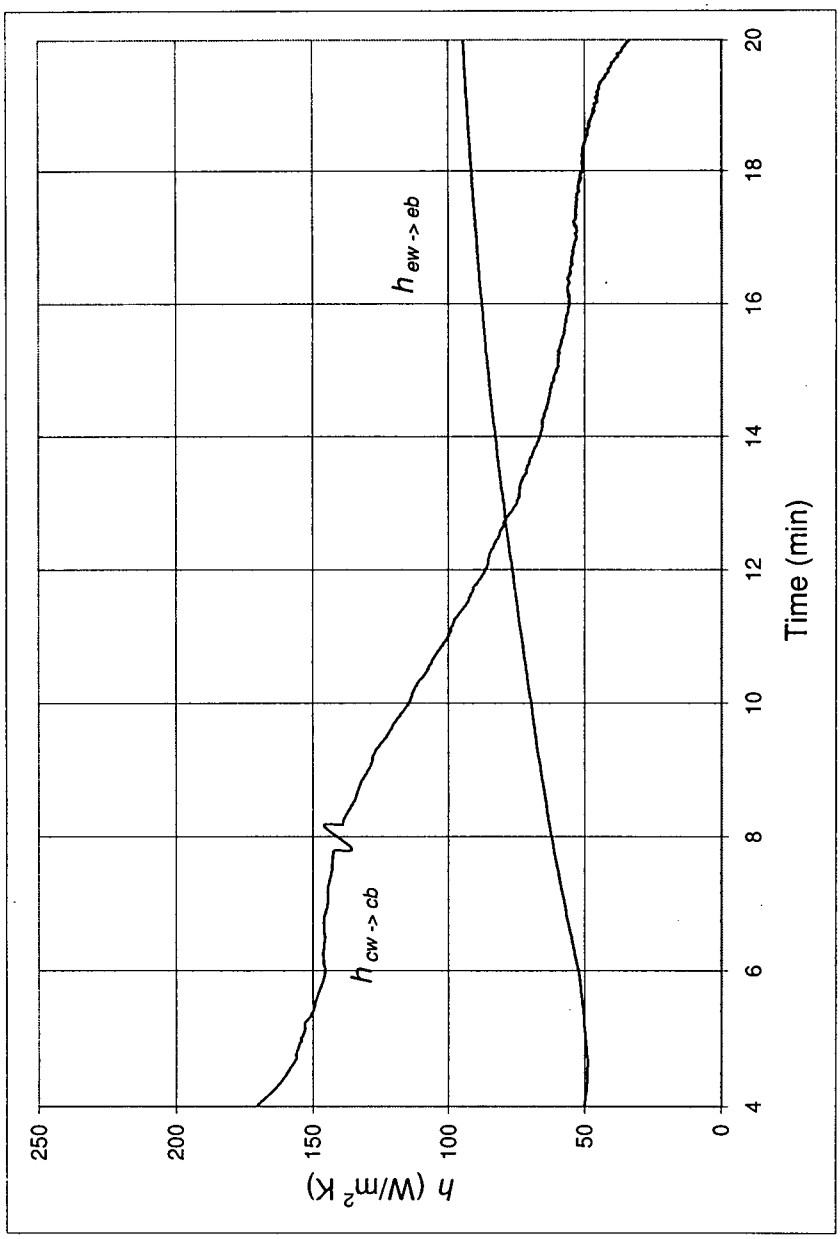

Figure F.33: Run 11 Exposed Wall to Exposed Bed, $h_{ew \to eb}$, and Covered Wall to Covered Bed, $h_{cw \to cb}$, Heat Transfer Coefficients. Mix 4 at 1 rpm ($\bar{d}_p = 3.0$mm, $\sigma_p^* = 0.09$, $n_{RR} = 15.5$)

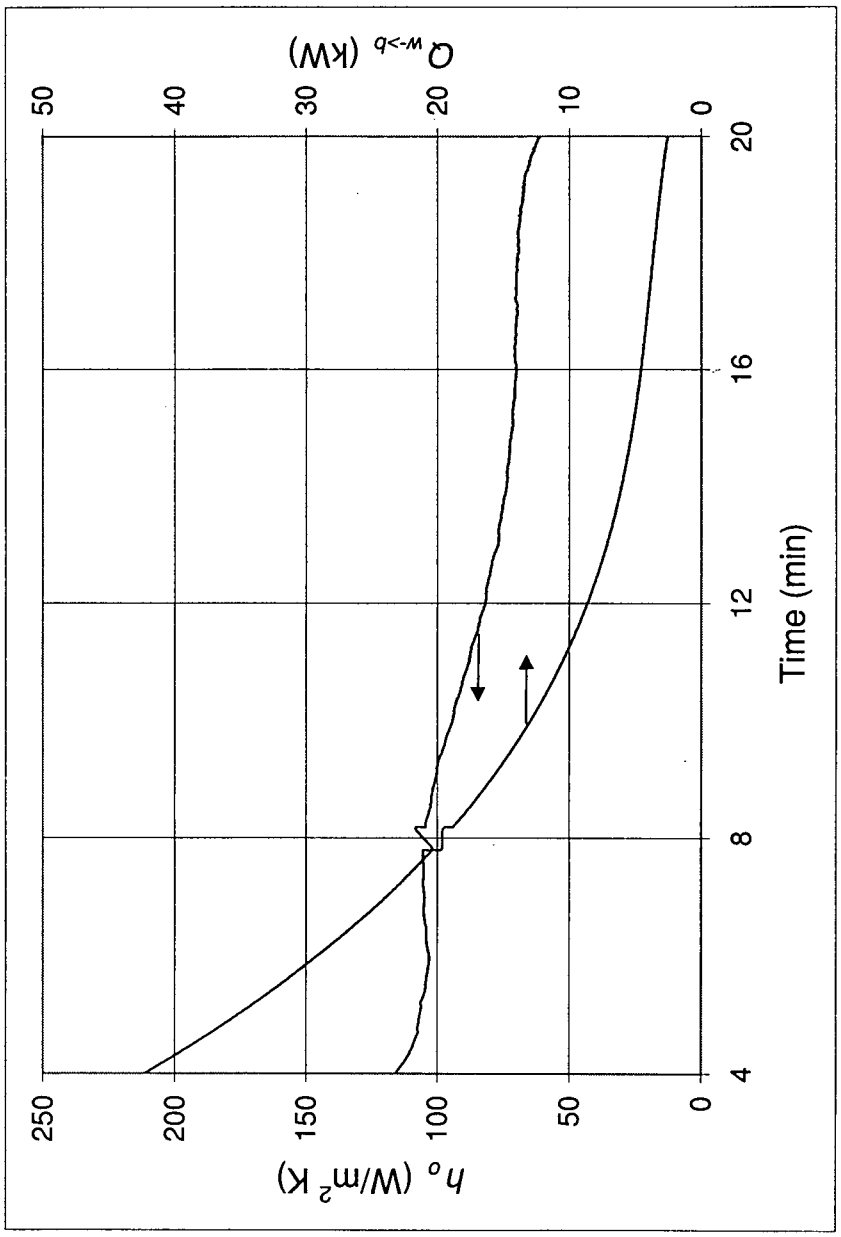

Figure F.34: Run 11 Overall Wall to Bed Heat Transfer Coefficient, h_o, and Heat Flow, $Q_{w \to b}$. Mix 4 at 1 rpm ($\bar{d}_p = 3.0$mm, $\sigma_p^* = 0.09$, $n_{RR} = 15.5$)

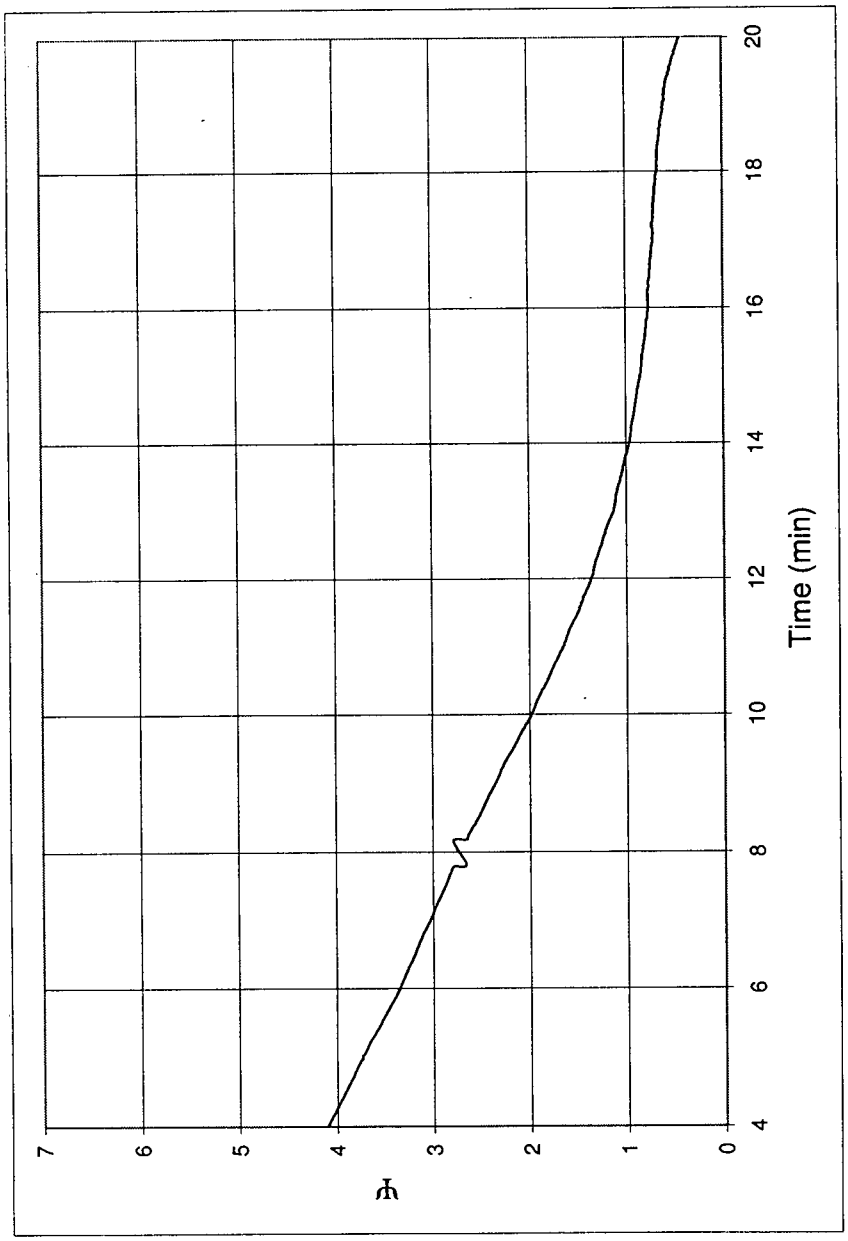

Figure F.35: Run 11 Ratio Between Heat Flow to Covered Wall and Exposed Wall, Ψ. Mix 4 at 1 rpm ($\bar{d_p} = 3.0$mm, $\sigma_p^* = 0.09$, $n_{RR} = 15.5$)

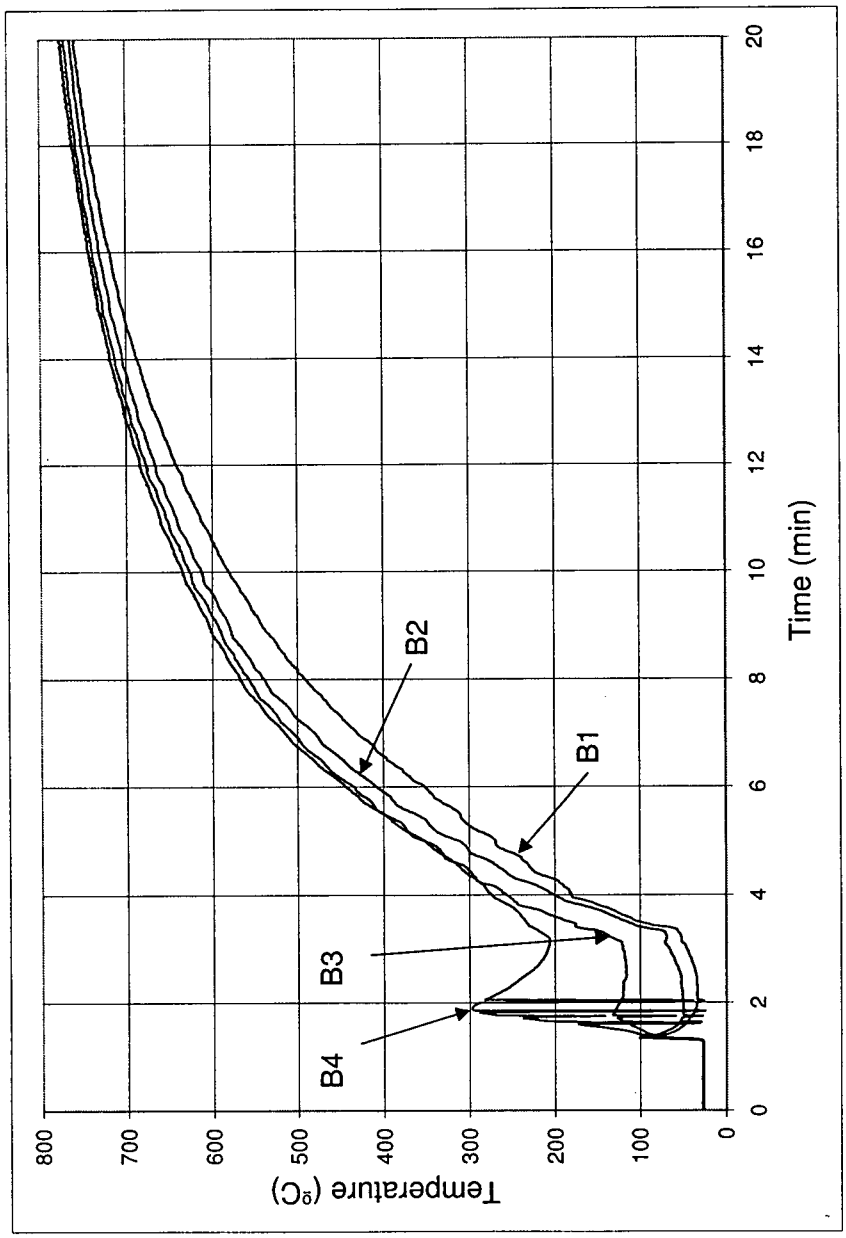

Figure F.36: Run 12 Bed Temperature History. Mix 6 at 1 rpm ($\bar{d}_p = 1.3$mm, $\sigma_p^* = 0.15$, $n_{RR} = 11.8$)

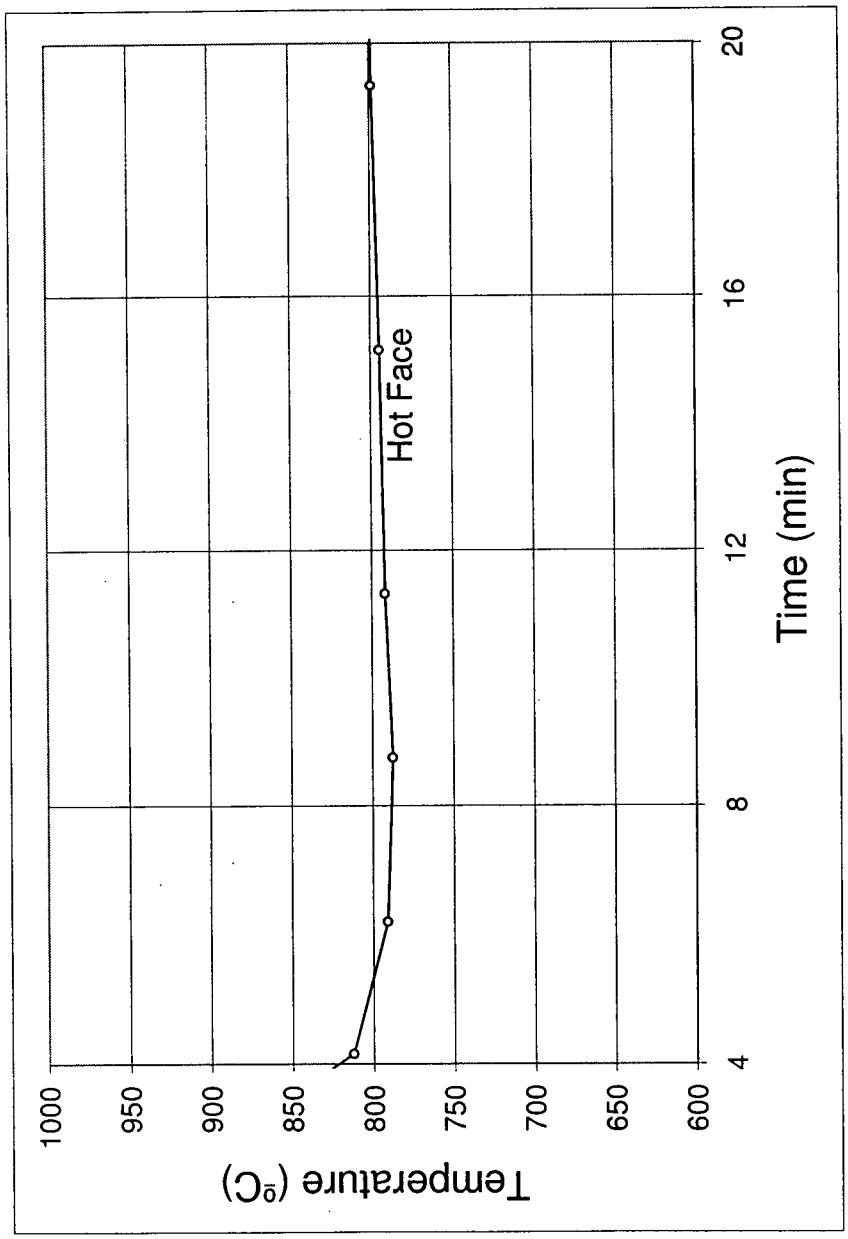

Figure F.37: Run 12 Wall Temperature History. Mix 6 at 1 rpm ($\bar{d}_p = 1.3$mm, $\sigma_p^* = 0.15$, $n_{RR} = 11.8$)

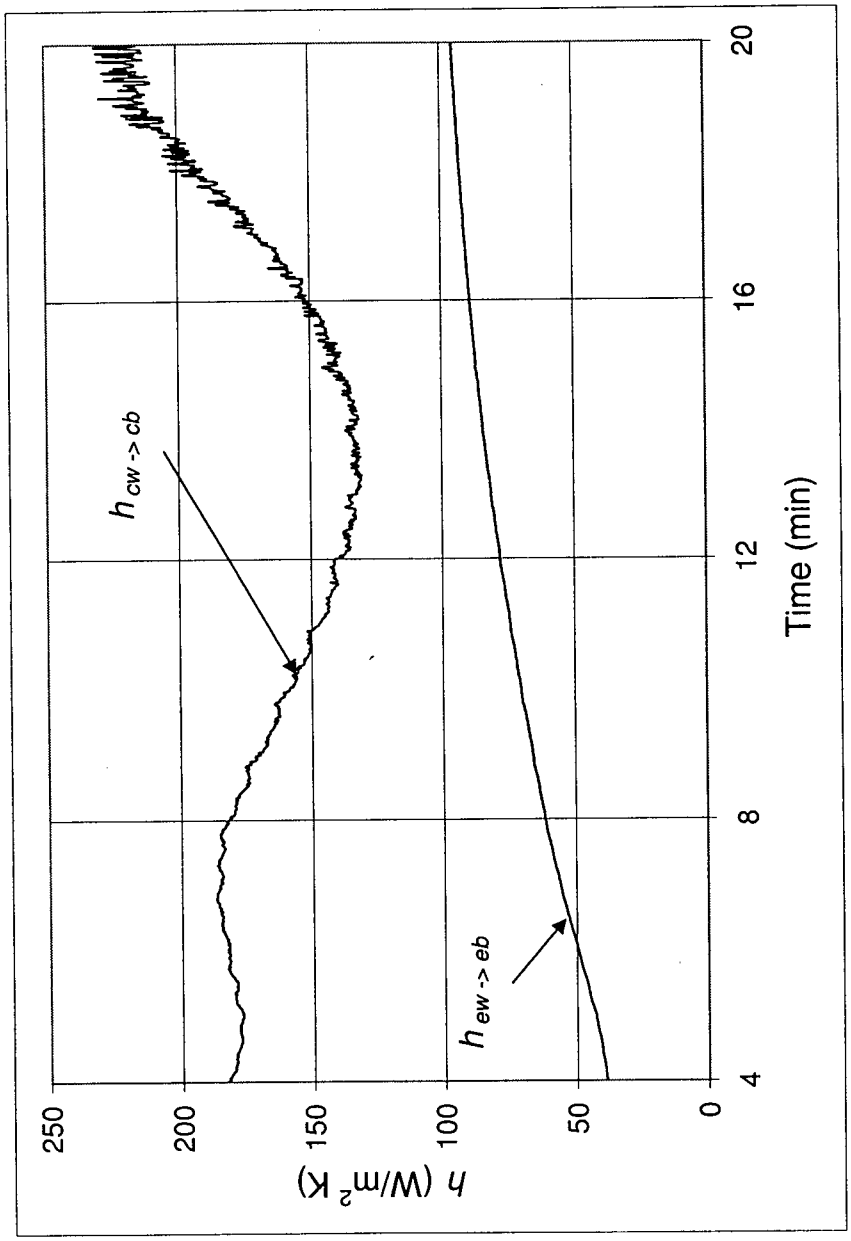

Figure F.38: Run 12 Exposed Wall to Exposed Bed, $h_{ew \to eb}$, and Covered Wall to Covered Bed, $h_{cw \to cb}$, Heat Transfer Coefficients. Mix 6 at 1 rpm ($\bar{d}_p = 1.3$mm, $\sigma_p^* = 0.15$, $n_{RR} = 11.8$)

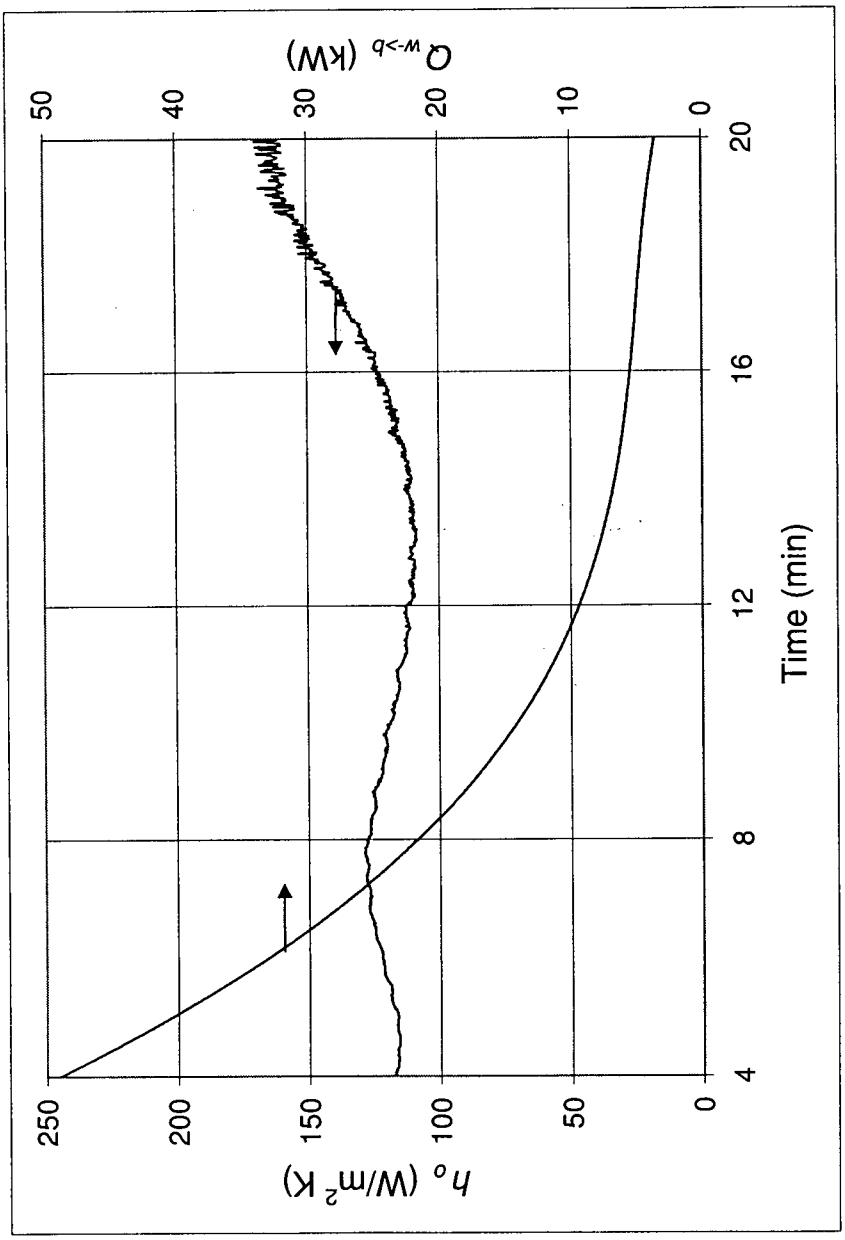

Figure F.39: Run 12 Overall Wall to Bed Heat Transfer Coefficient, h_o, and Heat Flow, $Q_{w\to b}$. Mix 6 at 1 rpm ($\bar{d}_p = 1.3$mm, $\sigma_p^* = 0.15$, $n_{RR} = 11.8$)

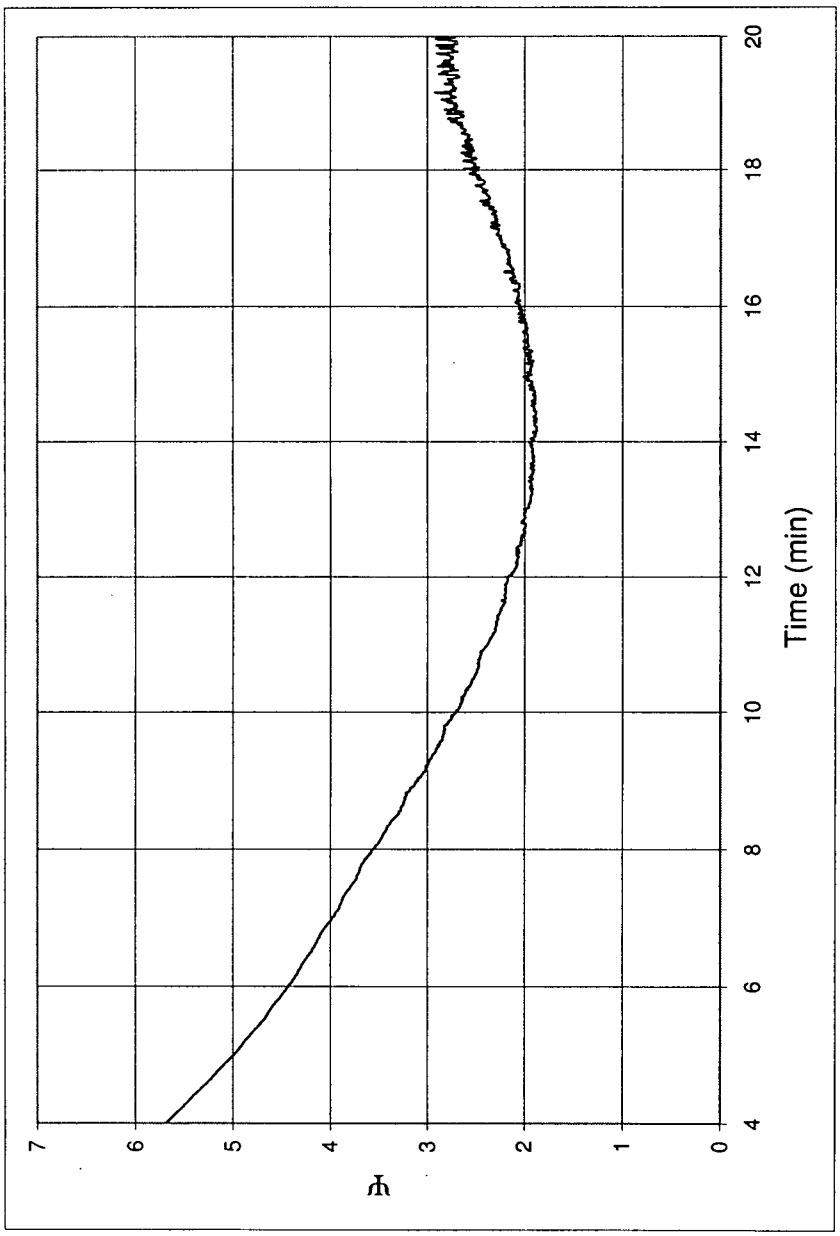

Figure F.40: Run 12 Ratio Between Heat Flow to Covered Wall and Exposed Wall, Ψ. Mix 6 at 1 rpm ($\bar{d}_p = 1.3$mm, $\sigma_p^* = 0.15$, $n_{RR} = 11.8$)

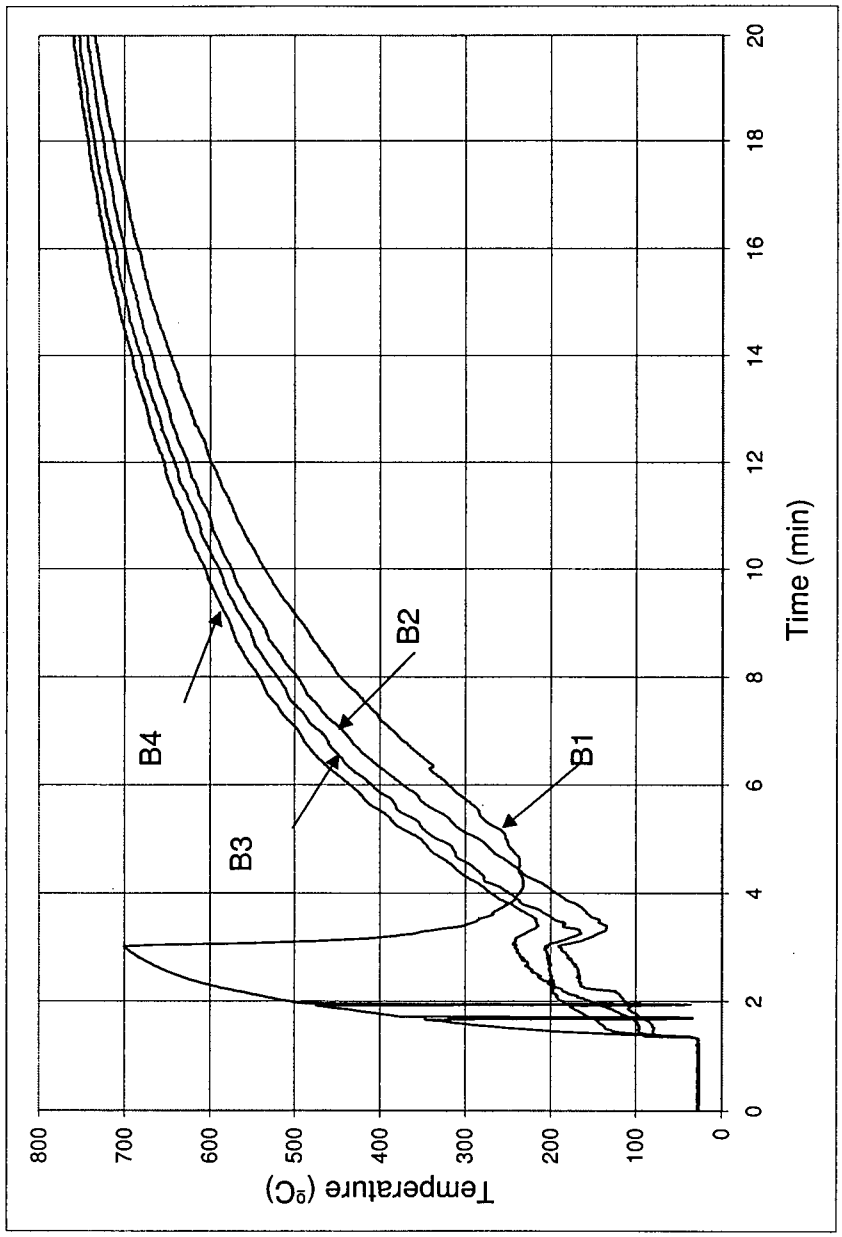

Figure F.41: Run 13 Bed Temperature History. Mix 5 at 1 rpm ($\bar{d}_p = 1.2$mm, $\sigma_p^* = 0.22$, $n_{RR} = 7.7$)

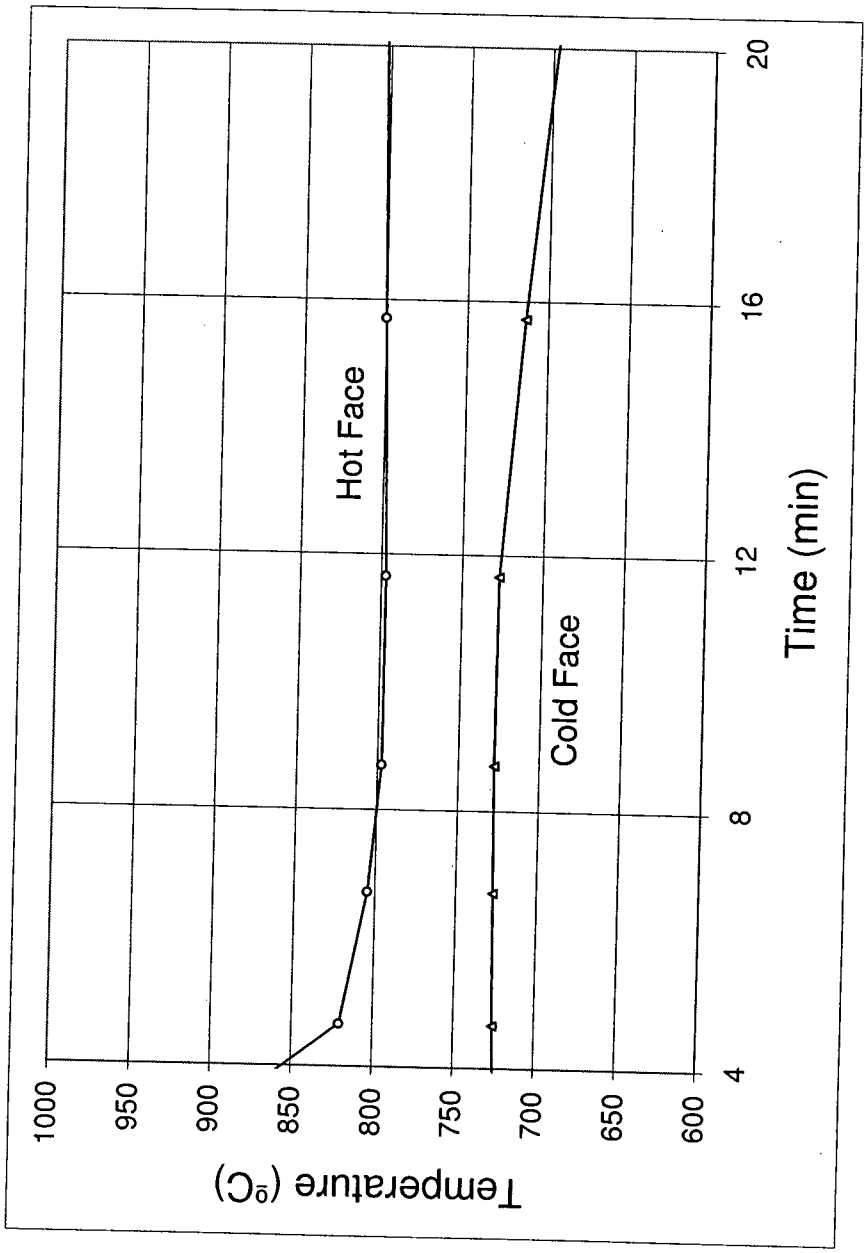

Figure F.42: Run 13 Wall Temperature History. Mix 5 at 1 rpm ($\bar{d}_p = 1.2$mm, $\sigma_p^* = 0.22$, $n_{RR} = 7.7$)

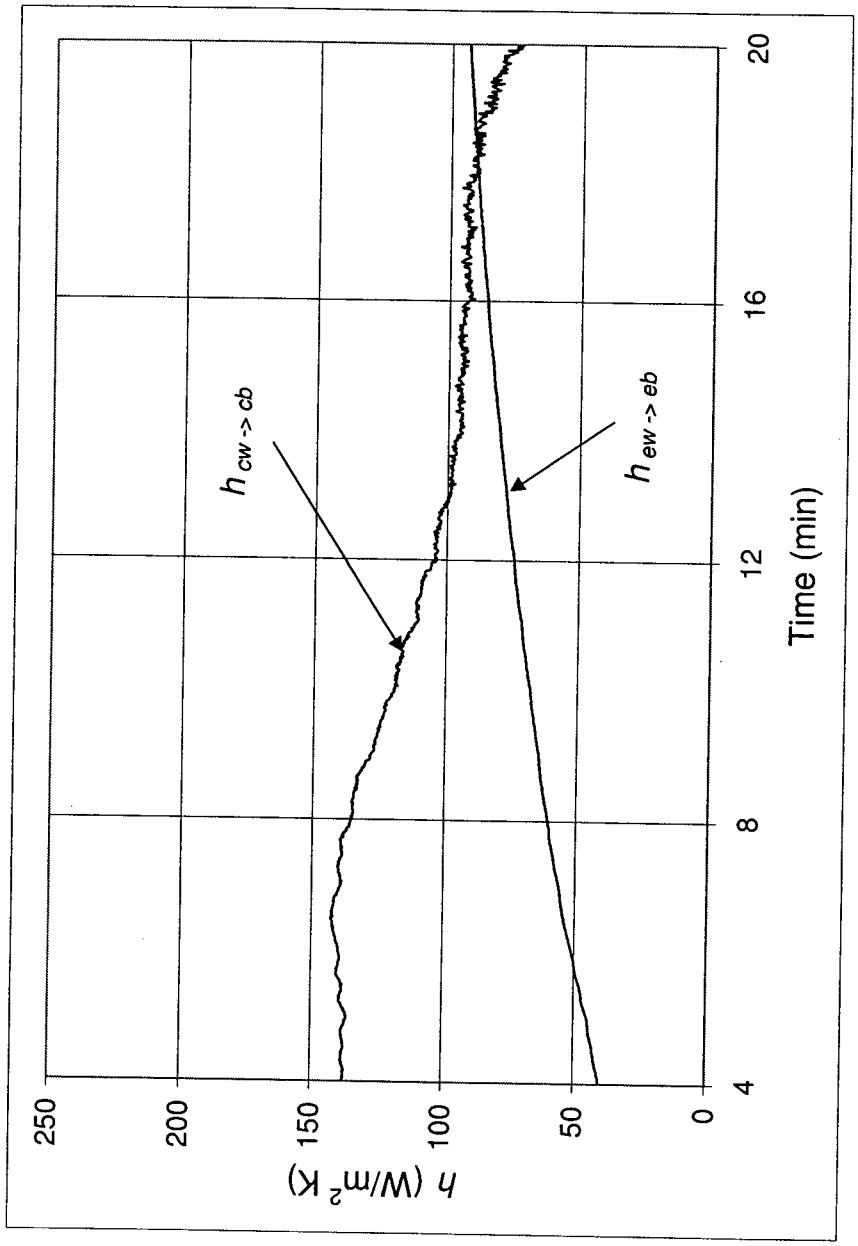

Figure F.43: Run 13 Exposed Wall to Exposed Bed, $h_{ew \to eb}$, and Covered Wall to Covered Bed, $h_{cw \to cb}$, Heat Transfer Coefficients. Mix 5 at 1 rpm ($\bar{d_p} = 1.2$mm, $\sigma_p^* = 0.22$, $n_{RR} = 7.7$)

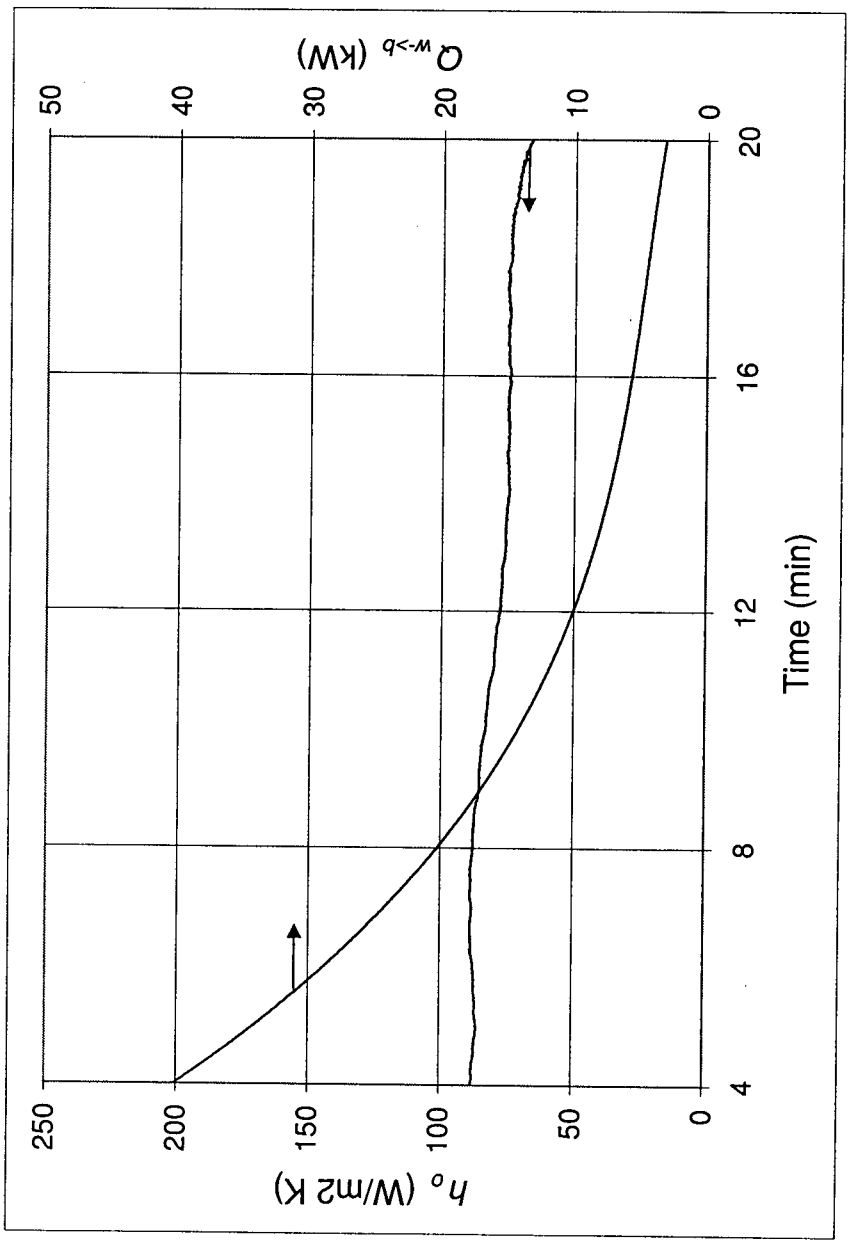

Figure F.44: Run 13 Overall Wall to Bed Heat Transfer Coefficient, h_o, and Heat Flow, $Q_{w \to b}$. Mix 5 at 1 rpm ($\bar{d}_p = 1.2$mm, $\sigma_p^* = 0.22$, $n_{RR} = 7.7$)

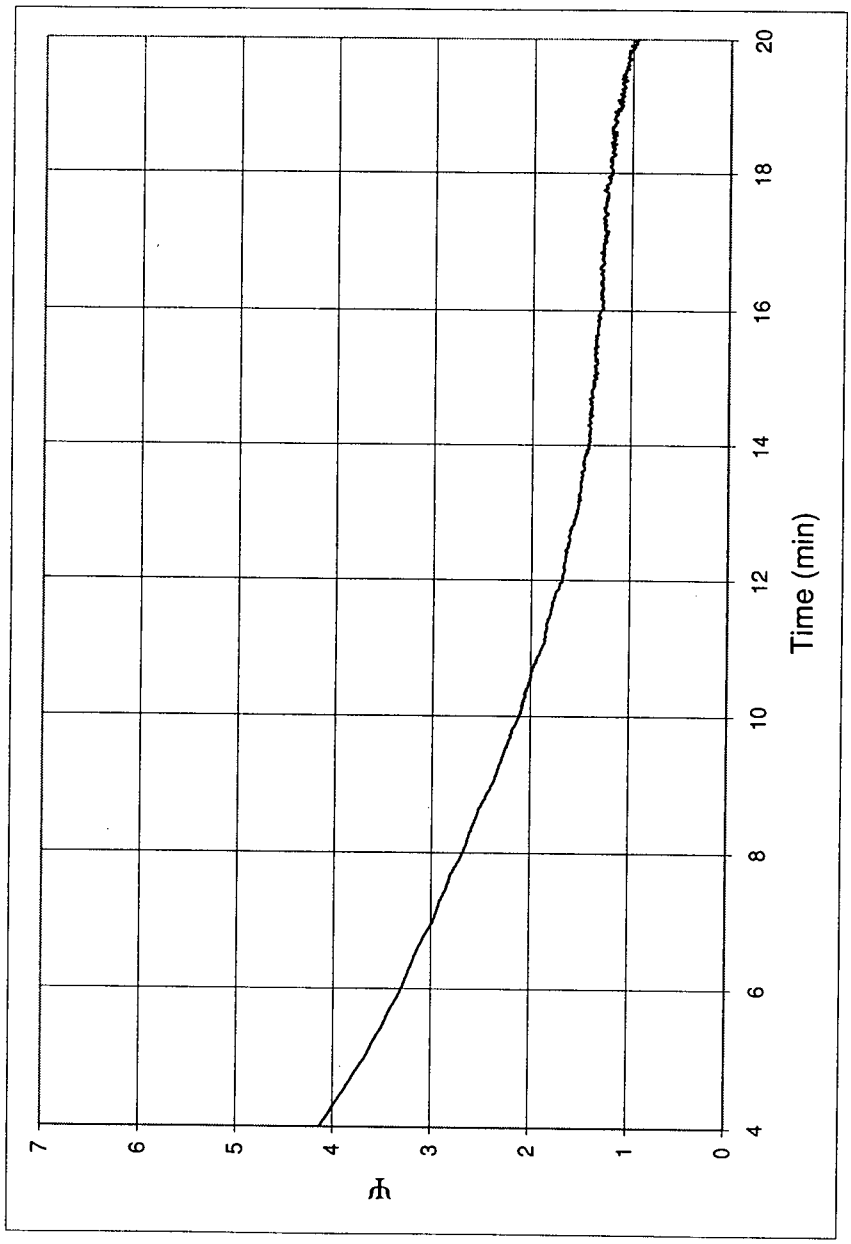

Figure F.45: Run 13 Ratio Between Heat Flow to Covered Wall and Exposed Wall, Ψ. Mix 5 at 1 rpm ($\bar{d}_p = 1.2$mm, $\sigma_p^* = 0.22$, $n_{RR} = 7.7$)

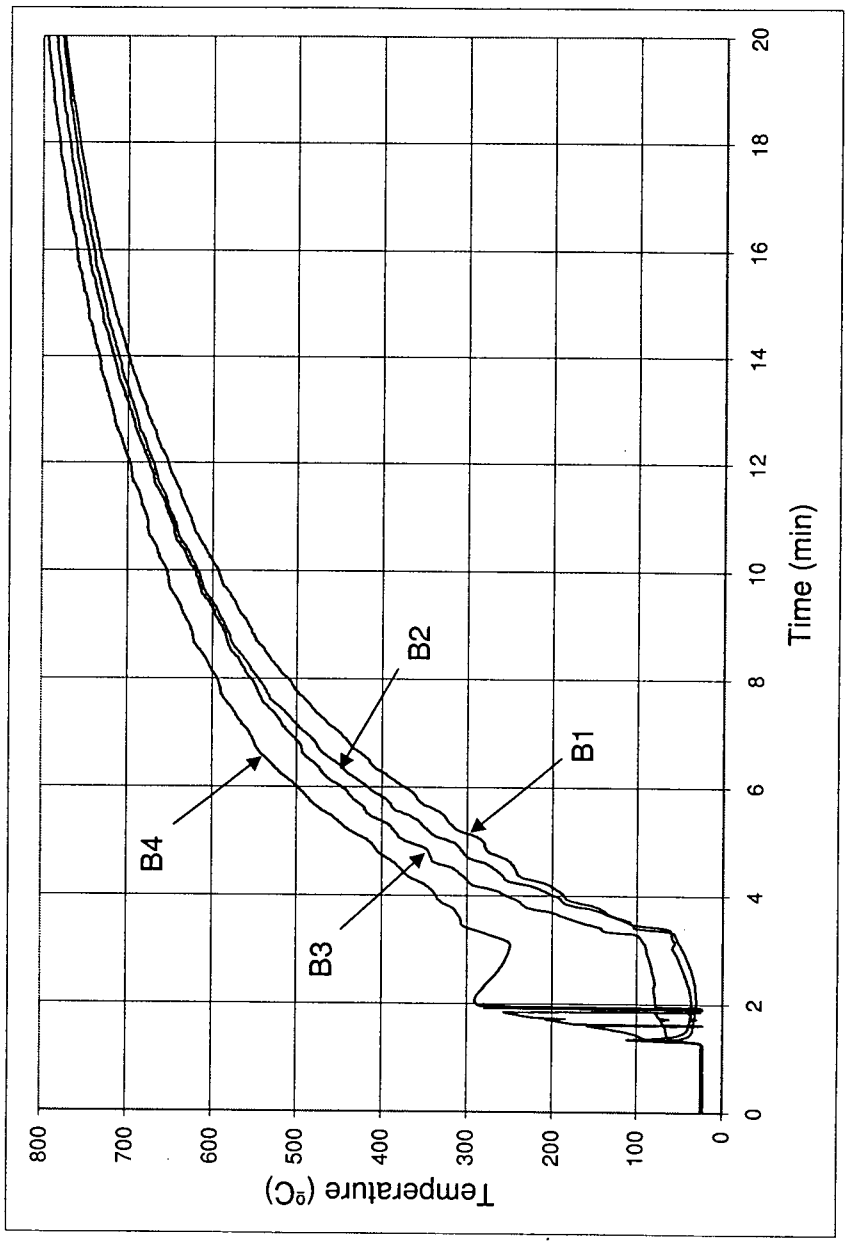

Figure F.46: Run 14 Bed Temperature History. Mix 5 at 1 rpm ($\bar{d}_p = 1.2$mm, $\sigma_p^* = 0.22$, $n_{RR} = 7.7$)

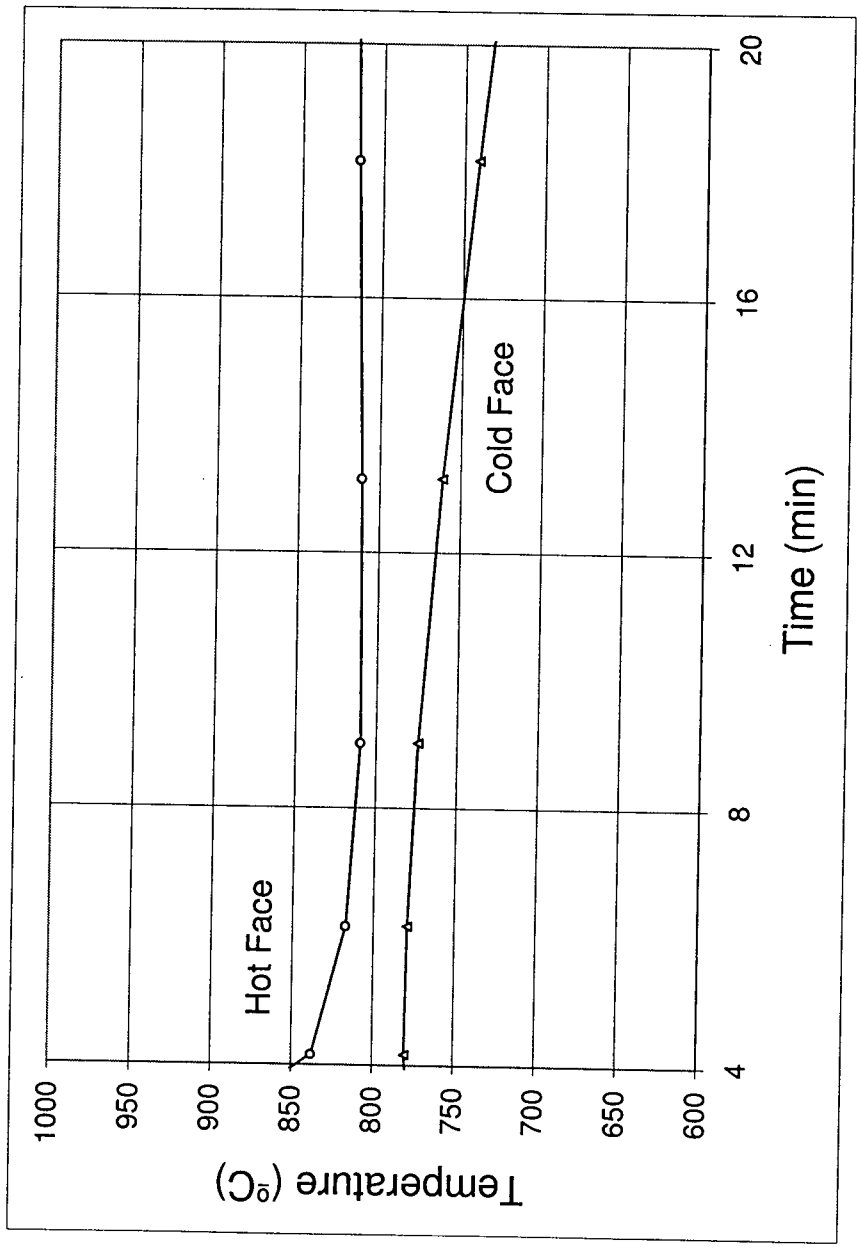

Figure F.47: Run 14 Wall Temperature History. Mix 5 at 1 rpm ($\bar{d_p} = 1.2$mm, $\sigma_p^* = 0.22$, $n_{RR} = 7.7$)

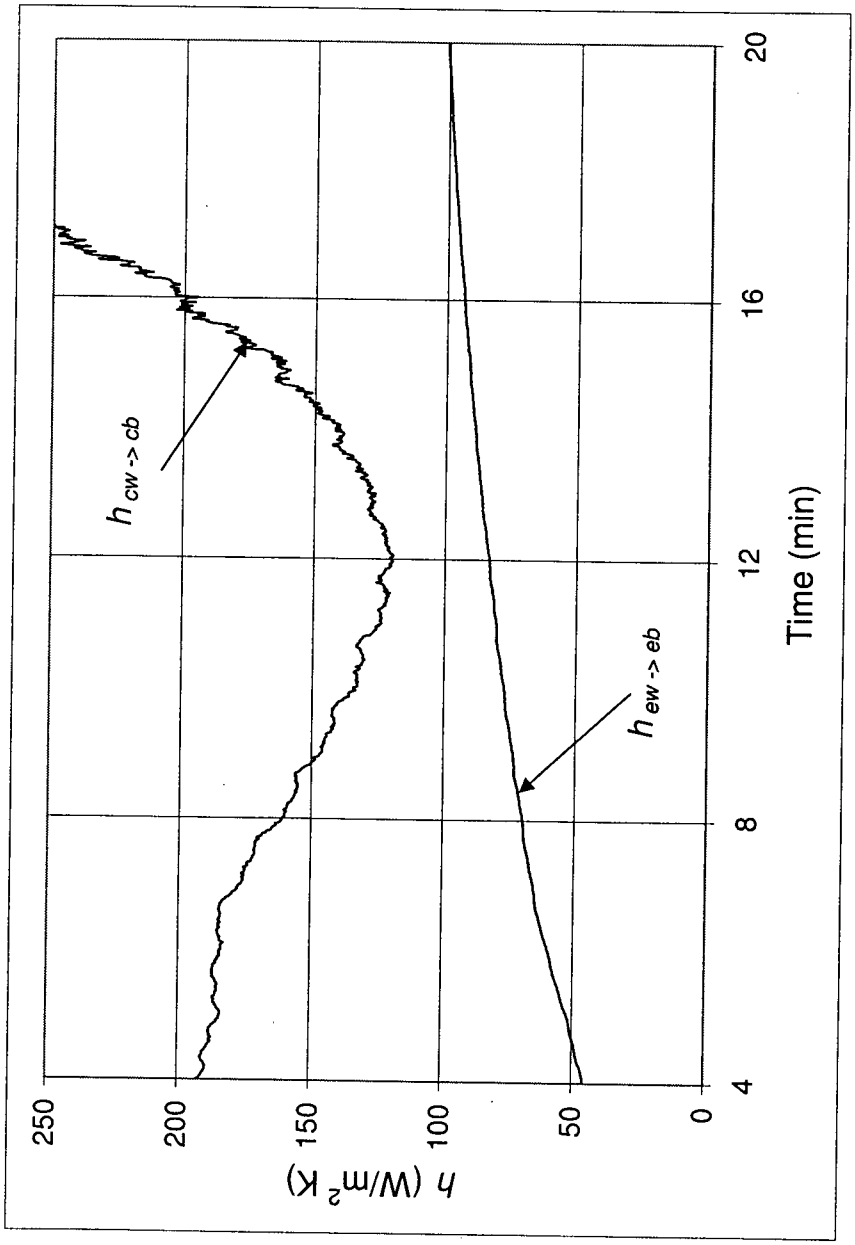

Figure F.48: Run 14 Exposed Wall to Exposed Bed, $h_{ew \to eb}$, and Covered Wall to Covered Bed, $h_{cw \to cb}$, Heat Transfer Coefficients. Mix 5 at 1 rpm ($\bar{d}_p = 1.2$mm, $\sigma_p^* = 0.22$, $n_{RR} = 7.7$)

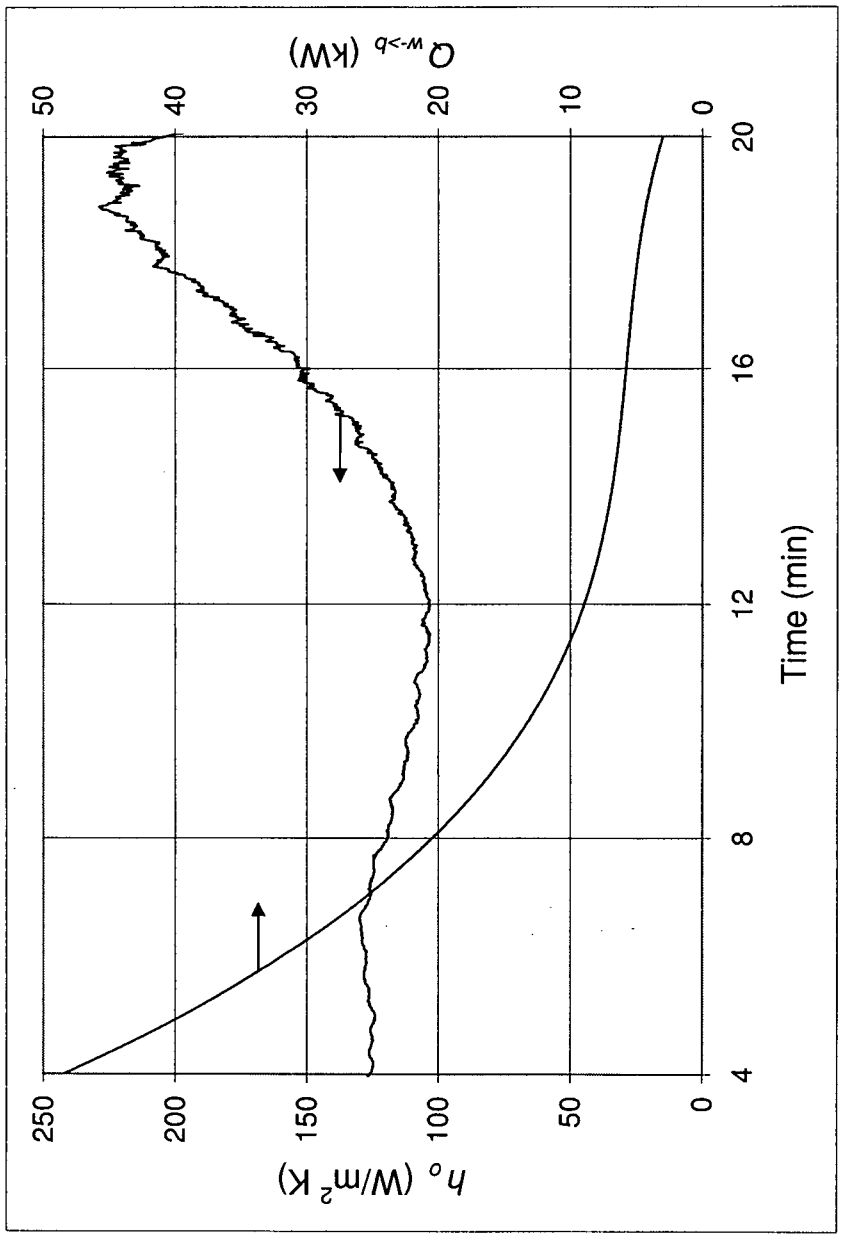

Figure F.49: Run 14 Overall Wall to Bed Heat Transfer Coefficient, h_o, and Heat Flow, $Q_{w \to b}$. Mix 5 at 1 rpm ($\bar{d}_p = 1.2$mm, $\sigma_p^* = 0.22$, $n_{RR} = 7.7$)

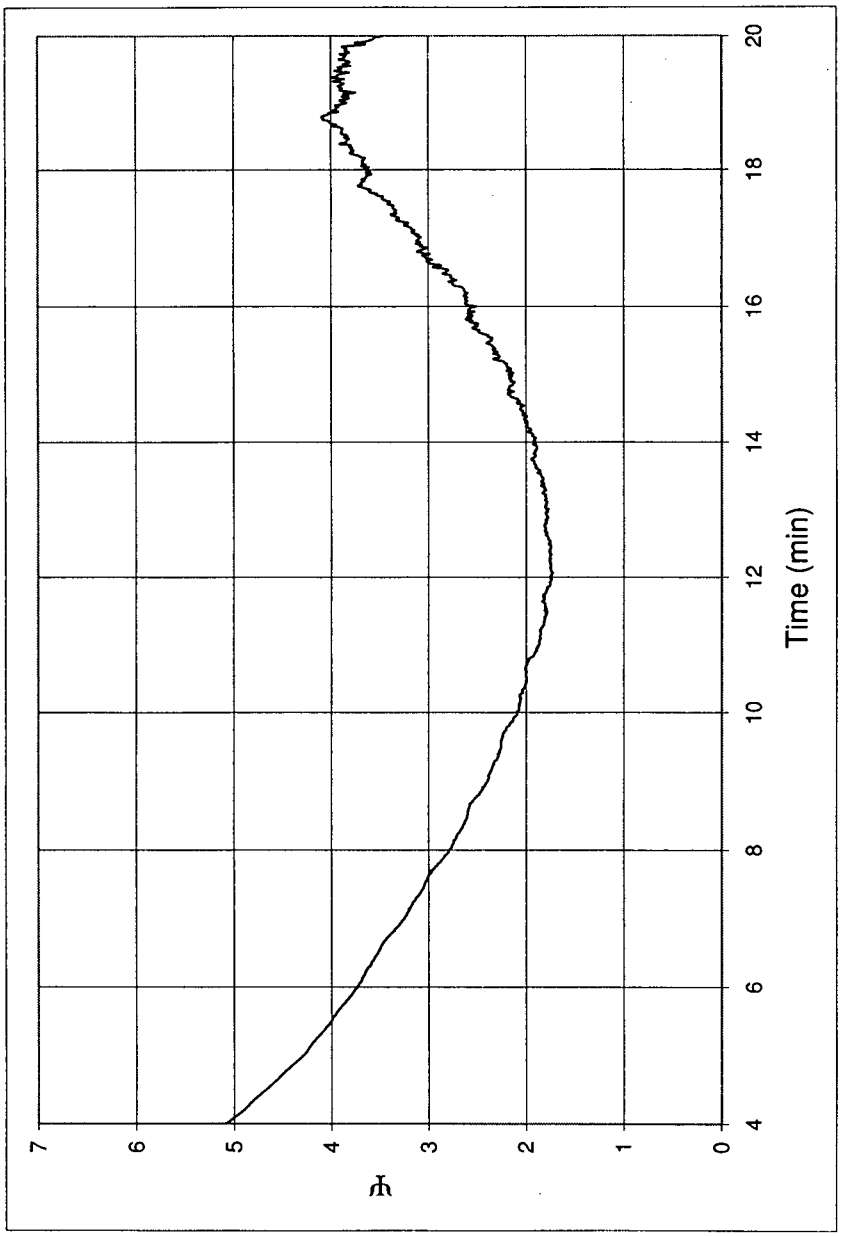

Figure F.50: Run 14 Ratio Between Heat Flow to Covered Wall and Exposed Wall, Ψ. Mix 5 at 1 rpm ($\bar{d_p} = 1.2$mm, $\sigma_p^* = 0.22$, $n_{RR} = 7.7$)

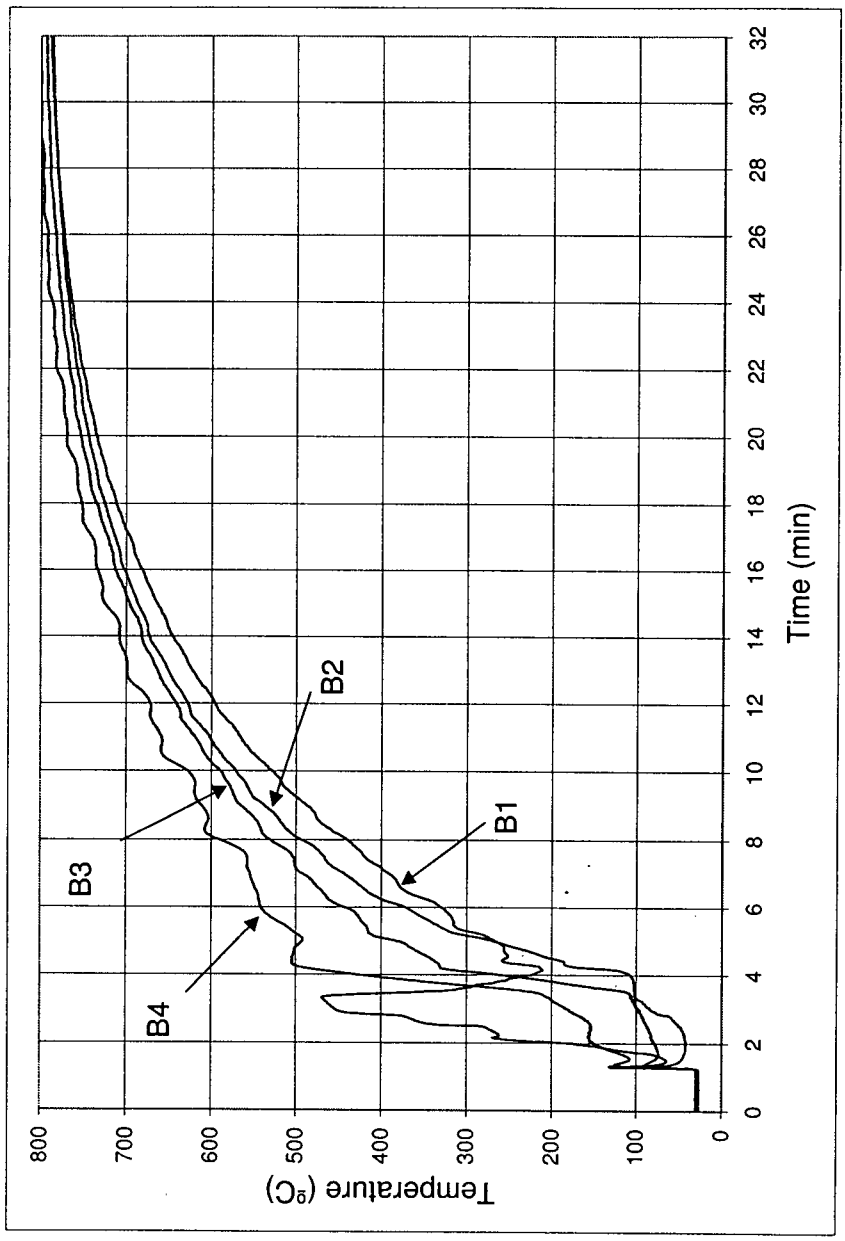

Figure F.51: Run 15 Bed Temperature History. Mix 5 at 0.43 rpm ($\bar{d}_p = 1.2$mm, $\sigma_p^* = 0.22$, $n_{RR} = 7.7$)

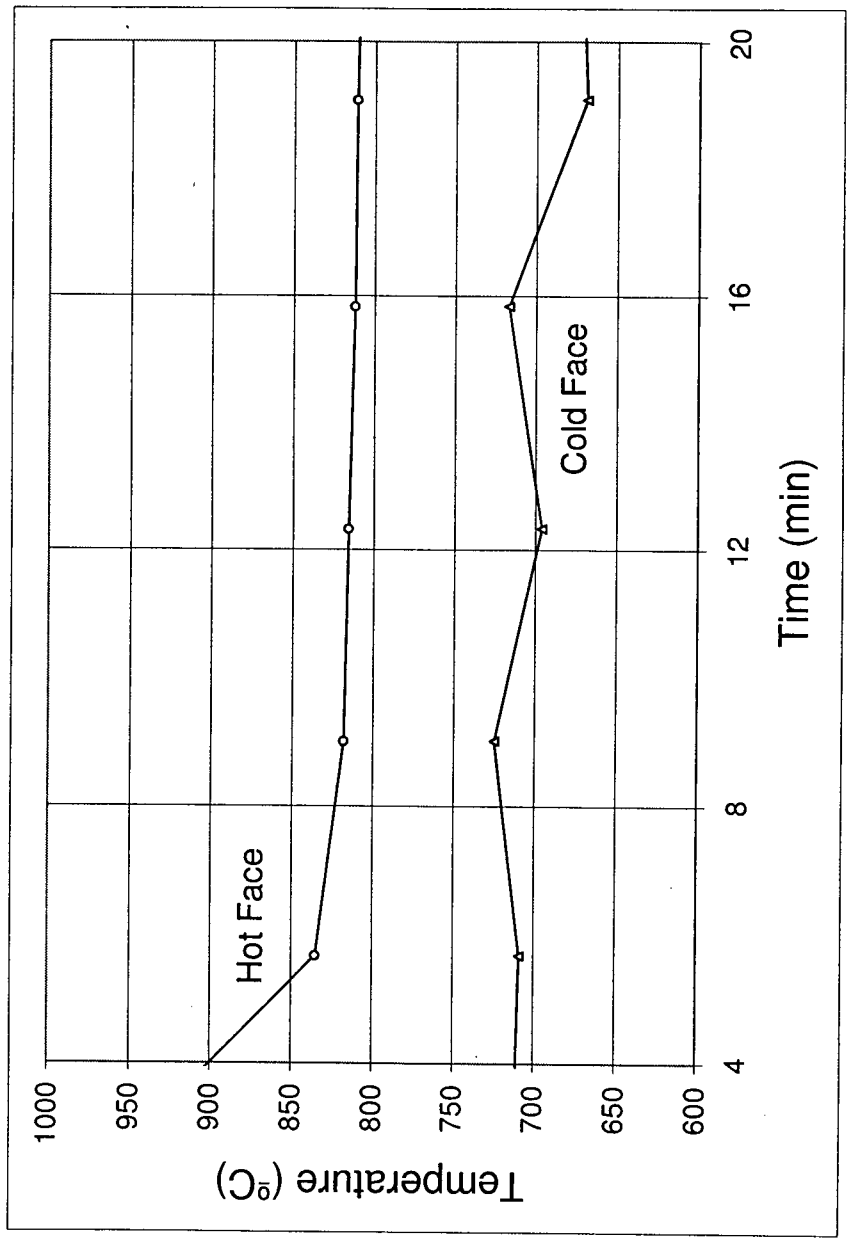

Figure F.52: Run 15 Wall Temperature History. Mix 5 at 0.43 rpm ($\bar{d}_p = 1.2$mm, $\sigma_p^* = 0.22$, $n_{RR} = 7.7$)

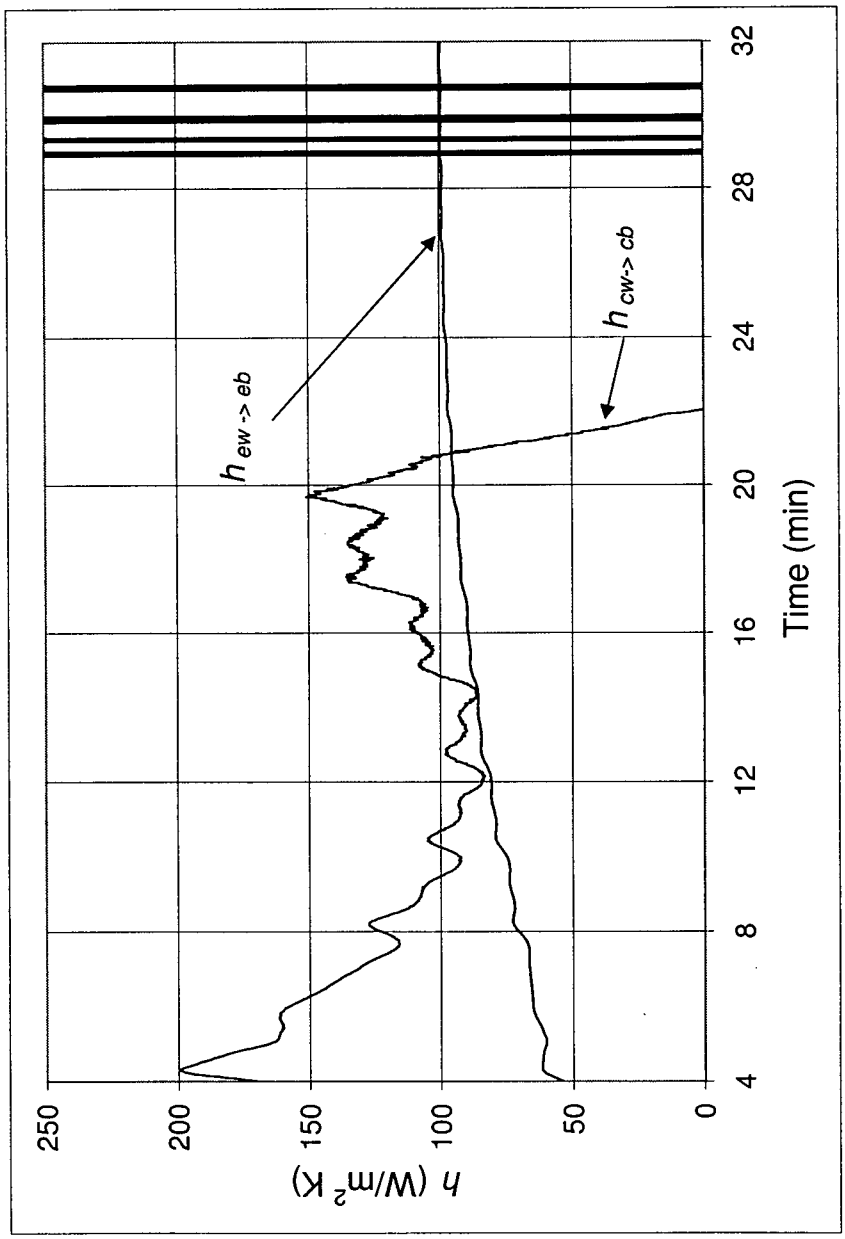

Figure F.53: Run 15 Exposed Wall to Exposed Bed, $h_{ew \to eb}$, and Covered Wall to Covered Bed, $h_{cw \to cb}$, Heat Transfer Coefficients. Mix 5 at 0.43 rpm ($\bar{d}_p = 1.2$mm, $\sigma_p^* = 0.22$, $n_{RR} = 7.7$)

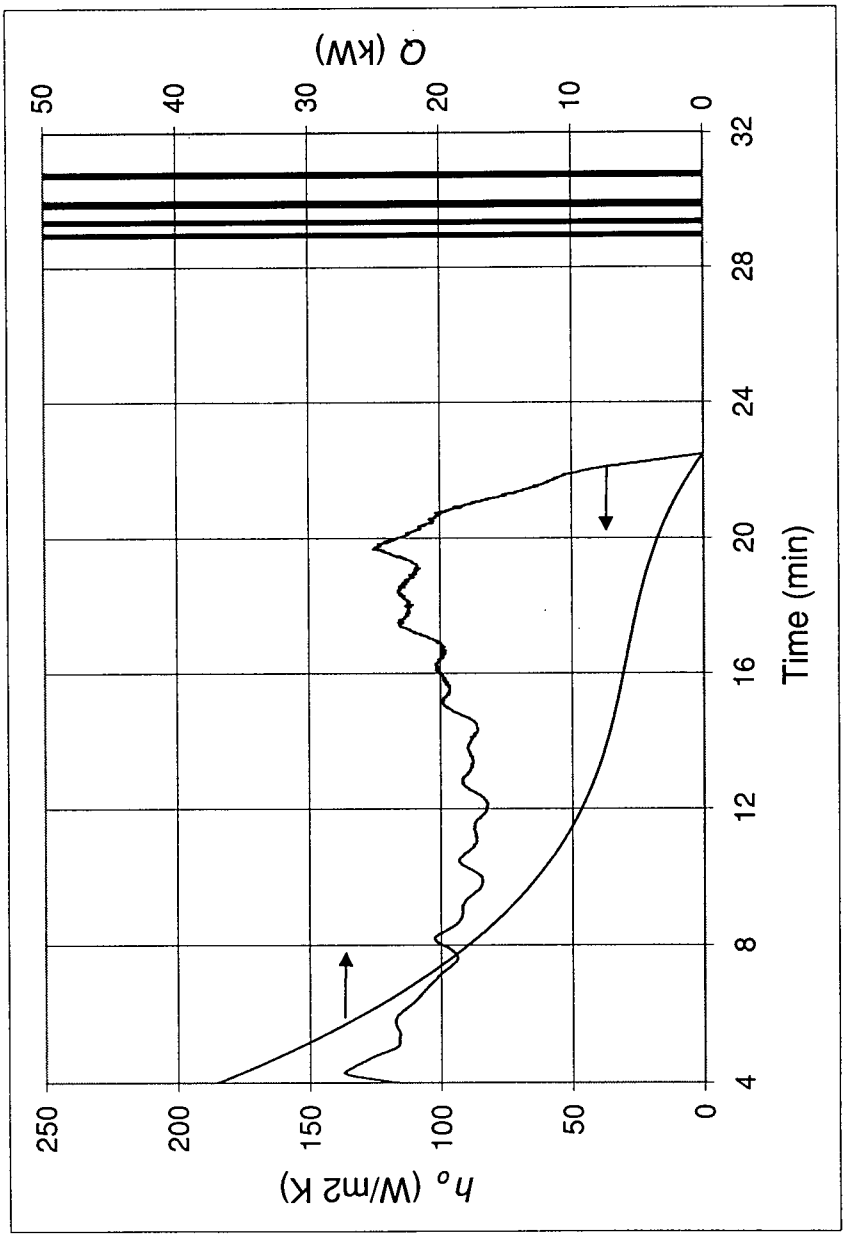

Figure F.54: Run 15 Overall Wall to Bed Heat Transfer Coefficient, h_o, and Heat Flow, $Q_{w \to b}$. Mix 5 at 0.43 rpm ($\bar{d}_p = 1.2$mm, $\sigma_p^* = 0.22$, $n_{RR} = 7.7$)

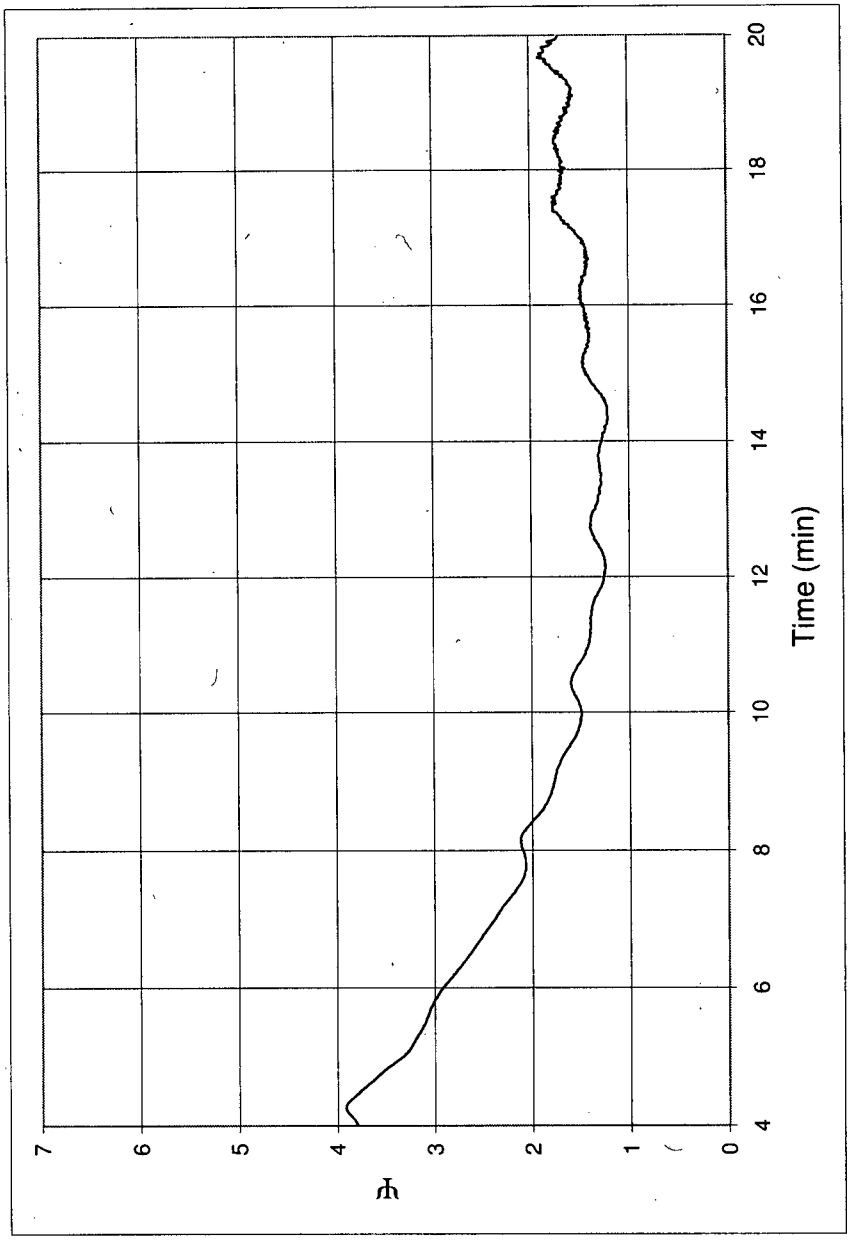

Figure F.55: Run 15 Ratio Between Heat Flow to Covered Wall and Exposed Wall, Ψ. Mix 5 at 0.43 rpm ($\bar{d}_p = 1.2$mm, $\sigma_p^* = 0.22$, $n_{RR} = 7.7$)

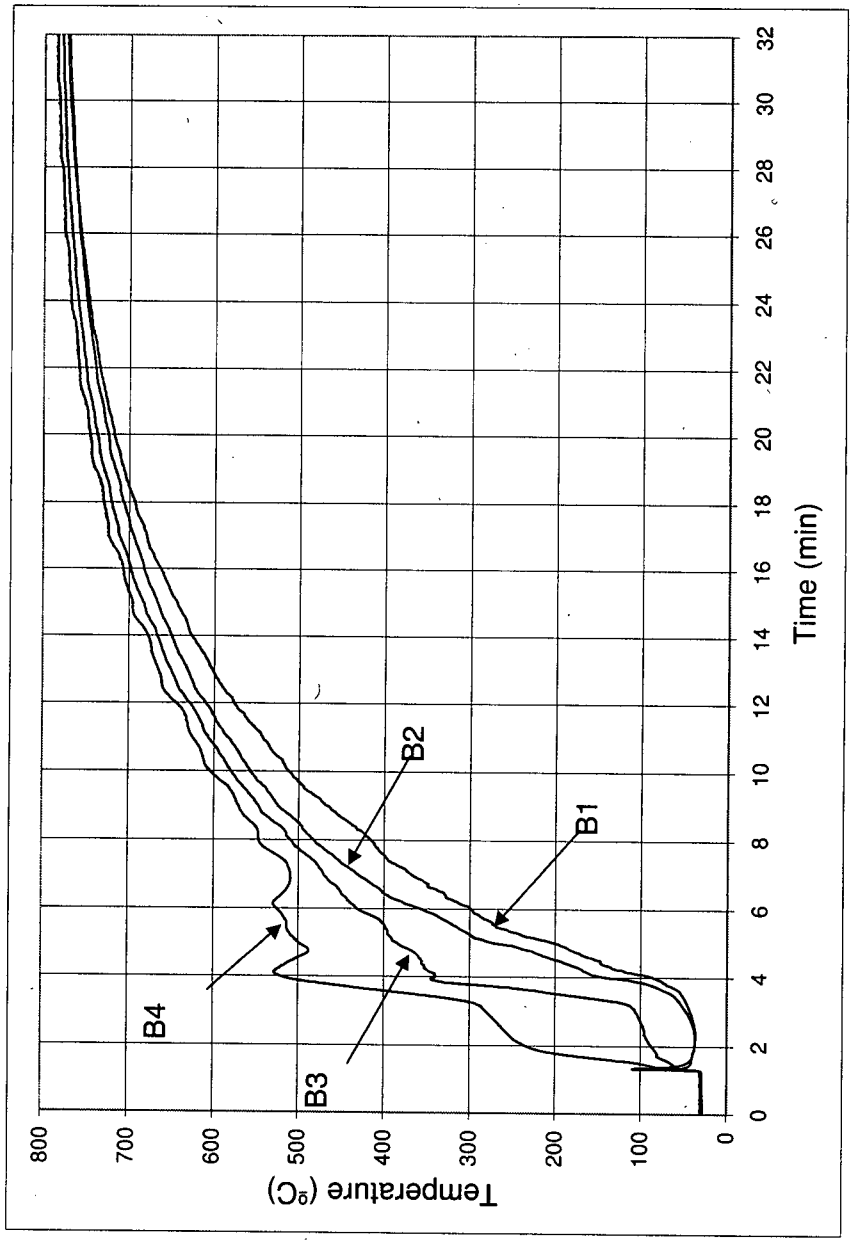

Figure F.56: Run 16 Bed Temperature History. Mix 4 at 0.43 rpm ($\bar{d}_p = 3.0$mm, $\sigma_p^* = 0.09$, $n_{RR} = 15.5$)

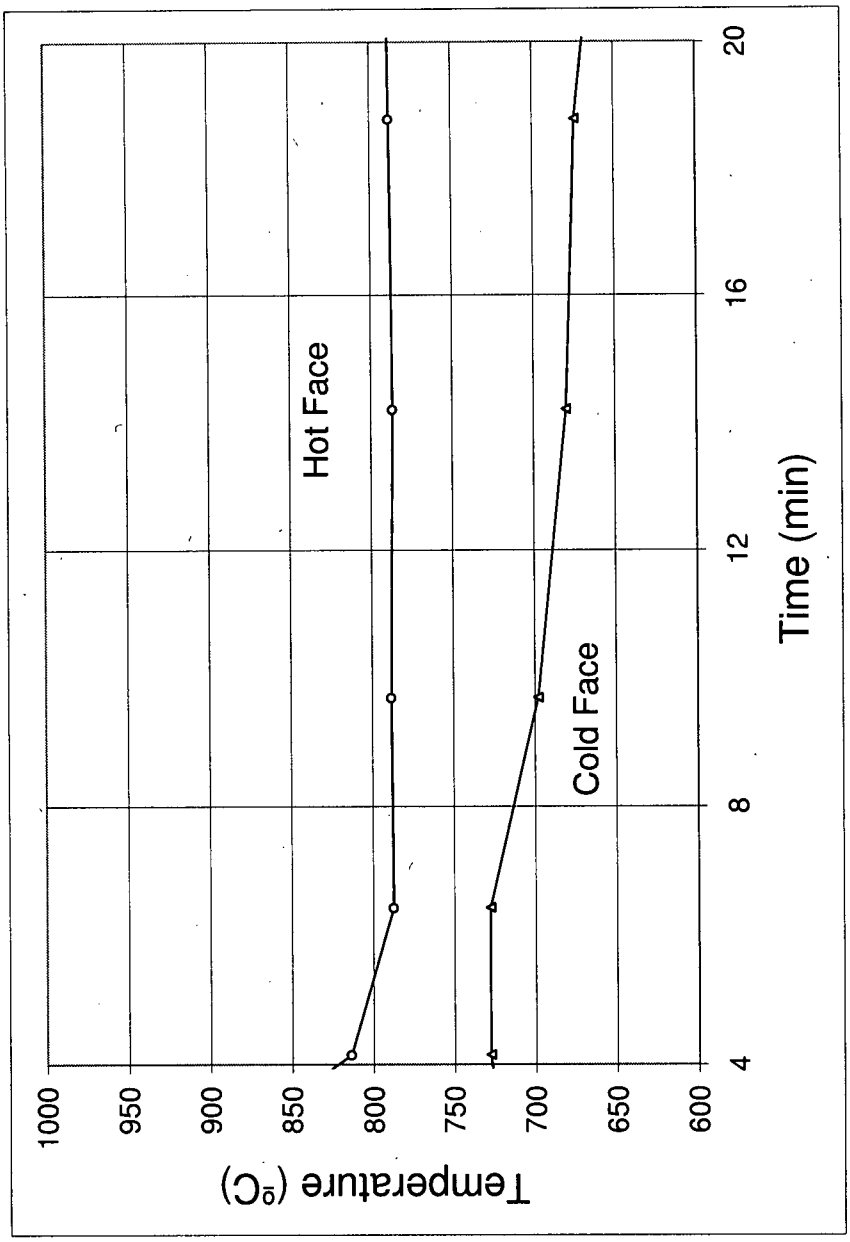

Figure F.57: Run 16 Wall Temperature History. Mix 4 at 0.43 rpm ($\bar{d}_p = 3.0$mm, $\sigma_p^* = 0.09$, $n_{RR} = 15.5$)

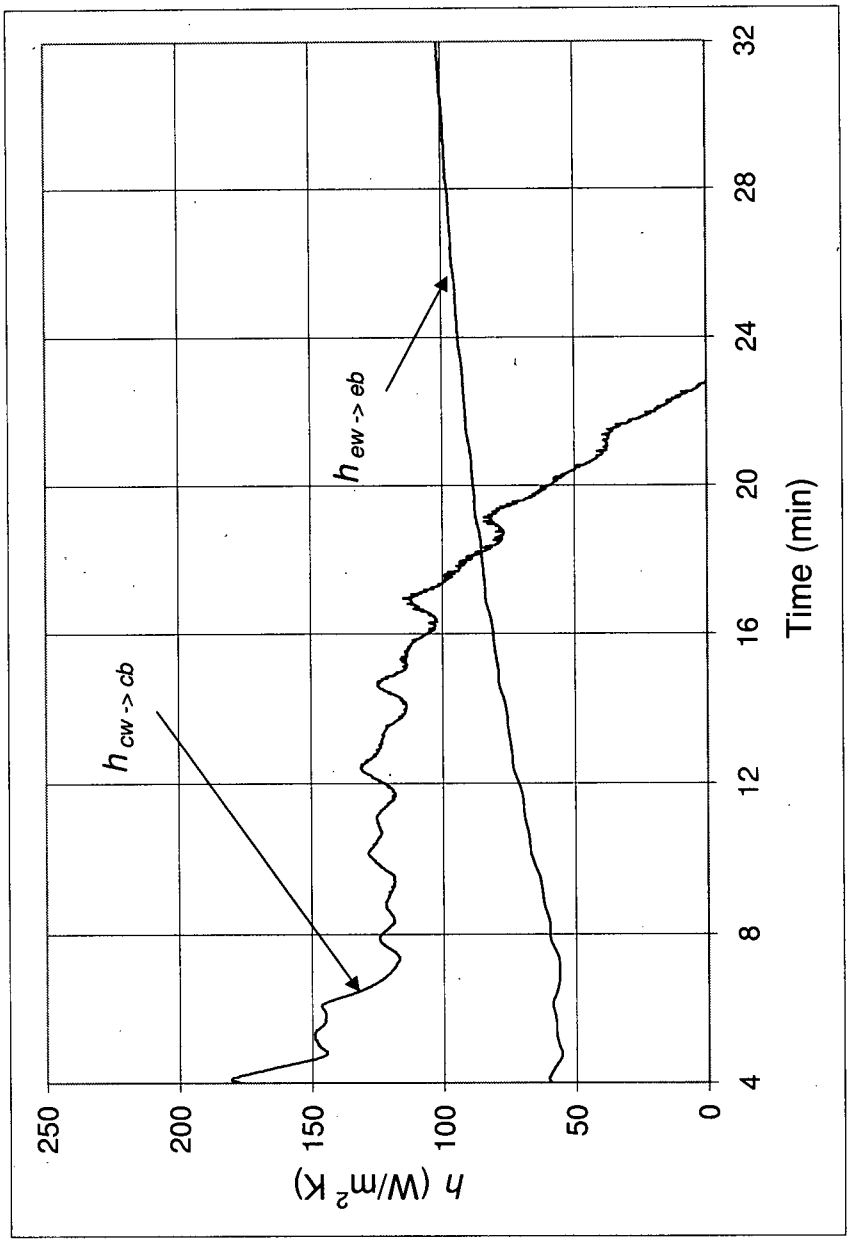

Figure F.58: Run 16 Exposed Wall to Exposed Bed, $h_{ew \to eb}$, and Covered Wall to Covered Bed, $h_{cw \to cb}$, Heat Transfer Coefficients. Mix 4 at 0.43 rpm ($\bar{d}_p = 3.0$mm, $\sigma_p^* = 0.09$, $n_{RR} = 15.5$)

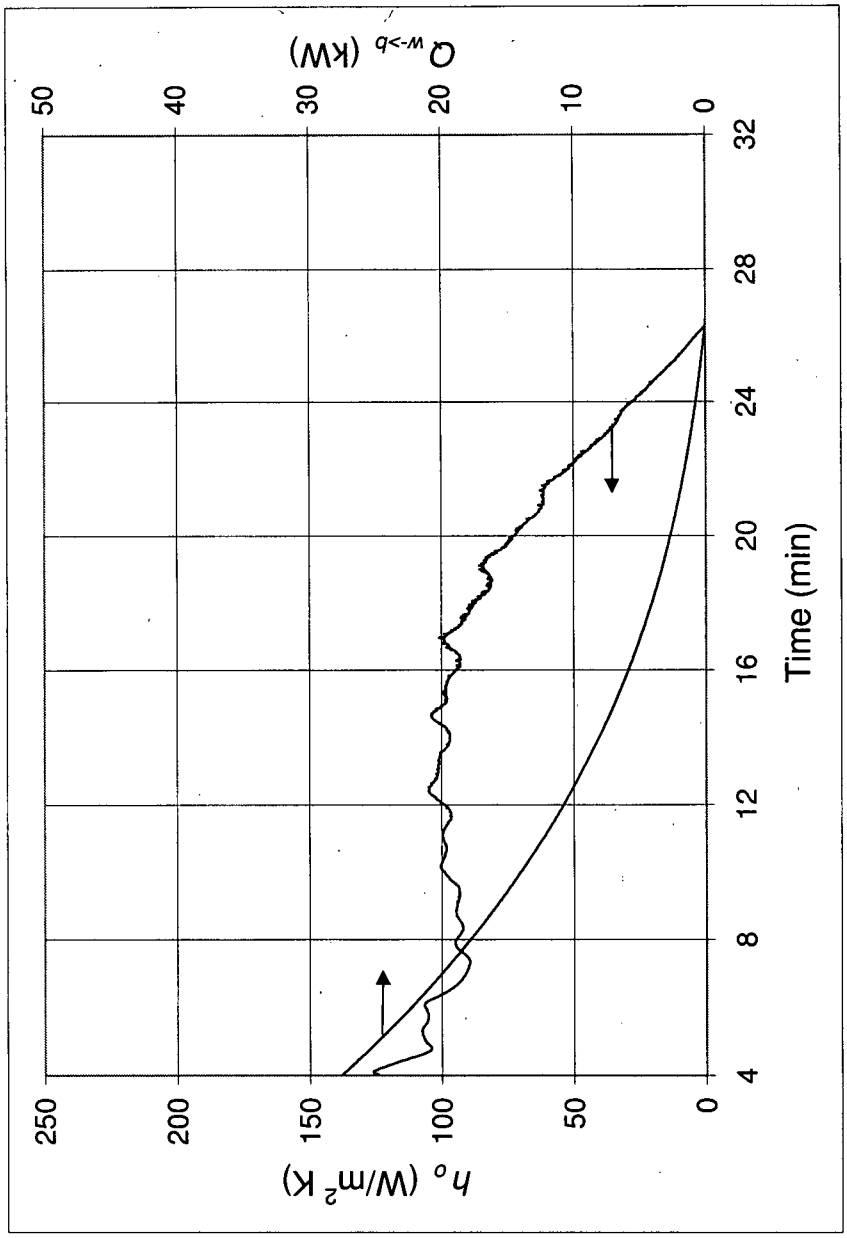

Figure F.59: Run 16 Overall Wall to Bed Heat Transfer Coefficient, h_o, and Heat Flow, $Q_{w\to b}$. Mix 4 at 0.43 rpm ($\bar{d}_p = 3.0$mm, $\sigma_p^* = 0.09$, $n_{RR} = 15.5$)

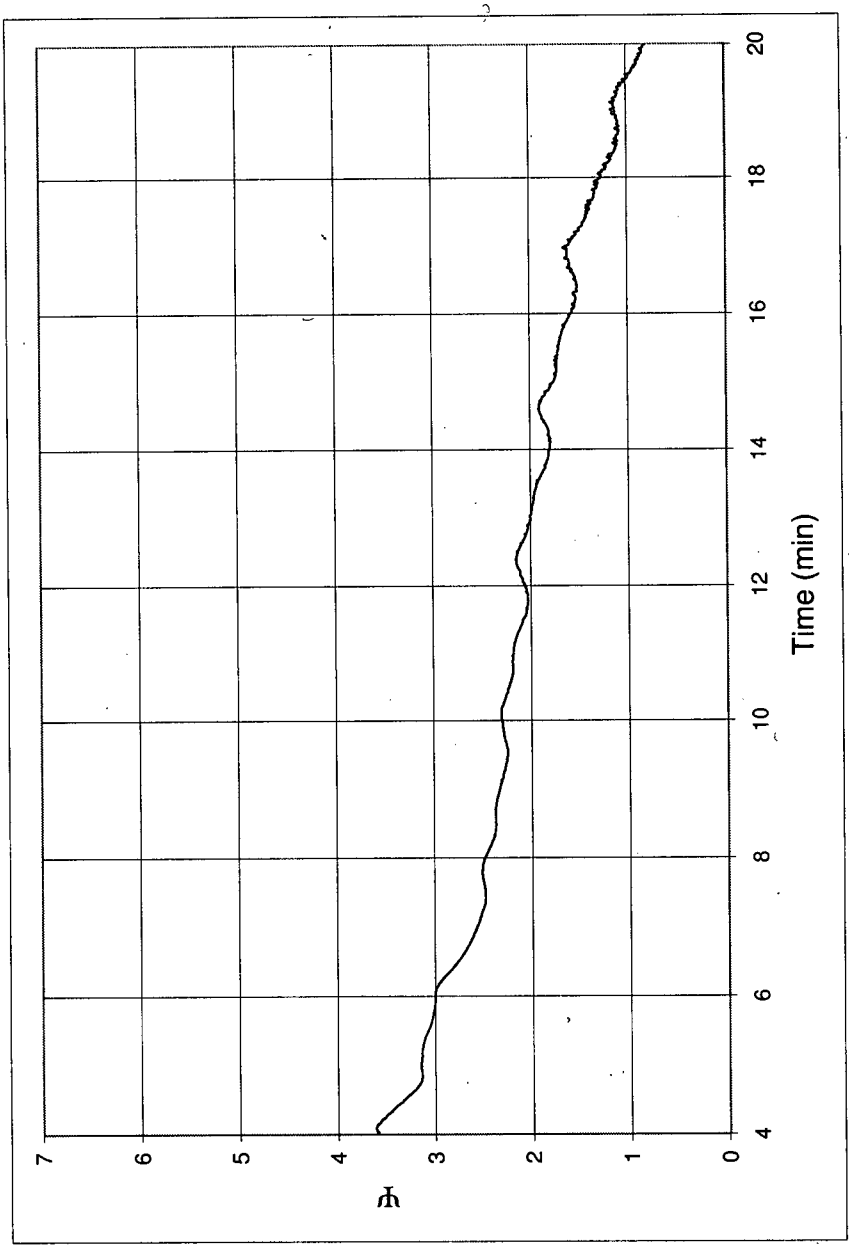

Figure F.60: Run 16 Ratio Between Heat Flow to Covered Wall and Exposed Wall, Ψ. Mix 4 at 0.43 rpm ($\bar{d_p} = 3.0$mm, $\sigma_p^* = 0.09$, $n_{RR} = 15.5$)

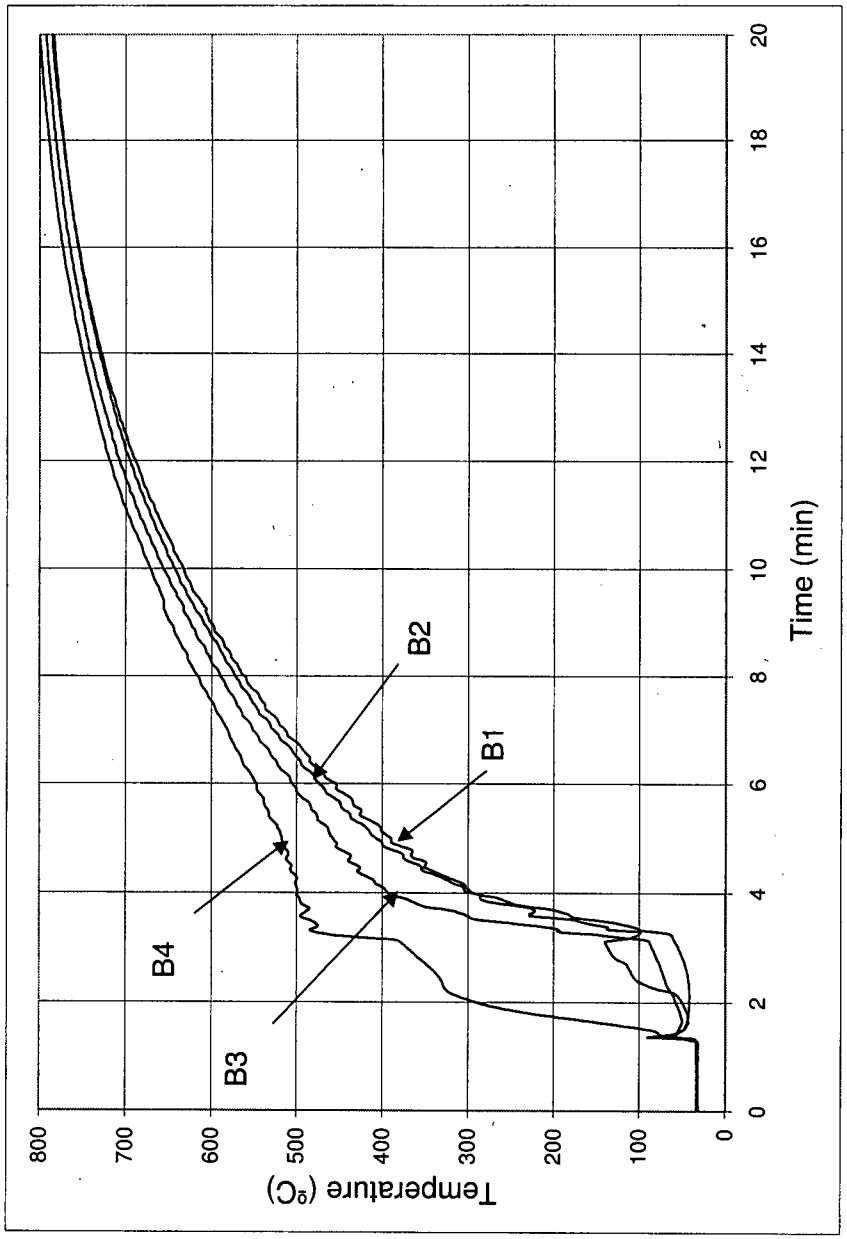

Figure F.61: Run 17 Bed Temperature History. Mix 5 at 2 rpm ($\bar{d_p} = 1.2$mm, $\sigma_p^* = 0.22$, $n_{RR} = 7.7$)

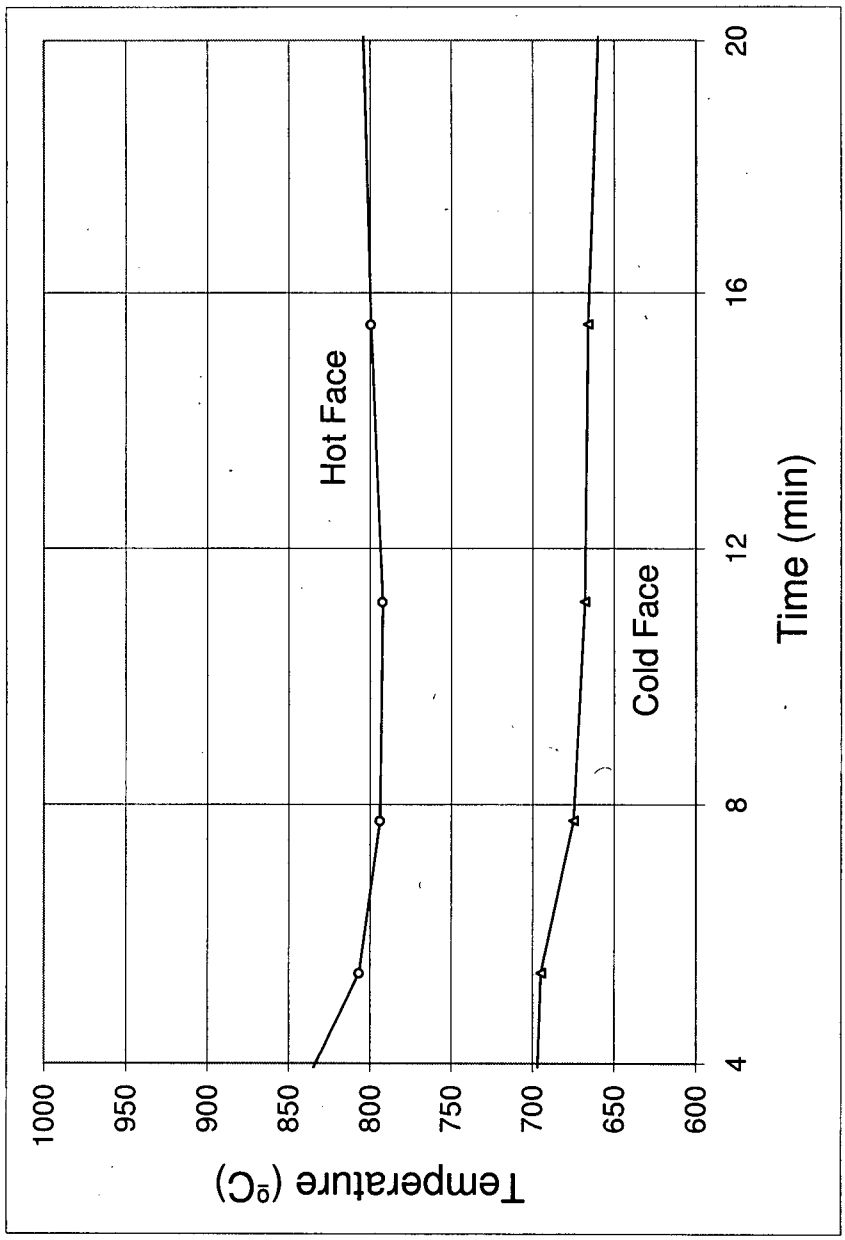

Figure F.62: Run 17 Wall Temperature History. Mix 5 at 2 rpm ($\bar{d}_p = 1.2$mm, $\sigma_p^* = 0.22$, $n_{RR} = 7.7$)

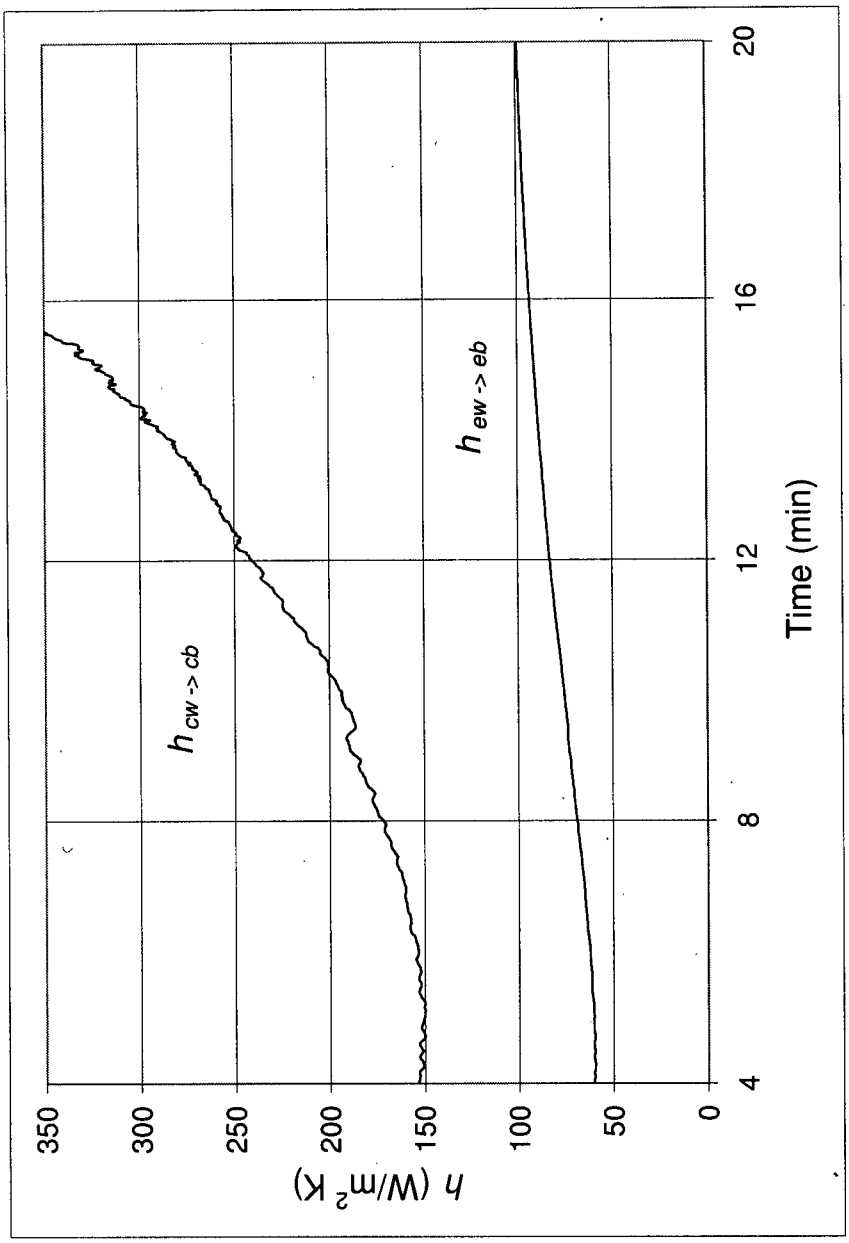

Figure F.63: Run 17 Exposed Wall to Exposed Bed, $h_{ew \to eb}$, and Covered Wall to Covered Bed, $h_{cw \to cb}$, Heat Transfer Coefficients. Mix 5 at 2 rpm ($\bar{d}_p = 1.2$mm, $\bar{\sigma}_p^* = 0.22$, $n_{RR} = 7.7$)

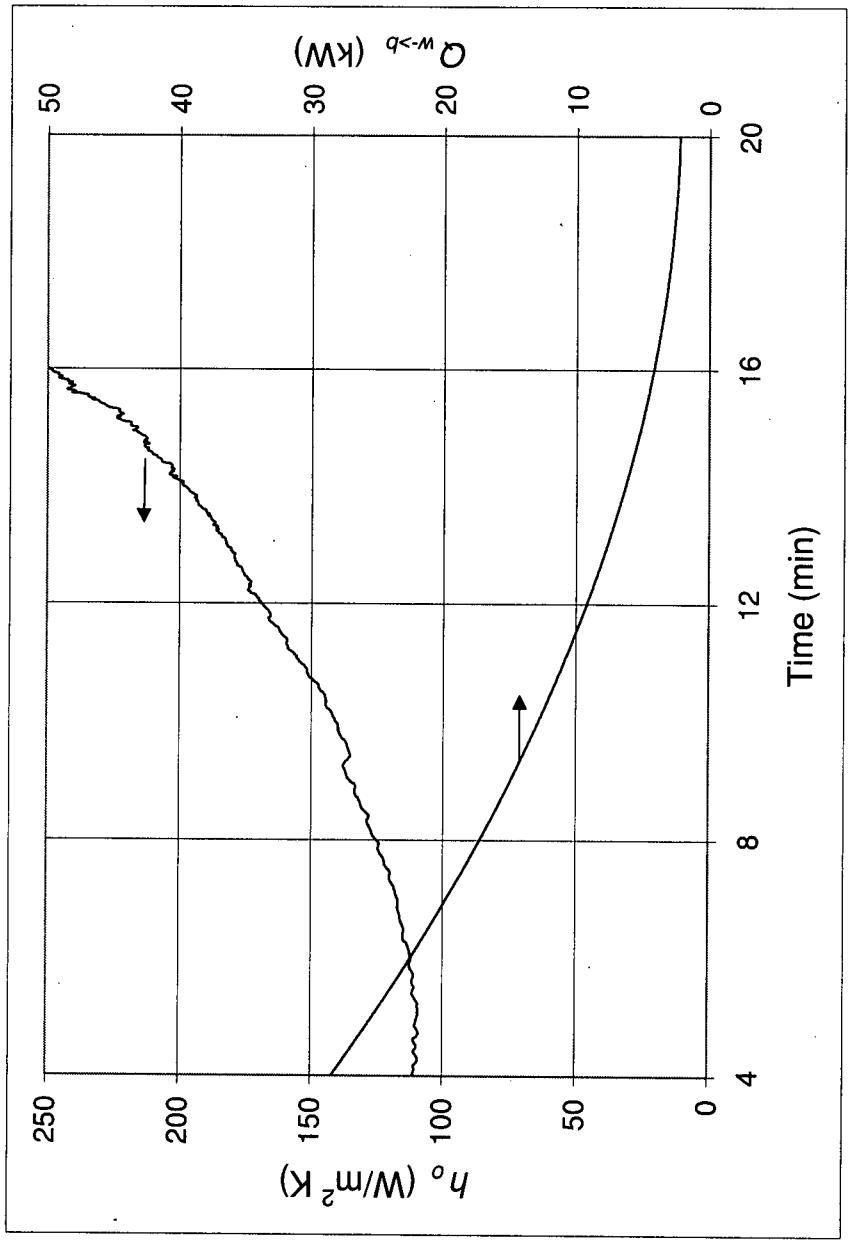

Figure F.64: Run 17 Overall Wall to Bed Heat Transfer Coefficient, h_o, and Heat Flow, $Q_{w \to b}$. Mix 5 at 2 rpm ($\bar{d_p} = 1.2$mm, $\sigma_p^* = 0.22$, $n_{RR} = 7.7$)

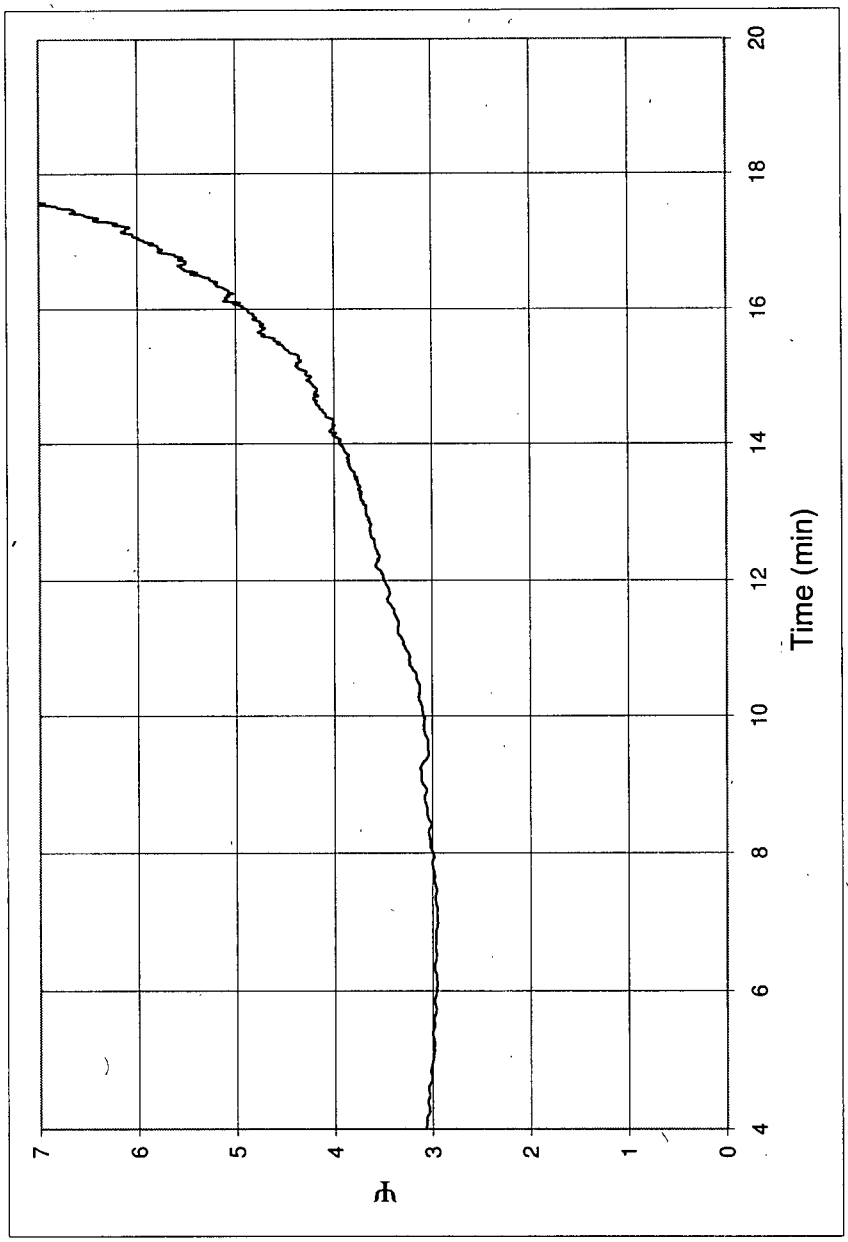

Figure F.65: Run 17 Ratio Between Heat Flow to Covered Wall and Exposed Wall, Ψ. Mix 5 at 2 rpm ($\bar{d}_p = 1.2$mm, $\sigma_p^* = 0.22$, $n_{RR} = 7.7$)

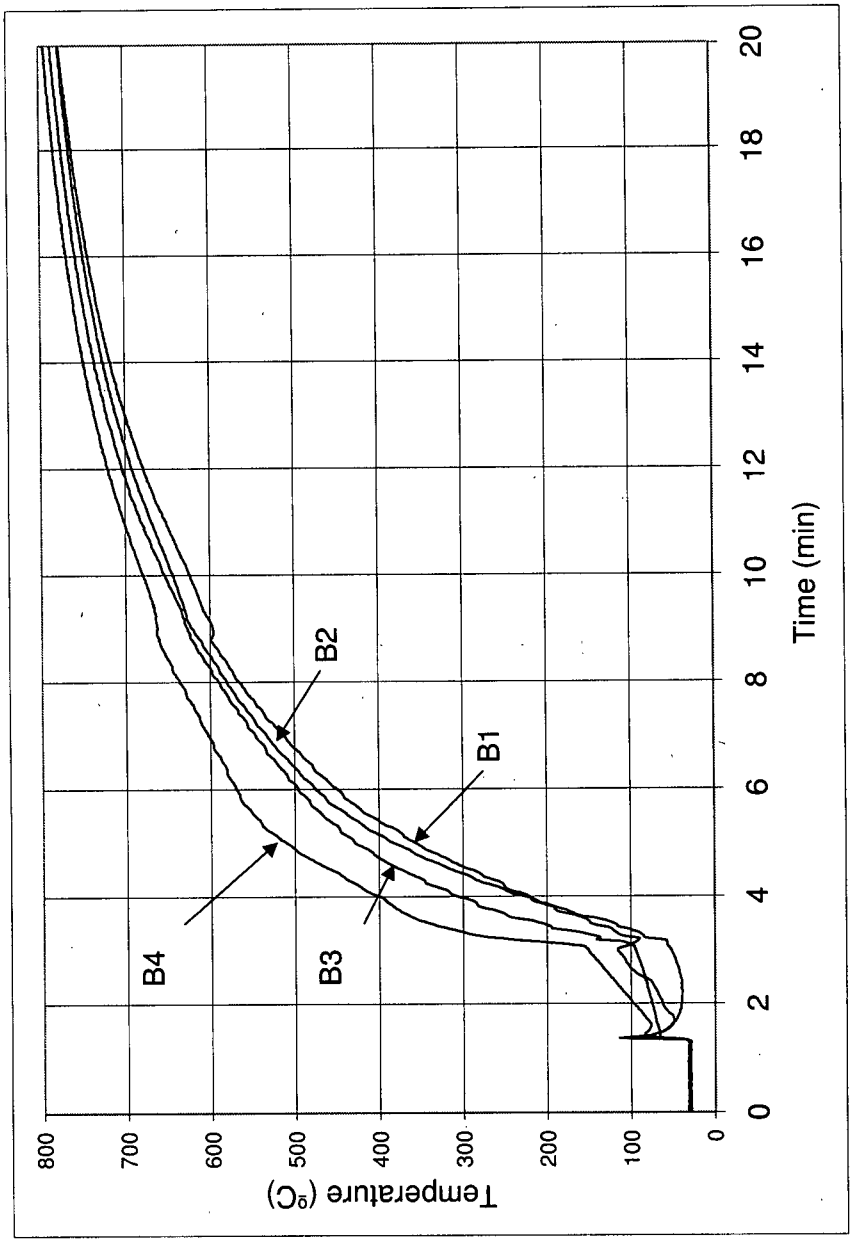

Figure F.66: Run 18 Bed Temperature History. Mix 6 at 2 rpm ($\bar{d}_p = 1.3$mm, $\sigma_p^* = 0.15$, $n_{RR} = 11.8$)

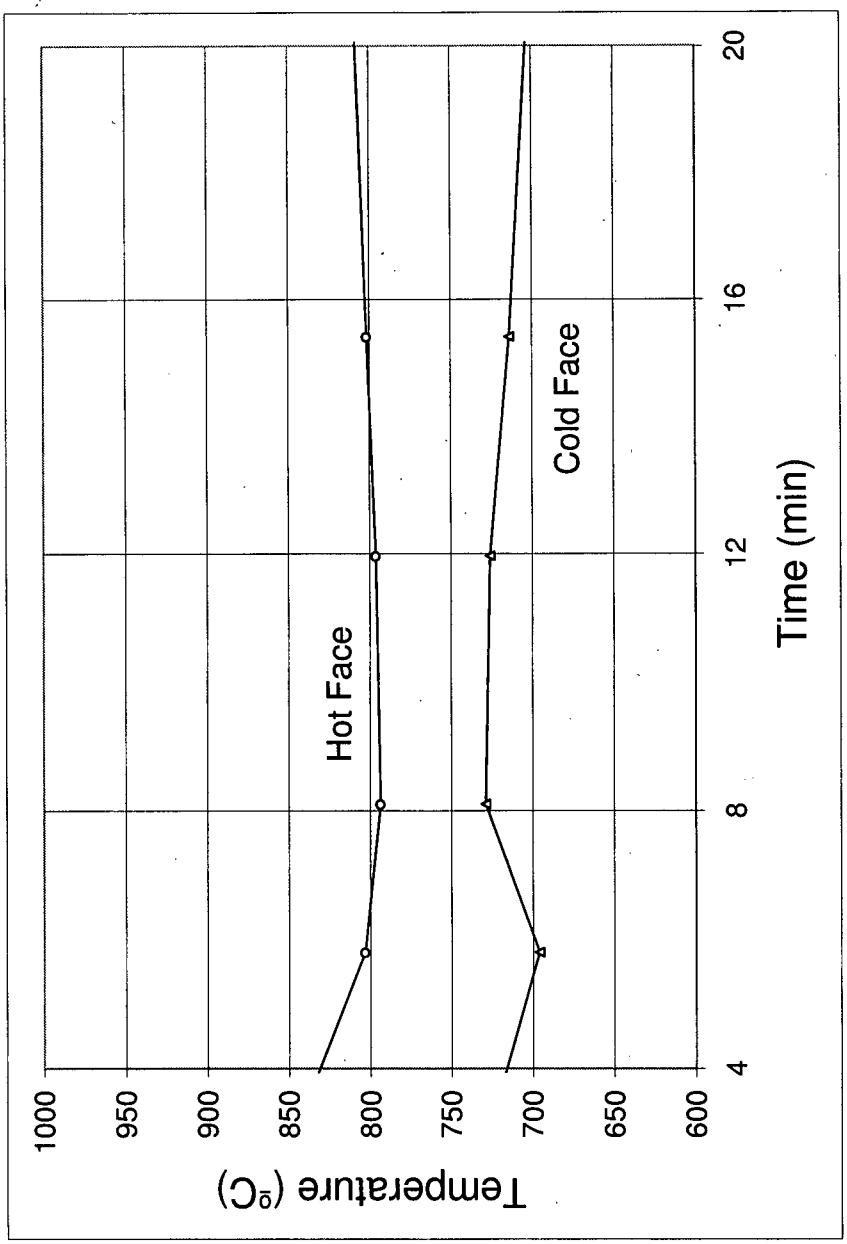

Figure F.67: Run 18 Wall Temperature History. Mix 6 at 2 rpm ($\bar{d}_p = 1.3$mm, $\sigma_p^* = 0.15$, $n_{RR} = 11.8$)

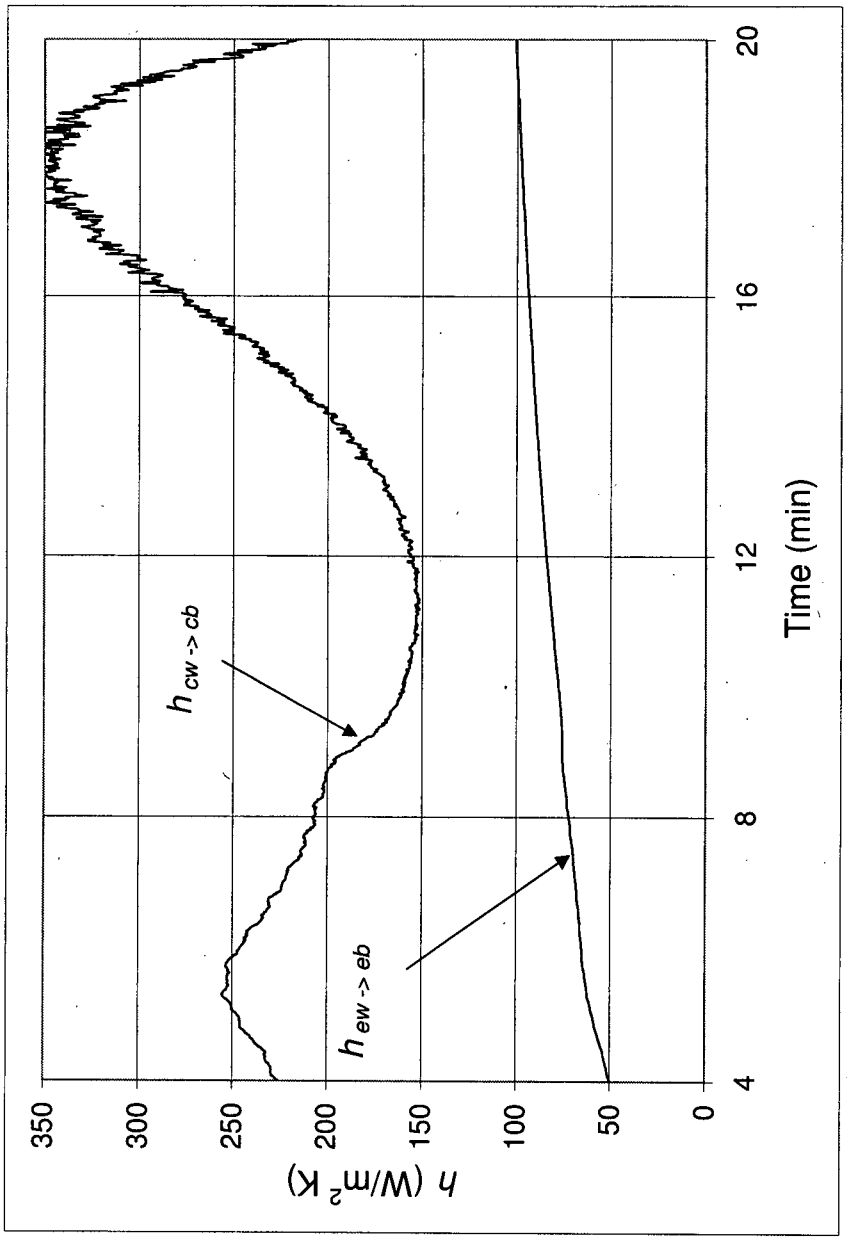

Figure F.68: Run 18 Exposed Wall to Exposed Bed, $h_{ew \to eb}$, and Covered Wall to Covered Bed, $h_{cw \to cb}$, Heat Transfer Coefficients. Mix 6 at 2 rpm ($\bar{d}_p = 1.3$mm, $\sigma_p^* = 0.15$, $n_{RR} = 11.8$)

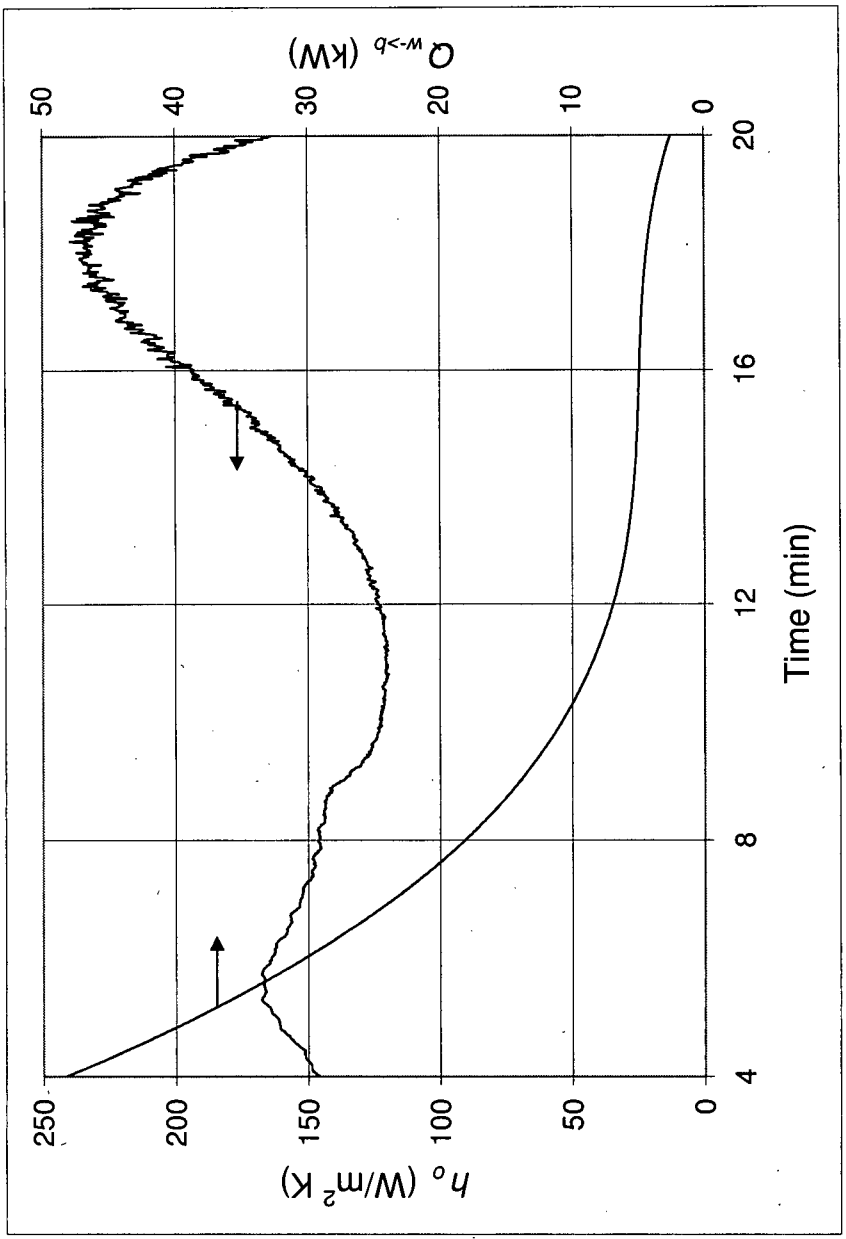

Figure F.69: Run 18 Overall Wall to Bed Heat Transfer Coefficient, h_o, and Heat Flow, $Q_{w\to b}$. Mix 6 at 2 rpm ($\bar{d}_p = 1.3$mm, $\sigma_p^* = 0.15$, $n_{RR} = 11.8$)

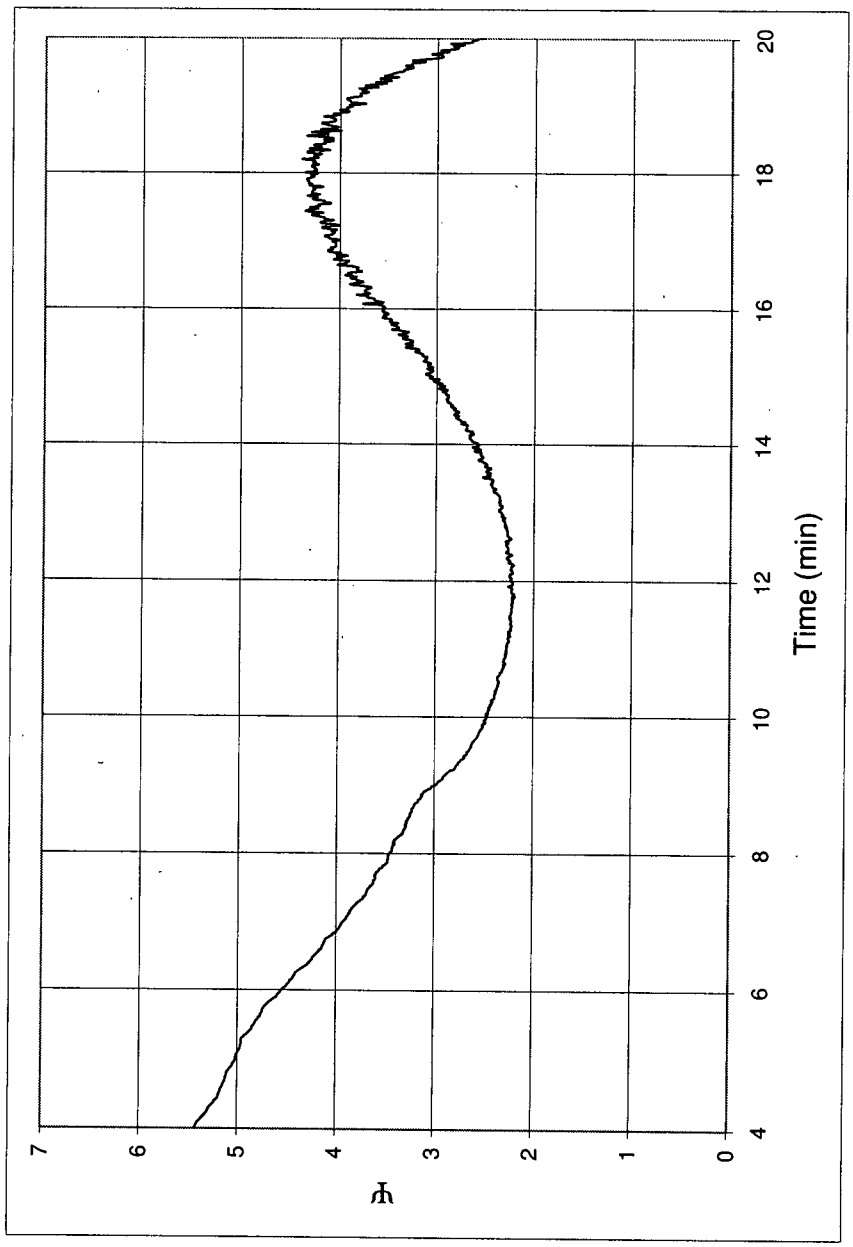

Figure F.70: Run 18 Ratio Between Heat Flow to Covered Wall and Exposed Wall, Ψ. Mix 6 at 2 rpm ($\bar{d}_p = 1.3$mm, $\sigma_p^* = 0.15$, $n_{RR} = 11.8$)

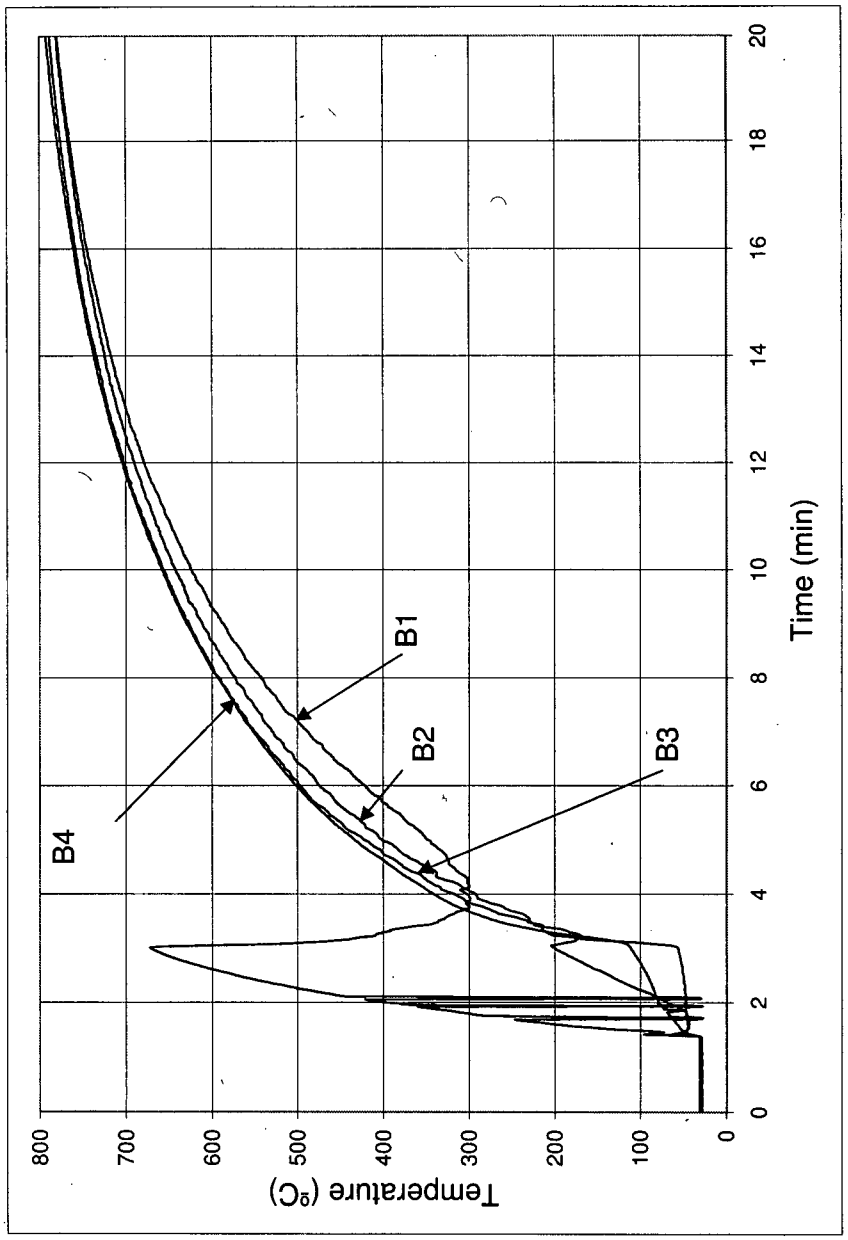

Figure F.71: Run 19 Bed Temperature History. Mix 4 at 2 rpm ($\bar{d_p} = 3.0$mm, $\sigma_p^* = 0.09$, $n_{RR} = 15.5$)

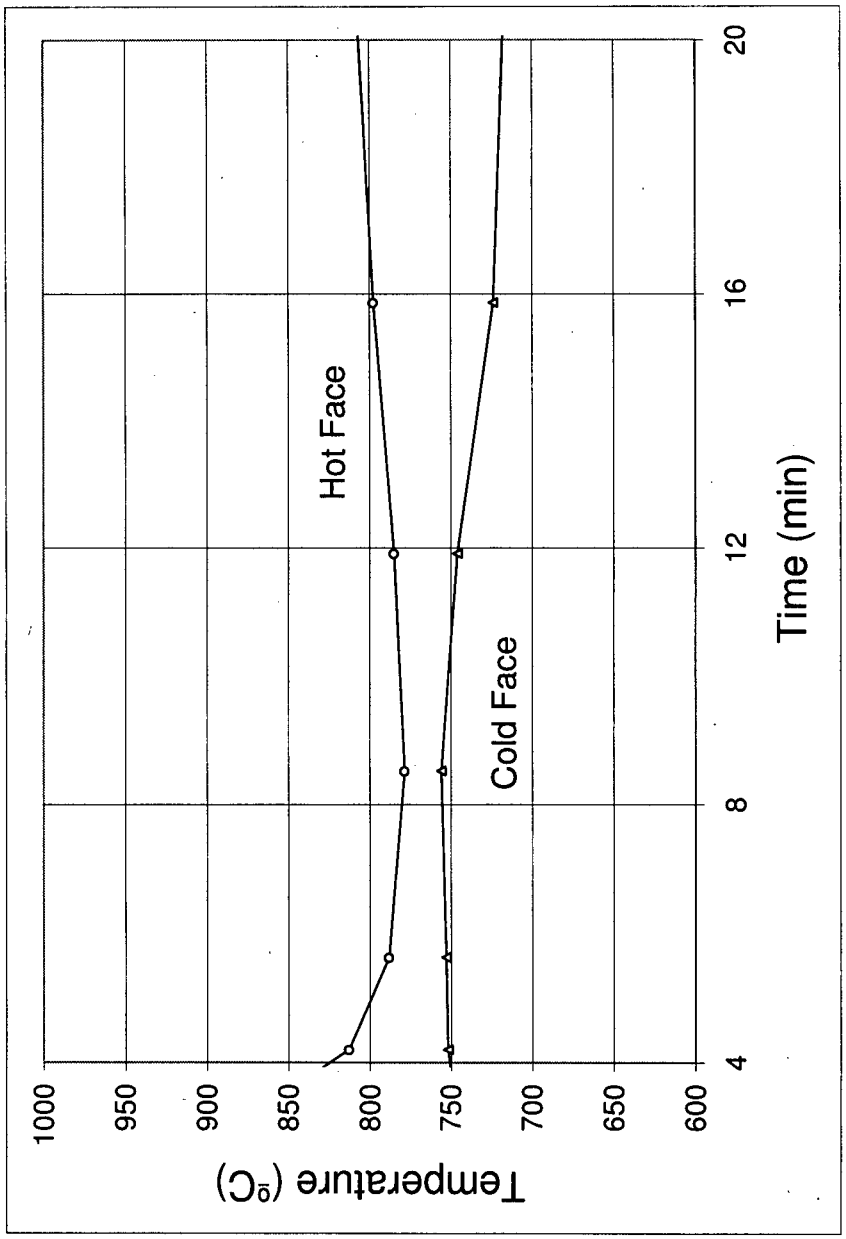

Figure F.72: Run 19 Wall Temperature History. Mix 4 at 2 rpm ($\bar{d}_p = 3.0$mm, $\sigma_p^* = 0.09$, $n_{RR} = 15.5$)

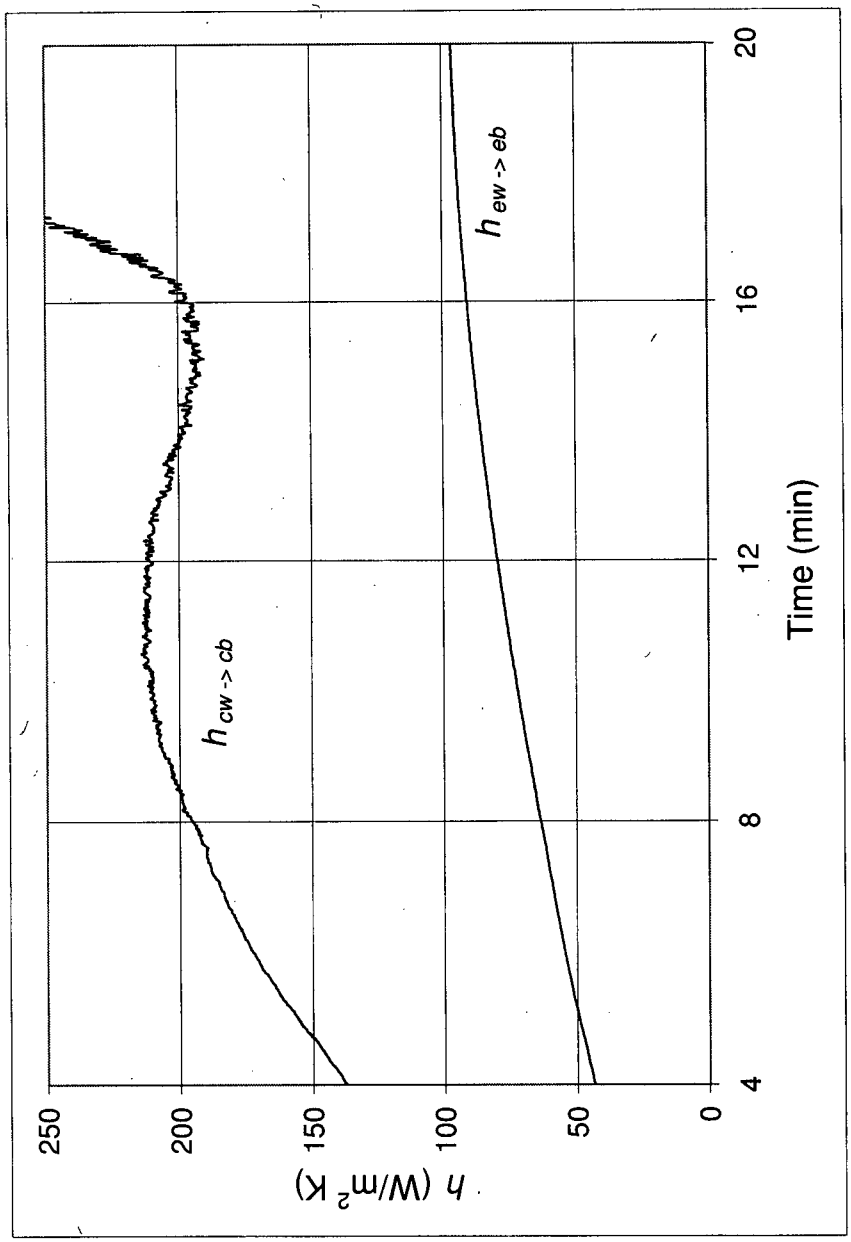

Figure F.73: Run 19 Exposed Wall to Exposed Bed, $h_{ew \to eb}$, and Covered Wall to Covered Bed, $h_{cw \to cb}$, Heat Transfer Coefficients. Mix 4 at 2 rpm ($\bar{d}_p = 3.0$mm, $\sigma_p^* = 0.09$, $n_{RR} = 15.5$)

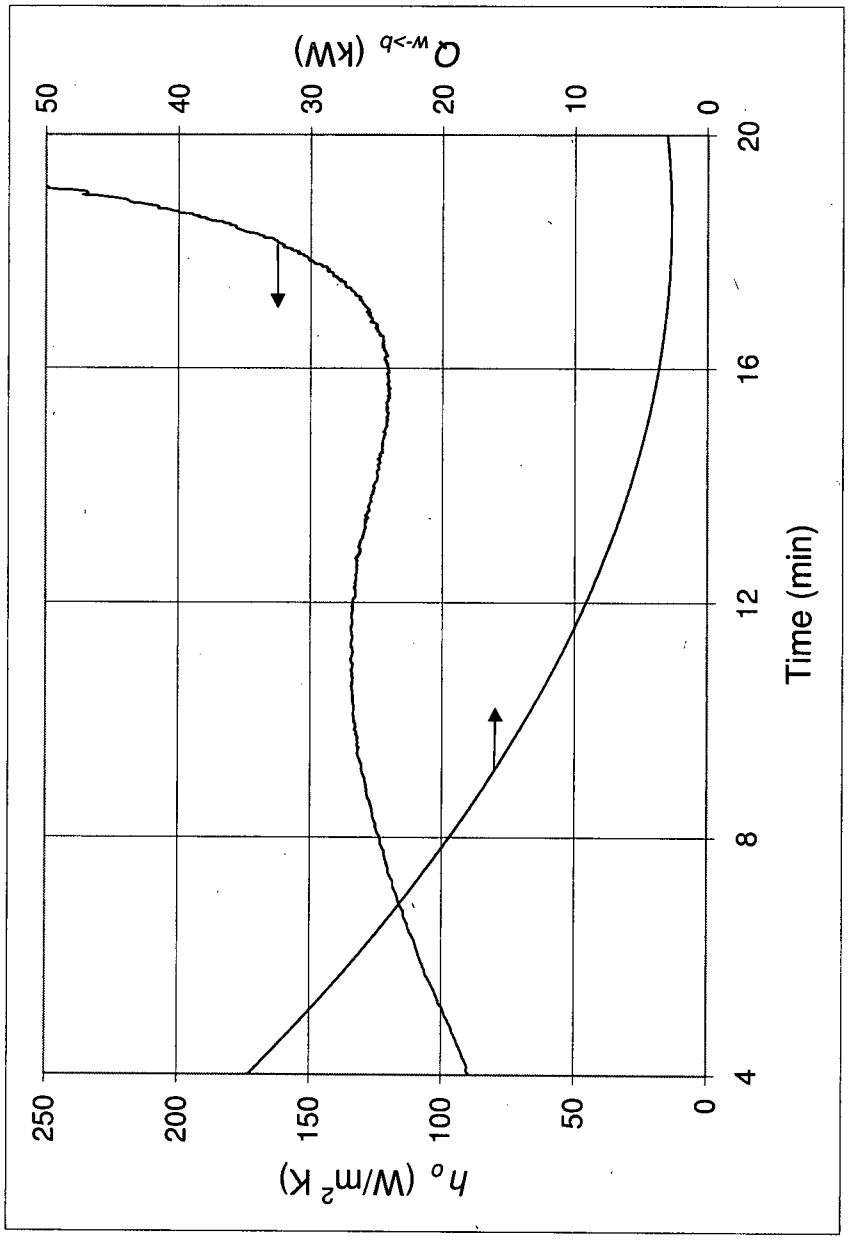

Figure F.74: Run 19 Overall Wall to Bed Heat Transfer Coefficient, h_o, and Heat Flow, $Q_{w\to b}$. Mix 4 at 2 rpm ($\bar{d}_p = 3.0$mm, $\sigma_p^* = 0.09$, $n_{RR} = 15.5$)

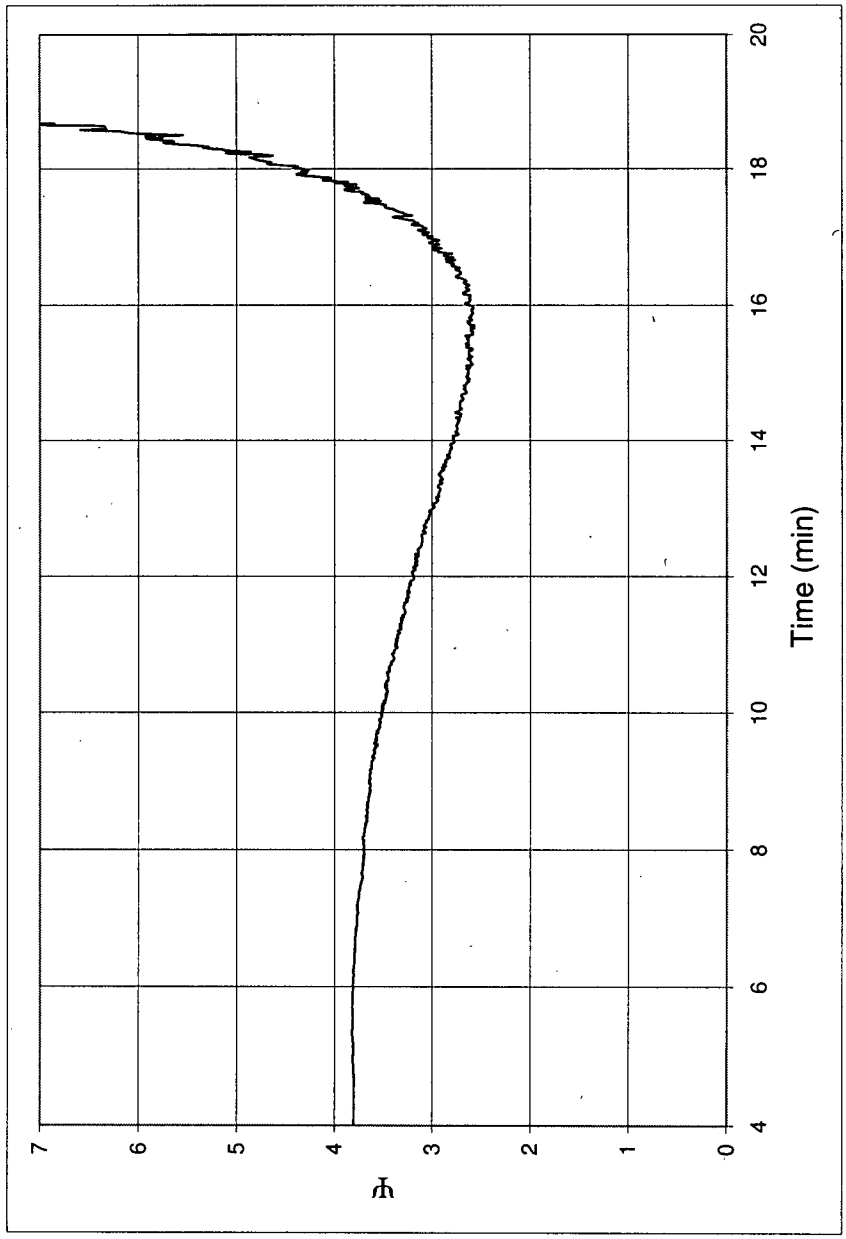

Figure F.75: Run 19 Ratio Between Heat Flow to Covered Wall and Exposed Wall, Ψ. Mix 4 at 2 rpm ($\bar{d}_p = 3.0$mm, $\sigma_p^* = 0.09$, $n_{RR} = 15.5$)

Table F.1: Bed Temperatures at Select Times

Run	Time (min)	B1 °C	B2 °C	B3 °C	B4 °C	Ave Temp °C
3	4.98	221.5	282.9	345.4	399.8	312.4
	5.00	222.7	283.9	347.1	402.2	314.0
	5.02	223.6	285.3	348.9	405.5	315.8
	7.48	407.2	450.5	510	537.6	476.3
	7.50	408.7	451.2	511.1	539.4	477.6
	7.52	410	452.2	511.7	540.6	478.6
	9.99	546	552.4	592.2	611.4	575.5
	10.00	546.8	553.1	592.9	612.3	576.3
	10.02	547.5	553.4	593.6	612.9	576.9
	12.49	616.9	623	654	667.5	640.4
	12.50	617.3	623.1	654.5	667.5	640.6
	12.52	617.7	623.4	654.8	667.9	641.0
	14.99	675.3	670.9	695	705	686.6
	15.01	675.7	671.5	695	705	686.8
	15.02	675.9	671.9	695.4	705.3	687.1
	17.49	708.1	709	726	732.3	718.9
	17.51	708.2	709.3	726.2	732.6	719.1
	17.52	708.3	709.2	726.2	732.6	719.1
	19.99	734.9	732.5	744.9	749.8	740.5
	20.01	734.9	732.7	744.8	749.9	740.6
	20.02	735.1	732.9	744.9	749.8	740.7

4	4.99	357	347.4	453.2	466.4	406.0
	5.01	358.4	349.6	454.4	467.1	407.4
	5.02	360.2	351	455.7	468.6	408.9
	7.49	528.5	545.6	594.9	599	567.0
	7.51	529.6	546	596	599.2	567.7
	7.53	530.6	546.7	596.2	600	568.4
	9.99	618.2	630.2	660	664	643.1
	10.01	619.1	630.9	660.9	664	643.7
	10.03	620	631.4	661	664.5	644.2
	12.48	678.8	683.1	704.1	705.5	692.9
	12.49	679.3	683.4	704.3	705.7	693.2
	12.51	679.5	683.6	704.8	705.7	693.4
	15.00	719.7	720.3	734.6	734.5	727.3
	15.02	719.8	720.7	734.5	734.6	727.4
	15.03	720.2	720.8	735	734.7	727.7
	17.48	746.9	744.3	754.6	753.1	749.7
	17.50	747	744.4	754.8	753.2	749.9
	17.52	747.3	744.6	755.1	753.4	750.1
	19.98	765.3	760.4	768	766.4	765.0
	20.00	765.2	760.4	768	766.3	765.0
	20.02	765.4	760.5	768.1	766.4	765.1
5	5.00	316.1	321.2	395.6	408.6	360.4
	5.01	316.5	323.3	400	409.5	362.3
	5.03	316.9	324.8	402.5	410.6	363.7
	7.49	484.7	512.2	566.6	575.9	534.9
	7.50	485.5	513.3	566.7	576.7	535.6
	7.52	486.7	514.6	567.8	577.5	536.7
	9.99	600.7	611.9	645	652.4	627.5
	10.01	600.7	611.9	645	652.4	627.5
	10.03	601.3	612.6	645.6	653.1	628.2
	12.50	669.5	674.6	697.2	700.7	685.5
	12.52	670	674.8	697.3	700.9	685.8
	12.54	670.6	675.1	697.9	701.3	686.2
	14.99	716.7	716.1	731.3	733.2	724.3
	15.01	716.8	716.2	731.4	733.6	724.5
	15.02	717	716.3	731.7	733.4	724.6
	17.50	747.8	745	756.5	754.6	751.0
	17.51	747.8	745.3	756.7	754.6	751.1
	17.53	748	745.6	757	754.7	751.3
	19.98	769.1	764.5	772.3	770.6	769.1
	20.00	769.1	764.7	772.4	770.6	769.2
	20.02	769.3	764.9	772.5	770.7	769.4

8	4.99	173.3	269	340.2	350.7	283.3
	5.01	175.1	270.9	341.4	352.6	285.0
	5.03	176.5	272.7	342.7	354	286.5
	7.47	351.6	446.3	501.1	508.6	451.9
	7.49	352.7	447.3	501.9	509	452.7
	7.51	353.6	448.6	503	510.1	453.8
	9.99	494.6	553.8	595	596.4	560.0
	10.01	495.3	554.7	595.7	597.1	560.7
	10.03	496	555.9	595.7	597.8	561.4
	12.48	581.3	623.4	656.6	656.5	629.5
	12.50	581.6	623.7	656.6	656.7	629.7
	12.52	582.4	624.2	656.8	657	630.1
	14.98	645.4	675.1	700.4	698.1	679.8
	15.00	645.6	675.4	700.7	698.3	680.0
	15.02	645.7	676.1	700.7	698.5	680.3
	17.50	693.2	713.4	732.2	728.5	716.8
	17.52	693.4	713.6	732.4	728.8	717.1
	17.54	693.8	713.8	732.5	728.9	717.3
	19.99	727.4	741.6	756.2	751	744.1
	20.01	727.5	741.8	756.7	751.3	744.3
	20.03	727.6	742.2	756.6	751.4	744.5
9	5.00	298.5	347.3	416.4	419.5	370.4
	5.01	300.7	350.2	417.5	421.6	372.5
	5.03	302.5	352.5	418	423.4	374.1
	7.49	515.7	533.5	572.7	568.9	547.7
	7.51	515	533.7	574.4	569.4	548.1
	7.53	514.3	534.3	575.9	570	548.6
	9.99	606.2	613.7	642.1	635.2	624.3
	10.01	606.7	614.5	642.4	635.5	624.8
	10.03	606.7	615.3	642.6	636	625.2
	12.49	660.8	670.5	691.4	684.2	676.7
	12.51	661.6	670.7	691.7	684.6	677.2
	12.53	661.7	671.3	691.8	684.8	677.4
	14.99	694.5	706.6	725.7	718	711.2
	15.01	695.3	706.6	725.9	718.1	711.5
	15.03	695.6	706.8	726.4	718.4	711.8
	17.48	729.1	735.8	752.1	742.6	739.9
	17.50	728.9	736.3	752.3	743	740.1
	17.52	728.9	736.5	752.7	743	740.3
	19.98	755.8	759.3	773	763.3	762.9
	20.00	757.3	759.7	773.2	763.6	763.5
	20.02	758.2	759.6	772.8	763.6	763.6

10	5.00	352.4	406	435.9	457.1	412.9
	5.02	355.8	407.2	437.5	458.6	414.8
	5.03	357.6	409.4	439.3	459.5	416.5
	7.49	512.3	562.8	576.5	575.8	556.9
	7.51	513.2	563.3	577.2	576.4	557.5
	7.53	513.6	564.3	577.9	577.4	558.3
	9.99	611	639.8	652.9	650.4	638.5
	10.01	611.8	639.9	653	650.5	638.8
	10.03	612.3	640.5	652.9	651.6	639.3
	12.49	676.9	696.5	706	704.1	695.9
	12.51	677.4	696.5	706.4	704.4	696.2
	12.53	677.6	696.7	706.7	704.7	696.4
	14.99	720.3	732.5	741.2	739.4	733.4
	15.01	720.7	732.5	741.7	739.5	733.6
	15.03	720.9	732.5	741.6	739.8	733.7
	17.49	750.5	757.2	764.6	762.1	758.6
	17.51	750.7	757.2	764.8	762.9	758.9
	17.53	751.3	757.2	765.1	762.3	759.0
	19.99	769.1	772.5	779.9	778.5	775.0
	20.00	769.2	772.7	780.1	778.1	775.0
	20.02	769.5	773.1	780	778.5	775.3
11	4.97	294.2	323.7	354.3	396.9	342.3
	5.01	296.6	327	357.4	398.9	345.0
	5.03	297.6	328	358.9	399.2	345.9
	7.49	478.5	524.6	529.2	533.8	516.5
	7.51	479.4	526.2	531	534.5	517.8
	7.53	480.8	527.4	531.9	535.4	518.9
	9.99	586.4	611	617.4	618.3	608.3
	10.01	586.3	611.6	617.5	619	608.6
	10.02	587	612.6	618	619.3	609.2
	12.48	650.3	667	672.6	674.1	666.0
	12.50	650.5	667.6	673	674.7	666.5
	12.52	651	668.1	674	675	667.0
	15.00	697.6	705.7	711.1	713.8	707.1
	15.02	698	705.9	711.6	713.8	707.3
	15.04	698.3	706.2	712.1	714	707.7
	17.49	727.8	733.5	739.1	741.1	735.4
	17.51	727.8	734	739.2	741.2	735.6
	17.53	728.2	733.9	739.3	741.5	735.7
	19.99	749.7	752.4	758.6	760.2	755.2
	20.01	749.8	752.6	758.7	760.6	755.4
	20.03	749.9	752.7	758.9	760.6	755.5

12	5.00	268.7	310.7	351.6	351.2	320.6
	5.02	269.2	313.8	354.3	353.3	322.7
	5.03	270.9	317.3	357.7	355.1	325.3
	7.49	461.8	511.5	532.9	542.8	512.3
	7.51	462.5	512.7	534.4	543.4	513.3
	7.53	464.3	513.5	535.1	544.2	514.3
	9.99	579.9	611.7	625.9	634.2	612.9
	10.01	580.7	612.7	626.7	634.8	613.7
	10.03	580.9	612.8	626.5	635.3	613.9
	12.49	653.9	676.5	686.1	692.2	677.2
	12.51	653.9	677.1	686.9	693.1	677.8
	12.53	655.1	677.9	687.5	692.8	678.3
	14.99	705.1	718.5	727.1	731.5	720.6
	15.01	705.2	718.8	727	731.9	720.7
	15.03	705.4	718.5	726.9	733	721.0
	17.49	737.3	746.1	753.1	758.1	748.7
	17.51	736.9	745.5	753	757.4	748.2
	17.53	737.8	746.3	753.6	757.4	748.8
	19.99	758.8	764.6	771.4	775.4	767.6
	20.00	758.5	764.2	771.8	776.8	767.8
	20.02	759.3	764.7	772.4	776	768.1
13	5.00	252	284	332.9	351.5	305.1
	5.02	252.9	285.5	334.9	354.1	306.9
	5.04	253	288.2	337.1	355.7	308.5
	7.50	416.1	474.3	501.4	522.5	478.6
	7.51	417.3	475.4	502.5	523.3	479.6
	7.53	418.2	476.8	503.4	525.1	480.9
	9.99	535.5	574.6	588.9	605.9	576.2
	10.01	536.2	574.9	589.5	606.1	576.7
	10.03	537.1	575.8	590.1	607	577.5
	12.49	610	639	653.8	664.8	641.9
	12.51	610.7	638.8	653.5	666.4	642.4
	12.53	611.5	639.8	654.3	665.8	642.9
	14.99	667.5	684.7	697.9	706.9	689.3
	15.01	667.4	684.7	698	706.8	689.2
	15.03	668.4	685.3	697.9	708.4	690.0
	17.49	706.7	719.8	730.6	738.8	724.0
	17.51	706.9	720.5	729.6	738.1	723.8
	17.53	706.3	720.3	730.7	738.5	724.0
	19.99	734.2	743.2	752.2	759	747.2
	20.01	734	742.8	752.8	759.1	747.2
	20.03	734.5	743.3	753	759.7	747.6

14	4.99	281.4	320.8	372.7	416.1	347.8
	5.01	282.6	323.4	374.4	417	349.4
	5.03	284.1	326.2	376.2	419	351.4
	7.49	483.3	521.4	534.6	579.1	529.6
	7.51	484.5	523.3	536.1	580.1	531.0
	7.53	485.1	524.9	537.9	581.2	532.3
	9.99	593.3	616.9	620.1	653.5	621.0
	10.01	593.3	617.6	620.2	654.8	621.5
	10.03	593.7	618.3	621.3	654.2	621.9
	12.49	666	681.2	686.7	708.5	685.6
	12.51	665.7	682	687.2	708.1	685.8
	12.53	665.9	682.2	687.5	708.8	686.1
	14.98	717.2	725.8	731.8	746.6	730.4
	15.00	717.4	726.1	732.6	747.6	730.9
	15.02	717.5	726.6	732.4	746.7	730.8
	17.48	751.2	756.1	763.8	775.7	761.7
	17.50	750.9	756.3	763.7	776.3	761.8
	17.52	751.4	756.8	764	776.2	762.1
	20.00	774.8	776.6	783.8	794.4	782.4
	20.02	774.8	776.6	784.1	794.5	782.5
	20.04	774.9	777	784.3	794.5	782.7
15	4.99	264.4	266.7	378.6	492.6	350.6
	5.01	266.2	269.1	382.2	492.7	352.6
	5.03	267.2	271.4	385.6	492.2	354.1
	7.49	419.5	467.2	503.5	557.4	486.9
	7.51	420.3	468.2	504.4	557.9	487.7
	7.53	421.1	468.8	505.1	557.9	488.2
	9.98	527.5	570.1	588.8	627.2	578.4
	10.00	528.4	571.1	589.7	627.9	579.3
	10.02	529.6	571.4	590.2	629.7	580.2
	12.50	609.3	639.9	654	688.3	647.9
	12.52	610.3	640.8	654.6	689.2	648.7
	12.54	610.4	641.1	655.4	690	649.2
	15.00	663.9	686.5	696.2	724.6	692.8
	15.01	664.5	687.2	696.3	725.2	693.3
	15.03	664.6	687	696.5	726.1	693.6
	17.49	704.2	719	728.7	749.9	725.5
	17.51	704.7	719.3	729.3	751.1	726.1
	17.53	704.4	719.9	729.5	750.2	726.0
	19.99	734.6	744	752.6	769	750.1
	20.01	734.3	744.2	752.7	769.2	750.1
	20.03	734.4	744.2	752.8	768.9	750.1

16	4.99	197.8	269.1	383.9	498.9	337.4
	5.01	200.9	273	385.4	500.6	340.0
	5.03	203.5	275.8	386.6	501.6	341.9
	7.49	397.9	457.2	486.8	521.8	465.9
	7.51	398.2	457.9	487.8	522.6	466.6
	7.53	398.7	458.4	488.9	524	467.5
	9.99	511.4	557.2	579.5	603.8	563.0
	10.01	512.1	557.2	580.1	604.7	563.5
	10.03	512.9	557.5	580.3	605.4	564.0
	12.49	590.6	623.2	642.2	660.6	629.2
	12.50	590.9	623.3	642.8	661.4	629.6
	12.52	591.3	623.4	643.2	660.8	629.7
	14.98	643.2	666.4	682.5	695.4	671.9
	15.00	643.8	666.7	682.9	695.5	672.2
	15.02	644.3	667.1	683.6	695.7	672.7
	17.50	687.5	700	716.1	726.1	707.4
	17.52	687.8	700.5	715.6	725.6	707.4
	17.54	688.2	701	716.3	725.6	707.8
	20.00	718	724.4	737.5	745.8	731.4
	20.02	717.8	724.6	737.8	745.7	731.5
	20.03	717.8	724.8	737.6	745.8	731.5
17	4.99	389.1	407	457.7	517.7	442.9
	5.01	390.7	408.4	458.4	517.8	443.8
	5.03	392.9	409.7	459.7	517.8	445.0
	7.49	538.3	551.7	571	598.1	564.8
	7.51	540.2	552.1	571.5	599.4	565.8
	7.53	541.2	552.8	571.8	600.2	566.5
	9.99	632.5	642.8	656	670.9	650.6
	10.01	632.6	643.4	656.6	671.6	651.1
	10.03	633.4	644.2	657	672	651.7
	12.49	699.9	705.4	716.1	727.3	712.2
	12.51	700.4	705.5	716.3	727.6	712.5
	12.52	701	705.5	716.5	727.9	712.7
	14.98	743	743.9	753.7	762.3	750.7
	15.00	743.4	744.1	754.1	762.4	751.0
	15.02	743.6	744.5	754.6	762.9	751.4
	17.48	769.1	768.6	777.9	785.7	775.3
	17.50	769.3	768.8	778.2	786	775.6
	17.52	769.3	769.2	778.3	786.1	775.7
	20.00	785.7	783.8	792.6	800.2	790.6
	20.02	785.9	783.7	792.7	800.3	790.7
	20.04	785.9	783.7	792.8	800.3	790.7

18	4.99	355.4	381	427.6	508.8	418.2
	5.01	357.3	383.8	429.1	510.7	420.2
	5.03	359.7	387	429.7	512.6	422.3
	7.49	539.8	557.4	567.8	618.9	571.0
	7.51	541	558.4	569.2	619.2	572.0
	7.53	543	558.8	570.1	619.8	572.9
	9.98	623.5	643.8	653	678.7	649.8
	10.00	624.2	643.9	653.7	679.4	650.3
	10.02	624.7	644.4	654.1	679.6	650.7
	12.50	689.1	701.7	712.6	729.2	708.2
	12.52	690	701.9	713.2	729.6	708.7
	12.54	690	702.6	713.2	729.9	708.9
	15.00	731.7	738.2	747.9	760	744.5
	15.02	732	738.4	748.3	760.4	744.8
	15.03	732.6	738.8	748.5	760.9	745.2
	17.49	758.3	761.8	770	780.8	767.7
	17.51	758.4	762	769.8	780.4	767.7
	17.53	758.6	762.1	770.7	780.6	768.0
	19.99	776.6	777	786.9	794.2	783.7
	20.01	776.4	777.6	787.2	794.4	783.9
	20.03	776.7	777.6	786.8	794.2	783.8
19	5.00	346.8	401.2	421.4	432.9	400.6
	5.01	349.7	402.6	423.4	434.2	402.5
	5.03	350.5	404.4	423.9	435.7	403.6
	7.49	519.2	551.3	570.2	572.5	553.3
	7.51	519.5	552	571.6	573.3	554.1
	7.53	520.5	551.9	573.2	573.7	554.8
	9.99	623.7	641.7	656	658	644.9
	10.01	624.6	642.5	656.7	658.1	645.5
	10.03	625	643.3	657.3	658.5	646.0
	12.49	688.7	699.3	711.2	713.1	703.1
	12.51	688.9	700	711.9	713.4	703.6
	12.53	689.4	700.2	712.1	713.9	703.9
	14.99	731.2	737.1	747.8	749.6	741.4
	15.01	731.7	737.7	747.4	749.7	741.6
	15.02	731.8	737.7	747.4	750	741.7
	17.48	760.6	762.6	771.3	775.2	767.4
	17.50	760.7	762.7	772.1	775.9	767.9
	17.52	761.1	763.3	771.5	775.2	767.8
	19.98	779.6	780.3	788.3	791.8	785.0
	20.00	780	780.7	788.4	791.9	785.3
	20.02	779.4	780.3	788.9	792.7	785.3

Table F.2: Run 3 Wall Temperatures

Time (min.)	R1 °C	R2 °C	R3 °C	R4 °C	R5 °C	R6 °C	R7 °C	R8 °C	R9 °C
0.0	953	951	808	816	992	751	963	930	851
2.3	750	872	806	815	914	748	796	864	845
5.3	745	790	803	817	842	744	781	778	840
7.3	739	774	797	797	824	740	774	767	829
9.3	741	772	787	796	814	735	773	764	811
11.3	743	769	776	776	813	729	772	768	797
13.3	750	770	763	771	813	722	775	769	781
15.3	754	770	751	762	811	714	776	771	765
20.3	766	773	721	739	812	693	779	770	731

Table F.3: Run 4 Wall Temperatures

Time (min.)	R1 °C	R2 °C	R3 °C	R4 °C	R5 °C	R6 °C	R7 °C	R8 °C	R9 °C
0.0	987	974	821	1008	1029	759	1013	930	-
2.0	741	885	822	752	936	755	830	864	-
4.3	733	826	819	740	848	755	820	778	-
6.7	719	790	815	741	822	752	807	767	-
8.7	724	779	807	748	820	748	802	764	-
10.7	733	780	797	755	817	743	800	768	-
12.5	745	778	785	767	827	735	794	769	-
14.5	747	778	773	770	826	729	798	771	-
20.3	767	780	736	789	828	703	795	770	-

Table F.4: Run 5 Wall Temperatures

Time (min.)	R1 °C	R2 °C	R3 °C	R4 °C	R5 °C	R6 °C	R7 °C	R8 °C	R9 °C
0.0	776	918	812	776	961	734	845	886	872
3.8	779	833	813	746	859	739	815	794	872
5.8	753	797	810	769	852	735	795	785	866
7.9	750	789	804	769	840	734	795	778	854
9.9	753	788	796	763	835	732	796	774	839
11.9	759	788	785	774	833	726	794	776	822
15.0	768	789	765	782	833	715	800	772	795
20.0	781	790	735	798	834	695	802	770	760

Table F.5: Run 8 Wall Temperatures

Time (min.)	R1 °C	R2 °C	R3 °C	R4 °C	R5 °C	R6 °C	R7 °C	R8 °C	R9 °C
0.0	1028	989	842	1038	1057	749	1041	-	-
3.7	791	832	843	808	908	748	852	-	-
5.5	762	818	841	788	866	746	842	-	-
7.6	763	816	836	791	860	745	824	-	-
9.5	768	815	827	790	854	743	826	-	-
11.5	773	813	816	792	850	738	825	-	-
13.6	778	810	804	796	848	732	825	-	-
16.4	781	790	735	798	834	695	802	-	-
20.4	784	808	785	802	847	721	823	-	-
24.4	791	805	759	807	846	704	822	-	-
28.4	795	800	738	812	843	687	819	-	-

Table F.6: Run 9 Wall Temperatures

Time (min.)	R1 °C	R2 °C	R3 °C	R4 °C	R5 °C	R6 °C	R7 °C	R8 °C	R9 °C
0.0	1011	-	836	1025	1047	747	1032	-	905
4.5	767	-	834	777	884	747	823	-	896
6.5	754	-	831	770	853	747	822	-	887
8.5	758	-	823	774	849	745	819	-	872
12.5	775	-	803	803	845	736	823	-	842
19.3	790	-	757	757	849	743	830	-	784

Table F.7: Run 10 Wall Temperatures

Time (min.)	R1 °C	R2 °C	R3 °C	R4 °C	R5 °C	R6 °C	R7 °C	R8 °C	R9 °C
0.0	1028	1065	832	1041	1059	767	1039	1046	885
4.6	787	857	830	772	873	754	831	842	879
6.8	724	801	827	773	851	754	812	825	870
9.3	751	784	819	776	848	750	804	810	853
12.3	759	785	801	785	846	741	806	811	828
15.3	763	791	780	796	841	727	810	813	802
21.3	784	798	742	807	842	700	811	811	761
25.3	787	800	722	810	839	684	808	811	741

Table F.8: Run 11 Wall Temperatures

Time (min.)	R1 °C	R2 °C	R3 °C	R4 °C	R5 °C	R6 °C	R7 °C	R8 °C	R9 °C
0.0	1051	1077	833	1051	1063	733	1039	1044	869
4.3	773	845	830	792	887	729	823	863	864
5.8	720	794	828	766	853	728	804	817	859
8.9	732	769	820	763	833	705	788	797	842
11.9	742	767	803	771	829	699	784	793	818
16.5	759	778	774	778	829	655	788	790	781
20.3	769	785	747	789	828	626	790	793	753
24.3	776	787	721	796	825	588	791	793	726

Table F.9: Run 12 Wall Temperatures

Time (min.)	R1 °C	R2 °C	R3 °C	R4 °C	R5 °C	R6 °C	R7 °C	R8 °C	R9 °C
0.0	1030	1064	825	1045	1062	-	1042	1049	874
4.2	789	849	823	777	898	-	817	829	871
6.2	761	805	820	774	864	-	804	810	864
8.8	759	792	814	777	851	-	802	807	852
11.3	765	789	799	781	837	-	808	815	824
15.2	769	787	776	794	838	-	808	813	799
19.3	778	793	752	801	837	-	808	812	771
24.7	788	800	723	804	833	-	805	806	740

Table F.10: Run 13 Wall Temperatures

Time (min.)	R1 °C	R2 °C	R3 °C	R4 °C	R5 °C	R6 °C	R7 °C	R8 °C	R9 °C
0.0	1045	1078	830	1060	1076	720	1059	1065	890
4.7	752	834	827	795	882	726	854	867	884
6.7	756	803	824	790	864	727	832	841	875
8.7	749	790	817	790	850	728	825	832	863
11.7	756	793	802	792	843	727	820	824	840
15.7	768	792	777	799	840	714	818	822	808
20.7	778	794	747	806	839	694	815	819	772
25.7	781	795	725	809	836	679	812	815	750
30.3	782	794	699	808	830	643	806	806	722

Table F.11: Run 14 Wall Temperatures

Time (min.)	R1 °C	R2 °C	R3 °C	R4 °C	R5 °C	R6 °C	R7 °C	R8 °C	R9 °C
0.0	1043	1080	853	1065	770	751	1071	1078	918
4.2	807	868	849	799	780	748	852	862	907
6.2	781	828	844	796	779	744	835	845	899
9.0	776	808	834	802	774	740	828	834	879
13.2	780	804	809	808	761	735	828	834	848
18.2	789	806	777	818	741	729	828	832	844
24.3	796	810	742	824	714	722	827	830	771
30.5	798	810	715	822	689	714	822	822	742
34.5	792	807	700	822	673	693	817	818	726

Table F.12: Run 15 Wall Temperatures

Time (min.)	R1 °C	R2 °C	R3 °C	R4 °C	R5 °C	R6 °C	R7 °C	R8 °C	R9 °C
0.0	1036	1066	833	1054	1074	715	1058	1062	893
5.7	803	845	827	810	892	709	844	873	885
9.0	778	808	816	812	862	725	843	848	868
12.3	790	809	801	809	856	696	825	844	845
15.8	779	802	782	813	845	717	830	835	821
19.1	789	804	763	809	845	669	822	830	798
25.3	786	796	733	814	839	677	818	818	764
33.5	785	795	699	802	827	623	804	806	726
40.7	772	786	675	797	814	613	795	791	698
47.7	768	777	656	783	803	584	780	781	680

Table F.13: Run 16 Wall Temperatures

Time (min.)	R1 °C	R2 °C	R3 °C	R4 °C	R5 °C	R6 °C	R7 °C	R8 °C	R9 °C
0.0	1017	1051	834	1036	1062	709	1038	1045	889
4.2	761	833	825	790	846	728	848	835	879
6.4	738	791	819	776	832	728	819	813	871
9.7	756	785	806	777	833	698	802	820	851
14.2	759	779	781	780	826	680	802	813	818
18.8	764	780	754	786	824	674	801	810	784
25.7	773	784	717	792	821	646	799	804	745
32.6	775	783	689	791	815	624	792	796	714
39.5	771	777	665	784	805	599	782	785	690
46.4	761	768	647	775	793	584	771	773	671
48.8	758	765	642	772	789	579	767	767	665

Table F.14: Run 17 Wall Temperatures

Time (min.)	R1 °C	R2 °C	R3 °C	R4 °C	R5 °C	R6 °C	R7 °C	R8 °C	R9 °C
0.0	1048	1074	839	1061	1081	700	1061	1066	901
3.8	786	877	885	782	893	697	853	884	896
5.4	756	821	832	780	865	695	829	847	892
7.8	752	793	825	777	840	675	818	828	880
11.2	756	785	810	788	837	668	813	819	854
15.5	768	787	783	805	840	666	816	820	819
21.3	781	794	748	816	842	658	817	818	778
26.3	786	797	722	820	840	646	817	817	749
31.3	788	796	697	815	834	625	812	812	724
36.3	783	793	681	812	828	615	806	806	709

Table F.15: Run 18 Wall Temperatures

Time (min.)	R1 °C	R2 °C	R3 °C	R4 °C	R5 °C	R6 °C	R7 °C	R8 °C	R9 °C
0.0	1042	1075	819	1066	1087	709	1066	1072	887
3.8	786	879	820	776	892	719	851	883	886
5.8	755	812	818	781	861	696	825	842	881
8.1	752	789	811	783	843	729	816	827	871
12.0	762	787	794	792	839	726	817	823	843
15.4	773	790	774	803	839	714	819	823	816
20.3	784	798	745	813	840	703	822	825	781
25.6	791	801	717	817	838	678	821	821	752
30.5	792	801	697	815	834	661	816	816	731
35.3	790	797	680	810	826	643	809	809	713
40.4	785	791	665	804	818	637	800	800	698

Table F.16: Run 19 Wall Temperatures

Time (min.)	R1 °C	R2 °C	R3 °C	R4 °C	R5 °C	R6 °C	R7 °C	R8 °C	R9 °C
0.0	1037	1070	833	1059	1082	732	1061	1068	897
4.2	763	845	830	771	873	752	830	854	893
5.6	743	800	828	756	845	753	813	829	889
8.5	736	776	819	763	825	756	803	814	874
11.9	749	776	802	778	826	746	807	815	847
15.9	768	786	777	796	833	724	816	821	813
20.7	785	798	747	812	838	717	821	824	779
25.6	794	805	722	818	840	695	822	824	752
30.5	795	805	700	819	837	672	818	819	732
35.3	794	802	684	814	830	661	811	811	716
40.8	788	795	667	808	821	642	802	802	700